The Dissertation Committee for Yunhan Huang Certifies that this is the approved version of the following Dissertation:

Behavior of Laterally Loaded Offshore Wind Monopiles in Sands

Committee:

Robert Gilbert, Supervisor

Kenneth Stokoe

John Tassoulas

Shin Tower Wang

Behavior of Laterally Loaded Offshore Wind Monopiles in Sands

by

Yunhan Huang

Dissertation

Presented to the Faculty of the Graduate School of

The University of Texas at Austin

in Partial Fulfillment

of the Requirements

for the Degree of

DOCTOR OF PHILOSOPHY

The University of Texas at Austin

May 2019

Dedicated to my family.

Acknowledgements

I would like to thank the following people who made invaluable contribution to help me complete the research: My supervisor, Dr. Robert Gilbert gave me the opportunity to work on this interesting topic, kindly shared his knowledge with me, and guided me to be a qualified engineer. Dr. Kenneth Stokoe gave his expertise on the small-strain behavior of soil and provided professional service of measuring the small-strain properties of soil in the field and in the laboratory. Dr. Shin Tower Wang, from Ensoft Inc., was very general to help and advise me on the research and solve my questions about the use of the software LPILE. Dr. Hossein Fadaifard, from Ensoft Inc., wrote the subroutine of the soil constitutive model in Abaqus and kept supporting me to make sure the proper use of the model. Dr. John Tassoulas help me complete the definition of the constitutive model and provided valuable advice and feedback which refined the theory.

My research was happy and meaningful because of the colleagues that I met in the last six years. At first, I worked with Hande, Asitha, and Ying in the geotechnical laboratory at Pickle Research Campus. They let me know how to enjoy the life in the lab and gave me suggestion whenever I needed help. Then James and Jonas joined the research group and help me build the robust loading frames and soil tank used for the research. Zhongze provided high quality data of the resonant column and torsional shear tests and Reihaneh conducted the geophone tests to measure accurate shear velocity profiles in the sand test bed. In the last year of my Ph.D. study, Lucas and Chihun made the atmosphere of doing the lab tests happy and enjoyable. I am so lucky to have Ahmed in the research team, he was always generous to help and work with me to solve many problems in the research and in the life.

My personal life in Austin was full of fun with my friends here. I had a wonderful roommate Kai who was kind and easy to get along with. I could not forget the countless coffee afternoons and PS4 game nights with Yumeng and Benchen, which made my life in Austin happy and colorful. In the last year on campus, I met Mieke, Jodie, Thiago, Meibai, and Jiali. We made nice memories when we play board games together, shared funny videos, and discussed JoJo's Bizarre Adventure.

My parents, Jialin and Rong, were constant source of strength of motivation supporting me complete this academic challenge, without them it would not have been possible.

Behavior of Laterally Loaded Offshore Wind Monopiles in Sands

Yunhan Huang, Ph.D.

The University of Texas at Austin, 2019

Supervisor: Robert Gilbert

To develop a more rigorous design approach for laterally loaded monopiles of offshore wind turbines under service loading, the conventional design approach needs to be modified and improved. The most commonly used conventional design approaches include API RP 2GEO (2014) and DNV (2018). The suitability of the conventional design approach was evaluated for the design of laterally-loaded piles at small displacements, which consisted of comparing (1) the measured and predicted lateral load versus displacement curves in the field tests, and (2) the monitored and estimated natural frequencies of the offshore wind turbines in Belgium using the conventional design approach. To improve the design approach, a soil constitutive model representing small-strain properties of sand was applied with three-dimensional finite element method (3-D FEM) models to simulate the laterally loaded piles. The maximum shear modulus of sand could be measured in situ by propagating shear waves through the soil. The non-linearity of the shear modulus with shear strain could be measured in the laboratory using resonant column and torsional shear tests. The 3-D FEM models were verified by element tests and performed on (1) laboratory foundation model tests using laterally-loaded spheres in sand beds, (2) field shallow foundation tests at Texas A&M University, and (3) field laterally-loaded pile test conducted on Mustang Island in 1966 that provided the original basis for the conventional design approach.

The following major conclusions are drawn from this research: (1) the analysis on the field laterally-loaded pile and the natural frequencies of the offshore wind turbine shows that the p-y method from the conventional design approach underestimates the initial stiffness for laterally-loaded piles and does not capture the non-linearity of the stiffness at small displacements, and (2) the predictions from the 3-D FEM models have a good agreement with the measurement from the laboratory foundation model tests and field tests by using the proposed soil constitutive model which captures the maximum shear modulus at very small strains and the relationship between the shear modulus, shear strain, and mean effective stress.

These conclusions lead to the following recommendations for the design of laterally loaded monopiles in sands: (1) the use of the conventional design approach should be avoided on the design of the offshore wind turbine monopiles under service loading, (2) small-strain properties of sand need to be known to capture the initial stiffness and non-linearity of laterally loaded piles at small lateral displacements, and (3) improved p-y curves could be established by extracting the p-y curves from the 3-D FEM models using the proposed soil constitutive model.

Table of Contents

List of Tables

List of Figures

Chapter 1: Introduction

In global, the installed capacity of offshore wind turbines has been increasing rapidly in the last few years. The U.S. offshore wind industry is planning to construct multiple large offshore wind farms at East Coast in the coming years. For the wind industry to be economic, the costs of the construction need to be significantly reduced in the future projects. The cost of the foundation of the offshore wind turbine can be further reduced by using better design, cheaper fabrication, and more efficient installation. Large diameter monopile is the most common foundation type used for offshore wind turbines built in the shallow water. However, the conventional design approach, which was calibrated based on field tests on slender piles, may not be suitable for the design of monopiles anymore. This research evaluated the feasibility of the conventional design approach and provided recommendations for improving the conventional design approach for monopiles.

1.1 BACKGROUND

The global market of offshore wind turbines has kept growing in the recent years. From the report of Offshore Wind Technologies Market (Beiter et al., 2018), in global, more than 3.5 GW of installed capacity was added during 2017, which made the installed capacity of cumulative offshore wind 16.3 GW by the end of 2017. Figure 1.1 shows the growth of the cumulative offshore wind capacity by country from 2001 to 2017. United Kingdom had the largest percentage of installed capacity in the world in 2017. Offshore wind projects in U.S. comprised only 0.2% of the installed global capacity at the end of 2017.

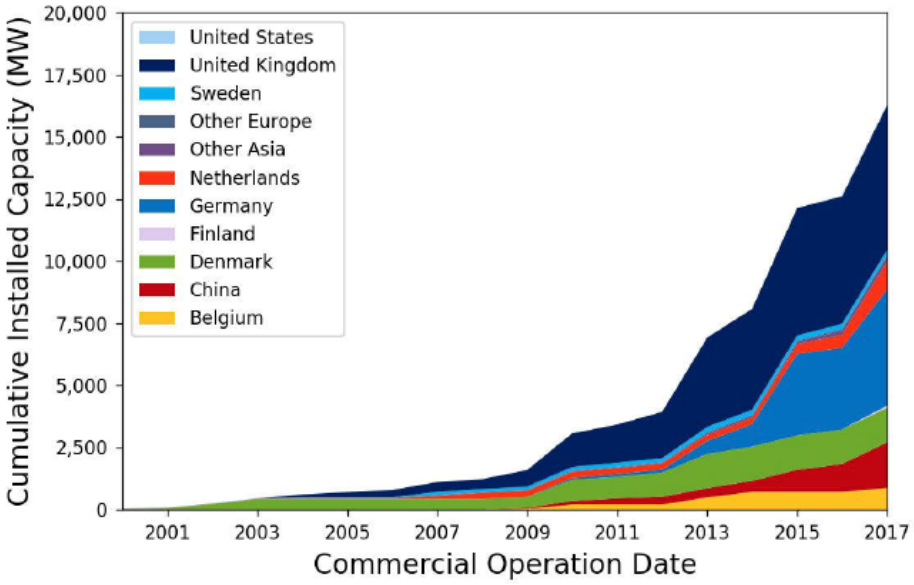

Figure 1.1: Share of cumulative installed offshore wind capacity by country (Beiter et al., 2018).

The global development pipeline announced by the developers in 2017 indicated that the growth rate of installed capacity would be 24% through 2023 (Figure 1.2). The development of the U.S. offshore wind industry would take off in the next few years. As of June 2018, the developers in the U.S. wind market announced a wind capacity of 1,906 MW to be installed by 2023.

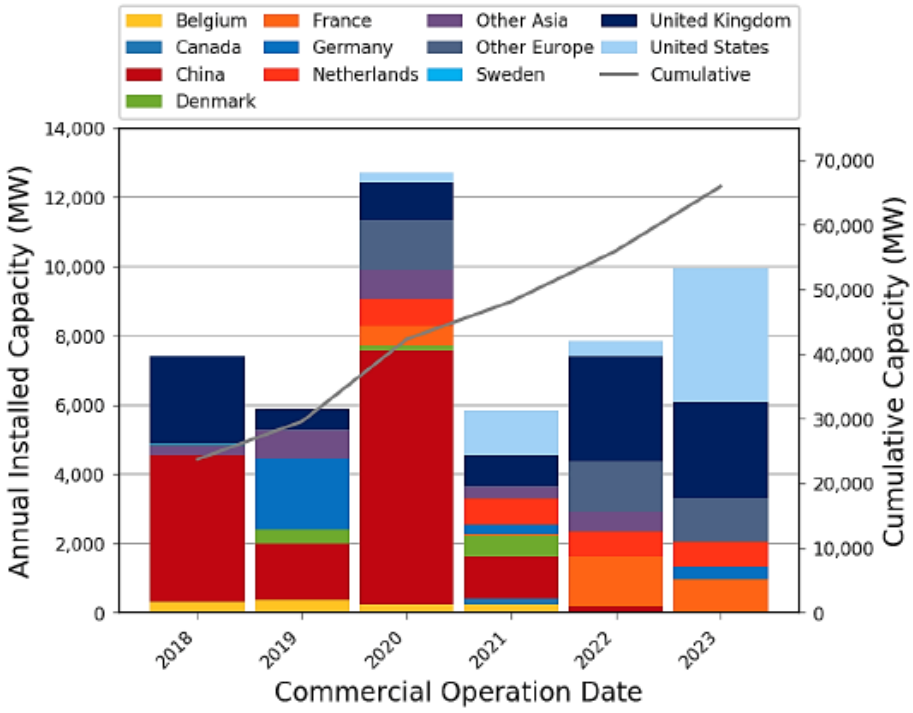

Figure 1.2: Developer-announced project pipeline through 2023 (Beiter et al., 2018).

The wind-rich areas of the U.S. East Coast are currently selected to develop more offshore wind projects. Figure 1.3 shows the map of U.S. offshore wind lease and call areas. According to the project pipeline, the state of Massachusetts sets a target of purchasing 1.6 GW of offshore wind by 2027. New York aims for 2.4 GW of offshore wind by the end of 2023 by adding a project of 800 MW of offshore wind capacity in 2018-2019. New Jersey moves toward a goal of 3.5 GW of offshore wind by 2030.

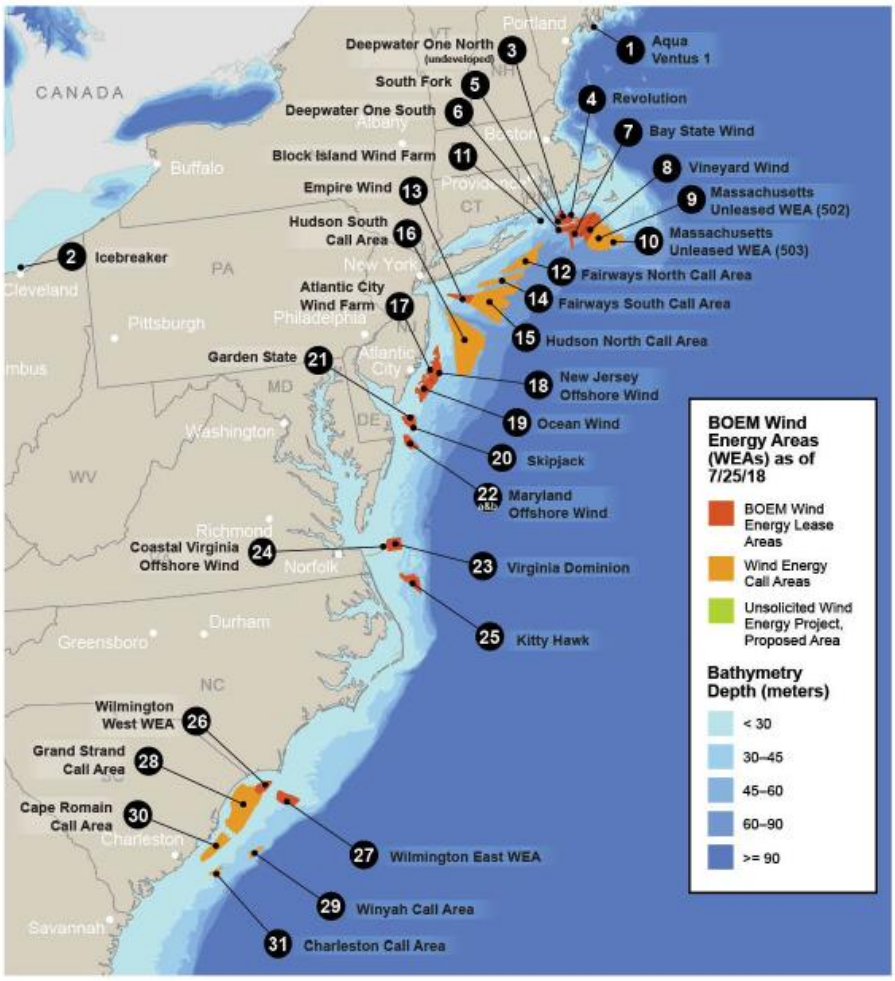

Figure 1.3: Map of U.S. offshore wind lease and call areas (Beiter et al., 2018).

The higher wind speed and shallower water depth determine East Coast to be the most attractive and economic area in the U.S. for now. In relatively shallow water up to 60 meters, fixed foundations are employed by almost all currently operating offshore wind turbines.

1.2 FOUNDATION FOR OFFSHORE WIND TURBINES

Types of fixed foundations for offshore structures include (a) gravity-based foundation, (b) monopile foundation, (c) caisson foundation, (d) multiple foundation, (e) multi-caisson foundation, and (f) jacket foundation (Figure 1.4). The monopile foundation is preferred for the global offshore wind turbines in relatively shallow water, which is commercially and technically compared to the other foundation types (Kallehave et al., 2015). The monopile foundation is also accepted as the major foundation type for the offshore wind turbines in the east coast of U.S.

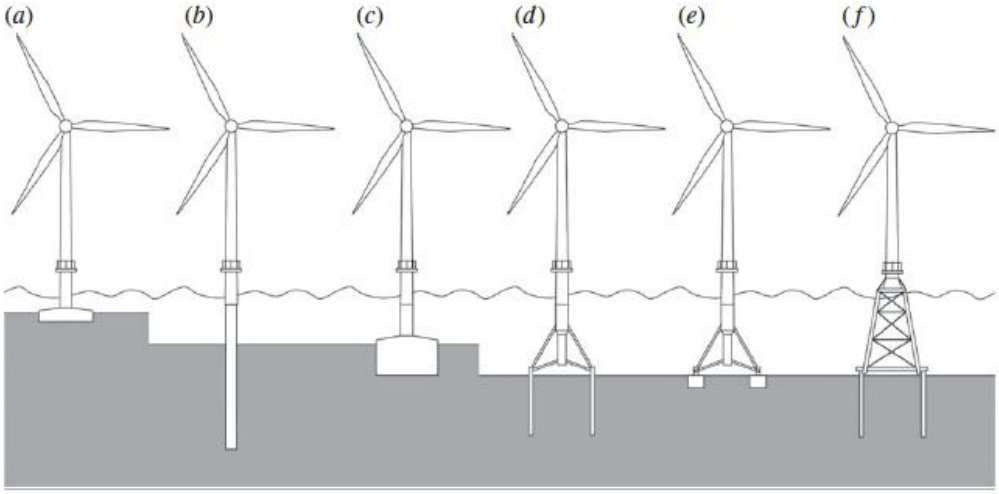

Figure 1.4: Different types of fixed foundations for offshore structures (Kallehave et al., 2015).

The structure of the monopile is made of a cylindrical steel tube with large diameter and small length to diameter ratio. To pursue more abundant wind resources, the offshore wind turbines are intended to be built in the relatively deep sea (around 60 meters). As the scale of the turbines increases with the higher wind speed, the size of the monopile increases too. In the recent design, the diameter of the monopile can be extended to 10 meters (Byrne et al., 2017). Figure 1.5 shows the monopile with diameter of 7.5 meters

which is designed to be feasible in water depths up to 35 meters. The larger wind turbine brings the challenge of the design for larger monopiles, especially the wave and wind load act with the dynamics of the turbine structures.

Figure 1.5: A 7.5-meter diameter monopile for Gode Wind Offshore Wind Farm (Kallehave et al., 2015).

1.3 CONVENTIONAL DESIGN APPRAOCH

The conventional design approach of offshore wind turbines uses frequency-based method. The natural frequencies of offshore wind turbines should be designed to avoid the range of operational frequencies of turbines. The natural frequencies of turbines that are concerned in the design are first mode natural frequency (fundamental natural frequency, f_0) and second mode natural frequency (second natural frequency, f_1) as shown in Figure 1.6. The operation frequencies (f_{op0}, f_{op1}, etc.) are from the dynamic loads of wind,

waves, rotation of the rotor, and etc. The natural frequencies should be separated from the operation frequencies with safety margins in the design (Figure 1.7).

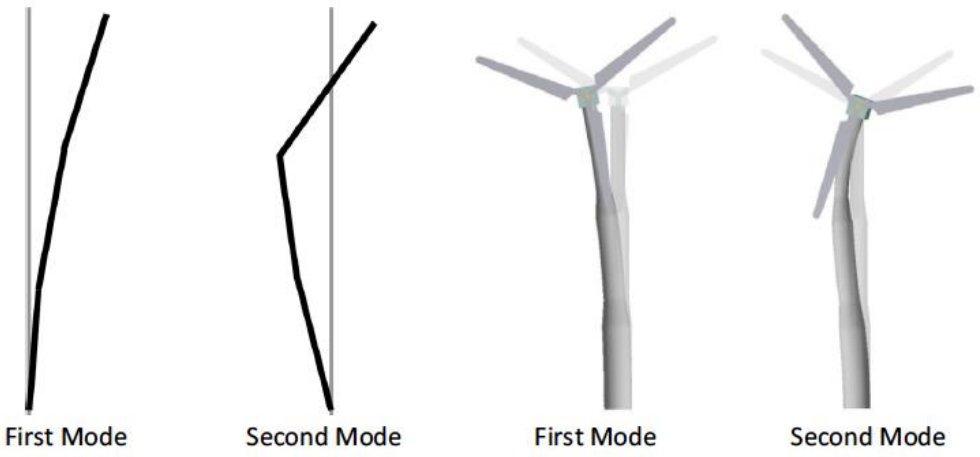

Figure 1.6: Natural models of a typical turbine (Austin and Jerath, 2017).

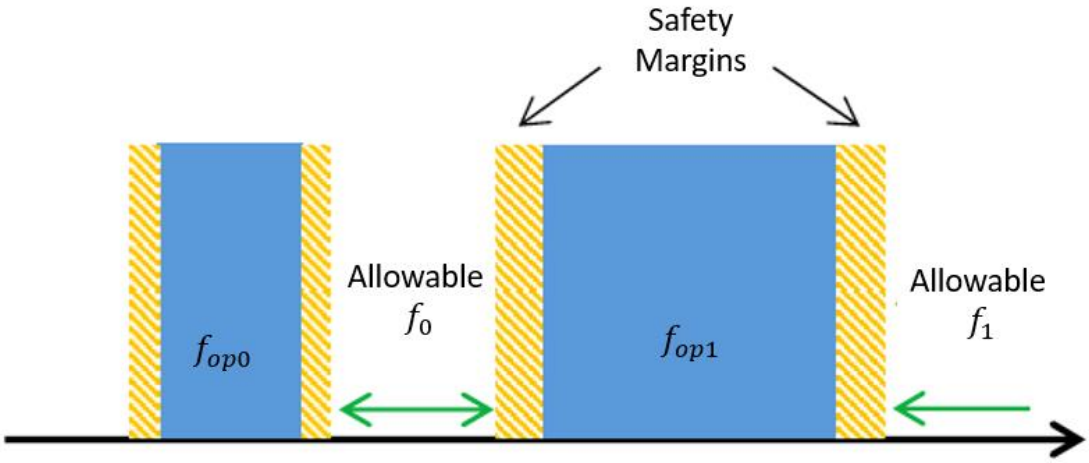

Figure 1.7: Allowable frequency range in frequency-based design (Austin and Jerath, 2017).

Figure 1.8 shows an integrated computer model of a typical offshore wind turbine including the wind turbine tower, transition piece, and foundation. The offshore wind turbine is modeled as a Euler-Bernoulli elastic beam. The beam is divided into finite elements with distributed mass from the structure material and water and soil inside of the structure. The soil around the elements is represented as a set of non-linear elastic springs acting along the embedded part of foundation. The non-linear elastic springs are commonly simulated using p-y curves (p-y method), where "p" is the lateral resistance from soil induced by the pile lateral deflection "y" at a given depth. DNV (2018) recommends that the p-y curves for design of piles with diameter of more than 1.0 m (e.g., monopiles) should to be validated for such use, e.g. by means of FE analysis.

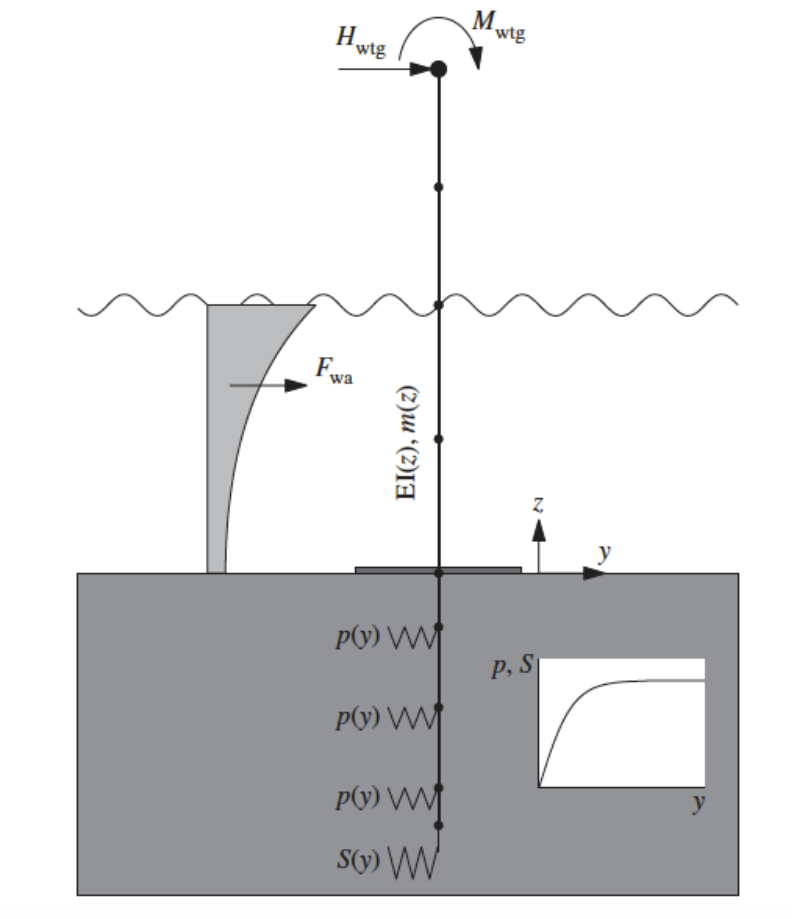

Figure 1.8: Integrated computer model applied in the design of monopile foundation; horizontal load from wind turbine generator, H_{wtg}; overturning moment, M_{wtg}; wave load, F_{wa}; bending stiffness, EI; distributed mass, m; non-linear elastic spring using p-y method, $p(y)$ (Kallehave et al., 2015).

Figure 1.9 shows the comparison of measured and designed fundamental natural frequencies for 400 offshore wind turbine structures supported by monopiles within different soil condition. The comparison indicates the fundamental natural frequency is underestimated by the conventional design approach. The inaccurate estimation of the pile-soil response by the conventional p-y method at small displacements is the major reason

of under-predicting the natural frequencies of offshore wind turbines (Kallehave et al., 2015).

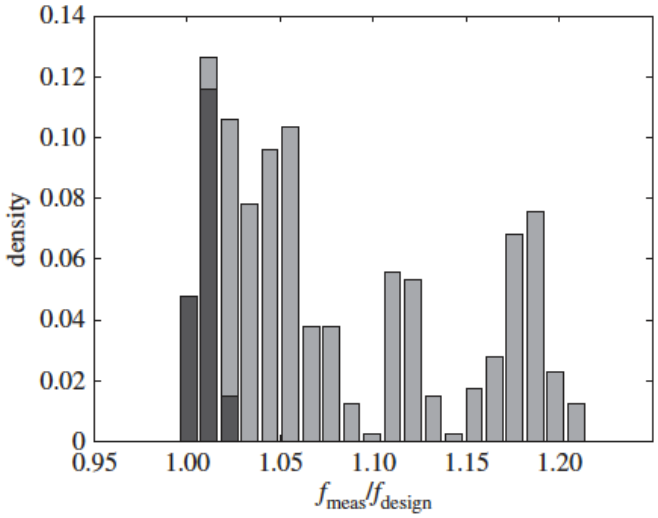

Figure 1.9: Comparison of measured and designed fundamental natural frequencies for 400 offshore wind turbines (Kallehave et al., 2015).

1.4 OBJECTIVES

The objectives of the research consist of:

(1) Evaluating the performance of the suitability of the conventional design approach for the prediction of the natural frequencies of the offshore wind turbines under service loading.

(2) Developing a soil constitutive model used in the three-dimensional finite element method (3-D FEM) to represent the small-strain behavior of sand in numerical modeling.

(3) Comparing the measurements from the laboratory foundation model tests and field tests with the predictions from the 3-D FEM models.

(4) Developing design recommendations based on the analysis results.

1.5 ORGANIZATION OF DISSERTATION

The dissertation consists of eight chapters:

Chapter 1 – Introduction: The background of the offshore wind energy industry, accepted foundation types for offshore wind turbines, challenges of current design methods for monopiles, research motivation, research objectives, and methodology for this study are presented.

Chapter 2 – Literature Review: The common practices of designing laterally loaded piles including the p-y method and 3-D finite element method (FEM) are presented. Several tests results from field-scale piles are analyzed to evaluate the feasibility of the conventional p-y method.

Chapter 3 – Dynamic Analysis on Offshore Wind Turbines: Wind turbines design report and field monitoring data provided by Parkwind in Belgium are summarized and analyzed.

Chapter 4 – Development of the Soil Constitutive Model with Non-linear Small-strain Behavior: A soil constitutive model is proposed to simulate the behavior of the sand at small strains for numerical modeling of 3-D FEM model in Abaqus. Element tests are conducted to check the performance of the proposed soil constitutive model.

Chapter 5 – Comparisons of the Measurements from Laboratory Foundation Model Tests with the Numerical Modeling Predictions: Laboratory foundation model tests are conducted, by laterally pushing a sphere into sand, to verify the performance of the proposed soil constitutive model used in 3-D FEM model.

Chapter 6 – Comparisons of the Measurements from Field Tests with the Numerical Modeling Predictions: Two field tests, including a settlement test on shallow foundation and a laterally load test on pile, are analyzed using 3-D FEM models with the proposed soil constitutive model.

Chapter 7 – Recommendations for improving p-y methods: Recommendations have been proposed to incorporate from this research into practical applications for the design of laterally loaded monopiles in sand.

Chapter 8 – Conclusions: The conclusions based on analyses and summary in the previous chapters, recommendations for the conventional p-y method, and future work are presented.

Chapter 2: Literature Review

In the current engineering practice, the p-y method based on Euler-Bernoulli elastic beam is the preferred option to analyze the lateral loaded piles. In the theory of Euler-Bernoulli elastic beam, the pile is considered as a beam supported by independent non-linear elastic springs which represent the local lateral soil reactions. The non-linear elastic springs are modeled using p-y curves (p-y method), where "p" is the spring soil reaction as a function of the pile lateral deflection "y" at a given depth. The p-y method has a good prediction on the ultimate capacity and non-linear response for the lateral loaded slender piles at large displacements. Also, the p-y method needs less computation effort than using finite element method. Two conventional p-y methods for sand are widely accepted and used in the current practice: Reese p-y method (Reese et al., 1974) and API p-y method (API RP 2GEO, 2014). However, the conventional p-y methods are developed by the in-situ field tests on slender piles and they are functions of the pile-soil system rather than a property of soil along. Therefore, the conventional p-y methods may not perform well on the lateral loaded monopiles with relatively large diameters and short lengths. To make the p-y methods perform better on large diameter monopiles, several improved p-y methods have been proposed in the recent years, such as Small Strain Overlay model (Hanssen, 2015), PISA p-y method (Beuckelaers ,2017), etc.

2.1 P-Y METHODS

P-y method was originally developed to solve the problem of slender piles under lateral loading for offshore oil industry in the 1950's and 1960's. The conventional p-y methods, such as Reese (1974) and API (2014), were designed for slender piles subjected to exceptionally large lateral forces induced by storm waves and wind. In recent years, the

conventional p-y methods have increasingly been applied to the design of monopiles which typically have relatively large diameters and small length to diameter ratios. The field monitoring (Kallehave et al., 2017) and numerical analyses (Zdravković et al., 2015) confirmed that the conventional p-y methods might not be suitable for the design of large diameter monopiles. Therefore, several calibrated p-y methods were proposed to improve the performance of the p-y methods on the design of large diameter monopiles, such as Hanssen (2015), PISA (Beuckelaers, 2017), etc. The following p-y methods for sand were summarized in this section:

(1) Reese p-y method for sand (Reese et al., 1974)

(2) API p-y method for sand (API RP 2GEO, 2014)

(3) Small Strain Overlay to the API p-y curves for Sand (Hanssen, 2015)

(4) PISA p-y method (Beuckelaers, 2017)

2.1.1 Conventional Computer Model of p-y Method

A conventional computer model of laterally loaded pile using p-y method is shown in Figure 2.1. The loadings at the top of the pile consist of shear force, overturning moment, and axial force. The soil around the pile is represented by a set of non-linear elastic springs (soil springs). The deformation of the non-linear elastic spring is equal the pile lateral deflection, y, and the reaction force of the non-linear elastic spring represents the resistance of the soil, p, induced by the pile lateral deflection. The stiffnesses of the non-linear elastic springs vary along the depth of the pile section, z, below the soil surface.

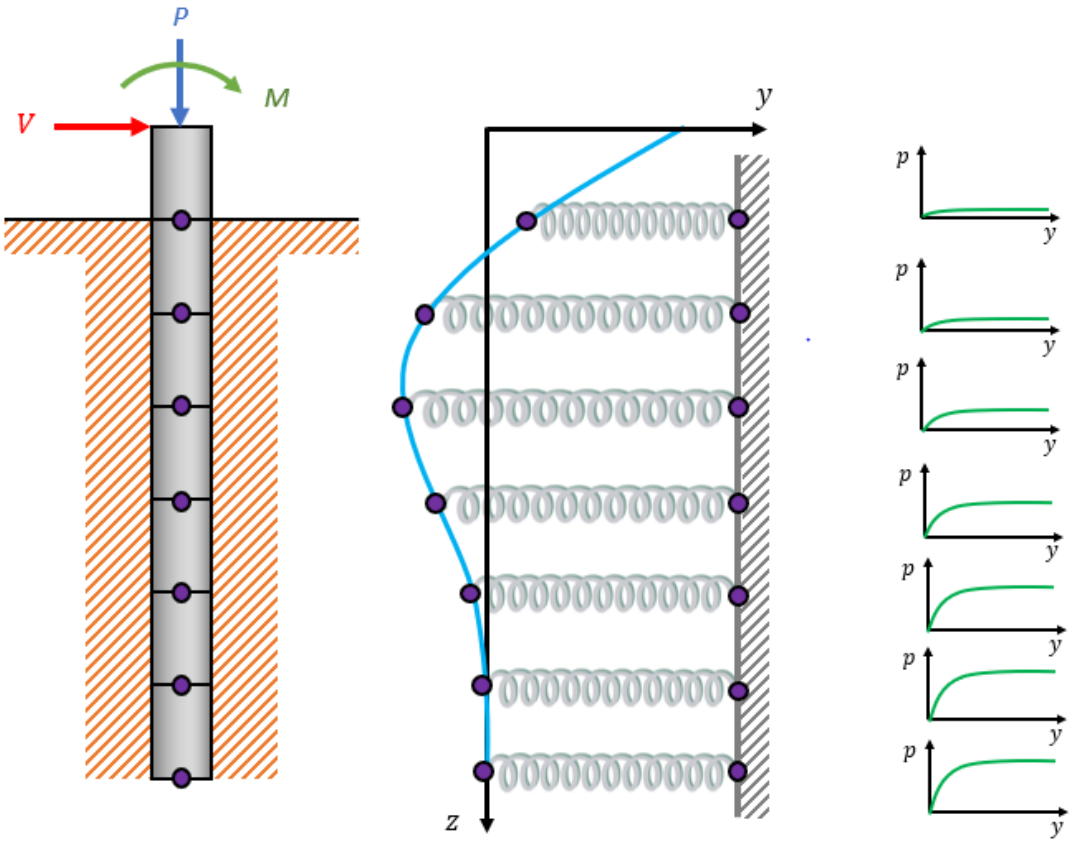

Figure 2.1: Model of a pile under lateral loading and p-y curves.

Figure 2.2 explains the concept of p-y curves. Figure 2.2a shows a pile driven into the soil with the layer of soil at depth x_1 which is examined in Figures 2.2b and 2.2c. Figure 2.2b shows the distribution of the soil stress around the layer of soil 'A-A' prior to lateral loading. Figure 2.2c shows that the resistance of soil, p_1, is developed by the deflection of the pile, y_1. Figure 2.1 shows a set of p-y curves representing soil behavior along the laterally loaded pile with depth (Meyer and Reese, 1979).

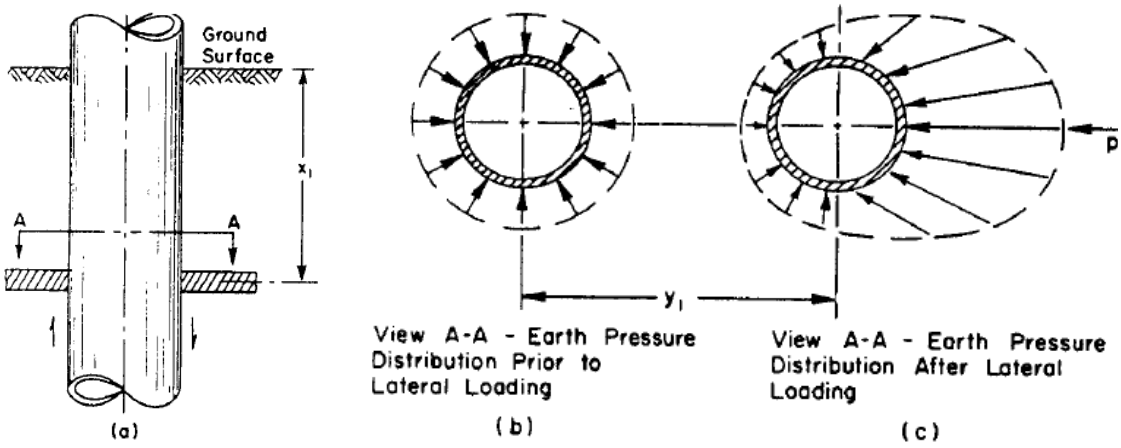

Figure 2.2: Graphical Definition of p and y (Barry and Reese, 1979).

To solve the shear force and the lateral displacement at the top of the pile, the force and moment equilibrium and compatibility need to be satisfied with deformations and deflections in the pile and the soil springs. The pile is divided into multiple sections with soil spring spaced at every node between the sections. At any nodal along the pile, the equilibrium of force and moment leads to the following governing differential equation (in the z direction).

$$\frac{d^2M}{dz^2} - p = 0 \tag{2.1}$$

where: M is the bending moment, p is the force per unit length (z direction) due to the deflection of the soil spring at that location. The compatibility of deformations and deflections provides the governing differential equation:

$$EI\frac{d^4y}{dz^4} - kz = 0 \tag{2.2}$$

where: EI is the flexural rigidity of pile and k is the stiffness of the soil spring at that location. The boundary condition for a typical laterally loaded pile will be no shear and

moment at the base of the pile. Because EI and k are not necessarily constant with y and z, solution of this differential equation requires numerical trial and error to be solved. The solution of the differential equation was introduced by Barry and Reese (1979).

2.1.2 Reese p-y Method (1974)

A series of lateral load tests on slender piles were performed to calibrate p-y curves for sand at a test site on Mustang Island, near Corpus Christi, Texas (Cox et al., 1974). The soil at the test site was classified cohesionless, uniformly graded sand with an effective unit weight of 66 pcf. Two steel-pipe piles with a diameter of 24 inches were driven into sand with an embedment length of 69 feet. One of the piles was subjected to monotonic lateral loading and the other one to cyclic loading. The two piles were instrumented with strain gages to record the behavior of the piles during monotonic and cyclic lateral loading, which were used to calibrate the p-y curves. Figure 2.3 shows the general shape of the Reese p-y curves, which could be computed by the following procedure:

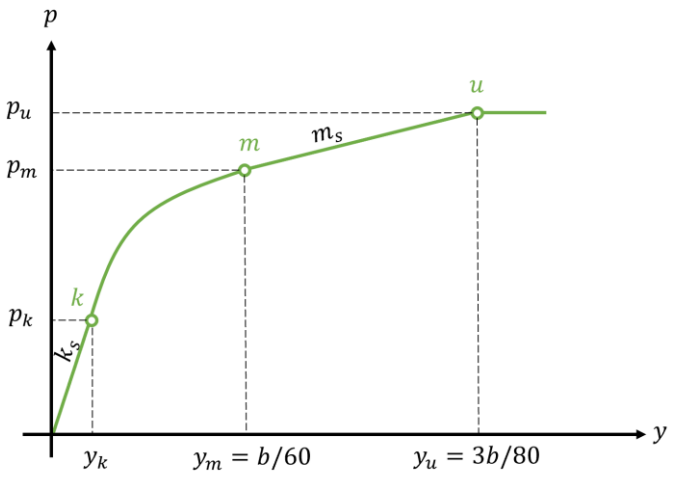

Figure 2.3: Characteristic Shape of p-y Curves for Reese (1974).

(1) Compute the parameters:

$$\alpha = \frac{\phi}{2},\ \ \beta = 45° + \frac{\phi}{2},\ \ K_0 = 0.4, \text{ and } \ K_A = \tan^2(45° - \frac{\phi}{2}) \tag{2.3}$$

where ϕ is the friction angle of the soil.

(2) Calculate the ultimate soil resistance unit length of pile, p_s, by choosing the minimum value between p_{st} in Equation 2.4 and p_{sd} in Equation 2.5,

$$\begin{aligned} p_{st} = \gamma' x[&\frac{K_0 x \tan\phi \sin\beta}{\tan(\beta-\phi)\cos\alpha} + \frac{\tan\beta}{\tan(\beta-\phi)}(b + x\tan\beta\tan\alpha) \\ &+ K_0 x \tan\beta(\tan\phi\sin\beta - \tan\alpha) - K_A b] \end{aligned} \tag{2.4}$$

$$p_{sd} = K_A b\gamma' x(\tan^8\beta - 1) + K_0 b\gamma' x \tan\phi \tan^4\beta \tag{2.5}$$

$$p_s = \min(p_{st}, p_{sd}) \tag{2.6}$$

where γ' is the effective unit weight of soil, x is the depth of the p-y curve, b is the pile diameter.

(3) Compute ultimate lateral displacement, y_u, by using

$$y_u = \frac{3b}{80} \tag{2.7}$$

Compute ultimate unit lateral resistance, p_u, defining point u for static loading conditions by using

$$p_u = A_s p_s \tag{2.8}$$

Or for cyclic loading conditions using

$$p_u = A_c p_s \tag{2.9}$$

The values of parameters A_s or A_c could be obtained from Figure 2.4 as function of the nondimensional depth according to the type of loading (either static or cyclic).

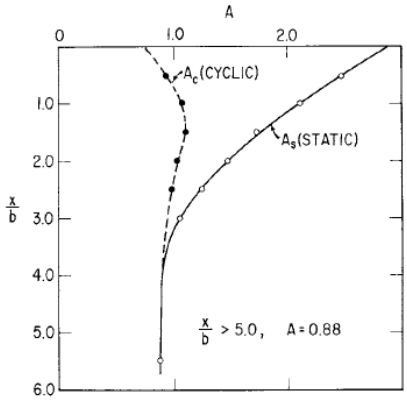

Figure 2.4: Non-dimensional Coefficient A for ultimate soil resistance versus depth (Reese et al., 1974).

(4) The value of lateral displacement, y_m, at point *m* can be calculated by using

$$y_m = \frac{b}{60} \tag{2.10}$$

The value of unit lateral resistance, p_m, at point *m* for static loading condition could be calculated using:

$$p_m = B_s p_s \tag{2.11}$$

Or for cyclic loading conditions using

$$p_m = B_c p_s \tag{2.12}$$

The values of B_s and B_c can be obtained from Figure 2.5 as a function of the nondimensional depth and the type of loading (either the static and cyclic).

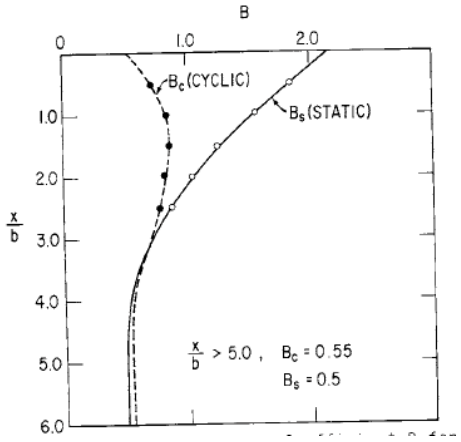

Figure 2.5: Non-dimensional Coefficient B for soil resistance versus depth (Reese et al., 1974).

(5) The initial linear portion of the p-y curves could be established by using

$$p = (k_s x) y \tag{2.13}$$

The value of k_s can be determined by Tables 2.1 and 2.2 for fine sand either below the water table and above the water table.

Table 2.1: Recommended values of k_s for fine sand below water table (Reese et al., 1974).

Recommended k	**Relative Density of sand**		
	Loose	**Medium**	**Dense**
pci	20	60	125

Table 2.2: Recommended values of k_s for fine sand above water table (Reese et al., 1974).

Recommended k	**Relative Density of sand**		
	Loose	**Medium**	**Dense**
pci	25	90	225

(6) The parabola curve between point *k* and point *m* could be established as follows:

a. The slope between point m and point n can be calculated by

$$m_s = \frac{p_u - p_m}{y_u - y_m} \tag{2.14}$$

b. The power of the parabolic section can be calculated as

$$n = \frac{p_m}{my_m} \tag{2.15}$$

c. The coefficient $\overline{C}$ is obtained by using

$$y_k = (\frac{\overline{C}}{kx})^{\frac{n}{n-1}} \tag{2.16}$$

The value of unit lateral resistance, p_k, at point *k* could by calculated using

$$p = \overline{C}xy_k \tag{2.17}$$

The value of p can be calculated along the parabolic section of the p-y curve between point *k* and *m* by using

$$p = \overline{C}y^{1/n} \tag{2.18}$$

2.1.3 API p-y Method (2014)

The p-y curves for sand are given by API RP 2GEO (2014) for both short-term static loading and cyclic loading. In order to generate the API p-y curve at given depth, the following procedure needs to be completed:

1) Obtain the ultimate bearing capacity that is the smallest value of ultimate resistances given by Equations 2.19 and 2.20:

$$p_{us} = (C_1 z + C_2 D) r' z \tag{2.19}$$

$$p_{ud} = C_3 D r' z \tag{2.20}$$

$$p_u = \min(p_{us}, p_{ud}) \tag{2.21}$$

where, p_u is the ultimate unit lateral resistance (force/unit length), γ' is the effective unit weight of soil, z is the depth below the original seafloor, D is the outer diameter of the pile, and C_1, C_2, and C_3 are the coefficients determined as the function of the angle of internal friction of sand ϕ' in Figure 2.6.

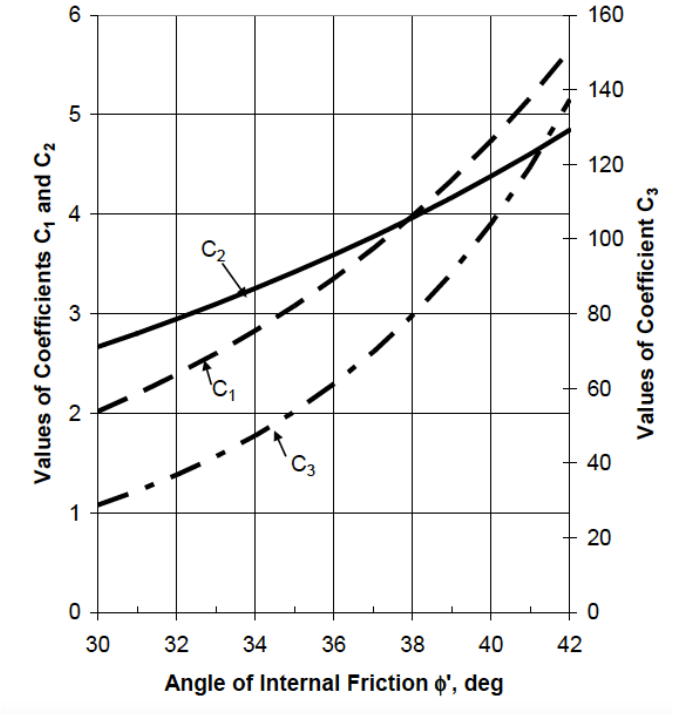

Figure 2.6: Coefficients C_1, C_2, and C_3 as function of ϕ' (API RP 2GEO, 2014).

2) The relationship between the soil resistance, p,and the lateral displacement, y, is generated by Equation 2.22 for creating the p-y curve for sand at any specific depth, z:

$$p = Ap_u \tanh(\frac{kz}{Ap_u} y) \quad (2.22)$$

where,

A is the factor to account for cyclic or static loading condition, evaluated by

$A = 0.9$ for cyclic loading

$A = (3.0 - 8.0 \times z/D) \geq 0.9$ for static loading,

p_u is the ultimate lateral resistance at depth ,

k is elastic subgrade modulus representing the increasing rate of subgrade reaction with depth, see Figure 2.7,

y is the lateral deflection at depth z.

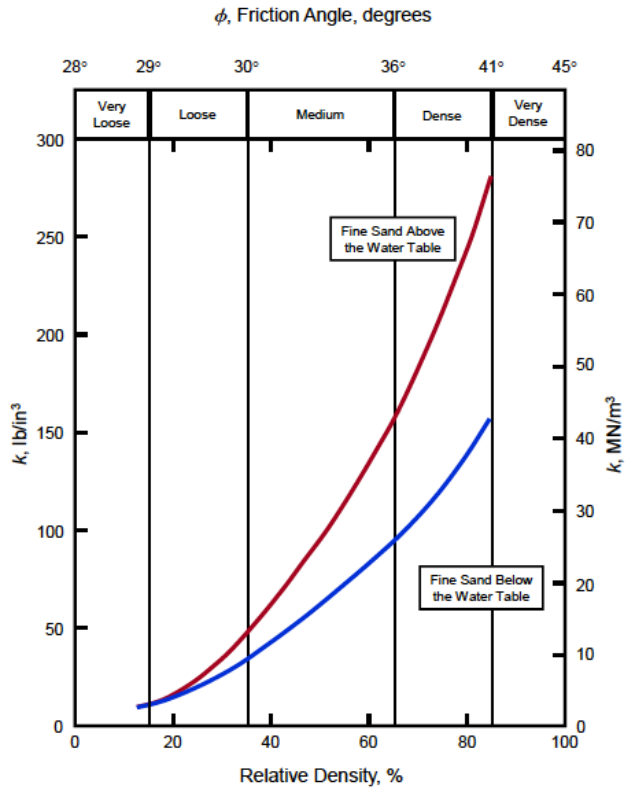

Figure 2.7: Value of k for API p-y curves method for sands (Isenhower and Wang, 2018).

2.1.4 Small Strain Overlay to API p-y curves for Sand (Hanssen, 2015)

Hanssen (2015) proposed a small strain overlay to the API p-y curves for sand, which was an upper-bound solution according to cavity expansion theory along with shear modulus degradation curve from Hardin-Drnevich (1972).

Based on the assumption of Terzaghi (1995), the relationship of the horizontal displacement and the pressure on a pile segment can be approximated by using:

$$\Delta = q \times B \times I_p \times \frac{1-\mu^2}{E} \tag{2.23}$$

where: Δ is the lateral displacement, q is the pressure on the foundation, I_p is the influence value depending upon shape and rigidity of the foundation, μ is the Poisson's ratio, and E is the Young's modulus. In the notation of the p-y method concept, Equation 2.23 is written as:

$$y = p \times I_p \times \frac{1-\mu^2}{E} \tag{2.24}$$

where: y is the lateral displacement, p is the lateral load per unit length on the pile. By rearranging the format of Equation 2.24, Equation 2.25 can be obtained:

$$\frac{p}{y} = \frac{E}{(1-\mu^2)I_p} \tag{2.25}$$

Equation 2.25 is on the format of:

$$\frac{p}{y} = \delta \times E \tag{2.26}$$

According to the theory of cylindrical cavity expansion, the parameter δ can be expressed as:

$$\delta = \frac{4}{2(1+\mu)} \tag{2.27}$$

Because Young's modulus can be related to the shear modulus based the elastic theory by using the equation:

$$E = 2(1+\mu)G \tag{2.28}$$

Substitute Equations 2.27 and 2.28 into Equation 2.26, Equation 2.29 can be obtained:

$$\frac{p}{y} = 4G \tag{2.29}$$

where: G is the shear stiffness which has the relationship with the shear strain γ and mean effective stress σ_0' as shown in Equations 2.30 and 2.31 respectively.

$$G_s(\gamma) = \frac{1}{1+\frac{\gamma}{\gamma_r}[1+a\exp(-b\frac{\gamma}{\gamma_r})]} G_{\max} \tag{2.30}$$

$$G_{\max} = J\frac{(a_1-e)^2}{1+e}(P_a)^{1-n}(\sigma_0^{'})^n \tag{2.31}$$

where: γ_r is the reference shear strain defined as $\gamma_r = \tau/G_{max}$, a and b are empirical constants, constant parameter J can be expressed as $J = 1563 + 3.13C_u^{2.98}$, constant parameter a_1 can be expresses as $a_1 = 1.94\exp(-0.066C_u)$, e is the void ratio, and P_a is one atmosphere pressure.

The Equation 2.30 can be modified to fit the p-y concept by replacing shear strain γ by horizontal displacement y and replacing reference strain γ_r by reference displacement y_r:

$$\frac{p}{y} = \frac{1}{1+\frac{y}{y_r}[1+a\exp(-b\frac{y}{y_r})]} 4G_{\max} \tag{2.32}$$

where: the reference displacement y_r is defined as $y_r = (Ap_u)/(4G_{max})$, A is the empirical correction value for ultimate soil resistance in Equation 2.22.

2.1.5 PISA p-y method (Beuckelaers, 2017)

PISA p-y curves were developed in the Pile Soil Analysis (PISA) project which was led by DONG Energy, in partnership with other companies active in the offshore wind industry, to address the shortcomings of the conventional p-y method (e.g., Reese, API). The PISA p-y method not only considers the soil reaction, at specific depth, as a function of the local pile displacement and rotation, but also includes distributed moment curves, a base shear curve and a base moment curve as illustrated in Figure 2.8.

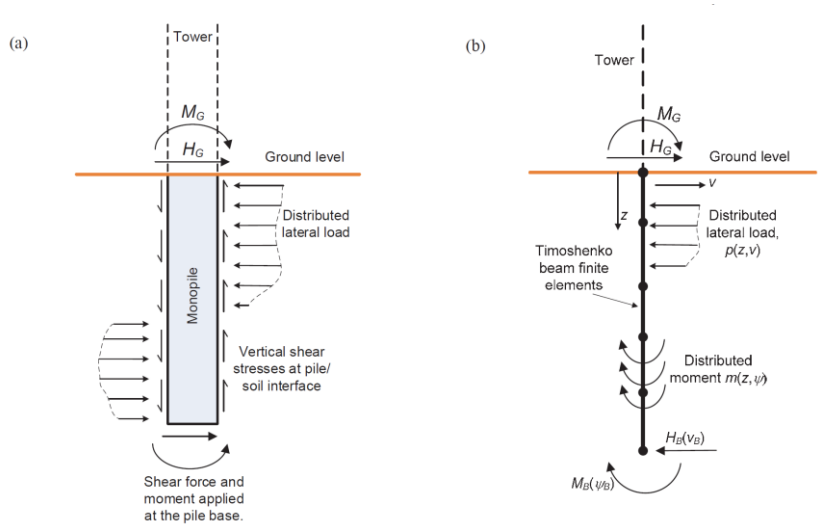

Figure 2.8: (a) Soil reaction components incorporated in the PISA p-y method, and (b) 1D FE model employed in the PISA p-y method (Byrne et al., 2017).

To describe the shape of the p-y curves, the PISA project uses the following conic function:

$$-n\left(\frac{\bar{s}}{s_u}-\frac{\bar{e}}{e_u}\right)^2+(1-n)\left(\frac{\bar{s}}{s_u}-\frac{\bar{e}k_0}{e_u}\right)\left(\frac{\bar{s}}{s_u}-1\right)=0 \qquad (2.33)$$

where $\bar{\sigma}$ is corresponded to a normalized load variable in Table 2.3 and $\bar{\varepsilon}$ refers to a normalized displacement variable.

Table 2.3: Normalized of pile reaction components for the PISA p-y method (Beackelaers, 2017).

Component	Clay normalisation	Sand normalisation
Distributed load, $\bar{p}$	$\frac{p}{s_u D}$	$\frac{p}{\sigma'_{v0} D}$
Lateral displacement, $\bar{v}$	$\frac{v}{D} I_R$	$\frac{v}{D} I_s \sqrt{\frac{p_a}{\sigma'_{v0}}} \left[= \frac{v}{D} \frac{G_0}{\sigma'_{v0}} \right]$
Distributed moment, $\bar{m}$	$\frac{m}{s_u D^2}$	$\frac{m}{\lvert p \rvert D}$
Pile cross section rotation, $\bar{\psi}$	ψI_R	$\psi I_s \sqrt{\frac{p_a}{\sigma'_{v0}}} \left[= \psi \frac{G_0}{\sigma'_{v0}} \right]$
Base shear load, $\bar{H}_B$	$\frac{H_B}{s_u D^2}$	$\frac{H_B}{\sigma'_{v0} D^2}$
Base moment, $\bar{M}_B$	$\frac{M_B}{s_u D^3}$	$\frac{M_B}{\sigma'_{v0} D^3}$

where the real positive roots of $\bar{\sigma}$ in Equation 2.33 are calculated as:

$$\bar{s} = \bar{s}_u \frac{2c}{-b + \sqrt{b^2 - 4ac}} \quad \text{for } 0 < \bar{\varepsilon} < \bar{\varepsilon}_u \tag{2.34}$$

$$\bar{s} = \bar{s}_u \quad \text{for } \bar{\varepsilon}_u < \bar{\varepsilon}$$

where:

$$a = 1 - 2n$$

$$b = 2n \frac{\bar{e}}{e_u} - (1 - n)\left(1 + \frac{\bar{e} k_0}{s_u}\right)$$

$$c = \frac{\bar{e} k_0}{s_u}(1 - n) - n \frac{\bar{e}^2}{e_u^2}$$

The conic expression is defined by four parameters: $\bar{\varepsilon}_u$, $\bar{\sigma}_u$, k_0, and n, where $0 \leq n < 1$ and $k_0 \bar{\varepsilon}_u > \bar{\sigma}_u$. The four parameters can be found in Table 2.4 for each kind of load component.

Table 2.4: Parameters for the soil reaction curves (Beackelaers, 2017).

Soil reaction component	Parameter	Clay expression	Sand expression
Distributed lateral load, $\bar{p}$	Ultimate strain, $\bar{v}_u$	200	53.1
	Initial stiffness, k_{0_p}	$-1.11\frac{z}{D}+8.17$	$-0.85\frac{z}{D}+7.46$
	Curvature, n_p	$-0.07\frac{z}{D}+0.92$	0.944
	Ultimate reaction, $\bar{p}_u$	$11.66-8.64e^{-0.37\frac{z}{D}}$	$-0.05\frac{z}{L}+21.61$
Distributed moment, $\bar{m}$	Ultimate rotation, $\bar{\psi}_u$	10	20
	Initial stiffness, k_{0_m}	$-0.12\frac{z}{D}+0.98$	20
	Curvature, n_m	0	0
	Ultimate reaction, $\bar{m}_u$	$-0.05\frac{z}{D}+0.38$	$-0.05\frac{z}{L}+0.21$
Base shear, $\bar{H}_B$	Ultimate strain, $\bar{v}_{B_u}$	300	$-0.29\frac{L}{D}+2.31$
	Initial stiffness, $k_{0_{H_B}}$	$-0.32\frac{L}{D}+2.58$	$-0.38\frac{L}{D}+3.02$
	Curvature, n_{H_B}	$-0.04\frac{L}{D}+0.76$	$-0.05\frac{L}{D}+0.94$
	Ultimate reaction, $\bar{H}_{B_u}$	$0.07\frac{L}{D}+0.59$	$-0.07\frac{L}{D}+0.62$
Base moment, $\bar{M}_B$	Ultimate rotation, $\bar{\psi}_{B_u}$	200	50
	Initial stiffness, $k_{0_{M_B}}$	$-0.002\frac{L}{D}+0.19$	0.29
	Curvature, n_{M_B}	$-0.15\frac{L}{D}+0.99$	0.89
	Ultimate reaction, $\bar{M}_{B_u}$	$-0.07\frac{L}{D}+0.65$	$-0.05\frac{L}{D}+0.38$

Figure 2.9 shows the shape of the conic curve formed by the Equation 2.34.

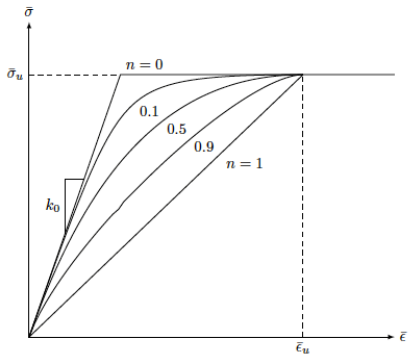

Figure 2.9: Illustration of the conic curve (Beackelaers, 2017).

The expression of Equation 2.34 gives the positive normalized stress for a positive normalized strain. When the strain is negative, the stress is calculated by the positive magnitude of strain in Equation 2.35.

$$\bar{s} = S(\bar{e})\bar{s}_u \frac{2c}{-b+\sqrt{b^2-4ac}} \quad \text{for } |\bar{\varepsilon}| \le \bar{\varepsilon}_u \tag{2.35}$$

$$\bar{s} = S(\bar{e})\bar{s}_u \text{ for } |\bar{\varepsilon}| > \bar{\varepsilon}_u$$

where:

$$a = 1-2n$$

$$b = 2n\frac{|\bar{e}|}{\bar{e}_u} - (1-n)\left(1+\frac{|\bar{e}|k_0}{\bar{s}_u}\right)$$

$$c = \frac{|\bar{e}|k_0}{\bar{s}_u}(1-n) - n\frac{\bar{e}^2}{\bar{e}_u^2}$$

However, without calibration, the PISA p-y method cannot predict well about the initial stiffness and the ultimate capacity of the lateral loaded monopile. Figure 2.9 shows the comparison between the lateral load versus displacement curves measured from the field test in PISA project and predicted by the PISA p-y method without and with calibration.

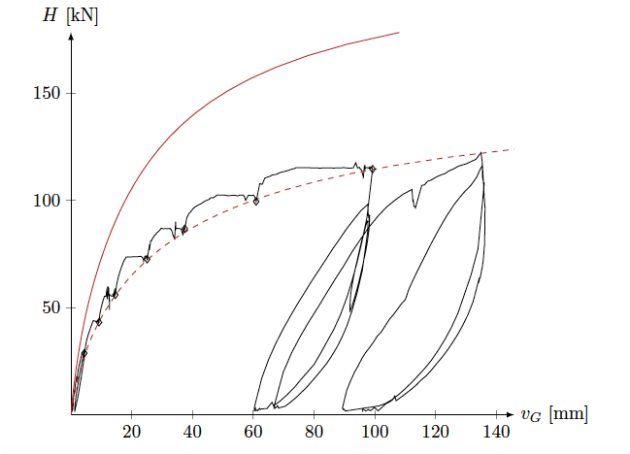

Figure 2.10: Comparison of the field test response with calculated back bone curve using the initial and modified parametrized soil reaction curves, calibrated to the points at the end of the hold phases (Beackelaers, 2017).

For calibration, the following modification are made, scaling the curves in both the load and displacement directions.

$$\overline{s}_u^* = A_u \overline{s}_u \tag{2.36}$$

$$k_0^* = A_0 k_0 \tag{2.37}$$

$$\overline{e}_0^* = \frac{A_u}{A_0} \overline{e}_u \tag{2.38}$$

The dashed line in Figure 2.10 is predicted by the calibrated PISA curves, but just for one monopile. Table 2.5 shows the calibration factors for nine different monopiles. The values of the calibration factors varied with the test site and the dimensions of the monopiles.

Table 2.5 : Correction factors for the backbone curve of the PISA pile tests (Beackelaers, 2017).

Pile	CS2	CM9	CL2	CM1	CM6
A_0	0.1518	0.4161	0.9424	0.5713	0.2777
A_u	0.4108	0.7152	0.6927	0.6720	0.6268

Pile	DM9	DS1	DL2	DM6
A_0	0.7059	0.5004	0.7264	0.5652
A_u	1.2231	1.5992	1.0500	1.2178

2.1.6 Examples of Using API p-y Method

Three field tests were used to verify the performance of the API p-y method for predicting the lateral stiffness of piles in the range of small displacement. The three field tests included the Mustang Island test (Cox et al., 1974), Houston test (Little and Briaud, 1988), and Blessington test (Murphy et al., 2018). The description of the tests set-up and the soil profiles were summarized in this section. The predicted curves were calculated by using LPILE which was a computer program for analyzing piles under lateral loading using the p-y method. For each test, the measured load versus displacement curve was compared to the curve predicted by the API p-y method using LPILE. The comparison indicated that the lateral stiffness of pile was underestimated by the API p-y curves method at small displacements.

2.1.6.1 Mustang Island test (Cox, Reese, and Grubbs, 1974)

In 1966, a series of lateral load tests was conducted on Mustang Island to develop the p-y curves method for the design of laterally loaded piles in sand. Cox, Reese and Grubbs (1974) reported the results of the site investigation (location of piles, log of boring, laboratory tests, etc.), preparation of test piles, and procedure of the tests. Reese, Cox, and

Koop (1974) compared the load versus displacement curves measured in the field and predicted by the developed p-y curves method in the range of large displacement (5% of pile diameter).

The pile had an outer diameter of 24 inches, a wall thickness of 0.375 inch, and an embedment length of 69 feet. The loading point was 1 foot above the ground surface. The pile was instrumented with strain gauges at regular intervals along its length. The pile with free head conditions was tested under monotonic loading. Figure 2.11a shows the schematic diagram of the pile. Two borings logs were taken at the test site on Mustang Island. The sand from 0 to 20 feet was classified as medium dense and from 20 to 70 feet was classified as dense. Figure 2.11b shows the result of the standard penetration tests (SPT) at the two borings, which was consistent with the soil strata as classified by boring logs. Dasguapta (2017) found the friction angle of the sand was 35 degrees by back calculating to match the overall response of the lateral loaded pile using the API p-y method. It was corresponding to an average SPT N value of around 25 at the shallow depths using the chart of correlation between SPT N value and internal angle of friction (Figure 2.12).

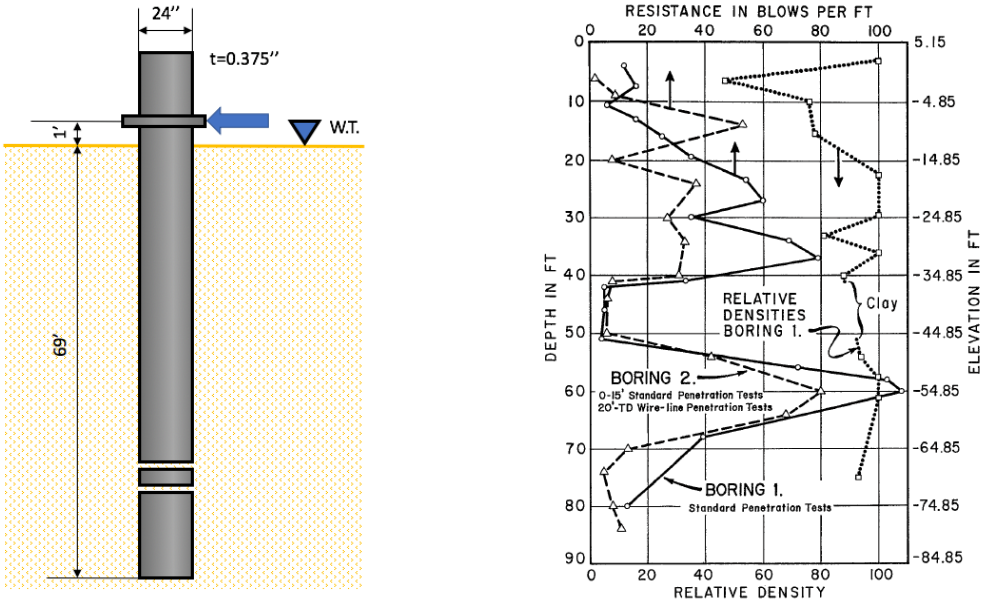

(a) (b)

Figure 2.11: (a) the schematic diagram of the piles, (b) results of standard penetration test and relative density from piston samples of the Mustang Island test.

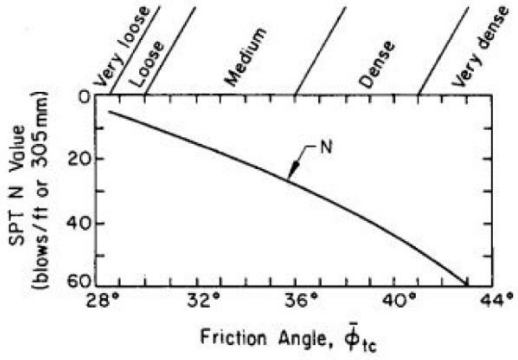

Figure 2.12: Chart for correlation between SPT N value and internal angle of friction (Peck et al., 1974).

Figure 2.13 shows the load versus displacement curves at the loading point under monotonic condition. The test was conducted at 16 days after the pile was driven. The first lateral load was 1 kips applied on the pile and then the loads increased to 2 kips and 2.5

kips. After the load of 2.5 kips, the loads were applied 2.5 kips increments to 15 kips and then increments of 1.25 kips from 15 kips to a maximum 60 kips.

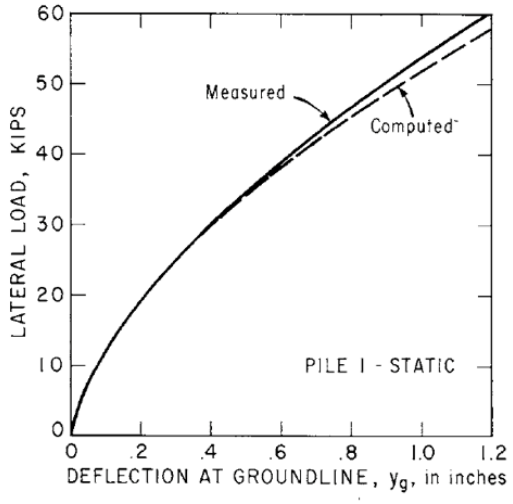

Figure 2.13: Comparison between monotonic load versus displacement curves measured from Mustang Island test and computed with the Reese p-y curves method.

Table 2.6 summarizes the input parameters of the test pile and Table 2.7 summarizes the input parameters of the soil used by the API p-y method for the Mustang Island test.

Table 2.6: Dimensions of the pile used in the Mustang Island test.

Embedded length (ft)	Diameter (in.)	Wall thickness, t (in.)	L/D ratio	Load eccentricity (in.)
69	24	0.375	34.5	12

Table 2.7: Input parameters of the soil for the Mustang Island test.

Depth below soil surface (ft)		Effective unit weight (pcf)	Friction angle (deg.)	k (pci)
From	To			
0	69	66	35	85

Figure 2.14 shows the comparison between the field tests and the predictions from the API p-y method for the Mustang Island test. The prediction using the API p-y method has a good overall fit with the measured curve in the full-displacement. However, the comparison shows the API p-y curves method underestimates the lateral stiffness of the pile and does not capture the non-linearity of the response in the range of the small displacement (0.5% of pile diameter).

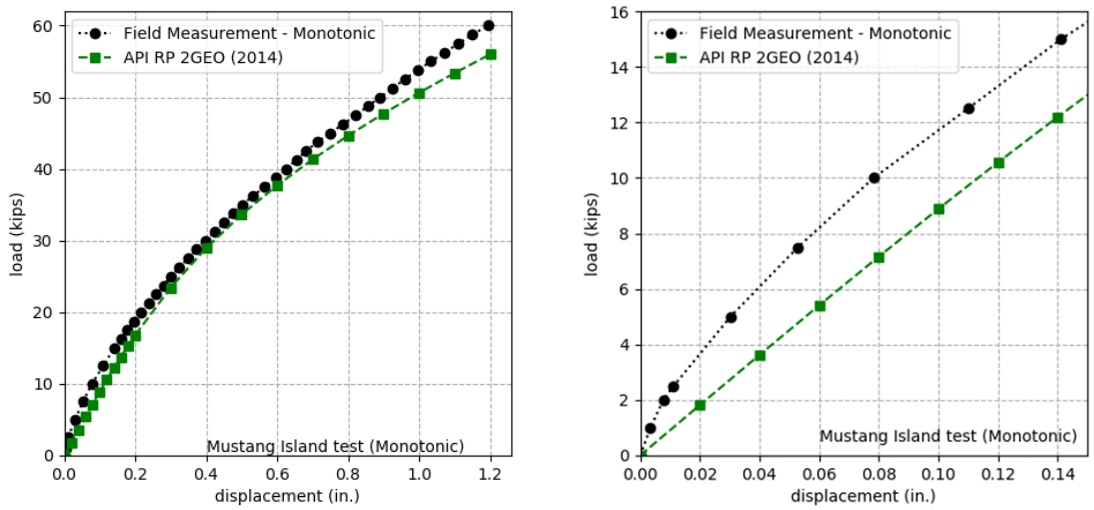

(a) (b)

Figure 2.14: Comparison between the monotonic load versus displacement curves measured from the Mustang Island test and computed with the API p-y curves method, (a) full-displacement and (b) displacement less than 0.5% of the pile diameter.

2.1.6.2 Houston Tests (Little and Briaud, 1988)

Six existing piles were subjected to cyclic lateral loads to study the corresponding accumulated displacement and the potential of using the pressuremeter for predicting the lateral response of piles in sand (Little and Briaud, 1988). Five of them were concrete piles and one of them was steel pile. The steel pile was analyzed in this study by comparing load

versus displacement curves from the field measurement and the prediction using the API p-y curves method. The measured monotonic load versus displacement curve of the steel pile was the curve enveloping the response of piles subjected to the two series of cycles.

The steel pipe had an outer diameter of 24 inches, a wall thickness of 0.375 inch, and an embedment length of 90 feet. The loading point was 8.4 inches above the ground surface. Figure 2.15a shows the test set-up for the 24-inch steel pile. A boring log with standard penetration test was conducted at the test site to investigate the soil profile. The results showed the soil in the upper 73 feet was mainly loose to medium dense fine sand and stiff to very stiff clay was under the sand. Figure 2.15b shows the soil profile at the test site.

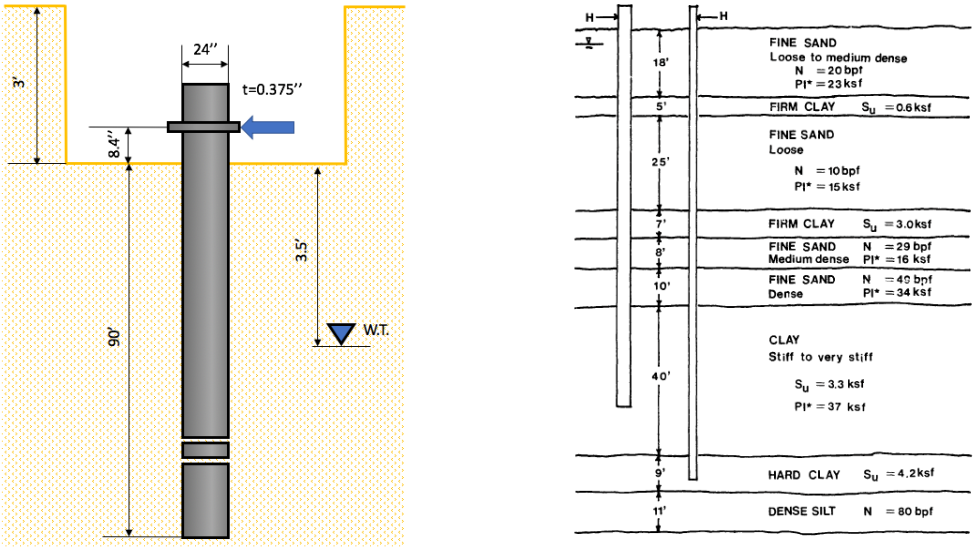

(a) (b)

Figure 2.15: (a) the schematic diagram of the piles and (b) soil profile at test site of the Houston test.

Before the lateral load tests, the soil was excavated to a depth of 3 feet to allow sufficient clearance for setting up the loading equipment and support frame. The water

table was 3.5 feet below the ground surface after the excavation. During the tests, the load was increased by an increment of five kips and two load levels were selected to perform 20 cycles of unloading and reload. Figure 2.16 shows the monotonic response envelopes of the six test piles and Pile 2 was the steel pile.

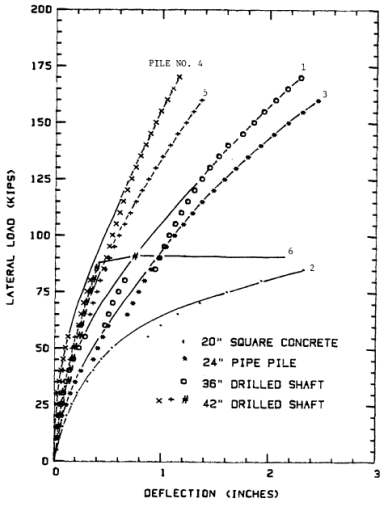

Figure 2.16: Monotonic response envelope measured results of the Houston test.

Table 2.8 summarizes the input parameters of the steel pile and Table 2.9 summarizes the input parameter of the soil strata for the Houston test using the API p-y method.

Table 2.8: Dimensions of the pile in the Houston tests.

Embedded length (ft)	Diameter (in.)	Wall thickness, t (in.)	L/D ratio	Load eccentricity (in.)
90	24	0.375	45	8.4

Table 2.9: Input parameters of the soil in the Houston tests.

Depth below soil surface (ft)		Effective unit weight (pcf)	Friction angle (deg.)	k (pci)	Undrained Cohesion (ksf)	Strain factor E50
From	To					
0	3.5	120	33	142	-	-
3.5	35	57.6	33	85	-	-
15	20	57.6	-	-	0.6	0.005
20	45	57.6	30	34	-	-
45	52	57.6	-	-	3.0	0.005
52	60	57.6	36	96	-	-
60	70	57.6	41	160	-	-
70	110	57.6	-	-	3.3	0.005

Figure 3.7 shows the comparison of the load versus displacement curves measured in the field and predicted by the API p-y method. Same with the analysis on the Mustang Island test, the predicted load versus displacement curve using the API p-y curves method has a good agreement with the measured curve in the full-displacement. The result of the comparison at small displacements shows that the predicted curve underestimates the lateral stiffness of the pile and does not predict the non-linearity of the response.

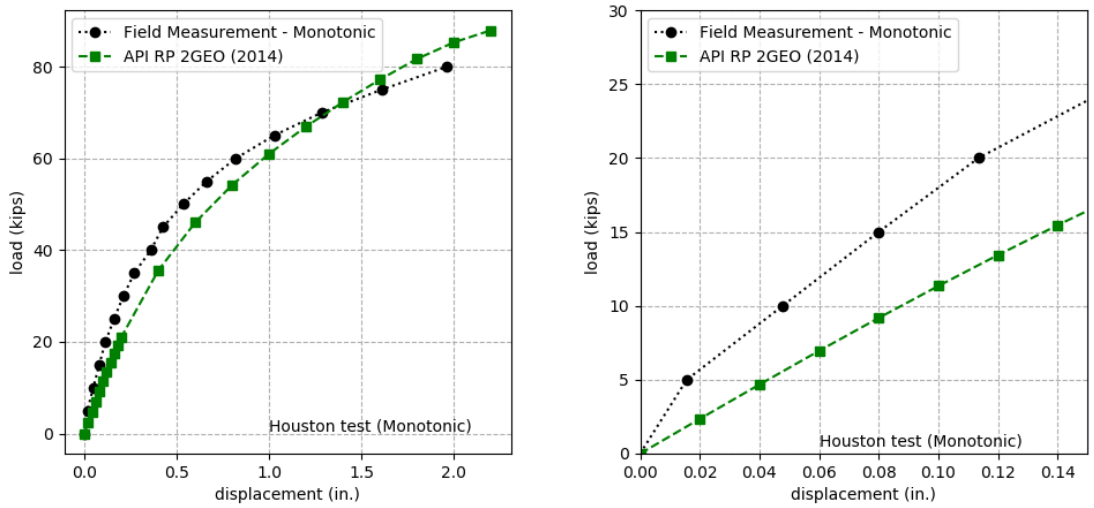

Figure 2.17: Comparison between the monotonic load versus displacement curves measured from Houston tests and computed with the API p-y curves method, (a) full-displacement and (b) displacement less than 0.5% of the pile diameter.

2.1.6.3 Blessington Tests

Unversity College Dublin conducted the lateral load tests on four monopiles to validate the 3-D FEM model using Hardening Soil model in Plaxis. The test site was located in Blessington, approximately 15 miles south-west of Dublin in Ireland (Murphy et al., 2018). The characteristics of the sand deposits the test site were similar to the strength and the stiffness properties of the sand encountered in offshore seabed deposits in the North Sea.

The monopiles were installed in an active quarry and they were prototype scale open-ended piles. The three monopiles had a diameter of 20 inches with different embedment lengths. The L/D ratios varied from three to six. The loading point was 40

inches above the soil surface for all the monopiles. Figure 2.18 shows the schematic diagram of the monopiles Table 2.10 shows the dimensions of the monopiles.

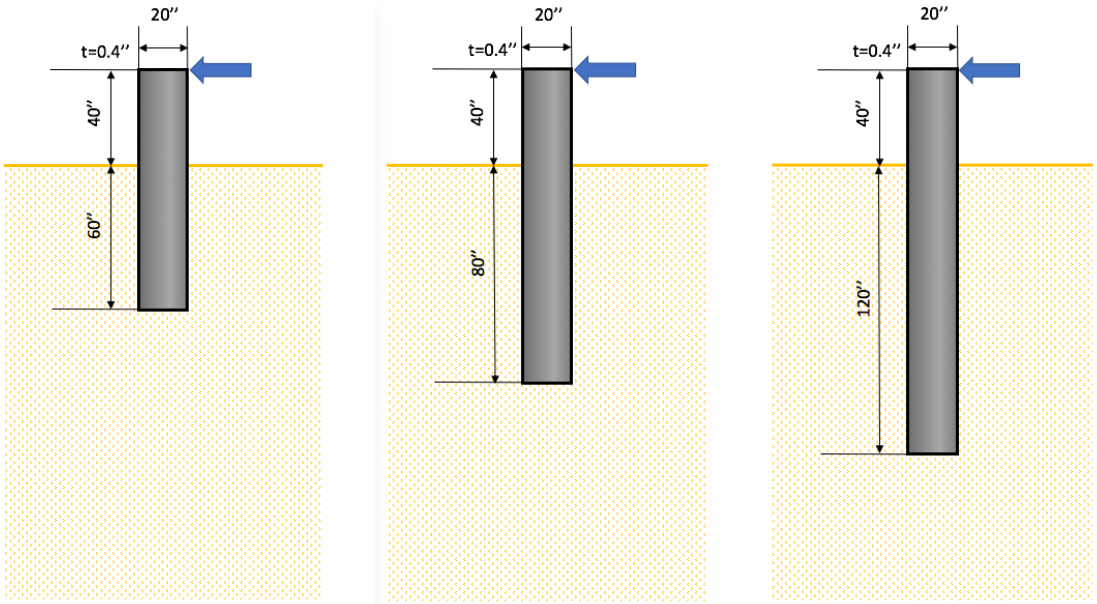

Pile #1 Pile #2 Pile #3

Figure 2.18: Schematic diagrams of the monopiles of Blessington tests.

Table 2.10: Dimensions of the monopiles in the Blessington tests.

Pile	Embedded length (in.)	Diameter (in.)	Wall thickness, t (in.)	L/D ratio	Load eccentricity (in.)
1	60	20	0.4	3	40
2	80	20	0.4	4	40
3	120	20	0.4	6	40

Cone penetration test (CPT) was performed at the test site to investigate the soil properties. The test site consisted of a uniformly graded, horizontally bedded, heavily over-consolidated, and very dense sand deposit. Figure 2.19 shows the friction angle versus depth profile at the test site. An average of friction angel of 45 degrees was accepted to present the strength of the soil. The effective unit weight of the soil was 128 pcf.

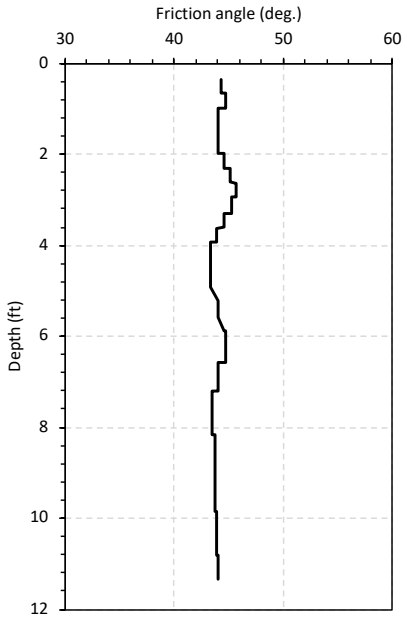

Figure 2.19: Friction angle versus depth profile at the test site of Blessington tests (Murphy et al., 2018).

During the test, the load was increased continuedly and measured by using an in-line load cell. The lateral displacement was measured using a linear displacement transducer at the same height of the load cell. Figure 2.20 shows the measured load versus displacement curves of the three monopiles.

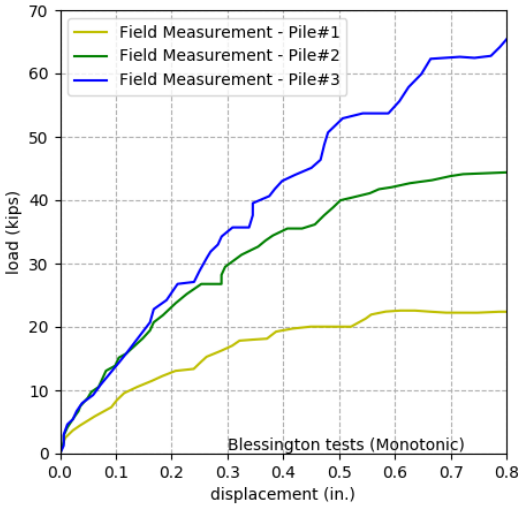

Figure 2.20: Load versus displacement curves measured from the Blessington tests for all the three monopiles (Murphy et al., 2018).

Figures 2.21 to 2.22 compare the load versus displacement curves measured in the field and predicted by the API p-y curves method for the three monopiles in the Blessington tests. Different from the analysis on the slender piles, the predicted curves underestimate the ultimate capacity of the monopiles at large displacements. It is because that the API p-y curves method does not include the components of (1) vertical shear tractions induced on the pile perimeter and (2) shear and moment developed at the pile base when monopiles rotate. These components become increasingly important as the ratio of pile length to the pile diameter reduces (Byron et al., 2017), which also can be observed in these comparisons. Same as the analysis on the slender piles, the API p-y curves method underestimates the lateral stiffness of the piles and does not capture the non-linearity of the response at small displacements.

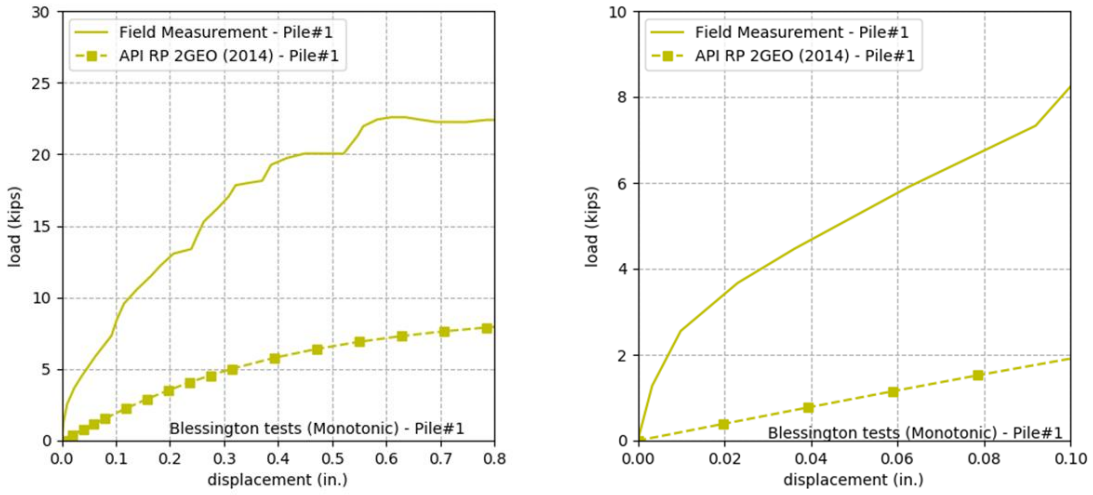

(a) (b)

Figure 2.21: Comparison between the monotonic load versus displacement curves measured from Blessington tests (Pile #1) and computed with the API p-y curves method, (a) full-displacement and (b) displacement less than 0.5% of the pile diameter.

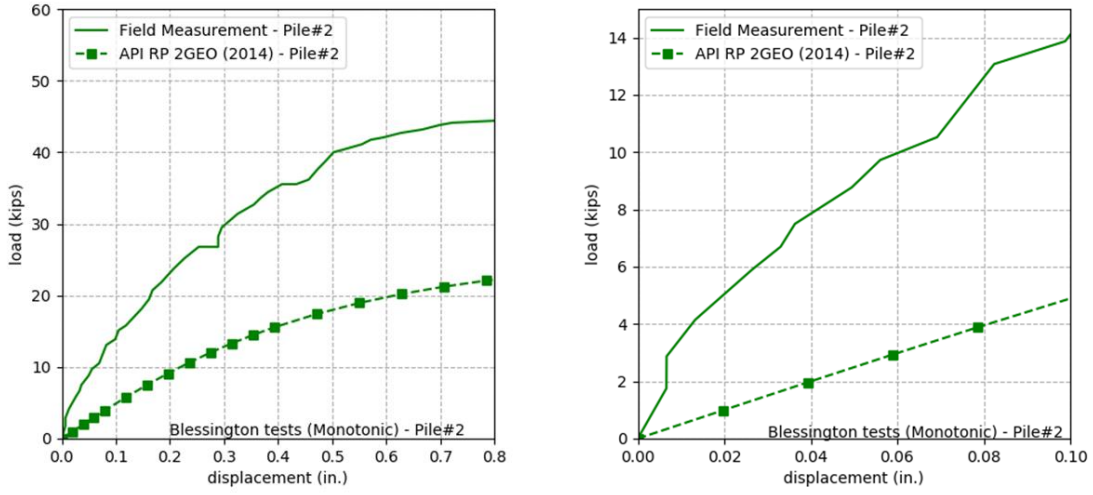

(a) (b)

Figure 2.22: Comparison between the monotonic load versus displacement curves measured from Blessington tests (Pile #2) and computed with the API p-y curves method, (a) full-displacement and (b) displacement less than 0.5% of the pile diameter.

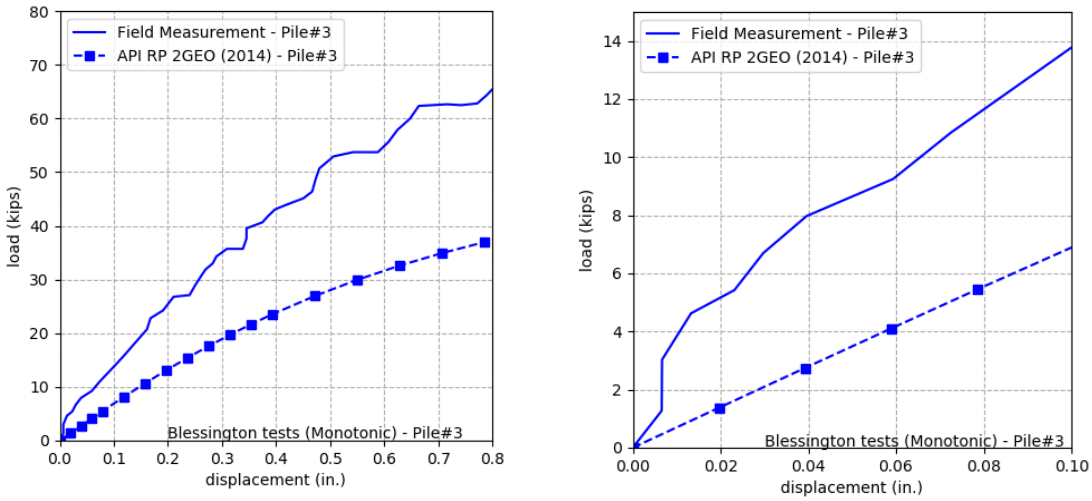

Figure 2.23: Comparison between the monotonic load versus displacement curves measured from Blessington tests (Pile #3) and computed with the API p-y curves method, (a) full-displacement and (b) displacement less than 0.5% of the pile diameter.

2.2 FINITE ELEMENT METHOD

The finite element method (FEM) is one of the numerical methods for solving the problems of engineering. The FEM can represent complex problems by dividing the domain of the problem into a set of subdomains consisting of smaller, simpler, and continuous parts, which are called finite elements. The finite elements can be represented by simple equations which are assembled to form a global system of equations that represent the entire problem. The problem could be simulated by solving the global system of equations. Because of this, the FEM needs intensive computing effort in order to obtain reliable results. However, the FEM can simulate complex behavior of soil by using advanced soil constitutive model to solve complicated interaction problem between

structure and soil. Therefore, the FEM is powerful tool used for research purpose. In the PISA project, the FEM analysis was performed to calibrate the PISA p-y method by matching the FEM results to the field tests on monopiles. Benz (2007) proposed a soil constitutive model to simulate the non-linear behavior of soil at small strains, which were used to solve the problem of settlement induced by foundation, tunneling, deep excavation, etc.

2.2.1 PISA 3-D FEM Model

Advanced 3-D FEM models in PISA project were carried out to develop a new design framework and calibrate p-y curves for laterally loaded piles utilized in the offshore wind industry. The analysis of the model was performed by modelling the behavior of monopiles driven at Cowden and Dunkirk where had similar ground conditions encountered in the North Sea. The p-y curves were extracted from the results of the 3-D FEM analysis to calibrate the PISA p-y curves by being normalized and parametrized.

For the stiff glacial clay till deposits at Cowden, an expanded generalized version of the Modified Cam Clay (MCC) model was used to simulate the behavior of the clay. For the sand deposits at Dunkirk, a bounding surface plasticity model was used to simulate the mechanical response of sand.

The 3-D FEM models were established to analyze the test monopiles at Cowden and Dunkirk with the soil constitutive model proposed above. A typical 3-D FEM model for monopiles is shown in Figure 2.24. Because the symmetric geometry and the loading on the pile, half of the pile-soil system was sufficient the model the behavior the test monopiles. The element of the soil was simulated as 20-noded hexahedral displacement-based isoparametric element. The element of the pile was represented with 8-noded shell

elements. The interface of the soil and the pile used 16-noded zero-thickness interface elements. The horizontal load was applied at the top of the monopile in a displacement controller manner, with increment of displacement along x-direction around the pile perimeter. The lateral load was obtained by extract the reaction to the applied displacement.

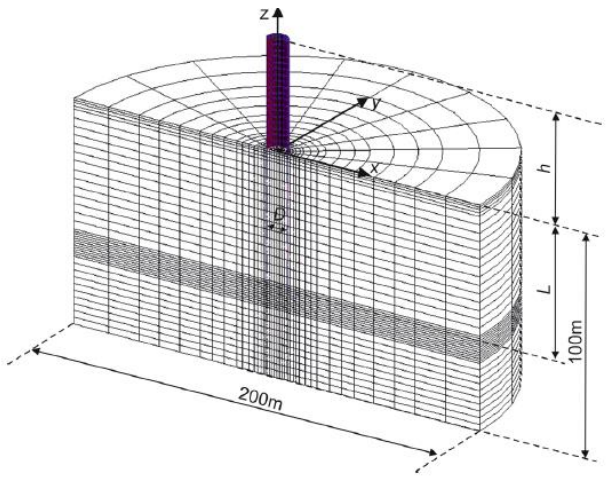

Figure 2.24: Typical FE mesh for monopile analyses (David et al., 2015).

Figure 2.25 shows the lateral load versus displacement predicted by the 3-D FEM model for stiff glacial clay till condition at Cowden. The monopiles have the same diameter of 10 meters. The length L, load eccentricity h, and the wall thickness t varied. The ultimate capacity of the pile increased with the increasing length L and the decreasing load eccentricity h. The wall thickness t had negligible effect on the ultimate capacity. Figure 2.26 shows the deflection of the piles with the displacement of 0.1 diameter at the mudline. It indicated that the shorter piles behaved more rigid and longer piles behaved in a more flexible manner.

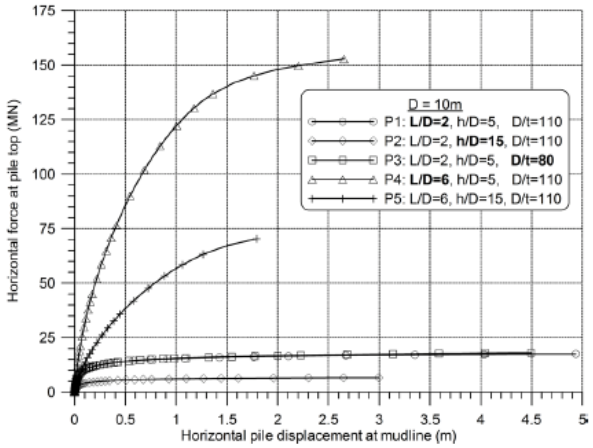

Figure 2.25: Deflection of D=10 meter piles in stiff clay till at Cowden (David et al., 2015).

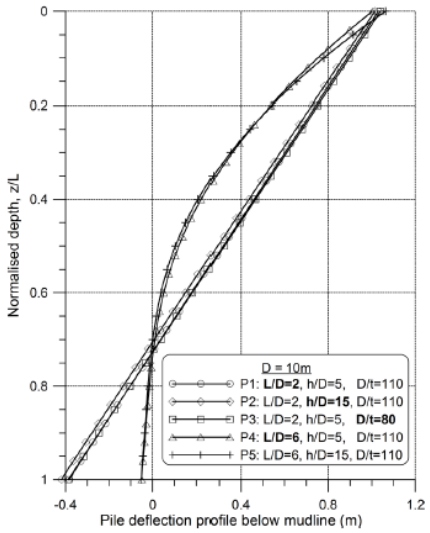

Figure 2.26: Deflections of D=10 m piles in stiff clay till at Cowden (David et al., 2015).

2.2.2 Benz (2006)

To enhance elasto-plastic models for highly non-linear behavior of soil at small strains, Benz (2006) proposed a soil constitutive model named ‘a small-strain extension of the Hardening Soil model’ (HS-Small model). This model could be used in FEM model to

simulate the settlements induced by the shallow foundation, tunneling, deep excavations, etc.

The output of the soil constitutive model was kept as isotropic, which could guarantee its compatibility with many existing constitutive models. The shear strain, γ, was defined as:

$$g = \sqrt{\frac{3}{2}(e_{ij} - \frac{1}{3}d_{ij}e_{kk})(e_{ij} - \frac{1}{3}d_{ij}e_{kk})} \tag{2.39}$$

A modified Hardin-Drnevich model (Santo and Correia, 2001) was used to define the relationship between the shear stiffness, G, and the shear strain, γ, as expressed in Equation 2.40.

$$G = \frac{G_0}{1 + a\frac{g}{g_{0.7}}} \tag{2.40}$$

where, G_0 is the initial (maximum) shear stiffness at very small strains, $\gamma_{0.7}$ is the shear strain at which shear stiffness reduces to $0.7G_0$, and a is a constant equal to 0.385 found by Santos and Correia (2001).

The solver of the FEM used by Ben (2006) was an incremental formulation, which the current elastic tangent shear modulus was best calculated by integrating the stiffness modulus reduction curve over the actual shear strain increment. To realize the incremental formulation, the secant modulus given in Equation 2.40 needed to be converted to a tangent modulus:

$$G = G_0(\frac{g_{0.7}}{g_{0.7} + ag})^2 \tag{2.41}$$

The current elastic tangent shear modulus could be calculated by:

$$G^{i+1} = \frac{G_0}{\gamma^{i+1} - \gamma^i}\left(\frac{\gamma^{i+1}}{1+\frac{0.385\gamma^{i+1}}{\gamma_{0.7}}} - \frac{\gamma^i}{1+\frac{0.385\gamma^i}{\gamma_{0.7}}}\right) \tag{2.42}$$

where: i and $i+1$ denoted quantities of the previous and current calculation steps, respectively.

The HS-Small model was validated by comparing the measured data from real problems and the predicted results. The construction of Steinhaldenfeld tunnel was simulated as a 2-D FEM model using PLAXIS to study the settlement caused by the construction of the tunneling as shown in Figure 2.27a. Figure 2.27b shows the settlements measured in the field and predicted by soil model of HS-Small model overlaying Mohr-Coulomb model. The comparison indicated the predicted settlement had a reasonable agreement with the measured settlement. A deep excavation problem at Offenbach was also simulated as a 2-D FEM model using PLAXIS as shown in Figure 2.28a. The settlement caused by the lateral deflection in the retaining structure at the end of excavation was studied. Figure 2.28b shows the predicted results in comparison with the available measurement at the end of excavation. The HS-Small model overlaying Matsuoka-Nakai model had the best fit with the measured settlement. In conclusion, the HS-S models performed well in the examples of tunneling construction and deep excavation.

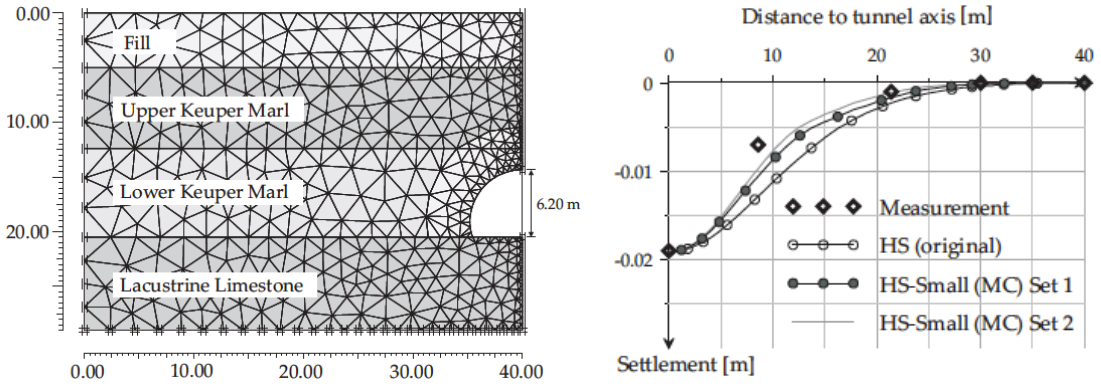

(a) (b)

Figure 2.27: (a) 2D mesh of Steinhaldenfeld NATM tunnel, and (b) Settlements due to construction of Steinhaldenfeld NATM measured in the field and predicted by HS-Small (MC) model (Benz, 2006).

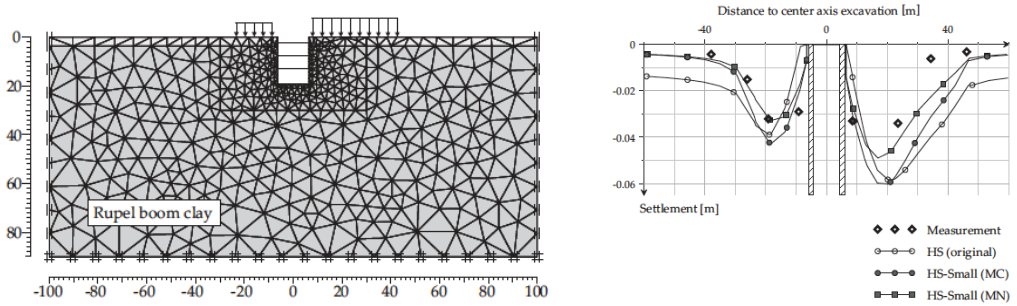

(a) (b)

Figure 2.28: (a) 2-D mesh of deep excavation in Rupel clay, and (b) Settlements induced by deep excavation predicted by HS-Small model and measured in the field after the final excavation step (Benz, 2006).

In both problems, the HS-Small model overestimated the settlement, which indicated the HS-S model still behaved soft in the performance. Also, the small-strain stiffness parameters were solely picked on the basis of data and empirical correlations without solid laboratory and field test data, which might be the reason that model did not capture the behavior of the soil accurately.

2.3 CONCLUSIONS

The following major conclusions are drawn from the literature review:

(1) From the measurements of the lateral load tests with enough resolution at small displacements, the initial relationship of the lateral load versus lateral displacement is non-linear and difficult to be captured by an elastic subgrade modulus, k, which is determined by the internal friction angle of the sand.

(2) The conventional design approaches, API RP 2GEO (2014), underestimates the initial stiffness of the laterally loaded pile and does not capture the non-linearity of the stiffness at small displacements.

Chapter 3: Dynamic Analysis on Offshore Wind Turbines

Data of offshore wind turbine performance was received from Parkwind for the Belwind Offshore Wind Farm and the Northwind Offshore Wind Farm. The data was reviewed, and the analyses were performed using the data to compare the measured and designed natural frequencies of wind turbines under the loads in service. The influence of the stiffness of the sand on the natural frequencies for wind turbines was analyzed to estimate the performance of the API p-y method used in the design. The lateral displacement of the monopile under service loads was re-estimated with the stiffness of the sand which made the design natural frequencies match the field observations.

3.1 Offshore Wind Farms

The Belwind Offshore Wind Farm and the Northwind Offshore Wind Farm are located in the Flrmish Banks area of the southern North Sea off the Belgian coast (Figure 3.1). Parkwind has been monitoring the behavior of the offshore wind turbines in these two wind farms for years. The field performance data obtained from the monitoring was provided for the purpose of research. The information consists of geotechnical reports, structure design reports for monopiles, reports of pile installation, and field monitoring results.

Figure 3.1: Locations of the Belwind Offshore Wind Farm and the Northwind Offshore Wind Farm (Google map).

3.1.1 Belwind Offshore Wind Farm

The Belwind Offshore Wind Farm has a total of 55 installed wind turbine generator (WTG) structures and one substation. The rated power output of each WTG is 3 MW. The support structures are driven monopiles with grouted transition pieces that support WTG tower structures. Figure 3.2 shows the layout of the Belwind Offshore Wind Farm and locations of its boreholes.

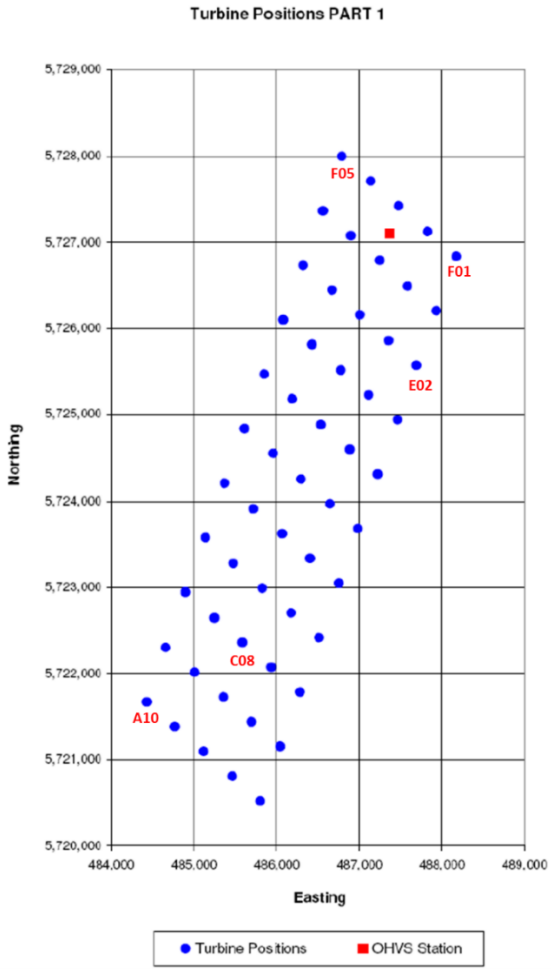

Figure 3.2: Layout of the Belwind Offshore Wind Farm and locations of boreholes.

The subsurface consists of 15 to 20 m of very dense sand with shell fragments underlain by an overconsolidated clay with varying silt content. The following geotechnical investigations were carried out:

1) Cone penetrometer (CPT) tests at 24 locations
2) Soil borings at 5 locations (A10, C08, E02, F01, F05 in Figure 2.2) with standard penetration test (SPT) sampling in the sand and driven tube sampling in the clay
3) Laboratory index property tests

4) Laboratory UU triaxial compression tests on clay samples

At different turbine locations, following design parameters for soil were determined by the geotechnical investigations: unit weight, friction angle, and undrained shear strength for clay versus depth.

The structure design reports provide the analyses of the environmental loads and estimated fundamental natural frequency for each foundation structure. The field monitoring results include the monitored fundamental and second natural frequencies versus time for wind turbine at location C01.

3.1.2 Northwind Offshore Wind Farm

The Northwind Offshore Wind Farm consists of 72 3-MW WTG structures and one substation that were installed in 2014 (Figure 3.3). Table 3.1 shows that the 72 WTG were divided into nine clusters based on water depth and soil conditions.

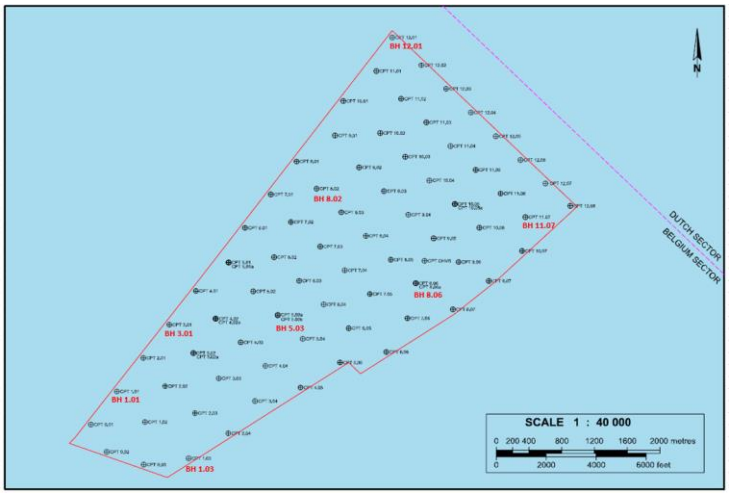

Figure 3.3: Layout of the Northwind Wind Farm and locations of boreholes.

Table 3.1: Clusters of wind turbines in the Northwind Offshore Wind Farm.

Cluster	Max. DSBL (m LAT)	Min. DSBL (m LAT)	No. Of WTGs	WTG ID.
1	-17.9	-17.9	1	F06
2	-18.5	-19.9	8	F05, G02, G03, G05, G06, H01, H05 and H06
3	-20.0	-20.8	11	A01, A02, B01, C01, G01, G04, G07, G08, H02, H03 and H07
4	-21.0	-22.0	13	A03, A04, A05, A07, B02, B03, F01, F02, F08, F09, H04, H08 and H09
5	-22.3	-23.0	10	A06, A08, A09, B07, E06, E09, F03, F07, F10 and G09
6	-22.6	-24.3	9	B04, B06, C02, D01, E01, E04, E05, E07 and F04
7	-25.1	-25.8	9	B05, C03, C07, D02, D08, D09, E02, E03 and E08
8	-26.1	-27.7	9	C04, C05, C06, C08, D03, D04, D05, D06 and D07
9	-28.9	-28.9	2	C09 and C10

The subsurface consists of 15 to 20 m of dense to very dense sand containing localized gravel underlain by stiff to very stiff clay. Rows 11 and 12 have a stratum of stiff to very stiff clay within the dense to very dense sand at approximately 13-17.5 m below the surface. The following geotechnical investigations were carried out:

1) 79 piezocone penetration tests (PCPTs) measuring net cone resistance, total cone resistance, friction ratio, and excess pore-water pressure ratio
2) 8 soil borings (BH 1.01, 1.03, 3.01, 5.03, 8.02, 8.03, 11.07, 12.01 in Figure 2.4) with SPT sampling in the sand, driven tube sampling in the clay, and down-the-hole (DTH) CPT tests in 6 of the boreholes
3) Laboratory index property tests
4) Laboratory UU and CU triaxial compression tests on clay samples

For different wind turbine locations, these geotechnical investigation results were used to establish design parameters for soil: unit weight, friction angle for sand, and undrained shear strength for clay versus depth.

The structure design reports included analyses of the environmental loads and the estimated fundamental natural frequency for each foundation structure. The field performance information provided the fundamental and second natural frequencies.

3.2 Analysis of the Monitoring Data of Natural Frequencies

With the given in-situ soil conditions and the dimensions of the structures, the fundamental natural frequency and second natural frequency were calculated for the wind turbines at the Belwind Offshore Wind Farm and the Northwind Offshore Wind Farm. The structure design reports of the two wind farms provided the designed fundamental natural frequency but did not include the designed second natural frequency. A self-design compute model was created to estimate the second natural frequency and incorporated the following objectives:

- Compare the fundamental and second natural frequencies from the in-situ measurement and those predicted by API p-y method;
- Conduct a sensitivity analysis to study the influence of soil stiffness on the prediction of natural frequencies using the self-design computer model;
- Estimate the lateral displacement of the monopile at mudline using API p-y method with stronger and more realistic soil stiffness under service load.

3.2.1 Modeling Natural Frequency

A computer model was needed to calculate the estimated second natural frequency not given in the design reports and investigate the sensitivity of the influence of the stiffness of the sand on the natural frequencies. The computer model was based on the theory of 1-D Euler-Bernoulli beam and written in the computer language Python. The similar

computer model was also used by Middleweerd (2017) to study the offshore wind turbines in the Eneco Luchterduinen Wind Farm.

The computer model consisted of two parts: the structure of wind turbine and the model of soil-structure interaction. The structure of wind turbine consisted of the nacelle and rotor, tower, transition piece, items on transition piece, and monopile. The model of soil-structure interaction was simulated as non-linear elastic springs based on API p-y method. The resistance induced by the soil-structure interaction at the tip was neglected due to small lateral displacement under service loading. Figure 3.4 shows the computer model of a 1-D model of wind turbine simplified as an Euler-Bernoulli beam model. The 1-D Euler-Bernoulli beam model was divided into multiple elements with lumped mass. The lumped mass could be from the structures, appurtenances, and water and soil inside of the hollow structures. The non-linear elastic springs were modeled as API p-y curves determined by the characteristics of the soil layers. The scour and scour protection would change the characteristics of the soil layers.

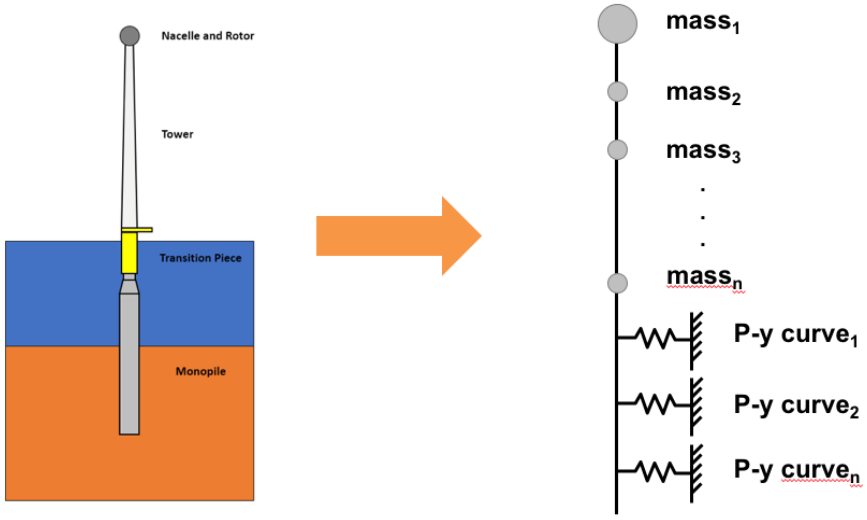

Figure 3.4: Simplified computer model of offshore wind turbine.

3.2.1.1 Mass and Stiffness Matrix

1-D Euler-Bernoulli beam model without damping was chosen to compute the natural frequencies of offshore wind turbines, which was programmed in Python. The wind turbine structure, including tower, transition piece, and monopile, is simplified to a 1-D Euler-Bernoulli beam model and divided into several elements.

A 1-D Euler-Bernoulli beam model with finite elements could be regarded as a 1-D Multi-Degree-of-Freedom (MDF) system. The 1-D MDF system without damping is governed by Equation 3.1:

$$\boldsymbol{m\ddot{u} + ku = 0} \tag{3.1}$$

Equation (4.1) represents N homogeneous differential equations that are coupled through the mass matrix, stiffness matrix for beam, and stiffness matrix for soil spring; N is the number of degree of freedoms and $N-1$ is the number of elements in the system. $\boldsymbol{m}$ is the system mass matrix, $\boldsymbol{k}$ is the system stiffness matrix, and $\boldsymbol{u}$ is the displacement vector including the displacement for each node. The mass stiffness matrix of one single element could be expressed by Equation 3.2:

$$M = \frac{\rho A l}{420}\begin{bmatrix} 156 & 22l & 54 & -13l \\ 22l & 4l^2 & 13l & -3l^2 \\ 54 & 13l & 156 & -22l \\ -13l & -3l^2 & -22l & 4l^2 \end{bmatrix} \tag{3.2}$$

where ρ is the equivalent density of the element, A is the equivalent cross-section area of the element, l is the length of the element. The stiffness matrix for beam and stiffness matrix for soil spring of one single element could be expressed using Equation 3.3 and 4.4, respectively:

$$K_e = \frac{EI}{l^3}\begin{bmatrix} 12 & 6l & -12 & 6l \\ 6l & 4l^2 & -6l & 2l^2 \\ -12l & -6l & 12 & -6l \\ 6l & 2l^2 & -6l & 4l^2 \end{bmatrix} \tag{3.3}$$

$$K_s = \frac{k_s l}{420}\begin{bmatrix} 156 & 22l & 54 & -13l \\ 22l & 4l^2 & 13l & -3l^2 \\ 54 & 13l & 156 & -22l \\ -13l & -3l^2 & -22l & 4l^2 \end{bmatrix} \tag{3.4}$$

where: E is the Young's modulus of the element, I is the equivalent area moment of inertia of the element, k_s is the stiffness of the soil spring. k_s is determined by using API p-y method of checking the Figure 2.7 showing the relationship between soil stiffness and the friction angle of the soil. The time variation of the displacements could be represented by a simple harmonic function:

$$\boldsymbol{u}(t) = \emptyset_n(A_n cos\omega_n t + B_n sin\omega_n t) \tag{3.5}$$

where: $\emptyset_n$ is the deflected shape, and ω_n is the natural circular frequency of vibration. Substitute Equation 3.5 into Equation 3.1, Equation 3.6 could be obtained:

$$[\boldsymbol{k} - \omega_n^2 \boldsymbol{m}]\emptyset_n = \boldsymbol{0} \tag{3.6}$$

Equation 3.6 has nontrivial solutions if:

$$det[\boldsymbol{k} - \omega_n^2 \boldsymbol{m}] = 0 \tag{3.7}$$

The N natural frequencies ω_n of vibration are the N roots of ω_n^2 by solving the eigenvalues of Equation 3.7. The roots, ω_n^2, of the Equation 3.7 are arranged in sequence from smallest to largest ($\omega_1^2 < \omega_2^2 < \cdots < \omega_n^2$). The natural cyclic frequency of vibration,

f_n, could by calculated by $f_n = \omega_n/2\pi$. Fundamental natural frequency, f_1, and second natural frequency, f_2, are evaluated in this research.

3.2.1.2 Contained Mass

The analysis of the natural frequency needed to take the mass of water and soil into account for the hollow structures submerged into the water and driven into soil. The contained mass included the mass of the sea water and the soil contained inside the monopile. Equation 3.8 gives the expression to evaluate the contained mass for each element in 1-d Euler-Bernoulli beam model:

$$m_{contained} = r\rho d^2 \Delta l / 4 \tag{3.8}$$

where ρ is the density of the seawater or soil, d is the internal diameter of the monopile, and Δl is the length of the divided element.

3.2.1.3 Scour Protection

Scour protections were used to prevent the removal of sediment from around offshore wind turbine, which was caused by the swiftly moving water. In the Belwind Offshore Wind Farm and North Offshore Wind Farm, the scour protection was post-installed by dumping the scour protection material in developed scour hole. According to the report of scour protection, a scour hole of three meters was approximated based on the observation of the scour test in the field. The internal friction of the scour protection material was assumed to be either $40°$ (lower design case) and $45°$ (upper design case). In this analysis, the lower design case was accepted.

3.2.1.4 Model Verification

For verification purposes, Table 3.2 shows the comparison between the predicted fundamental natural frequency from our computer model and it provided in the design reports. The predicted fundamental frequencies agreed well with the them provided in the design reports. It demonstrated that the self-design computer model worked same with the commercial software in the accepted tolerance.

Table 3.2: Comparison of first order resonance frequency (Belwind).

Wind Turbine #	Report (Hz)	Computer Model (Hz)	Difference (%)
A10	0.332	0.336	1.2%
B02	0.352	0.344	2.2%
C01	0.346	0.346	0.0%
D02	0.351	0.348	0.8%
E03	0.335	0.340	1.5%

3.2.2 Analysis of the Belwind Offshore Wind Farm

Weijtjens and Deviendt (2017) published the monitoring data on the natural frequencies of wind turbine C01 in the Belwind Offshore Wind Farm from 2012 to 2016. Figure 3.7 shows the evolution of the fundamental natural frequency over the five periods (2012 to 2016) of operational conditions. The fundamental natural frequency was slightly stiffening over time. The range of the measured fundamental natural frequency was from 0.358 Hz to 0.375 Hz.

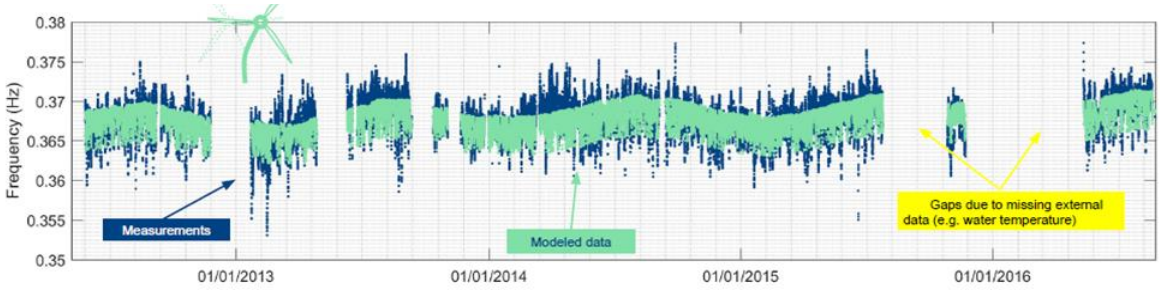

Figure 3.5: Measured fundamental natural frequency at Belwind (Weijtejens and Deviendt, 2017).

Figure 3.8 shows the evolution of the second natural frequency over 5 periods (2012 to 2016) of operational conditions. The second natural frequency was stiffening significantly over time. The range of the second natural frequency in 2012 was from 1.42 Hz to 1.5 Hz and in 2014 was from 1.47 Hz to 1.52 Hz. Figure 3.9 indicates an increase of 0.05 Hz (3%) in the second natural frequency over four years.

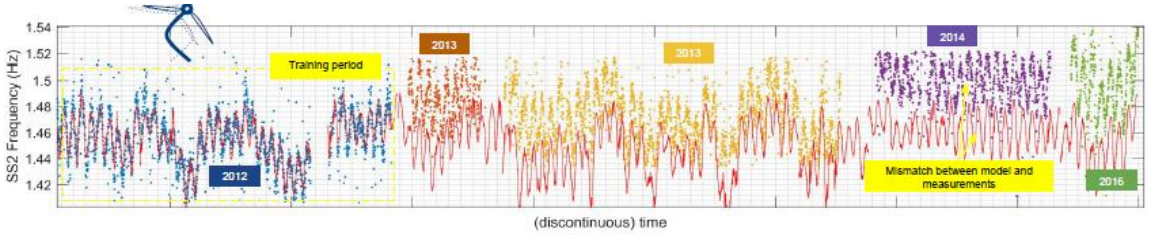

Figure 3.6: Measured second natural frequency at Belwind (Weijtjens and Deviendt 2017).

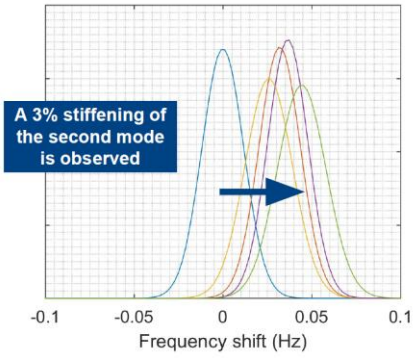

Figure 3.7: Frequency shift of the second natural frequency at Belwind (Weijtjens and Deviendt 2017).

Figure 3.10 compares the estimated fundamental natural frequency from the design reports with those measured in-situ for each wind turbine. Position C01 is where the wind turbine equipped with multi-physics sensors and has been measured for years. The result of the comparison shows that the predicted fundamental natural frequency of most wind turbines is below the monitoring range.

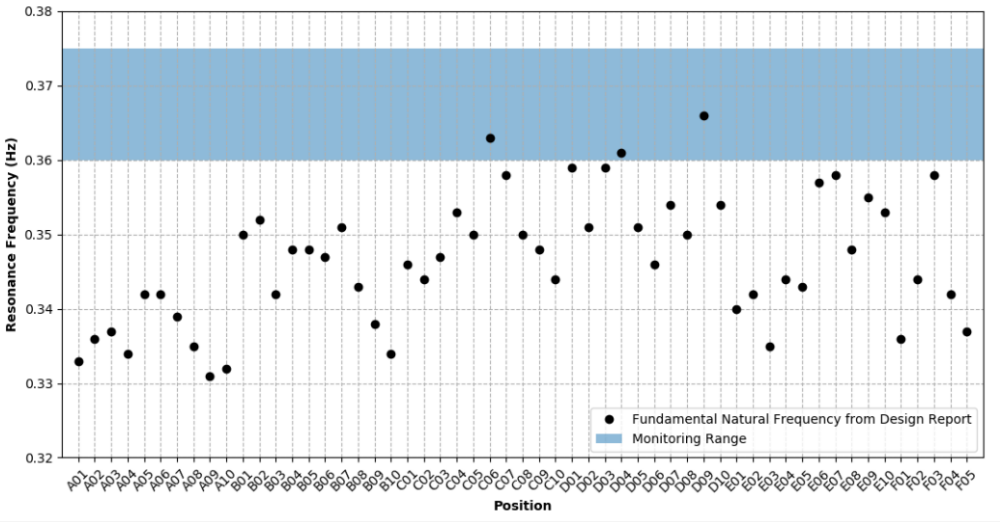

Figure 3.8: Fundamental natural frequencies from design reports and in-situ measurements at the Belwind Offshore Wind Farm (Gilbert et al., 2018).

The self-design computer model calculated the second natural frequencies for five wind turbines at Belwind. Beside the monitored wind turbine at position C01, four other wind turbines were randomly picked to calculate their second natural frequencies. Figure 3.11 compares the calculated and measured second natural frequencies. The result of the comparison indicates that the second natural frequency is also underestimated by the current design method.

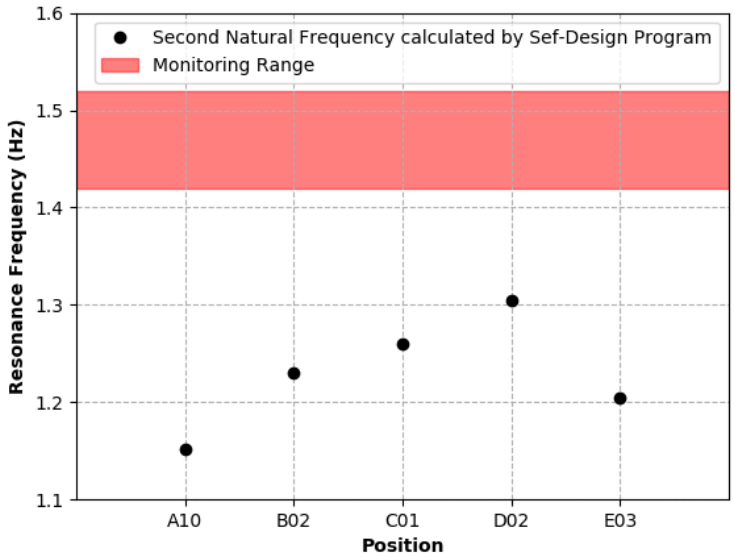

Figure 3.9: Second natural frequencies from design and in-situ measurements at the Belwind Offshore Wind Farm (Gilbert et al., 2018).

3.2.3 Analysis of the Northwind Offshore Wind Farm

The monitoring report included the measured fundamental natural frequencies from multiple wind turbines in the Northwind Offshore Wind Farm from 2014 to 2015. The range of measured fundamental natural frequency was from 0.275 Hz to 0.307 Hz. The maximum frequency of the 1P harmonic was at 0.24 Hz, which meant that the measured fundamental natural frequency was well above the 1P frequency.

The monitoring report also included the evolution of the measured second natural frequencies from 2014 to 2015. The mean value of the second natural frequency increased from 1.718 Hz in 2014 to 1.722 Hz in 2015. While not significant yet, the slight increasing trend in the monitoring indicated that the long-term behavior of the wind turbines in the

Northwind Offshore Wind Farm was similar to the behavior of them in the Belwind Offshore Wind Farm.

Figure 3.12 shows the comparison between the predicted and measured fundamental natural frequencies. The 72 wind turbine generators in the Northwind Offshore Wind Farm were divided into nine clusters based on water depth and soil conditions, and one design was determined for each cluster. The result of comparison indicated that the predicted fundamental natural frequencies from the design reports were all lower than the in-situ measurements.

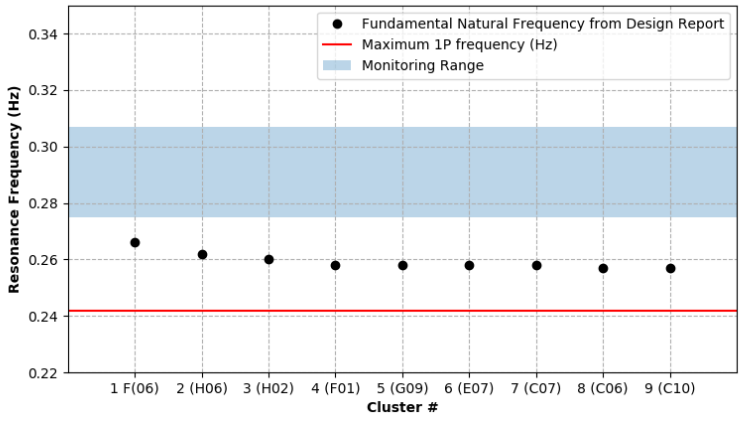

Figure 3.10: Fundamental natural frequencies from design and monitoring reports in the Northwind Offshore Wind Farm.

3.2.4 Influence of Sand Stiffness on Natural Frequencies

The self-design computer model was used to analyze the influence of the soil stiffness had on the fundamental and second natural frequencies. The stiffness of the sand was determined by the coefficient of the lateral soil reaction, k, which was determined by the internal friction angle of the sand. In this analysis, k was multiplied by an amplified coefficient to investigate the influence of the soil stiffness on the natural frequencies. Wind

turbines A10, B02, C01, D02, and E03 in the Belwind Offhore Wind Farm were chosen to be analyzed. The results show that the natural frequencies increase with increasing stiffness of the sand and the influence is larger for the second natural frequency than the fundamental natural frequency.

Figure 3.13 shows in the influence of the soil stiffness on the fundamental natural frequency of wind turbines in the Belwind Offshore Wind Farm. The fundamental natural frequencies increase with increasing sand stiffness. With the amplified coefficient from one to ten, the fundamental natural frequency of wind turbine C01 increases from 0.346 Hz to 0.362 Hz, an approximate 4.6% increase. When the amplified coefficient approaches seven, the fundamental natural frequency of wind turbine C01 reaches the lower bound of the measurement.

Figure 3.14 shows the influence of the soil stiffness on the second natural frequency of wind turbines in the Belwind Offshore Wind Farm. With the amplified coefficient from one to ten, the second natural frequency of wind turbine C01 increases from 1.26 Hz to 1.415 Hz, an approximate 12.6% increase. When the amplified coefficient approaches seven, as same with the analysis for the fundamental natural frequency, the second natural frequency of wind turbine C01 reaches the lower bound of the measurement.

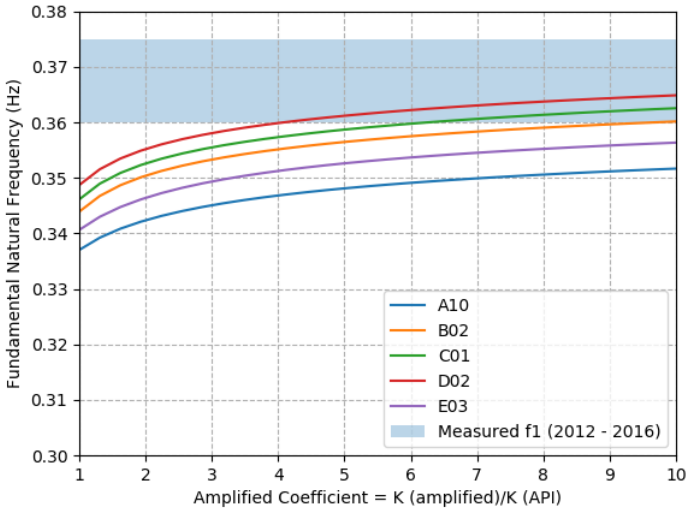

Figure 3.11: Influence of the sand stiffness on fundamental natural frequency in the Belwind Offshore Wind Farm (Gilbert et al., 2018).

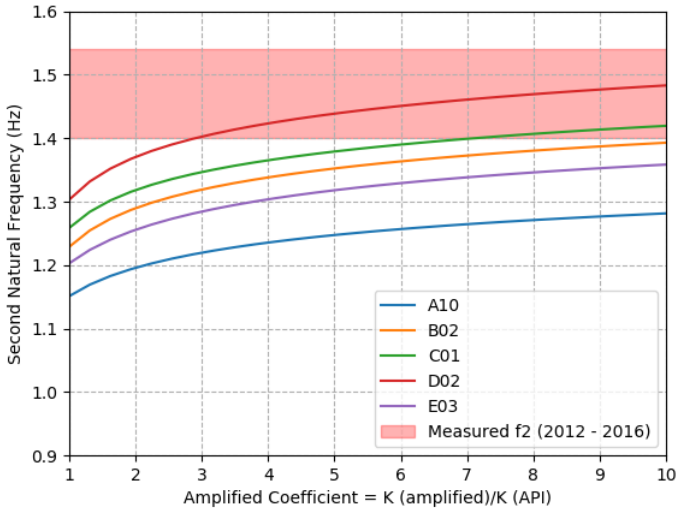

Figure 3.12: Influence of the sand stiffness on second natural frequency in the Belwind Offshore Wind Farm (Gilbert et al., 2018).

Table 3.3 shows the summary of the sensitivity of the sand stiffness (elastic subgrade modulus, k) on the natural frequencies of the offshore wind turbines at Belwind. The increasing sand stiffness increases the predicted natural frequencies of the offshore wind turbines and makes them closer to the range of the measured natural frequencies. The influence of the change of the sand stiffness is larger on the second natural frequency than the fundamental natural frequency.

Table 3.3: Influence of the sand stiffness on the natural frequencies.

	$f_0\ (Hz)$ $K_{amp} = 1.0$	$f_0\ (Hz)$ $K_{amp} = 10.0$	$Increment$	$f_1\ (Hz)$ $K_{amp} = 1.0$	$f_1\ (Hz)$ $K_{amp} = 10.0$	$Increment$
A10	0.336	0.351	4.3%	1.149	1.278	11.2%
B02	0.343	0.359	4.7%	1.226	1.388	13.2%
C01	0.346	0.362	4.7%	1.256	1.415	12.6%
D02	0.348	0.364	4.6%	1.300	1.478	13.7%
E03	0.340	0.356	4.6%	1.200	1.354	12.8%

f_0: Fundamental Natural Frequency
f_1: Second Natural Frequency
$Increment$: $(f_{K=10.0} - f_{K=1.0})/f_{K=1.0} * 100\%$

3.2.5 Assessment of Lateral Displacement of Monopile at Mudline under Service Loading

To estimate the displacement of the monopile at mudline under service loading, the p-y method was used with a stronger sand stiffness obtained from the previous analysis to match the measured natural frequencies. The previous sections indicate that the more realistic stiffness of the sand should be around seven times the designed sand stiffness determined by the internal friction angle of sand based on the API p-y method.

The monopile for wind turbine C01 was simplified to a pile with 5 meters diameter, 20 meters length, and 0.06 meters wall thickness. In the design report, with a wind speed of 12 m/s, the mean overturning moment was 30,000 kN-m and the mean horizontal force

was 310 kN for an operating wind turbine with wind and wave load. The profile of soil was assumed to be uniform. The submerged unit weight of the sand was 10 kN/m^3. The internal friction angle of sand was assumed to be 40 degrees. The coefficient of the elastic subgrade modulus, k, was multiplied by seven to make the fundamental and second natural frequencies reaching the range of measurement. k was equal to 290,000 kN/m^3 in this p-y analysis.

The predicted displacement of the monopile at mudline was 0.0019 m under the service load combination. The normalized displacement was 0.04% of the diameter of the pile. The result indicated the importance of finding an optimal method to measure the stiffness of the sand under small displacement and developing an advanced methodology to apply the small-displacement stiffness on the p-y methods.

With the stronger and more realistic elastic subgrade modulus and under the service load combination, the predicted displacement of the monopile at mudline was equal to 0.0019 m which was 0.04% of the diameter of the monopile. Figure 3.13 shows the measured overturning moment at mudline with time for an offshore wind supported by monopile under service loading based on wind speed on 12 m/s turbine at the Belwind Offshore Wind Farm. The lateral shear force at mudline was calculated by assuming that the shear force was only from the thrust load applied by the wind and the level arm was 100 meters. The thrust load reached maximum at the wind speed of 12 m/s (Noppe et al., 2016). Figure 3.14 shows the predicted normalized displacement of the monopile at mudline with time using the stronger elastic subgrade modulus, which shows the normalized displacement of the monopile at mudline is less than 0.07% under service loading.

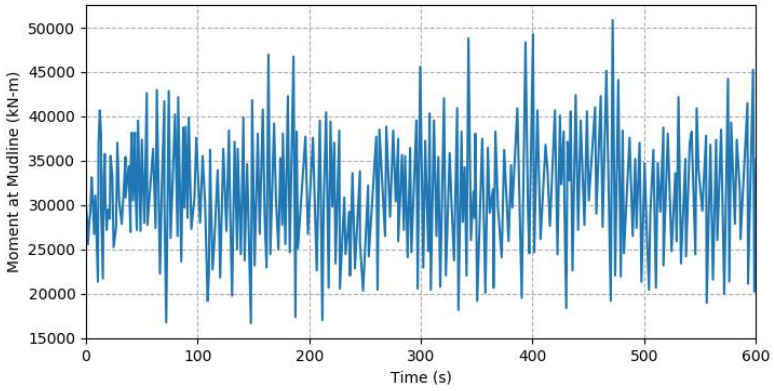

Figure 3.13: Overturning moment at mudline obtained for an operational wind turbine with wind and wave loads based on wind speed on 12m/s.

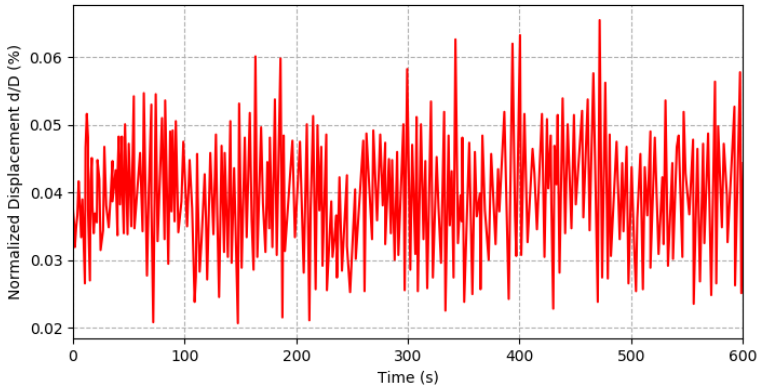

Figure 3.14: Predicted normalized displacement at mudline with the stronger elastic subgrade modulus at wind speed of 12m/s.

The analysis result indicates the necessity of using an optimal method to measure the sand stiffness at small lateral displacements under service loading and developing an advanced methodology to improve p-y methods.

3.3 CONCLUSIONS

The following major conclusions can be drawn from these analyses using API p-y method to predict the natural frequencies of the offshore wind turbines:

(1) The conventional design approach (e.g., API p-y method) underestimates the fundamental and second natural frequencies of the offshore wind turbines.

(2) In the field, the natural frequencies of the offshore wind turbines increase with time and the second natural frequency has more increment than the fundamental natural frequency.

(3) The influence of increasing sand stiffness is larger on the second natural frequency than the fundamental natural frequency.

(4) The prediction of the natural frequency is sensitive to an accurate evaluation of the sand stiffness and the elastic subgrade modulus, k, needs to be amplified by at least five times to match the field measurements.

(5) With a stronger and more realistic elastic subgrade modulus and under service loading, the predicted lateral displacement of the monopile at mudline is less than 0.05% of the pile diameter.

Chapter 4: Development of the Soil Constitutive Model with Non-linear Small-strain Behavior

A soil constitutive model is proposed to simulate the behavior of sand at small strains for numerical modeling of 3-D FEM model in Abaqus. The stiffness of sand increases with the mean effective stress and decreases non-linearly with increasing shear strain. The behavior of sand at small strains is described by (1) the relationship between the maximum shear modulus, G_{max}, versus the mean effective stress, σ_0', and (2) the relationship between the normalized shear modulus, G/G_{max}, versus the shear strain, γ, and mean effective stress, σ_0'. The equations proposed by Darendeli (2001) and Menq (2003) are used to determine the relationships. Element tests are conducted to check the performance of the proposed soil constitutive model by comparing the prediction with the measurements from laboratory tests. The laboratory tests consist of resonant column tests, torsional shear tests, and dynamic triaxial tests. The comparison shows the proposed soil constitutive model has a good performance of predicting the behavior of the soil element at small strains.

4.1 Soil Models of Small-strain Behavior

Based on the non-linear behavior of sand at small strains, a soil constitutive model of sand is proposed in this research. The observations of behavior of sand in small strain indicate that the shear modulus of sand increases with the mean effective stress and decreases non-linearly with increasing shear strain. Figure 4.1 shows that the normalized shear modulus, G/G_{max}, versus shear strain, γ, relationship of sand is separated into four strain ranges: (1) linear, (2) nonlinear elastic, (3) moderately nonlinear, and (4) highly nonlinear (Kacar, 2014).

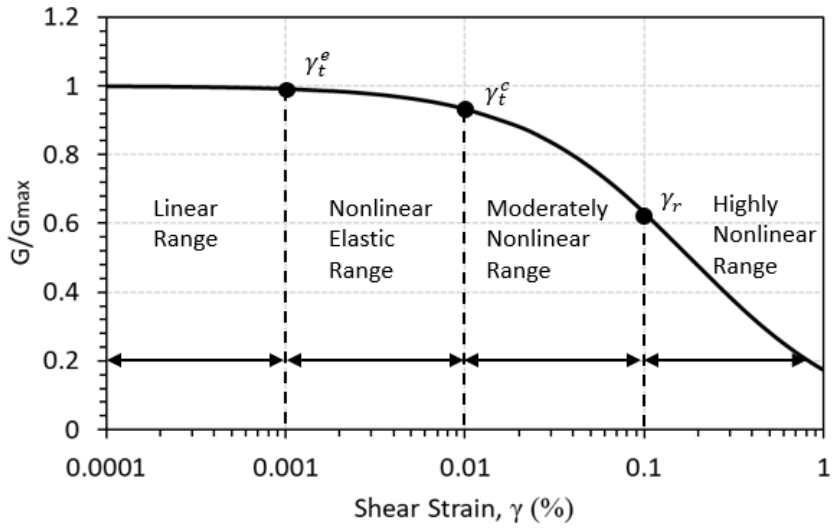

Figure 4.1: $G/G_{max} - \log\gamma$ curve with the linear, nonlinear elastic, moderately nonlinear, and highly nonlinear ranges (Kacar, 2014).

In the linear range, the shear modulus, G, keeps constant with the increase of the shear strain, γ, and is equal to the maximum shear modulus, G_{max}. Out of the linear range where shear strain γ is larger than the elastic threshold value of shear strain, γ_t^e, the shear modulus, G, becomes strain-dependent and decreases non-linearly with the increase of shear strain, γ. To investigate the linear and non-linear behavior of sand over a wide range of shear strains, dynamic laboratory testing methods are recommended to be performed, such as resonant column and torsional shear (RCTS) tests.

Mohr-Coulomb model is a simple and well-known linearly-elastic perfectly-plastic model. However, the soil stiffness in the Mohr-Coulomb model is determined by the conventional soil tests (e.g., triaxial compression tests), which causes that the soil stiffness is usually decreased to less than half of its initial value. In the proposed soil constitutive model, the soil stiffness is depended on the mean effective stress and the shear strain.

The following sections represent four different models to capture the non-linear stiffness of sand: Menq (2003), Hardin and Drnevich (1972), Ishibashi (1993), and Santo and Correla (2001).

4.1.1 Menq (2003)

To calculate the shear modulus, G, the maximum shear modulus, G_{max}, and the normalized shear modulus G/G_{max} must be known for a level of shear strain, γ, and mean effective stress, σ_0'. A series of studies were conducted by Darendeli (2001) and Menq (2003) at The University of Texas at Austin to provide the empirical equations for G_{max} and G/G_{max}.

4.1.1.1 Nonlinear Shear Modulus Reduction Curve, G/G_{max}

Darendeli (2001) proposed a modified hyperbolic model to express the dynamic soil properties in terms of normalized shear modulus. The expression of the modified hyperbolic model is as following:

$$\frac{G}{G_{\max}} = \frac{1}{1+\left(\frac{\gamma}{\gamma_r}\right)^a} \tag{4.1}$$

where, γ_r = reference strain at $G/G_{max} = 0.5$,

a = curvature coefficient, and,

G = shear modulus at a shear strain value of γ.

The following relationships for γ_r and a were recommended by Menq (2003) so that the Equation 4.1 could be used for nonplastic granular soil:

$$g_r = 0.12 \times C_u^{-0.6} \times \left(\frac{s_0^{'}}{P_a} \right)^{0.5 \times C_u^{-0.15}} \tag{4.2}$$

$$a = 0.86 + 0.1' \log(\frac{s_0^{'}}{P_a}) \tag{4.3}$$

where: C_u = uniformity coefficient

σ_0' = mean effective stress

P_a = pressure of one atmosphere

To make the shape of the $G/G_{max} - \log\gamma$ curve to be easily modified and match the laboratory tests, the Equation 4.4 and 4.5 are recommended to have following alternative formats:

$$\gamma_r = C_1 \times (\frac{\sigma_0^{'}}{P_a})^{C_2} \tag{4.4}$$

$$a = C_3 + C_4 \log(\frac{\sigma_0^{'}}{P_a}) \tag{4.5}$$

where parameters C_1, C_2, C_3, and C_4 provide more freedom to change the shape of the $G/G_{max} - \log\gamma$ curve.

4.1.1.2 Maximum Shear Modulus, G_{max}

The following parameters were studied by Menq (2003) on the maximum shear modulus, G_{max}: mean effective stress, σ_0', void ratio, e, coefficient of uniformity, C_u, median grain size, D_{50}, water content, w, and measurement frequency, f_m.

Menq (2003) proposed an expression of G_{max} as a function of the shear modulus at the mean effective stress, σ_0', of one atmosphere, C_{G1}, and proportional to the normalized mean effective stress raised to a power, n_g:

$$G_{\max} = C_{G1}\left(\frac{\sigma_0'}{P_a}\right)^{n_G} \tag{4.6}$$

The parameter C_{G1} could be expressed as a function of coefficient of uniformity, C_u, median grain size, D_{50}, and void ratio, e:

$$C_{G1} = C_{G3} \times C_u^{b1} \times e^{x} \tag{4.7}$$

where: C_{G3} = 67.1 MPa

C_u = coefficient of uniformity

D_{50} = median grain size (in mm)

b1 = −2.0

e = void ratio

$x = -1-(\frac{D_{50}}{20})^{0.75}$

$n_G = 0.48C_u^{0.09}$

4.1.2 Hardin & Drnevich (1972)

The relationship between shear stress and shear strain was regarded as the most import part for the critical soil properties by Hardin & Drnevich (1972). A simple relationship of shear stress and shear strain was proposed by investigating the data from measurements of the shear modulus for a wide variety of clean sands and cohesive soils.

The following equation was developed by Hardin & Drnevich (1972) to express the maximum shear modulus in very small strain:

$$G_{\max} = 1230 \frac{(2.973 - e)^2}{1+e} (OCR)^K \sigma_0'^{1/2} \tag{4.8}$$

where, e = void ratio,

OCR = overconsolidation ratio

σ_0' = mean effective stress

Table 4.1: Value of K (Hardin & Drnevich, 1972).

PI (Plasticity Index)	***K***
0	0
20	0.18
40	0.30
60	0.41
80	0.48
>=100	0.50

The following equations were developed by Hardin & Drnevich (1972) to express the non-linearity of the normalized shear modulus:

$$\frac{G}{G_{\max}} = \frac{1}{1+\gamma_h} \tag{4.9}$$

$$\gamma_h = \frac{\gamma}{\gamma_r} [1 + a \times e_{xp}^{-b(\gamma/\gamma_r)}] \tag{4.10}$$

$$\gamma_r = \frac{\tau_{\max}}{G_{\max}} \tag{4.11}$$

$$t_{max} = \left\{ \left[\frac{(1+K_0)}{2} s_v' \sin f + c \cos f \right]^2 - \left[\frac{(1+K_0)}{2} s_v' \right]^2 \right\}^{1/2} \quad (4.12)$$

where, K_0 = coefficient of lateral stress

σ_v' = vertical effective stress

c *and* ϕ = static strength parameters in terms of effective stress

Table 4.2: Values of a and b (Hardin & Drnevich, 1972).

Soil type (1)	Modulus or damping (2)	Value of a (3)	Value of b (4)
Clean dry sands	Modulus	$a = -0.5$	$b = 0.16$
	Damping[b]	$a = 0.6(N^{-1/6}) - 1$	$b = 1 - N^{-1/12}$
Clean saturated sands	Modulus[b]	$a = -0.2 \log N$	$b = 0.16$
	Damping[b]	$a = 0.54(N^{-1/6}) - 0.9$	$b = 0.65 - 0.65N^{-1/12}$
Saturated cohesive soils	Modulus	$a = 1 + 0.25 (\log N)$	$b = 1.3$
	Damping	$a = 1 + 0.2(f^{1/2})$	$b = 0.2f\left(e_{xp}^{-\bar{\sigma}_0}\right) + 2.25\bar{\sigma}_0 + 0.3 (\log N)$

[a] f is in cycles per second and $\bar{\sigma}_0$ is in kilograms per square centimeter.
[b] These values for modulus and damping of clean sands are for less than 50,000 cycles of loading. Beyond 50,000 cycles the damping begins to increase with number of cycles, possibly due to fatigue effects (2). The behavior of modulus for saturated sands beyond 50,000 cycles is not yet established.

4.1.3 Ishibashi (1993)

To study the relationship of shear modulus and shear strain, Ishibashi (1993) analyzed many laboratory dynamic tests of soils for general use. The soil included non-plastic sands to highly plastic clays.

Ishibashi (1993) proposed the shear modulus, G, is generally expressed in the form:

$$G = K(\gamma) f(e) \sigma_0'^{m(\gamma)} \quad (4.13)$$

where, $K(\gamma)$ is a decreasing function of shear strain, γ, and is unity at very small γ ($\leq 10^{-6}$), $f(e)$ is a function of void ratio, e, σ_0' is the mean effective stress, and power $m(\gamma)$ is an increasing function of γ. The maximum shear modulus, G_{max}, is the maximum value of G and is usually obtained at $\gamma = 10^{-6}$ or less. Therefore G_{max} is:

$$G_{\max} = K_0 f(e)\sigma_0^{'m_0} \tag{4.14}$$

where, $K_0 = K(\gamma \leq 10^{-6}) = 1.0$, and,

$m_0 = m(\gamma \leq 10^{-6})$.

From Equation 4.13 and Equation 4.14, Ishibashi (1993) obtained:

$$\frac{G}{G_{\max}} = K(\gamma)\sigma_0^{'m(\gamma)-m_0} \tag{4.15}$$

where,

$$K(\gamma) = 0.5\left[1 + \tanh\left\{\ln\left(\frac{0.000102}{\gamma}\right)^{0.492}\right\}\right] \tag{4.16}$$

$$m(\gamma) - m_0 = 0.272\left[1 - \tanh\left\{\ln\left(\frac{0.000556}{\gamma}\right)^{0.4}\right\}\right] \tag{4.17}$$

$K(\gamma)$ and $m(\gamma) - m_0$ values were regressed on experimental data for variant kinds of sand and developed specially for $\sigma_0' = 1.0kN/m^2$. σ_0' was the only parameter influencing the shape of the G/G_{max} curve.

4.1.4 Santo & Correla (2001)

Santo & Correla (2001) recommend to use a key parameter called "threshold" shear strain, $\gamma_{0.7}$, the describe the relationship of normalized shear modulus and shear strain. The "threshold" shear strain, $\gamma_{0.7}$, was defined as the shear strain at normalized shear modulus, G/G_{max}, equaling to 0.7. The finite element software PLAXIS uses Santo & Correla (2001) in the Hardening Soil Model with Small-Strain Stiffness (HSSMALL) constitutive model to capture the nonlinearly of soil stiffness decay.

Santo & Correla (2001) suggested the following stiffness decay with respect to strain:

$$\frac{G}{G_{\max}} = \frac{1}{1 + a\left|\frac{\gamma}{\gamma_{0.7}}\right|} \tag{4.18}$$

where, $a = 0.385$ and $\gamma_{0.7}$ is the γ corresponded to $G/G_0 = 0.722$.

4.1.5 Comparison of Different Soil Dynamic Models

To study the performance of the different soil models with small-strain behaviors, predicted $G/G_{max} - \log\gamma$ curves based on the different soil models were compared to them measured in the resonant column and torsional shear (RCTS) tests. Two kinds of sand were used in the comparison, one was the All-Purpose Sand purchased from Home Depot and the other one was collected from Mustang Island. Torsional shear tests were conducted on the All-Purpose sand and resonant column tests were conducted on the Mustang Island sand. The $G/G_{max} - \log\gamma$ curves were measured under two confining pressures of 2 psi and 4 psi for All-Purpose Sand and 12 psi and 48 psi for Mustang Island Sand.

Based on the comparisons shown from Figures 4.2 to 4.5, the $G/G_{max} - \log\gamma$ curves predicted by Menq (2003) have the best fit with the measured curves for the two kinds of sands under different confining pressures. The curves predicted by Menq (2003) have a good agreement with the measured curves from the linear range of the moderately non-linear range. The curves predicted by Hardin & Drnevich (1972) only match well with the measured curves in the linear range, but not have a good fit with the normalized shear modulus in the range from moderately to highly non-linear. The curves predicted by Ishibashi (1993) have a poor agreement with the measured curves, which is caused by that Ishibashi (1993) used a regression curve for variant kinds of sand with different uniformity coefficients. The curves predicted by Santo & Correia (2001) overestimate the stiffness for All-Purpose sand and underpredict the stiffness for Mustang Island sand. Therefore, the Menq (2003) approach provides the best fit to the measurements.

Table 4.3: Characteristics for All-Purpose Sand.

D50 (mm)	**Void Ratio**	**Cu**
0.67	0.56	4.9

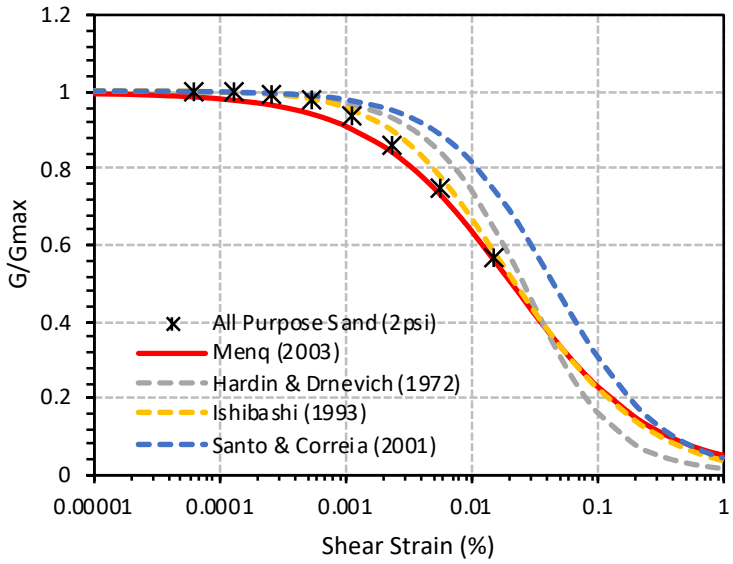

Figure 4.2: Comparison of All-Purpose Sand under 2psi confining pressure.

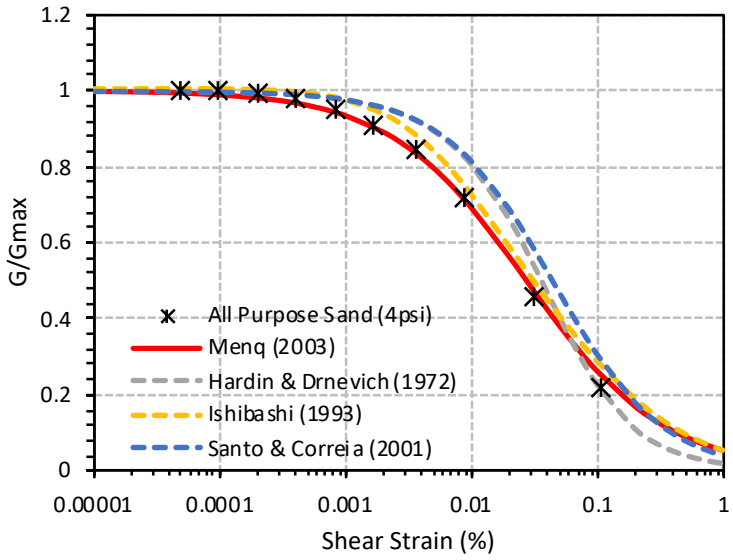

Figure 4.3: Comparison for All-Purpose Sand under 4 psi confining pressure.

Table 4.4: Characteristics of Mustang Island Sand.

D50 (mm)	Void Ratio	Cu
0.14	0.67	1.31

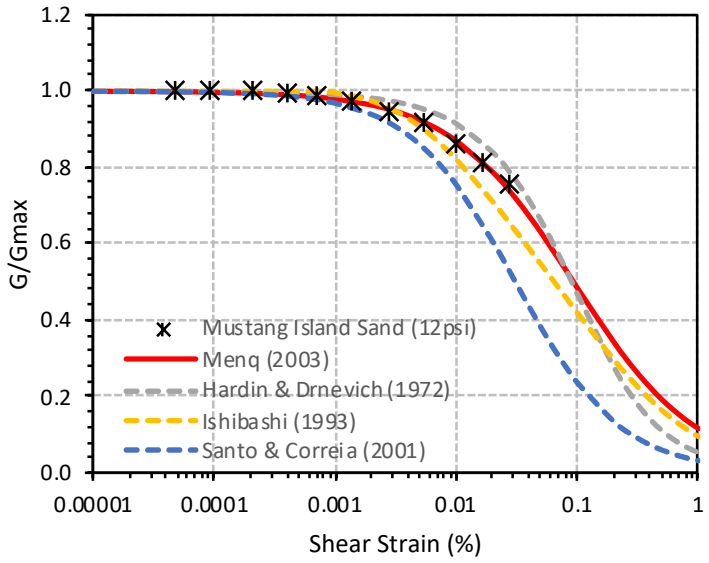

Figure 4.4: Comparison for Mustang Island Sand under 12 psi confining pressure.

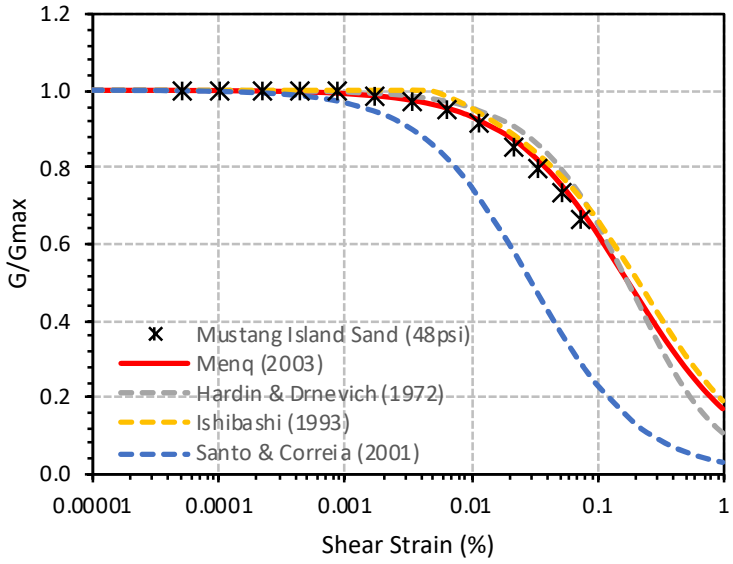

Figure 4.5: Comparison for Mustang Island Sand under 48 psi confining pressure.

4.2 DEVELOPMENT OF THE SOIL CONSTITUTIVE MODEL

This section presents the progress in developing the soil constitutive model. The soil constitutive model combines the form of the orthotropic material and the theory of Darendeli (2001) and Menq (2003). The soil constitutive model adds Masing's Rule to simulate the unloading and reloading behavior of the soil material. The Masing's Rule is not written into the subroutine of the soil constitutive model in the current stage, which will be completed in the future work.

4.2.1 Orthotropic

The soil constitutive model represents orthotropic linear behavior and strain-induced anisotropy. An orthotropic linear elastic material is on that has three orthogonal planes of microstructural symmetry. The stiffness matrix has nine independent elastic constants:

$$\begin{bmatrix} \sigma_{11} \\ \sigma_{22} \\ \sigma_{33} \\ \sigma_{23} \\ \sigma_{13} \\ \sigma_{12} \end{bmatrix} = \begin{bmatrix} C_{11} & C_{12} & C_{13} & & & \\ & C_{22} & C_{23} & & & \\ & & C_{33} & & & \\ & & & C_{44} & & \\ & & & & C_{55} & \\ & & & & & C_{66} \end{bmatrix} \begin{bmatrix} \varepsilon_{11} \\ \varepsilon_{22} \\ \varepsilon_{33} \\ 2\varepsilon_{23} \\ 2\varepsilon_{13} \\ 2\varepsilon_{23} \end{bmatrix} \tag{5.19}$$

Expressing the coefficient, C_{ij},in terms of Young's modulus, E, Poisson's ratio, υ, and shear modulus, G, the stiffness matrix can be inverted to a compliance matrix:

$$\begin{bmatrix} \varepsilon_{11} \\ \varepsilon_{22} \\ \varepsilon_{33} \\ 2\varepsilon_{23} \\ 2\varepsilon_{13} \\ 2\varepsilon_{12} \end{bmatrix} = \begin{bmatrix} \frac{1}{E_1} & -\frac{\nu_{21}}{E_2} & -\frac{\nu_{31}}{E_3} & & & \\ -\frac{\nu_{12}}{E_1} & \frac{1}{E_2} & -\frac{\nu_{32}}{E_3} & & & \\ -\frac{\nu_{13}}{E_1} & -\frac{\nu_{23}}{E_2} & \frac{1}{E_3} & & & \\ & & & \frac{1}{G_{23}} & & \\ & & & & \frac{1}{G_{13}} & \\ & & & & & \frac{1}{G_{12}} \end{bmatrix} \begin{bmatrix} \sigma_{11} \\ \sigma_{22} \\ \sigma_{33} \\ \sigma_{23} \\ \sigma_{13} \\ \sigma_{12} \end{bmatrix} \tag{4.20}$$

The nine independent constants are:

E_i is Young's modulus of the material in direction $i = 1,2,3$; for example, $\sigma_{11} = E_1\varepsilon_{11}$ for uniaxial tension in the direction 1.

υ_{ij} is Poisson's ratio representing the ratio of transverse strain to the applied strain in uniaxial tension; for example, $\upsilon_{ij} = -\varepsilon_{22}/\varepsilon_{11}$ for uniaxial tension in direction 1.

G_{ij} is the shear modulus in the corresponding plane; for example, G_{12} is the shear modulus for shearing in the 1-2 plane. From the symmetry of the stiffness matrix,

$$\nu_{23}E_3 = \nu_{32}E_2,\ \nu_{13}E_3 = \nu_{31}E_1,\ \nu_{12}E_2 = \nu_{21}E_1$$

If we assume that all values of Poisson's Ratio are equal to, say, ν,

$$E_1 = E_2 = E_3 = E$$

The compliance matrix can be written in simpler form in terms of five independent elastic constants:

$$\begin{bmatrix} \varepsilon_{11} \\ \varepsilon_{22} \\ \varepsilon_{33} \\ 2\varepsilon_{23} \\ 2\varepsilon_{13} \\ 2\varepsilon_{12} \end{bmatrix} = \begin{bmatrix} \frac{1}{E} & -\frac{\nu}{E} & -\frac{\nu}{E} & & & \\ -\frac{\nu}{E} & \frac{1}{E} & -\frac{\nu}{E} & & & \\ -\frac{\nu}{E} & -\frac{\nu}{E} & \frac{1}{E} & & & \\ & & & \frac{1}{G_{23}} & & \\ & & & & \frac{1}{G_{13}} & \\ & & & & & \frac{1}{G_{12}} \end{bmatrix} \begin{bmatrix} \sigma_{11} \\ \sigma_{22} \\ \sigma_{33} \\ \sigma_{23} \\ \sigma_{13} \\ \sigma_{12} \end{bmatrix} \tag{4.21}$$

Substituting γ_{23} for $2 \cdot \varepsilon_{23} = \varepsilon_{23} + \varepsilon_{32}$, γ_{13} for $2 \cdot \varepsilon_{13} = \varepsilon_{13} + \varepsilon_{31}$ and γ_{12} for $2 \cdot \varepsilon_{12} = \varepsilon_{12} + \varepsilon_{21}$, Darendeli (2001) and Menq (2003) expresses the shear moduli as:

(4.22)

$$\frac{G_{ij}}{G_{\max}} = \frac{1}{1+\left(\frac{\gamma_{ij}}{\gamma_r}\right)^a}$$

(4.23)

$$G_{\max} = C_{G3} \times C_u^{b1} \times e^x \times \left(\frac{s_0^{'}}{P_a}\right)^{n_G}$$

(4.24)

$$s_0^{'} = (s_{11} + s_{22} + s_{33})/3$$

Poisson's ratio, ν, can be assumed to be a reasonable constant value based on experience or experiment.

To obtain the relationship between Young's modulus, E, and Shear modulus, G, the octahedral shear strain is introduced into the model. The octahedral shear strain, γ_{oct}, is a measure of overall distortion:

$$\Upsilon_{oct} = \frac{2}{3}\sqrt{(\varepsilon_{11}-\varepsilon_{22})^2+(\varepsilon_{11}-\varepsilon_{33})^2+(\varepsilon_{22}-\varepsilon_{33})^2+6(\varepsilon_{12}{}^2+\varepsilon_{13}{}^2+\varepsilon_{23}{}^2)} \quad (4.25)$$

Replacing γ_{ij} in Equation 4.22 with γ_{oct}, we can calculate an "octahedral" shear modulus G_{oct}:

$$\frac{G_{oct}}{G_{\max}} = \frac{1}{1+\left(\frac{\gamma_{oct}}{\gamma_r}\right)^a} \quad (4.26)$$

So, Young's modulus, E, can be estimated as:

$$E = 2G_{oct}(1+\nu) \quad (4.27)$$

To summarize, five independent elastic constants of the compliance matrix in Equation 4.21 can be calculated based on mean effective stress and strain level.

The mean effective stress, σ_0', must be positive in the equations proposed by Menq (2003). To avoid substitution of negative mean effective stress in Equation 4.23, the definition of the mean effective stress, σ_0', should be modified. (note that compression is assumed positive and tension negative):

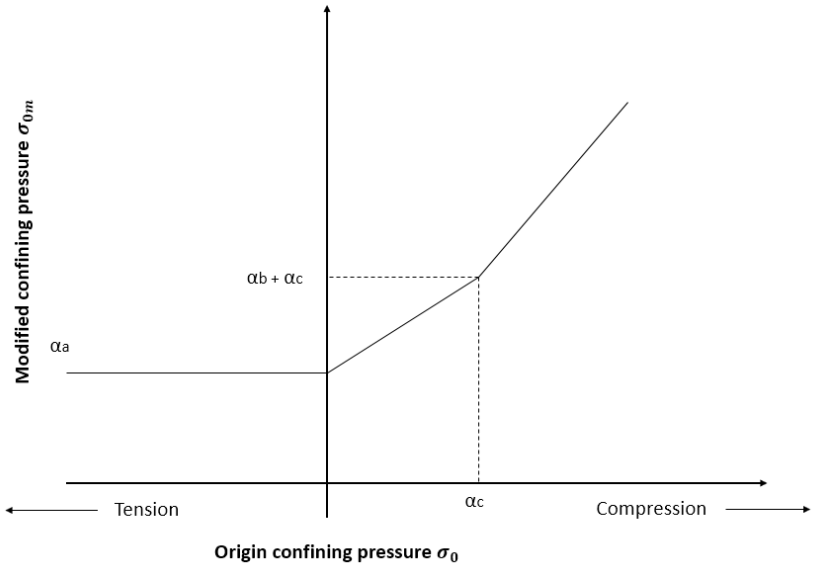

Figure 4.6: Relationship between origin and modified confining pressure.

$$s'_{0m} = \begin{cases} a_a & \text{for } s'_0 < 0 \\ a_a + \dfrac{a_b + a_c - a_a}{a_c} s'_0 & \text{for } 0 \le s'_0 \le a_c \\ a_b + s'_0 & \text{for } s'_0 > a_c \end{cases} \qquad (4.28)$$

α_a, α_b, and α_c are the parameters necessary to control the relationship between σ'_0 andσ'_{0m} .

- α_a is the parameter that maintains a low stiffness when the material is in tension. Also, It can prevent unrealistically small stiffness when the mean effective stress is low, for example, near ground surface.
- α_b is the parameter that prevents unrealistically small stiffness when the mean effective stress is low.
- α_c is the parameter allowing the σ'_{0m} to change smoothly from tension to compression.

4.2.2 Masing's Rule

When subjected to cyclic shear loading, the soil constitutive model must be modified to show typical hysteretic behavior as depicted in Figure 4.7.

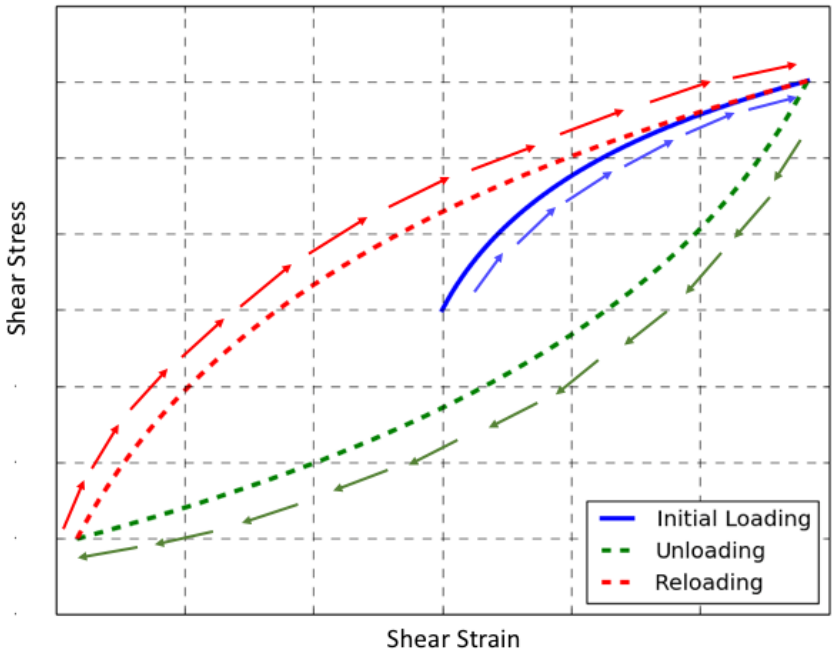

Figure 4.7: Hysteretic behavior of soil under cyclic shear loading.

In the cyclic shear tests shown in Figure 4.7, starting from the maximum shear modulus, G_{max}, the actual shear modulus will decrease with increasing shear strain as the blue curve. Upon load reversal, the shear modulus will restart from G_{max} and will decrease again until the next load reversal.

Masing (1926) described the hysteretic behavior of materials in unloading/reloading cycles according to the following rules:

- *The shear modulus in unloading is equal to the initial tangent modulus of the loading curve.*

- *The shape of the unloading and reloading curves is the same as the shape of the loading curve, but the size in terms of stress is double in terms of the above introduced threshold shear strain, γ_r, used in Equation 4.22, Masing's rule can be fulfilled by the following setting in the Hardin-Drnevich relation:*

$$\gamma_{r(un/re-loading)} = 2\gamma_{r(virgin-loading)} \tag{4.29}$$

The hysteresis effect described in Masing's second rule can be easily incorporated in both models using the expression:

$$\varepsilon_0 - \varepsilon_R = f\left(\frac{\sigma_0 - \sigma_R}{L}\right) \tag{4.30}$$

with shape factor $L = 1$ in initial loading and $L = 2$ in unloading or reloading. In Equation 4.30, $f(\sigma)$ represents the monotonic stress-strain relationship $\varepsilon = f(\sigma)$. The strain and stress levels ε_0 and σ_0 denote the last load reversal point in stress-strain space, where ε_R and σ_R specify the current strain and stress, respectively.

The procedure is separated into five steps to describe the methodology to apply the Masing's rules into the constitutive model:

Step-1: Determine a small increment length in each calculation step to make sure that the reversal points for switching between the reloading and unloading statues can be detected.

Step-2: Detect the reversal in the initial loading by detecting the octahedral shear strain, γ_{oct}: this detection is achieved by comparing the γ_{oct} in current calculation increment with the γ_{oct} in the previous increment. If the $current\ \gamma_{oct}$ exceeds the $previous\ \gamma_{oct}$, there is no load reversal at this

increment. If the $current\ \gamma_{oct}$ is less than the $previous\ \gamma_{oct}$, then there is a load reversal and tensors of stress and strain with the $previous\ \gamma_{oct}$ are stored as the reversal as in Equations 5.31 and 5.32:

$$\underline{\sigma_0} = \begin{bmatrix} \sigma_{11\_0} \\ \sigma_{22\_0} \\ \sigma_{33\_0} \\ \sigma_{23\_0} \\ \sigma_{13\_0} \\ \sigma_{12\_0} \end{bmatrix} \tag{4.31}$$

$$\underline{\varepsilon_0} = \begin{bmatrix} \varepsilon_{11\_0} \\ \varepsilon_{22\_0} \\ \varepsilon_{33\_0} \\ \gamma_{23\_0} \\ \gamma_{13\_0} \\ \gamma_{12\_0} \end{bmatrix} \tag{4.32}$$

Step-3: Determine the definition of the deviatoric strain during un/reloading: if the number of reversal points is larger than zero, the status of the loading will be changed to un/re-loading and the shape factor will be equal to two (Equation 4.30). The tensors of the stress and strain during un/re-loading are represented as:

$$\underline{\sigma_R} = \begin{bmatrix} \sigma_{11\_R} \\ \sigma_{22\_R} \\ \sigma_{33\_R} \\ \sigma_{23\_R} \\ \sigma_{13\_R} \\ \sigma_{12\_R} \end{bmatrix} \tag{4.33}$$

$$\underline{\varepsilon_R} = \begin{bmatrix} \varepsilon_{11\_R} \\ \varepsilon_{22\_R} \\ \varepsilon_{33\_R} \\ \gamma_{23\_R} \\ \gamma_{13\_R} \\ \gamma_{12\_R} \end{bmatrix} \tag{4.34}$$

The reversal will be regarded as the starting of the un/re-loading behavior. The tensor of the deviatoric strain during un/reloading relative to its reversal is represented as:

$$\underline{\Delta\varepsilon} = \begin{bmatrix} \varepsilon_{11\_R} \\ \varepsilon_{22\_R} \\ \varepsilon_{33\_R} \\ \gamma_{23\_R} \\ \gamma_{13\_R} \\ \gamma_{12\_R} \end{bmatrix} - \begin{bmatrix} \varepsilon_{11\_0} \\ \varepsilon_{22\_0} \\ \varepsilon_{33\_0} \\ \gamma_{23\_0} \\ \gamma_{13\_0} \\ \gamma_{12\_0} \end{bmatrix} = \begin{bmatrix} \Delta\varepsilon_{11} \\ \Delta\varepsilon_{22} \\ \Delta\varepsilon_{33} \\ \Delta\gamma_{23} \\ \Delta\gamma_{13} \\ \Delta\gamma_{12} \end{bmatrix} \tag{5.35}$$

Step-4: Calculate the deviatoric octahedral shear strain, $\Delta\gamma_{oct}$, during un/re-loading: the tensor of the deviatoric strain relative to its reversal is used to calculate the deviatoric octahedral shear strain during un/re-loading.

$$\Delta\gamma_{oct} = \frac{2}{3}\sqrt{(\Delta\varepsilon_{11} - \Delta\varepsilon_{22})^2 + (\Delta\varepsilon_{11} - \Delta\varepsilon_{33})^2 + (\Delta\varepsilon_{22} - \Delta\varepsilon_{22})^2 + 6(\Delta\varepsilon_{12}{}^2 + \Delta\varepsilon_{13}{}^2 + \Delta\varepsilon_{23}{}^2)} \quad (4.36)$$

The shear modulus during un/re-loading is calculated as:

$$\frac{G_{ij\_r}}{G_{\max}} = \frac{1}{1 + (\frac{\Delta\gamma_{ij}}{2\gamma_r})^a} \quad (4.37)$$

$$\frac{G_{oct\_r}}{G_{\max}} = \frac{1}{1 + (\frac{\Delta\gamma_{oct}}{2\gamma_r})^a} \quad (4.38)$$

Young's modulus during un/re-loading is calculated as:

$$E_r = 2G_{oct\_r}(1+\nu) \quad (5.39)$$

The compliance matrix based on un/re-loading Young's modulus and shear stiffness is:

$$\underline{\underline{C_r}} = \begin{bmatrix} \frac{1}{E_r} & -\frac{\nu}{E_r} & -\frac{\nu}{E_r} & & & \\ -\frac{\nu}{E_r} & \frac{1}{E_r} & -\frac{\nu}{E_r} & & & \\ -\frac{\nu}{E_r} & -\frac{\nu}{E_r} & \frac{1}{E_r} & & & \\ & & & \frac{1}{G_{23\_r}} & & \\ & & & & \frac{1}{G_{13\_r}} & \\ & & & & & \frac{1}{G_{12\_r}} \end{bmatrix} \tag{4.40}$$

$$\underline{\underline{D_r}} = (\underline{\underline{C_r}})^{-1} \tag{4.41}$$

The constitutive equations for un/re-loading can be built as:

$$\underline{\sigma_R} = \underline{\underline{D_r}}\,\underline{\Delta\varepsilon} + \underline{\sigma_0} \tag{4.42}$$

Step-5: Use the rule in Step-2 to repeat the comparison procedure to find the reversal point of switching between the unloading and reloading statues until the end of the calculation.

Figure 4.8 shows the flow chart of determining the reversal loading from initial loading to un/re-loading.

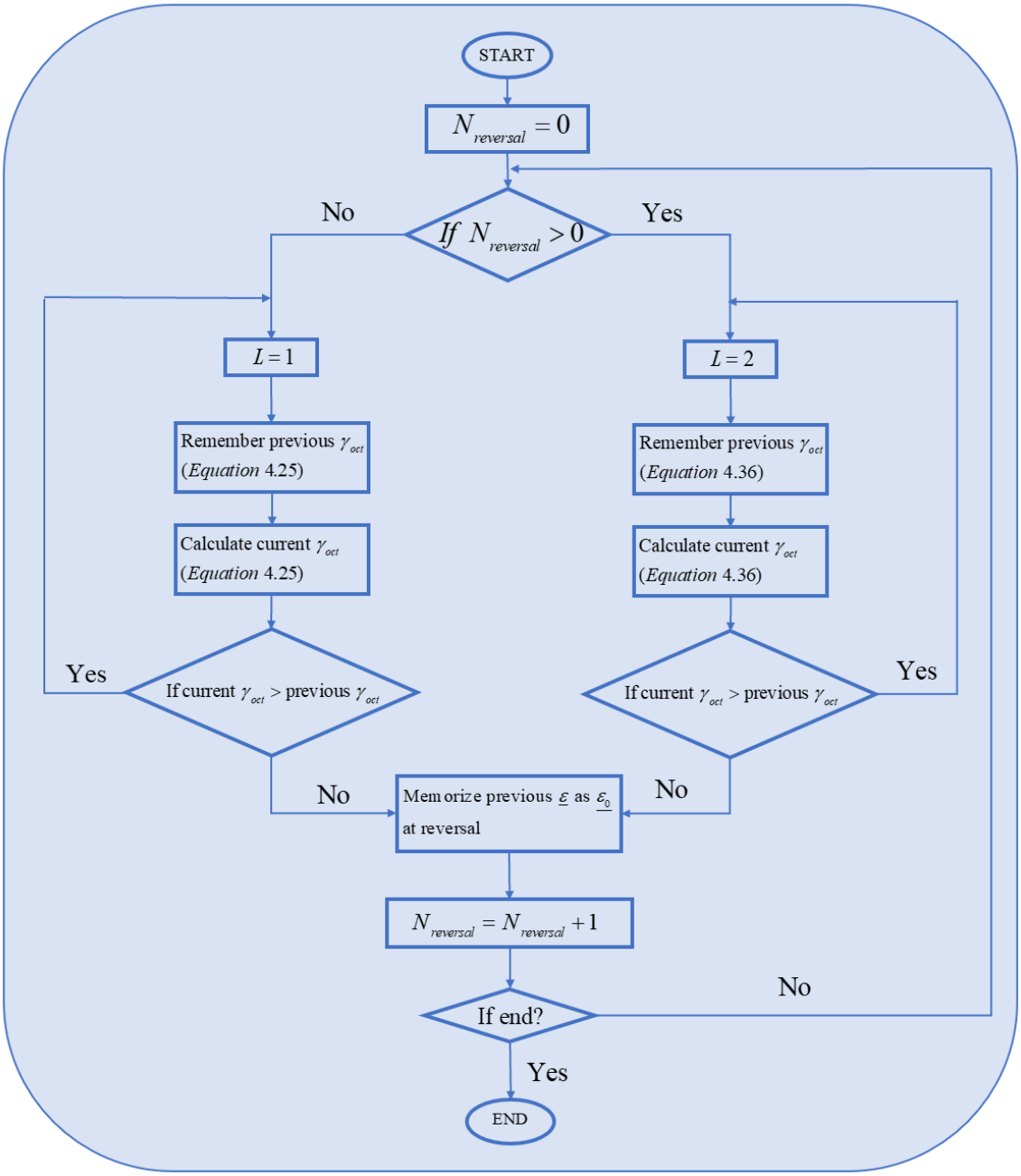

Figure 4.8: Flow chart of criteria of determining the reversal during re/un-loading.

Figure 4.9 shows an example of using a simulation of triaxial compression tests to illustrate the procedure to determine the reversal from initial loading to unloading. Following assumptions are made for the simulation:

(1) The shear stresses and shear strains are zero, which mean that the shear moduli G_{12}, G_{13}, and G_{23} are always equal to the maximum shear modulus, G_{max}.

(2) The mean effective stress is constant. It indicates that σ_{22} and σ_{33} keep constant during loading along the axial direction 11.

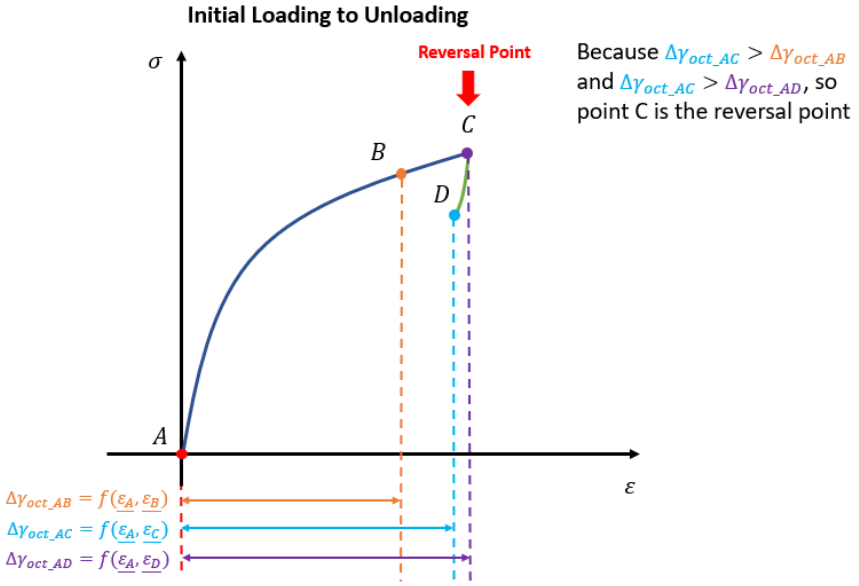

Figure 4.9: Example of determining the reversal point from initial loading to unloading.

The lengths of the straight lines with double arrows (orange, blue, and purple) are proportional to the magnitude of the deviatoric octahedral shear strain, $\Delta\gamma_{oct}$, between two points. In the case of initial loading, Point A is regarded as the "reversal point" and the $\Delta\gamma_{oct}$ between Point A to any point can be calculated through Equation 4.26. According

to the lengths of the arrows lines, the $\Delta\gamma_{oct}$ between points A and C is larger than the $\Delta\gamma_{oct}$ between Points A and B, so in this increment Point C is not determined as the next reversal point in this increment. In the next increment, the $\Delta\gamma_{oct}$ between Points A and D is smaller than the $\Delta\gamma_{oct}$ between points A and C, based on the flowchart of finding the reversal point, point C is determined as the next reversal point.

If the tensors of stresses and strains at Point A and tensor of strains at Point C are known, the tensor of stresses at Point C can be calculated by following procedure:

1) Use Equation 4.26 to calculate the $\Delta\gamma_{oct}$ between Point A and Point C.
2) Assume an effective stress, σ_{11C},along principle axis 11 and obtain the mean effective stress, σ_{0C} , for Point C through Equations 5.24 and 5.28. So the mean effective stress at point C, σ_{0C}, is a function of σ_{11C}: $\sigma_{0C} = f(\sigma_{11C})$.
3) Establish the maximum shear modulus, G_{maxC}, by the Equation 4.23 as the function of mean effective stress at point C, which means G_{maxC} is also a function of σ_{11C}: $G_{maxC} = gmax(\sigma_{11C})$.
4) Use the Equation 4.22 to calculate C_{ijC}/G_{maxC} and Equation 4.26 to calculate G_{octC}/G_{maxC} based on the value of σ_{0C} and $\Delta\gamma_{oct}$.
5) Set G_{12C}, G_{13C}, and G_{23C} equal to G_{maxC} because of no shear strains.
6) Relate G_{maxC} as a function of σ_{0C} and $\Delta\gamma_{oct}$: $G_{octC} = goct(\sigma_{0C}, \Delta\gamma_{oct})$.
7) Use the Equation 4.27 to calculate Young's modulus as: $E = e(\sigma_{0C}, \Delta\gamma_{oct})$.
8) Estalish the stiffness matrix, $\underline{\underline{D}}$,based on the Young's modulus and Shear moduluses: $\underline{\underline{D}}|_{\Delta\gamma_{oct},\sigma_{0C}}$.

9) Obtain the value of σ_{11C} by solving the implicit function using iteration: $\underline{\sigma_C} = \underline{\underline{D}}|_{\Delta\gamma_{oct},\sigma_{0C}} (\underline{\varepsilon_C} - \underline{\varepsilon_A}) + \underline{\sigma_A}$.

Point C is determined as the new reversal point from initial loading to unloading. Figure 4.10 shows the example of finding the next reversal point from unloading to reloading. The $\Delta\gamma_{oct}$ between Point C to any point can be calculated using Equation 4.36. According to the lengths of the straight lines with two arrows, the $\Delta\gamma_{oct}$ between Point C and Point F is larger than the $\Delta\gamma_{oct}$ between Point C and Point E and the $\Delta\gamma_{oct}$ between Point C and Point G, so the Point F is determined as the next reversal point from unloading to reloading.

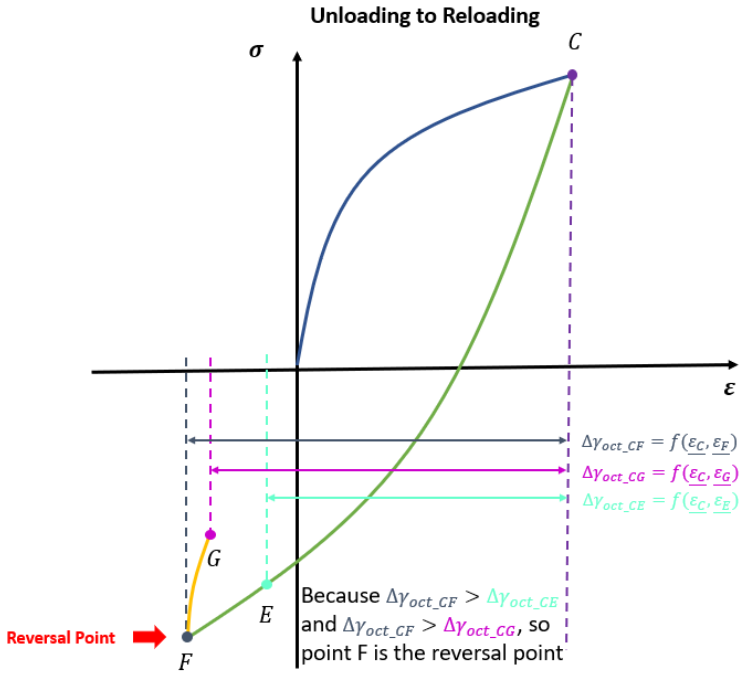

Figure 4.10: Example of determining the reversal from unloading to reloading.

If the tensors of stresses and strains at Point C and the tensor of strains at Point F are known, the tensor of stresses at Point F can be calculated as:

1) Use Equation 4.36 to calculate the $\Delta\gamma_{oct}$ between Point C and Point F.
2) Assume an effective stress, σ_{11F},along principle axis 11 for Point F and obtain the mean effective stress, σ_{0F}, at Point F through Equations 5.24 and 5.28. So the mean effective stress at point F, σ_{0F}, is a function of σ_{11F}: $\sigma_{0F} = f(\sigma_{11F})$.
3) Establish the maximum shear modulus, G_{maxF}, by the Equation 4.23 as the function of mean effective stress at point F, which means G_{maxF} is also a function of σ_{11F}: $G_{maxF} = gmax(\sigma_{11F})$.
4) Use the Equation 4.37 to calculate $\mathrm{G}_{ijF}/G_{maxF}$ and Equation 4.38 to calculate $\mathrm{G}_{octF}/G_{maxF}$ based on the value of σ_{0F} and $\Delta\gamma_{oct}$.
5) Set G_{12F}, G_{13F}, and G_{23F} equal to G_{maxF} because of no shear strains.
6) Relate G_{octF} as a function of σ_{0F} and $\Delta\gamma_{oct}$: $G_{octF} = goct(\sigma_{0F}, \Delta\gamma_{oct})$.
7) Use the Equation 4.27 to calculate Young's modulus as: $E = e(\sigma_{0F}, \Delta\gamma_{oct})$..
8) Estalish the stiffness matrix, $\underline{\underline{D}}$,based on the Young's modulus and Shear moduluses: $\underline{\underline{D}}|_{\Delta\gamma_{oct},\sigma_{0F}}$.
9) Obtain the value of σ_{11C} by solving the implicit function using iteration: $\underline{\sigma_F} = \underline{\underline{D}}|_{\Delta\gamma_{oct},\sigma_{0F}} (\underline{\varepsilon_F} - \underline{\varepsilon_C}) + \underline{\sigma_C}$.

4.2.3 Methods of Solving Implicit Function

To solve the implicit functions composed by tensors and stiffness matrix with unknown stresses, two numerical methods were used: Newton's method and secant method. Newton's method serves as the basis of the incremental-iterative solution technique used in Abaqus/Standard. Secant method is finite difference approximation of

Newton's method and is used to verify the accuracy of the results obtained by Newton' method in this study.

Newton's method is a root-finding algorithm using a succession of roots of tangent lines to find approximated root of an implicit function, $f(x) = 0$. The method can be accomplished by the following procedure:

(1) guess an initial value close to the true root, x_0,

(2) draw the tangent line at the initial guess,

(3) calculate the x-intercept of this tangent line, x_1

(4) draw the next tangent line at the x-intercept, $x = x_n$, to the curve of the implicit function,

$$y = f'(x_n)(x - x_n) + f(x_n) \tag{4.43}$$

where f' is the derivative of the function $f(x)$.

(5) calculate the next x-intercept, $x = x_{n+1}$, of the tangent line by solving Equation 4.43,

$$x_{n+1} = x_n - \frac{f(x_n)}{f'(x_n)} \tag{4.43}$$

(6) repeat step (4) and step (5) until the x-intercept is close enough to the root of the implicit function.

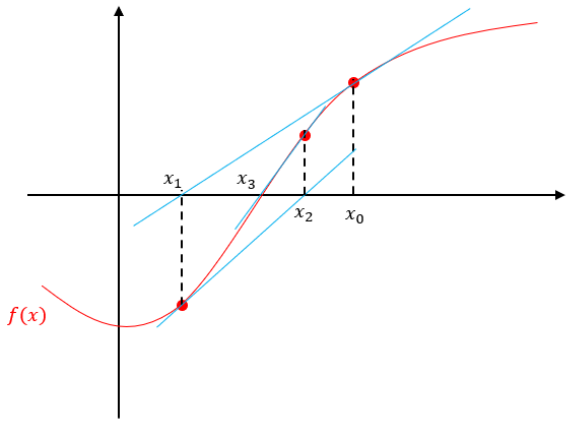

Figure 4.11: Example of Iteration using Newton's method.

Second method is a method of finding successively better approximations by using the secant lines. To find the rood of the function $f(x) = 0$, the method can be used by following the procedure:

(1) guess two initial values close to the root, x_0 and x_1,

(2) construct a secant line through points $(x_0, f(x_0))$ and $(x_1, f(x_1))$,

(3) compute the x-intercept of the secant line, x_2,

(4) construct the next secant line through points $(x_{n-1}, f(x_{n-1}))$ and $(x_n, f(x_n))$,

$$y = \frac{f(x_n) - f(x_{n-1})}{x_n - x_{n-1}}(x - x_n) + f(x_n) \tag{4.44}$$

(5) calculate the next x-intercept, x_{n+1}, by solving Equation 4.44,

$$x_{n+1} = x_n - f(x_n)\frac{x_n - x_{n-1}}{f(x_n) - f(x_{n-1})} \tag{4.45}$$

(6) Repeat step (4) and step (5) until a sufficiently high level of precision is reached (a sufficiently small difference between x_n and x_{n-1}).

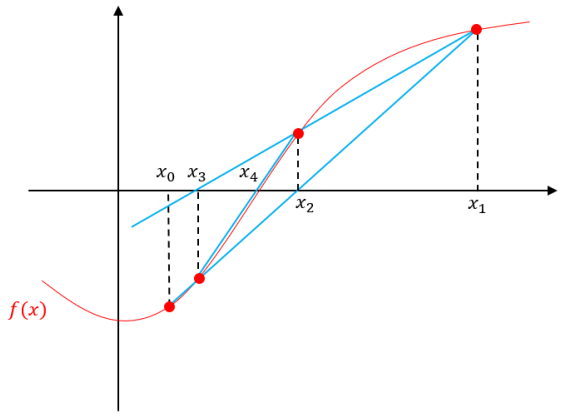

Figure 4.11: Example of Iteration using Secant method.

4.2.4 Verification of Subroutine Written for Abaqus

The subroutine of the soil constitutive model written for Abaqus was tested on a cubic element by axial loading. The Newton-Raphson method was used by Abaqus to solve the function iteratively and to find an approximate solution that minimize residuals. The results solved by the subroutine of Abaqus were compared to the results solved by the secant method written by Python.

Figure 4.12 shows an incremental prescribed axial displacement along the Y-direction with ultimate strain 0.01 applied on the top four nodes with a $1 \times 1 \times 1$ geometry. The bottom face of the cubic element was restrained from movement in Y-direction. The faces on the X-Y plane were restrained from movement in the Z-direction. The faces on the Y-Z plane were restrained from movement in the X-direction.

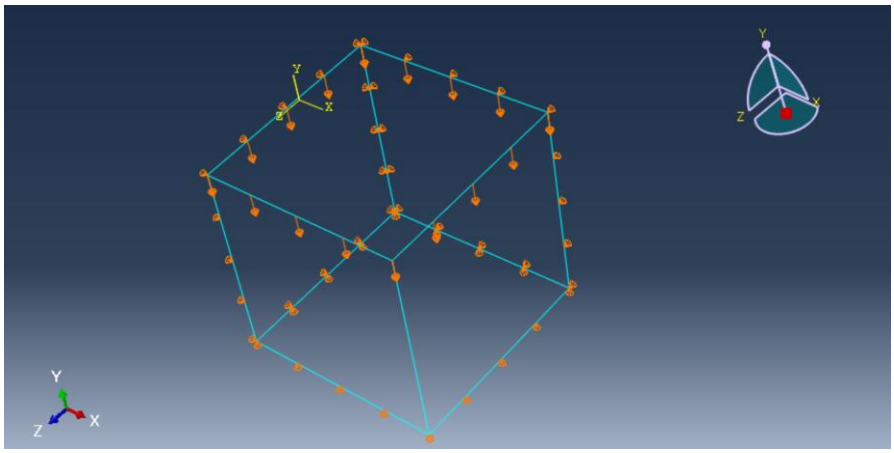

Figure 4.12: Axial loading test on one cubic element in Abaqus.

Two simulations using Abaqus and Python with different sand properties under different confining pressure were carried out. Table 4.5 shows the properties of the two sets of sands. C_{G1} and n_g are the parameters in Equation (5.1). C_1, C_2, C_3, and C_4 are the parameters in Equation (5.6) and (5.7). Figures 4.13 and 4.14 show the comparison between the results from Abaqus and Python. The curves are perfectly overlapped, which indicates that the subroutine of the soil constitutive model works correctly in monotonic loading.

Table 4.5: Input parameters of the constitutive model for verification tests.

Test #	**Test 1**	**Test 2**
$\boldsymbol{C_{G1}}$ $\boldsymbol{(psi)}$	15068	12375
$\boldsymbol{n_g}$	0.453	0.42
$\boldsymbol{C_1}$(%)	0.106	0.043
$\boldsymbol{C_2}$	0.311	0.406
$\boldsymbol{C_3}$	0.854	0.943
$\boldsymbol{C_4}$	0.311	0.0
$\boldsymbol{\alpha_a}$	0.001	0.001
$\boldsymbol{\alpha_b}$	0.001	0.001
$\boldsymbol{\alpha_c}$	0.001	0.001
$\boldsymbol{Poisson's\ ratio}$	0.3	0.3

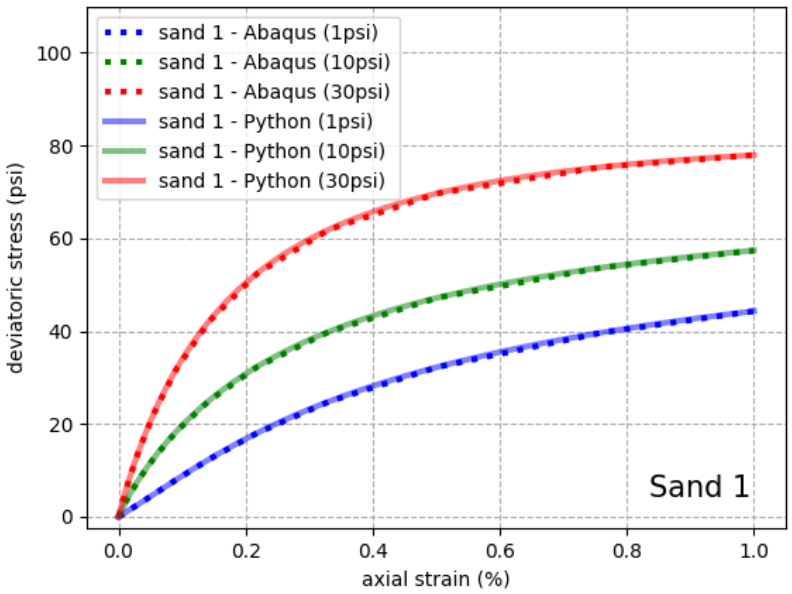

Figure 4.13: Example of verification of subroutine of Abaqus (Test 1).

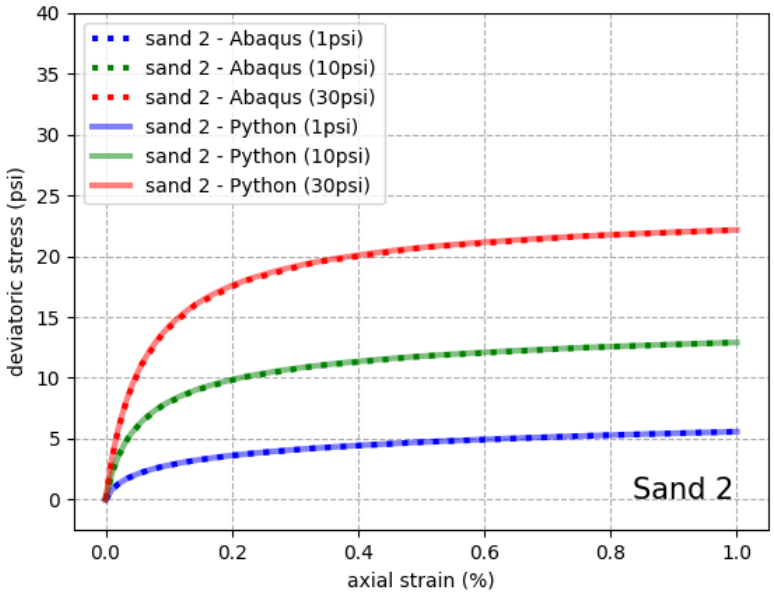

Figure 4.14: Example of verification of subroutine of Abaqus (Test 2).

4.3 COMPARISON BETWEEN PREDICTIONS AND MEASUREMENTS

The comparison includes the shear stress – shear strain relationship obtained from torsional shear tests and axial stress – axial strain relationship obtained from dynamic triaxial tests. The torsional shear tests were conducted in the soil dynamic laboratory at The University of Texas at Austin. The dynamic triaxial tests were carried out by Tokyo University under the JSSMFE Standard.

4.3.1 Shear Tests

Torsional shear test is one of the dynamic laboratory tests to measure the non-linearity relationship of the shear modulus with the shear strain and confining pressure. The relationship is best measured using resonant column (RC) and torsional shear (TS) tests on the sample collected from the field. UT Austin developed combined RCTS equipment to measure the stiffness and damping of the soil sample. Figure 4.15 shows the equipment used for a fixed-free configuration with bottom of the sample fixed and the top of the torsional excitation applied on the sample.

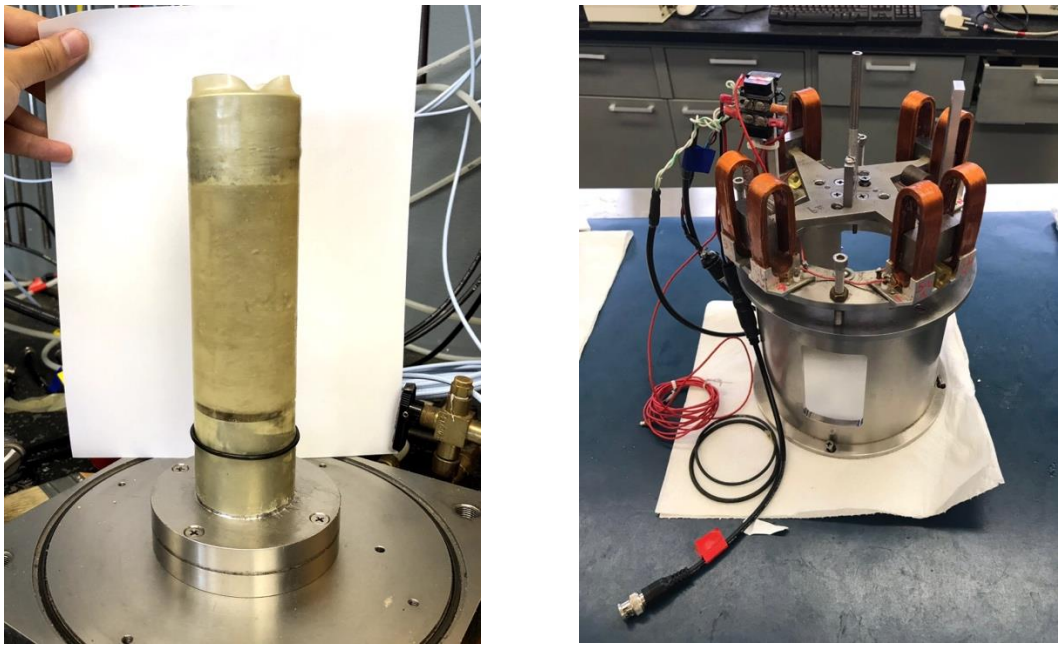

(a) (b)

Figure 4.15: Combined resonant column (RC) and torsional shear (TS) device; (a) fixed-free configuration, (b) resonant and cyclic torsional drive and monitoring systems.

UT Austin performed TS tests on the All-Purpose sand purchased which was also used in the laboratory foundation model tests. The properties of All-Purpose sand in TS test are summarized in Table 4.6.

Table 4.6: Properties of All-Purpose sand in TS tests.

C_u	G_s	$Void\ Ratio$	$D_{50}\ (mm)$
4.6	2.65	0.56	0.67

Figure 4.16 shows the comparison of the relationships of $\log G_{max} - \log \sigma_0$ obtained between the TS tests, empirical prediction using Equations 5.1 and 5.2, and modified prediction based on Menq (2003) and TS tests using Equations 5.6 and 5.7. The

value of G_{max} is underestimated by the empirical equations proposed by Menq (2003). After the modification, the predicted relationship of $\log G_{max} - \log \sigma_0$ matches well with the measured results of TS tests.

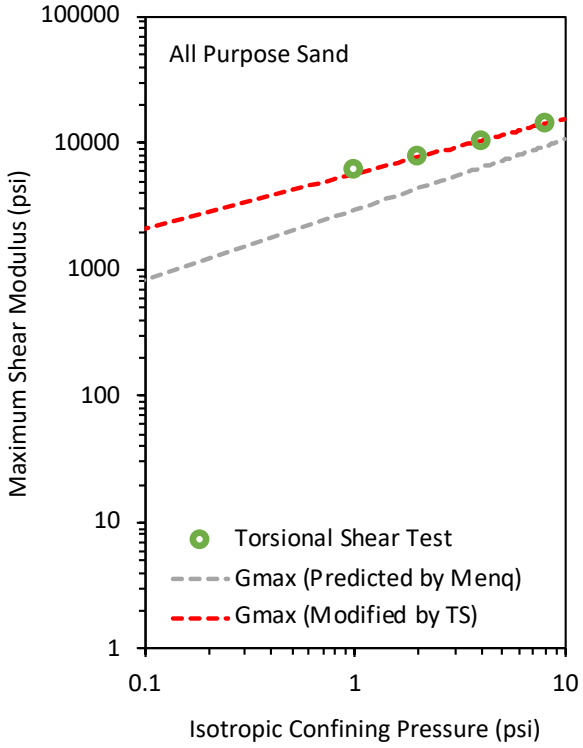

Figure 4.16: Modification of the relationship between G_{max} and confining pressure, σ_0.

Figure 4.17 shows the comparison of the relationships of $G/G_{max} - \log \gamma$ obtained between the TS tests and empirical predictions using Equations 5.2 and 5.3 and the modified predictions through Equations 5.4 and 5.5 based on TS tests. The empirical prediction have a good agreement with the results of TS tests. The modified predictions have a little improvement compared to the empirical prediction.

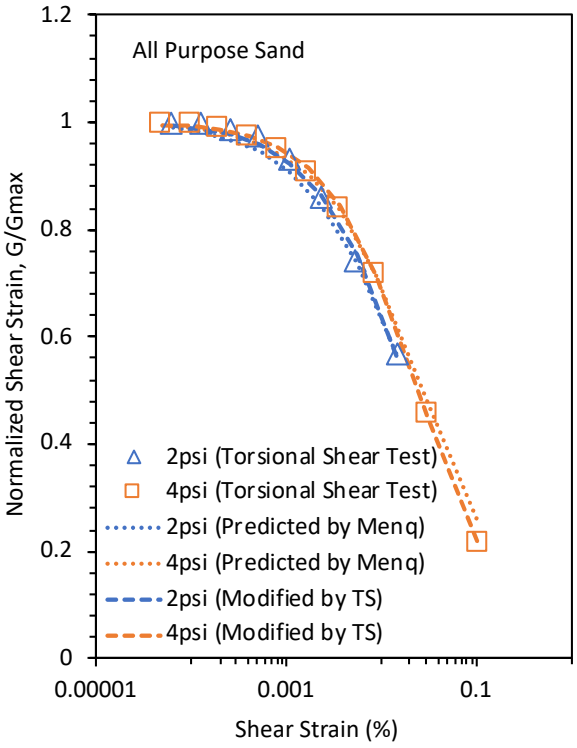

Figure 4.17: Modification of the relationships of $G/G_{max} - \log\gamma$.

Table 4.17 summarizes the input parameters for the soil constitutive model modified by the torsional shear tests.

Table 4.7: Input parameters of All-Purpose sand for the soil constitutive model.

C_{G1} (psi)	n_G	C_1 (%)	C_2	C_3	C_4	$\alpha_1, \alpha_2, \alpha_3$
18652	0.44	0.036	0.296	0.95	0.1	0.001

The measured shear stress was obtained by multiplication of shear strain by the secant shear modulus measured in TS tests. In Abaqus, a pure shear applied to a cubic element was used to verify the pure shear response of the soil constitutive model. Figure 4.18 shows the pure shear test on the cubic element. The bottom face of the element was

fixed and the top face of the element was applied by a force parallel to the top face. The predicted response of the shear strain and shear stress of the element is compared to the measurement in Figures 4.19 and 4.20. The prediction before modification underestimates the value of G_{max} as shown in Figure 4.19. After modifying the value of G_{max} based on laboratory tests, predictions after modification agree well with the stiffness of the sand.

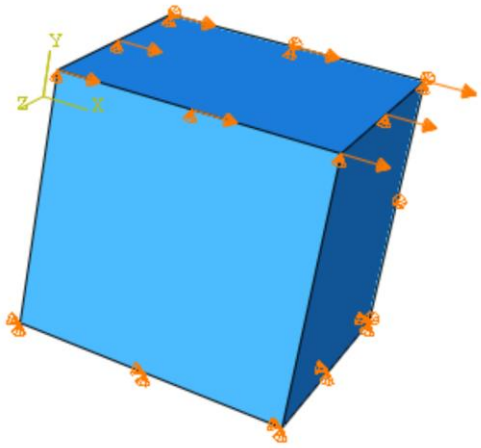

Figure 4.18: Pure shear element test in Abaqus.

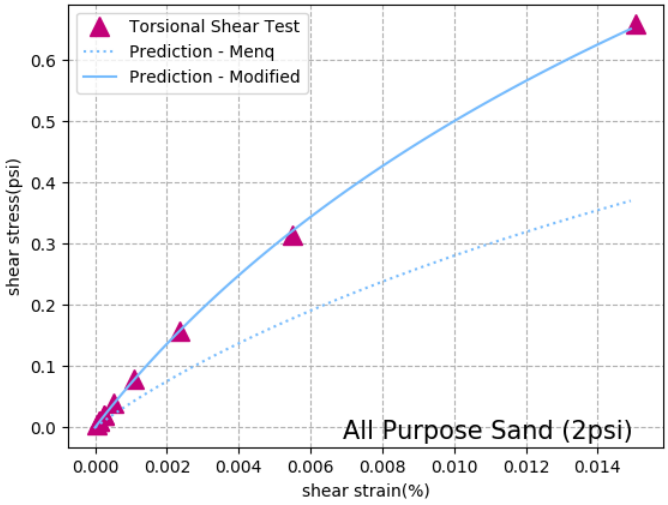

Figure 4.19: Comparison of the prediction and measurement for shear stress versus shear strain (2psi).

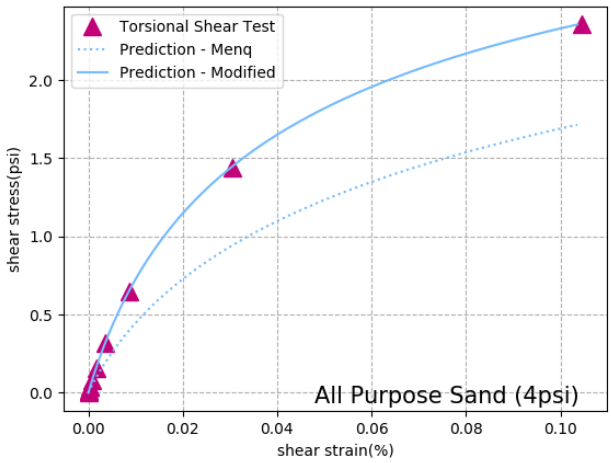

Figure 4.20: Comparison of the prediction and measurement of shear stress versus shear strain (4psi).

To investigate the hysteretic behavior simulated by the soil constitutive model using Masing's Rule, the hysteretic loop measured in the torsional shear tests was compared with

the predicted hysteretic loop. Figures 4.21 to 4.24 show different hysteretic loops measured at different levels of strain under a confining pressure of 4 psi. From Figures 4.21 to 4.24, the predicted loops have a good fit with the measured loops when the maximum shear strain is lower than 0.02%.

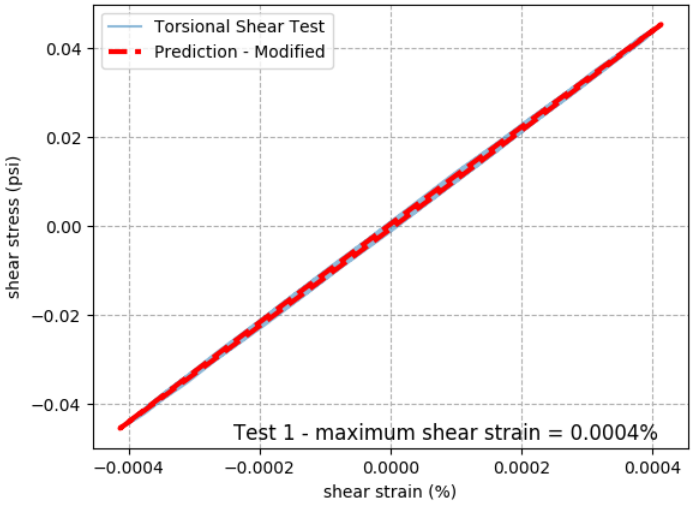

Figure 4.21: Hysteretic behavior (Test 1).

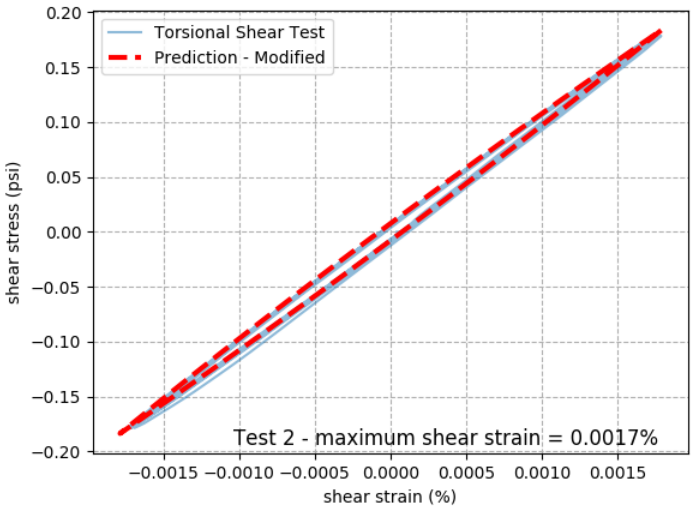

Figure 4.22: Hysteretic behavior (Test 2).

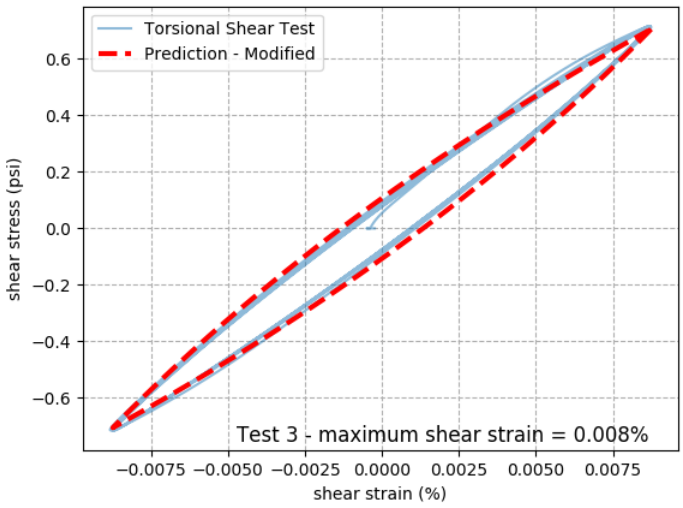

Figure 4.23: Hysteretic behavior (Test 3).

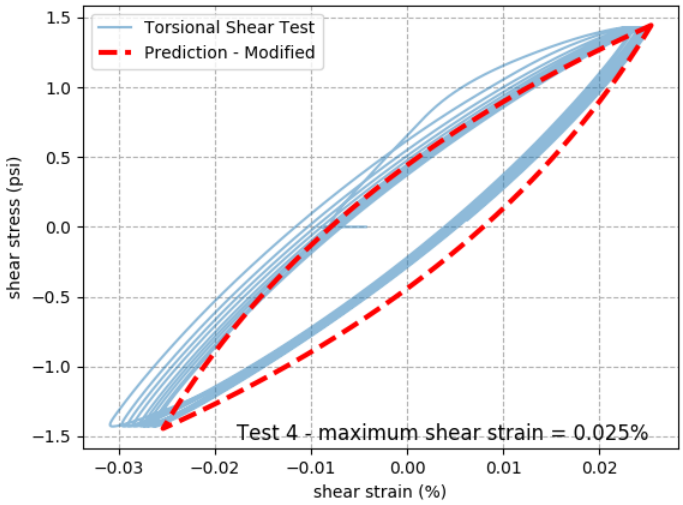

Figure 4.24: Hysteretic behavior (Test 4).

4.3.2 Triaxial Tests

In dynamic triaxial tests, the soil sample is under relatively fast cyclic loading conditions along vertical axis. Different from conventional triaxial compression tests, dynamic triaxial testing system is placed an internal load cell directly above the cap of specimens and installed a strain measurement along the lateral surface of the specimens. These arrangements help dynamic triaxial tests avoid the effect of bedding error which is induced by the lack of fit of the contacts between the specimens and the platen. Figure 4.25(a) shows the layout of a conventional triaxial compression testing system and Figure 4.25(b) shows the layout of a typical dynamic triaxial system.

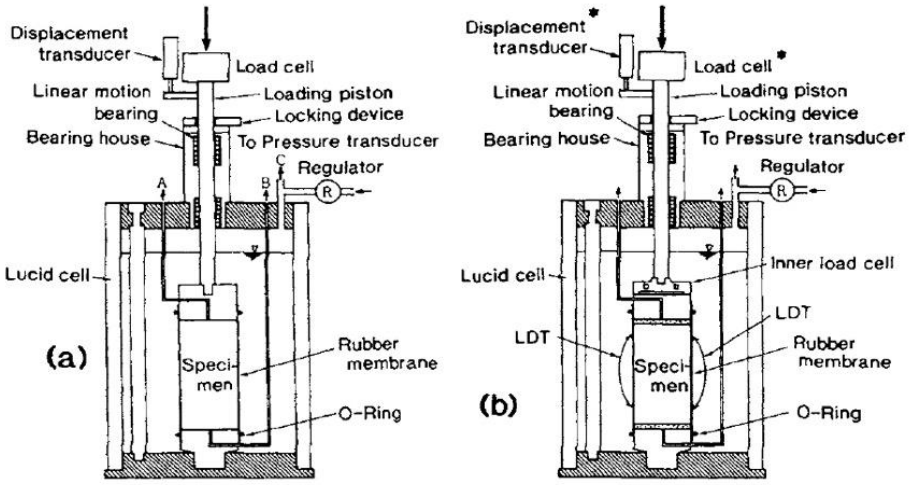

Figure 4.25: (a) Typical conventional triaxial compression testing system with a load cell and a LVDT located outside the triaxial cell and (b) Typical dynamic triaxial testing system with a load cell and local axial strain gage located inside the triaxial cell.

Tatsuoka et al. (1995) performed conventional and dynamic triaxial tests on dense and loose Toyoura sand. The Toyoura sand was a uniform quatz-rich fine sand with sub-angular particles with $\mathrm{D}_{50} = 0.18mm$, $C_u = 1.3$, $e_{min} = 0.617$, and $e_{max} = 0.982$. The specimens were prepared by pluviation of air-dried particles from nozzle at a constant fall height. The dimensions of the specimens were 7.5 cm (3 in.) in diameter and from 15 cm (6 in.) in diameter. The specimens were saturated and confining pressures of 78.5 kPa (11.3 psi) and 49 kPa (7.1 psi) were applied to dense and loose specimens respectively. The frequency of the sinusoidal cyclic deviator stresses was from 0.05 Hz to 0.5 Hz under drained conditions. The deformations of the specimens were measured both locally and externally. Figure 4.26 shows the relations of $E - \log(\varepsilon_a)$ from dynamic (cyclic) triaxial tests and monotonic loading tests for dense and loose Toyoura sand. Because of the bedding error, the secant Young's modulus measured in the monotonic loading tests was smaller than it measured in the dynamic triaxial tests.

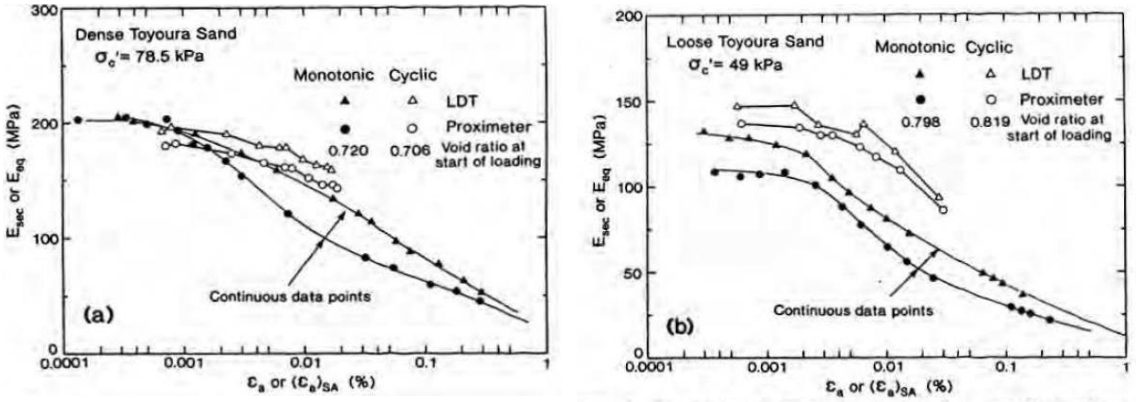

(a) (b)

Figure 4.26: Comparison of $E - \log(\varepsilon_a)$ relations from a dynamic triaxial tests with them from monotonic loading tests on (a) dense and (b) loose Toyoura sand.

Figure 4.27 shows the comparison of the shear modulus of dense Toyoura sand between monotonic loading (ML) and cyclic loading (CL) torsional shear tests using hollow cylindrical specimens. The shear modulus measured in the ML torsional shear tests was lower than it measured in the CL torsional shear tests.

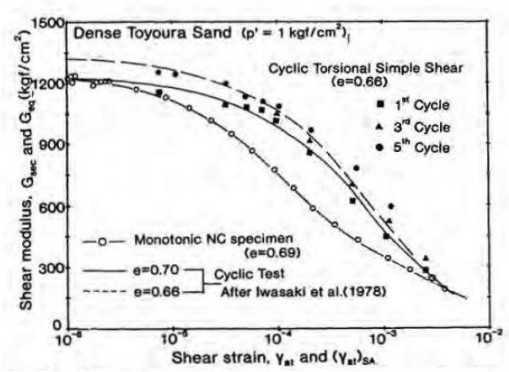

Figure 4.27: Comparison of shear modulus and shear strain relations of Toyoura sand from ML and CL torsional shear tests.

Figure 4.28 shows the comparison of the $G/G_{max} - \log\gamma$ curves obtained from the 5th cycle of the torsional shear test, the empirical prediction based on Equations 5.2 and

5.3 of Menq (2003), and the modified prediction through Equations 5.4 and 5.5 using torsional shear test. The empirical prediction from Equation was close to the $G/G_{max} - \log\gamma$ curve measured in the torsional shear test under the confining pressure of 14 psi. The modified prediction was obtained using Equations 5.4 and 5.5 to best match the result of the torsional shear test. After modification, the modified prediction would have perfect agreement with the $G/G_{max} - \log\gamma$ curve measured in the torsional shear test.

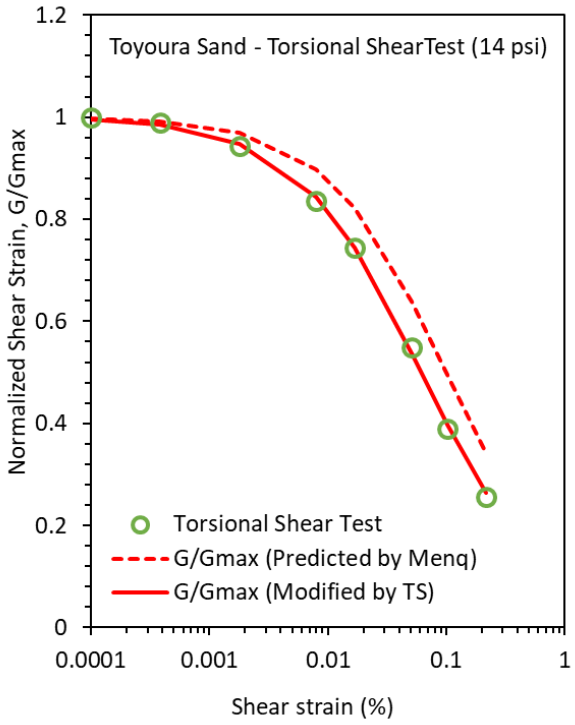

Figure 4.28: The comparison of the $G/G_{max} - \log\gamma$ curves from torsional shear test and predicted and modified Menq (2003) on dense Toyoura sand.

Equations 5.6 and 5.7 can be used to provide the empirical relationship between G_{max} and the mean effective stress, σ'_0. Table 4.8 summarizes the input parameters for the subroutine of the soil constitutive model for Toyoura sand.

Table 4.8: Input parameter of the soil constitutive model for Toyoura sand.

Toyoura sand	**Dense**	**Loose**
C_{G1} (psi)	13194	11326
n_g	0.49	
$C_1(\%)$	0.063	
C_2	0.349	
C_3	0.82	
C_4	0.099	
α_a	0.001	
α_b	0.001	
α_c	0.001	
$Poisson's\ ratio$	0.3	

A 3-D FEM model in Abaqus was built to simulate the monotonic loading test on the cylinder soil specimen as shown in Figure 4.29. The height of the cylinder specimen was 15 cm (6 inches) and the diameter of it was 7.5 cm (3 inches), which were same as the dimensions of the specimen in the dynamic triaxial test. In the initial step, all the three displacement components (X, Y, Z) on the face of the bottom of the specimen were constrained to be fixed. The horizontal displacement components (X, Y) on the face of the top of the specimen were constrained to be fixed. After the confining pressure was applied without any deformation, in the loading step, the monotonic loading was applied along direction Z on the top face of the specimen. The deviatoric stress was calculated through dividing the monotonic loading by the area of the top face. The axial strain was obtained through dividing the height of the specimen by the displacement of the top face.

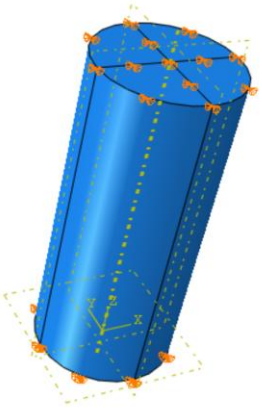

Figure 4.29: Axial loading test in Abaqus.

Figures 4.30 and 4.31 show the numerical prediction curves from Abaqus compared to the measurement from the dynamic triaxial tests on the dense and loose Toyoura sands. In both conditions, the predictions have good agreements with the measurement, which indicate the soil constitutive model has reasonably good performance in representing material behavior as measured in a laboratory test.

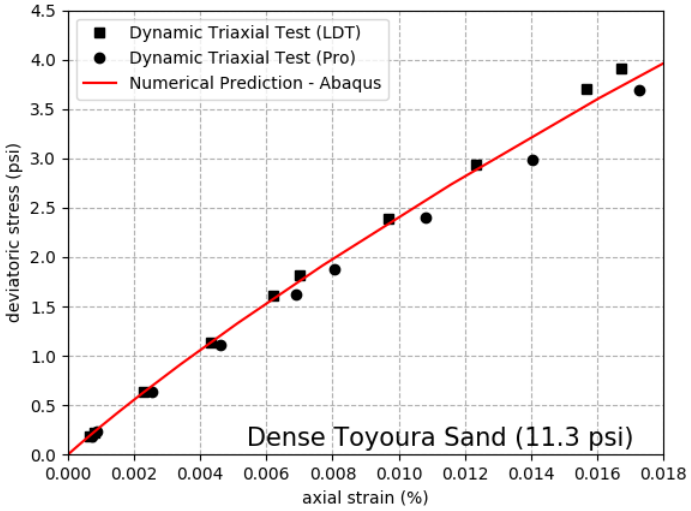

Figure 4.30: Comparison of the prediction and measurement of axial stress and axial strain (dense Toyoura sand).

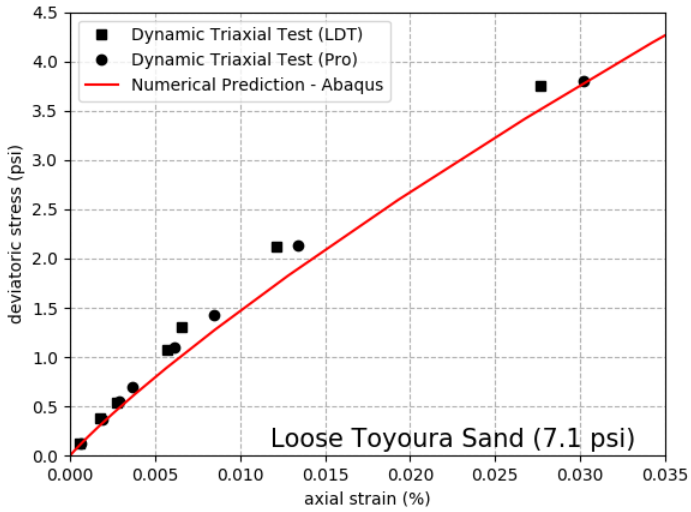

Figure 4.31: Comparison of the prediction and measurement of axial stress and axial strain (loose Toyoura sand).

4.4 CONCLUSIONS

The following major conclusions can be drawn from the development of the constitutive model.

(1) The proposed soil constitutive model based on Menq (2003) captures the initial stiffness and the non-linearity of sand at small strains.

(2) To improve the performance of the model, the relationship of the maximum shear modulus, G_{max}, and the mean effective stress, σ_0', and the relationship of the normalized shear modulus, G/G_{max}, and the shear strain, γ, must be modified based on resonant column and torsional shear tests.

(3) At relatively low levels of shear strain, the predicted hysteretic behavior of the soil constitutive model based on Masing's rule has a good agreement with the actual data from the torsional shear tests.

Chapter 5: Comparisons of the Measurements from Laboratory Foundation Model Tests with the Numerical Modeling Predictions

To better understand the soil-structure interaction for a monopile in sand, laboratory foundation model tests were conducted to achieve the following objectives: (1) gain insight into the small-strain behavior of the sand, (2) verify the performance of the proposed soil constitutive model used in 3-D DEM model, (3) suggest a procedure of modifying the proposed soil constitutive model based on laboratory tests. Instead of directly representing the performance of a full-scale pile driven in sand which had difference of scale, stress state, and the installation compared to a small-scale model, a sphere was used to load the sand to simplify the structure part of the problem.

Laboratory tests included grain size analyses, torsional shear tests, geophone tests to capture P-wave and S-wave velocities, and lateral push tests on spheres. Figure 5.1 shows the diagram of lateral push test on spheres. More details of development of the testing facilities and testing progress could be found in Munson (2018) and Bauer (2018).

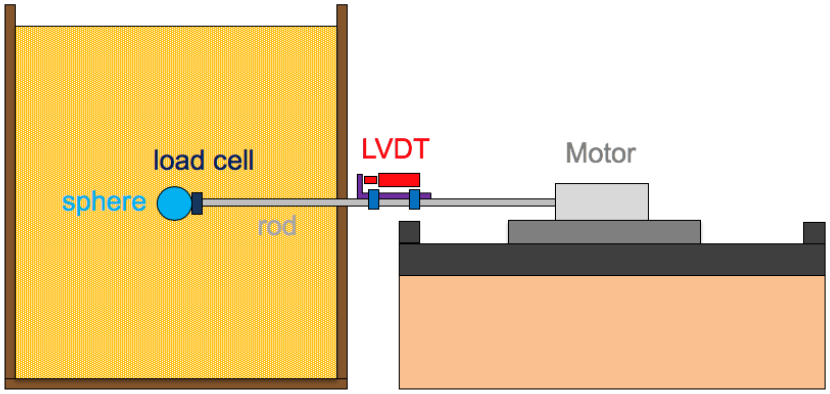

Figure 5.1: Diagram of lateral push test on spheres.

5.1 TESTING APPARATUS

The testing apparatus constituted of six major components: (1) linear actuators and stepper motors used to apply low-speed loads during testing; (2) a loading rod transferring the load from the linear actuator to the tested sphere; (3) a tested sphere; (4) a load cell with high resolution between the loading rod and the tested sphere; (5) a LVDT with high resolution measuring the displacement of the loading rod; and (6) a soil tank. Figure 5.2 shows the layout of the loading system.

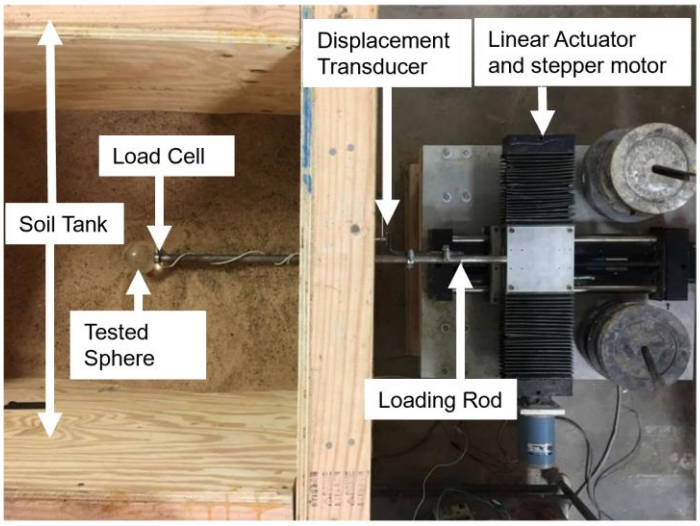

Figure 5.2: Layout of the set-up of the testing.

5.1.1 Linear Motion Systems and Stepping Motors

The linear motion system was fabricated by THOMSON and the type of it was 2DB16-200036. It was a screw-drive and ball-guided system with a resolution of 0.0002 inch. The stepping motor was fabricated by Superprior Electric and the type was MH-112-FF-206. Figure 5.3 shows the picture of the linear motion system. Figure 5.4(a) shows the

picture of the stepping motor, and Figure 5.4(b) shows its typical torque versus speed curves.

Figure 5.3: Linear motion system.

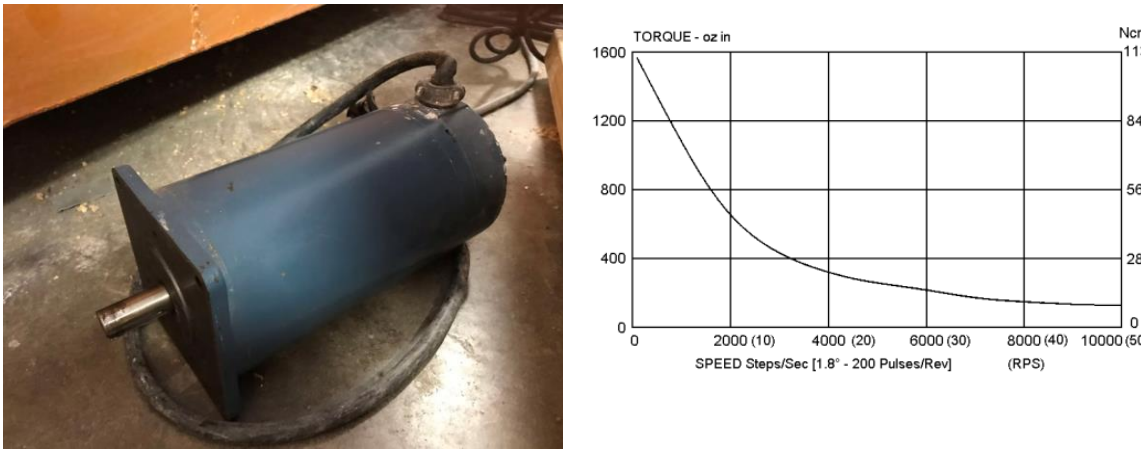

(a) (b)

Figure 5.4: (a) Stepping motor, (b) torque versus speed curves.

5.1.2 Loading Rod

The loading rod was made by steel and was fabricated to connect the linear actuator and the load cell. The length of the loading rod was 30 inches and the diameter of it was 3/4 inches. Figure 5.5 shows the technical plan of the loading rod and the pictures of its bolt end and the threaded housing end. The bolt end was for the female threads on the linear actuator system and the threaded housing end was for the load cell. More details about the loading rod can be found in Munson (2018).

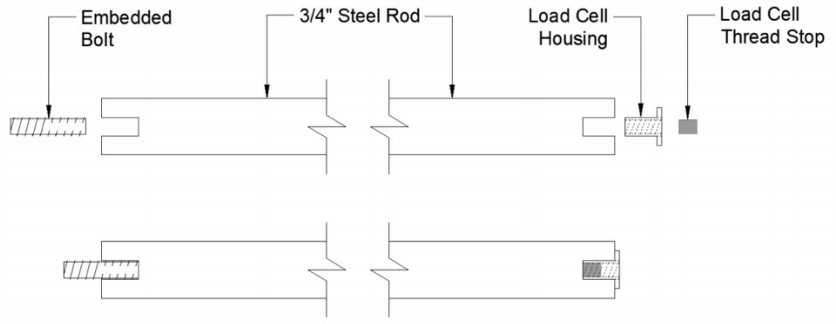

(a)

(b)

(c)

Figure 5.5: Loading rod assembly, (a) technical drawing, (b) connection to linear actuator system, and (c) load cell connection (Munson, 2018).

5.1.3 Tested Spheres

Three acrylic spheres with different diameters of 2 inches, 3 inches, and 4 inches were used in the laboratory foundation model tests. Each sphere had a circular cavity to

house the load cell. Figure 5.6(a) shows the spheres with different diameters and Figure 5.6(b) shows the recessed cavity in the sphere to connect the load cell. More details about the tested spheres could be found in Munson (2018).

(a)

(b)

Figure 5.6: (a) Tested spheres, (b) cavity and threaded connection in the spheres (Gilbert, 2018).

5.1.4 Load Cell and LVDT

The required capacity of the load cell was determined by a series of sphere penetration tests conducted by Munson (2018), which indicated the required load was lower than 100 lbs. The load cell used in this study had load capacity of 100 lbs and accuracy of 0.25% of its safe overload capacity. Figure 5.7 shows the miniature universal load cell fabricated by OMEGA with type of LC202-100. The diameter and the thickness of the load cell were one inch.

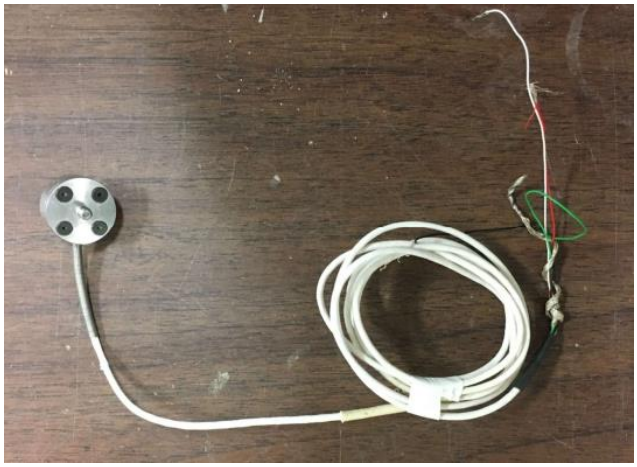

Figure 5.7: Load Cell (Munson, 2018).

The linear variable differential transformer (LVDT) was fabricated by OMEGA with type of LD230-2.5, which was a high accuracy AC LVDT displacement sensor (Figure 5.8). The range of the LVDT was ± 0.1 inch with accuracy of 0.0002 inch, which provided enough resolution to capture the movement of the spheres.

Figure 5.8: Linear variable differential transformer (Munson, 2018).

5.1.5 Soil Tank

A large wood tank was made in this study to make the sand test bed. The main dimensions of the tank were 7-ft long, 3-ft wide, and 3-ft and 4-inch high. The material of wood avoided the generation of complicated seismic waves during geophone tests by the

interaction of the waves with the cell. Figure 5.9 shows the picture of the wood tank and Figure 5.10 shows the rendering of the tank. More details about the construction of the tank can be found in Munson (2018).

Figure 5.9: Soil tank.

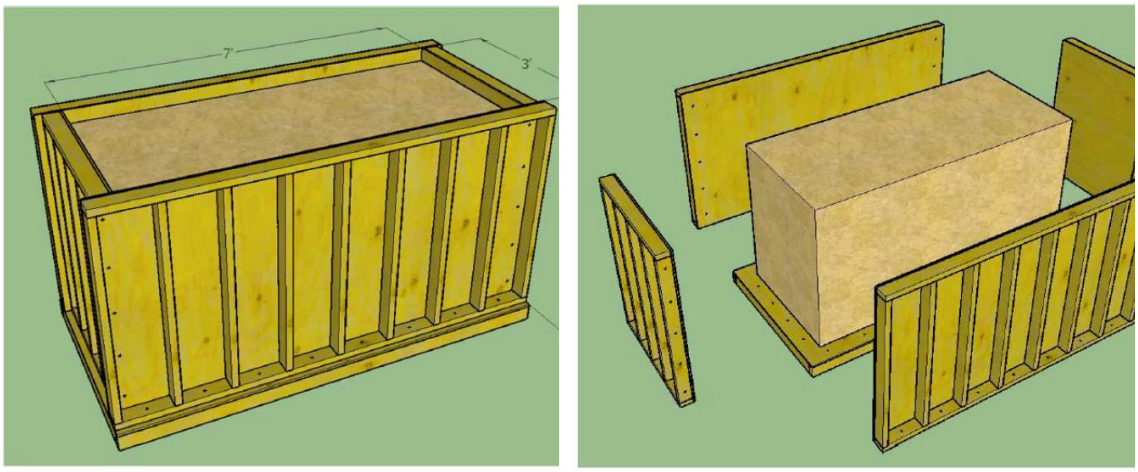

(a) (b)

Figure 5.10: Rendering of the soil tank (Munson, 2018).

5.2 Sand Placement Procedure for Laboratory Tests

To obtain reliable and repeatable results from the lateral push tests, developing a well-founded method of making the sand bed was critical. The method included of placing the sand around the sphere and measuring the void ratio of the sand in the soil tank.

The procedure of the method of placing the sand around the sphere was as follows:

1) Fill the sand to the bottom of the sphere and place an empty container of known weight and volume in the corner of the soil tank which was used to determine the void ratio of the sand at the level of the sphere.
2) Pluvaite the sand around the sphere and into the container using a funnel until the sphere was buried.
3) Add the sand around the sphere using pluviation from buckets from a constant drop height of 6 inches until the sand reached the top of the sphere.
4) Flatter the surface the sand at the top of the sphere.
5) Pluviate more sand into the tank to a target embedment depth.

The use of funnel mitigated the separation between larger than smaller particles of sand. In the initial tests, the sand was pluviated by buckets directly. It resulted in that the larger particles tended to roll down sand down while smaller particles would stay on the slopes, which created an uneven distribution of the particles. Using the funnel to place the sand around the sphere ensured a consistent gradation of sand particles around the sphere. Furthermore, using the funnel to fill the container ensured an accurate void ratio measurement of the sand around the sphere.

The void ratio of the specimens in torsional shear tests and triaxial compression tests was determined by the density measured using the container. Embedment depths for the lateral push tests were 10 and 20 inches from the center of the sphere to the surface of the sand. The total unit weight of the sand at the embedment depth of 20 inches was 105 pcf and the void ratio was 0.56. Figure 5.11 shows a summary of the procedure of preparing the sand bed for the advanced tests.

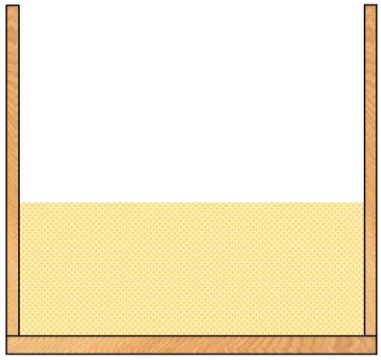	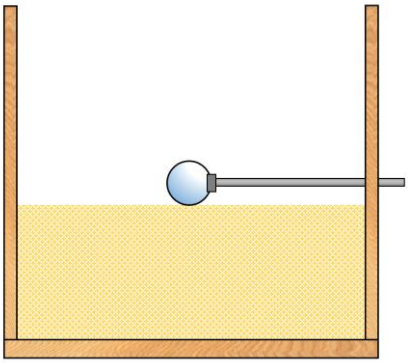
1. Fill the sand up to the bottom of the sphere	2. Place the sphere and the loading rod, make sure the bottom of the sphere touches the sand
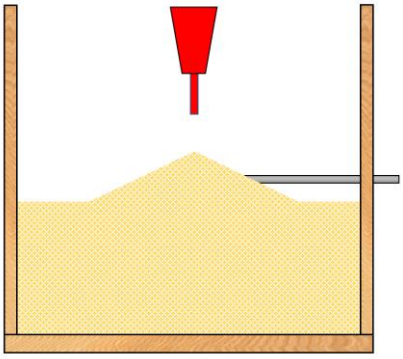	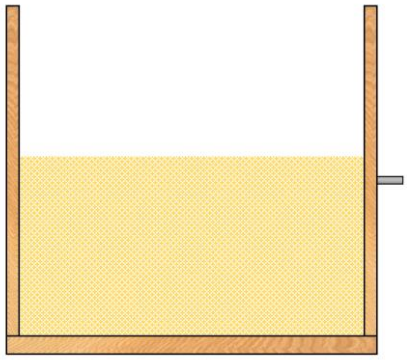
3. Use a funnel to pluviate the sand around the sphere to the top of the sphere	4. Pluviate the sand from buckets to fill the sand to the top of the sphere and flatten the surface
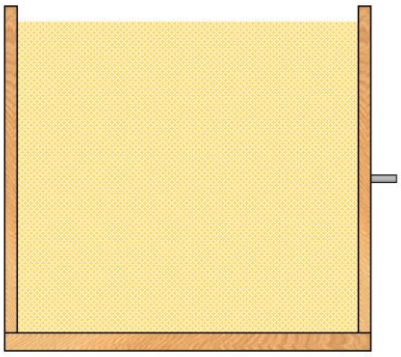	
5. Fill the sand up to the target height using the pluviation from buckets	

Figure 5.11: Procedure for preparing the sand bed.

5.3 PROPERTIES OF ALL-PURPOSE SAND

Sieve analyses, torsional shear tests, and triaxial compression tests were conducted to determine the properties of All-purpose sand. The combination of the results of the tests was used to decide the input parameters for the soil constitutive model.

5.3.1 Sieve Analysis

Tables 5.1 and 5.2 show the results of the grain size analysis of the All-Purpose sand. Figure 5.12 indicates that the All-Purpose sand is fairly uniform. The All-Purpose sand was used to prepare the medium dense siliceous sand bed in the tank.

Table 5.1: Sieve analysis on All-Purpose sand.

Sieve #	Opening (mm)	Wo (g)	Wf (g)	Wsoil (g)	Cum. Retained (g)	Passing
4	4.75	762.8	766.2	3.4	3.4	100%
8	2.3600	682.8	866.4	183.6	183.6	91%
20	0.8500	588.8	1263.6	674.8	858.4	59%
30	0.6000	609	914.4	305.4	1163.8	46%
40	0.4250	577.5	850.6	273.1	1436.9	33%
50	0.3000	332.3	595.2	262.9	1699.8	23%
100	0.1500	522.6	929.4	406.8	2106.6	5%
140	0.1060	357.9	416.9	59	2165.6	2%
200	0.0750	341.8	373.8	32	2197.6	1%
Pan	0.0000	383	396.4	13.4	2211	0%
Lid	-	241.9	241.9	0	2211	
Totals		5400.4	7614.8	2214.4		

Table 5.2: Coefficients of uniformity C_u and curvature C_c of All-Purpose sand.

	All-Purpose Sand
D_{10}	0.19 mm
D_{30}	0.38 mm
D_{50}	0.67 mm
D_{60}	0.87 mm
C_u	4.6
C_c	0.92

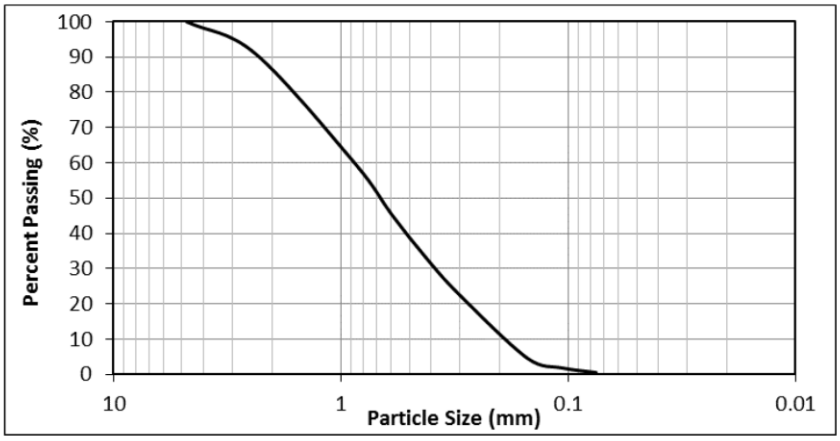

Figure 5.12: Gradation curves of All-Purpose sand.

5.3.2 Torsional Shear Test

The torsional shear test was used to determine the relationships of shear modulus, G, shear strain, γ, and mean effective stress, σ_0'. The relationship was measured by increasing the levels of stress and strain in the test step-by-step.

As shown in the element tests in Section 5.3.1, the empirical equations provided by Menq (2003) cannot predict the relationship of $\log G_{max} - \log \sigma_0'$ accurately. The empirical equations need to be modified based on torsional shear tests.

R-squared method was used to find the regression lines of G_{max} and $G/G_{max} - \log\gamma$ to best-fit the data measured in the torsional shear tests. Based on a preliminary numerical modeling, the largest stress in the sand caused by pushing the sphere was less than 4psi at small displacements. The regression analysis on the relationship between confining pressure and G_{max} was performed up to the confining pressure 8 psi. The regression analyses on the relationship of the $G/G_{max} - \log\gamma$ curves were performed on the curves with 2 psi and 4 psi confining pressure.

The modified procedure was shown in Section 5.3.1 and the soil properties which best-fit the torsional shear tests are listed in Table 5.3.

Table 5.3: Input parameters for All-Purpose sand in Abaqus.

$\mathbf{C_{G1}}$ (psi)	$\mathbf{n_G}$	C_1 (%)	C_2	C_3	C_4	$\alpha_1, \alpha_2, \alpha_3$
18652	0.44	0.036	0.296	0.95	0.1	0.001

5.3.3 Triaxial Compression Tests

To complement the limitation that the largest shear strain in the torsional tests was up to 0.1%, triaxial compression tests with three different confining pressures were carried out. The triaxial compression tests were used to modify the soil parameters for the soil constitutive model when the octahedral shear strain was larger than 0.1%. The density and the dimension of the specimen during the triaxial compression tests were controlled to be the same as in the torsional shear tests. Three levels of confining pressure, 2psi, 4psi, and 8psi, were selected for the triaxial compression tests, which were the same with the torsional shear tests. From the analysis on the triaxial compression tests using Mohr's circles, the friction angle of All-Purpose sand was 39 degrees when the total unit weight was 105 pcf (Figure 5.13).

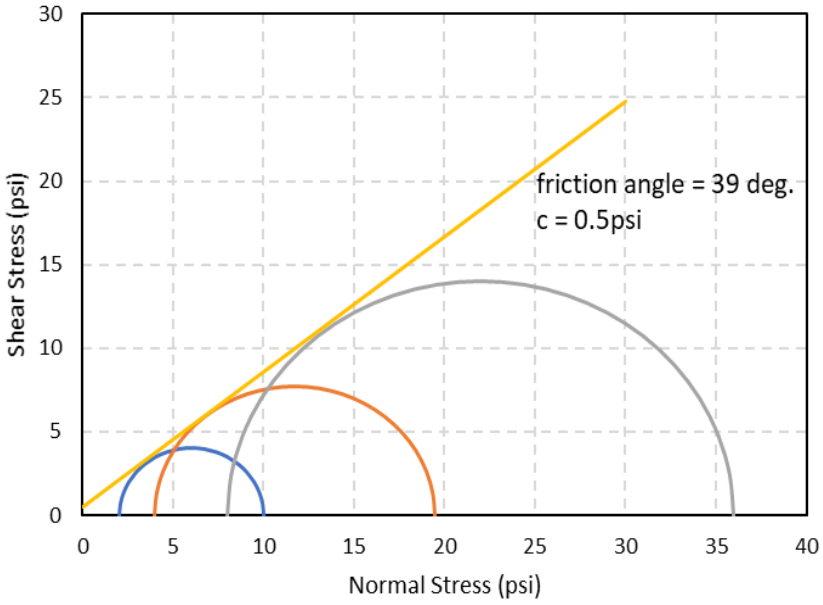

Figure 5.13: Mohr's circles of triaxial compression tests on the All-Purpose sand.

Figure 5.14 shows the comparison between the measurement and the numerical simulation of 3-D FEM model using the soil parameters in Table 5.3 before modifying the $G/G_{max} - \log\gamma$ curves. The numerical simulation overestimated the stiffness when the confining pressure was low, but it underestimated the stiffness when the confining pressure went higher.

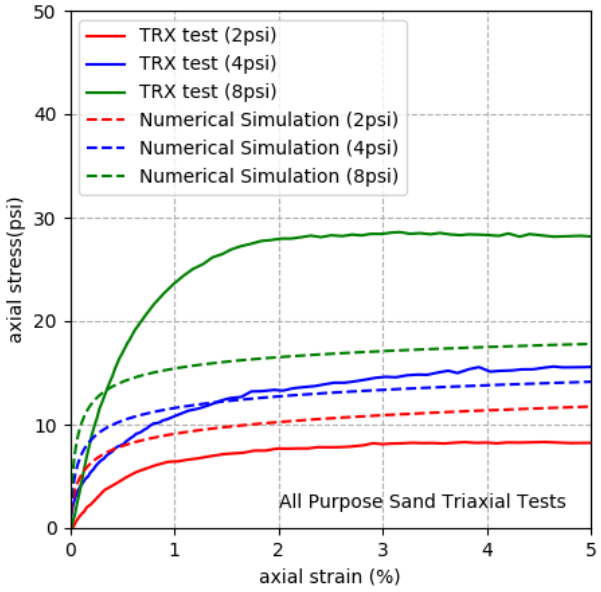

Figure 5.14: Comparison between the numerical modeling and triaxial tests (All-Purpose sand, before modification).

Table 5.4 shows the modified input properties of the constitutive model for All-Purpose sand modified by triaxial compression tests. Figure 5.15 shows the comparison of triaxial tests between the measurement and numerical simulation after the input properties were modified. The stress versus strain curves of numerical simulation had good agreements with the triaxial compression tests when the strain was larger than 2%. The triaxial compression tests could not capture the stiffness of the sand at small strains, so the numerical simulation did not try to match the curves under 2%.

Table 5.4: Input parameters for All-Purpose sand in Abaqus (after modification).

C_{G1} (psi)	n_G	C_1 (%)	C_2	C_3	C_4	$\alpha_1, \alpha_2, \alpha_3$
18652	0.44	0.062	0.8	1.0	0.13	0.001

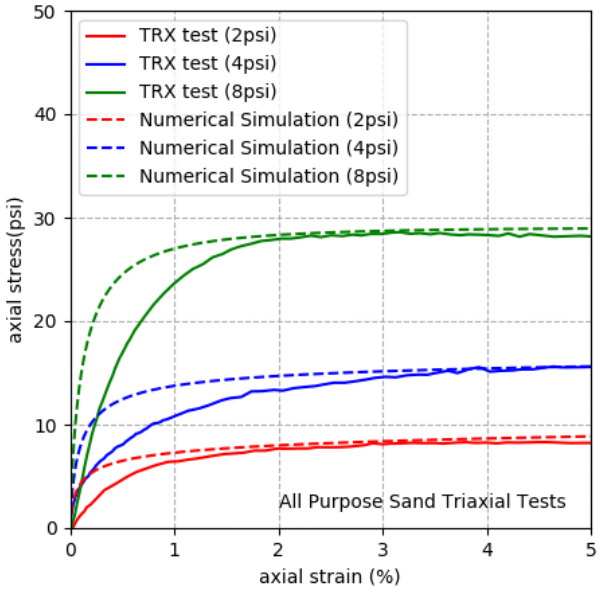

Figure 5.15: Comparison between the numerical modeling and triaxial tests (All-Purpose sand, after modification).

Figure 5.16 shows the numerical $G/G_{max} - \log\gamma$ curves based on the modified input parameters in Table 5.4. Though the modified numerical $G/G_{max} - \log\gamma$ curves did not best-fit with the results of the torsional shear tests anymore, they still had good fit with the measured $G/G_{max} - \log\gamma$ data. Therefore, the modification had little influence on the numerical simulation of the stiffness at small strains and it made the numerical $G/G_{max} - \log\gamma$ curves perform better at large strains.

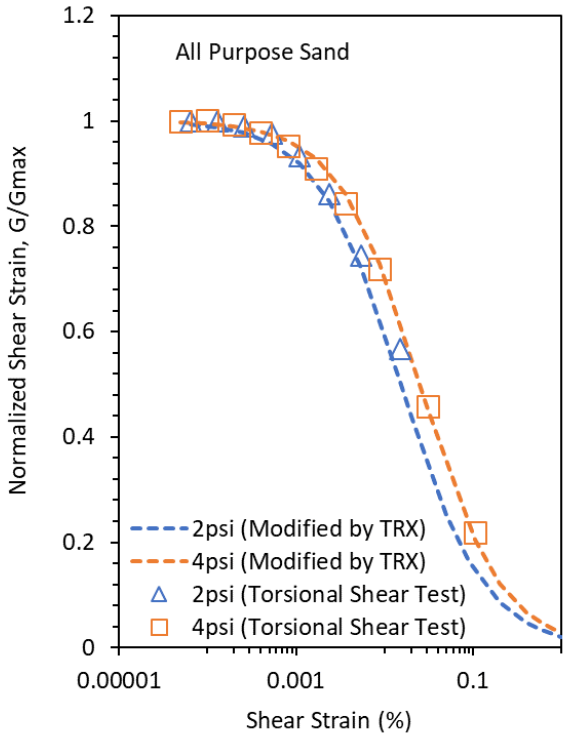

Figure 5.16: Modified relationship of $\mathrm{G}/\mathrm{G}_{max} - \log\gamma$ curves (All-Purpose sand).

5.4 GEOPHONE TESTS

Geophone tests were carried out to obtain the maximum shear modulus, G_{max}, and Poisson's ratio, υ, used in the proposed soil constitutive model for the in-situ sand. Geophone tests could measure the shear wave (S-wave) velocity and the confined compression wave (P-wave) velocity in the tank of sand. The magnitude of the S-wave velocity could be used to calculate the maximum shear modulus, G_{max}. The S-wave velocity and P-wave velocity could be combined to calculate the Poisson's ratio, υ.

5.4.1 Geophone Tests Equipment

The following equipment was used to perform the geophone tests:

- 4.5-Hz geophones as sources (Figure 5.17),

- 28-Hz geophones (GS-14-L3 epoxied inside plastic cases for protection) as receivers (Figure 5.18),
- BNC cables,
- Function generator (Keysight 33210A) to excite the source geophone (Figure 5.19), and
- Dynamic signal analyzer (Quattro by Data Physics) to record received signals (Figure 5.20)

Figure 5.17: 4.5-Hz geophone.

Figure 5.18: 28-Hz geophones (GS-14-L3 epoxied inside plastic cases for protection).

Figure 5.19: Function generator (Keysight 33210A).

Figure 5.20: Dynamic signal analyzer (Quattro by Data Physics).

5.4.2 Geophone Tests Set-up

The set-up of the geophone tests, for measuring the S-wave and P-wave velocities in the tank of sand, was similar to the configuration used for in-situ cross-hole tests where a source is placed in one borehole and two geophone receivers are used in the adjacent boreholes. In the geophone tests conducted in the tank of sand, the sources and the geophone receivers were embedded at the specific depth (the same depth at the center of the embedded sphere) and covered with sand. To have a consistent condition of sand bed for the laterally loaded sphere tests, the sand bed was prepared using the same way in section 5.2.

Figures 5.21 and 5.22 show the 3-D layout of the geophone tests in the tank of sand and the dimensions of geophones and spacing respectively. Two linear arrays were used in the geophone tests, one with vertical geophones for measuring S-wave velocity and the other with horizontal geophones for measuring P-wave velocity. The vertical source geophone generated horizontally propagating vertically polarized S-waves (S_{HV}) and the horizontal source geophone generated horizontally propagating P-waves (P_H). Figure 5.23 shows the placements of the geophones at specific depth before they were covered with sand.

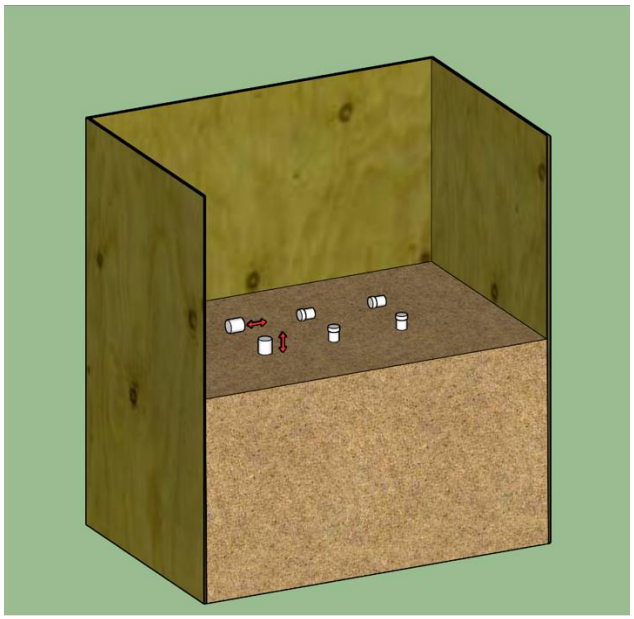

Figure 5.21: 3-D Layout of the geophones inside the sand tank (Gilbert et al., 2018).

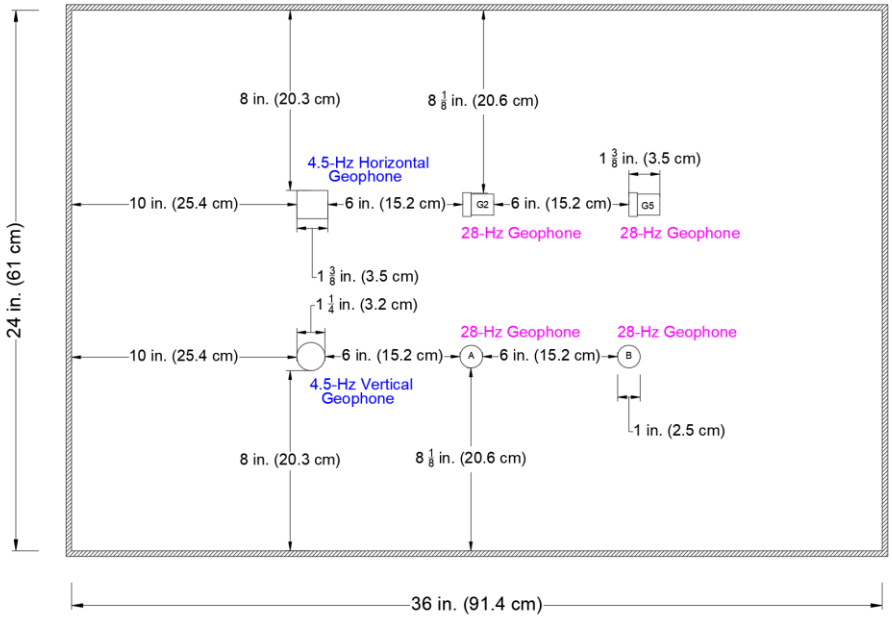

Figure 5.22: 2-D Layout of the geophones inside the sand tank (Gilbert et al., 2018).

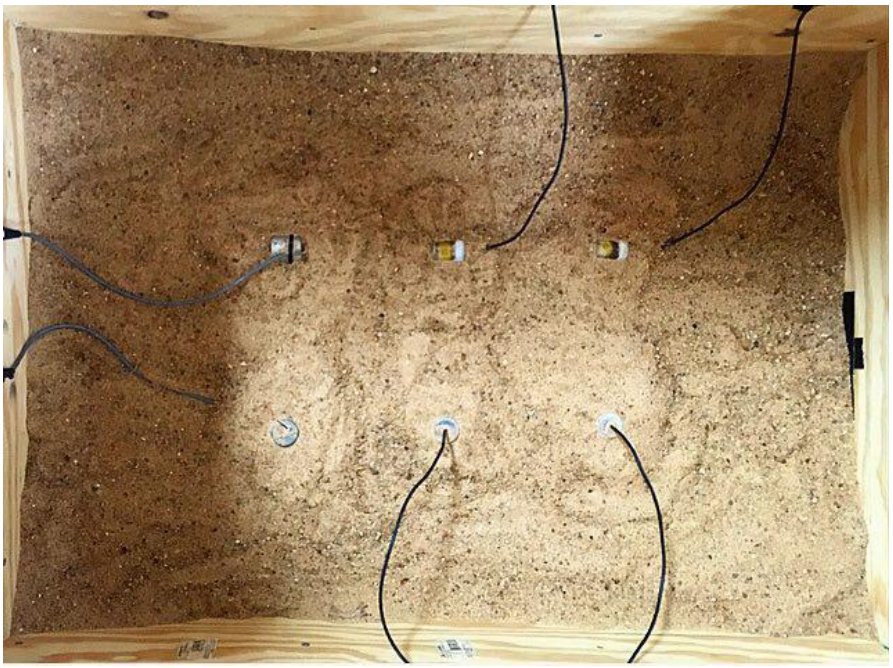

Figure 5.23: Geophones placed inside the sand tank (Gilbert el al., 2018).

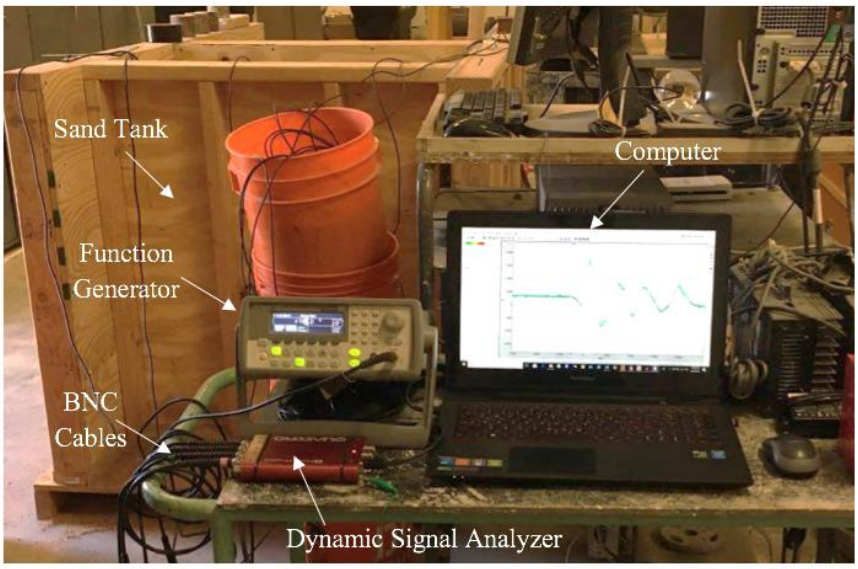

Figure 5.24: Set up used for generating waves and recording the signals (Gilbert et al., 2018).

5.4.3 Geophone Tests Procedure

The following steps were taken to prepare the sand bed inside the sand tank:

1) The sand was removed to the required depth.
2) The surface at the required depth was leveled.
3) The geophones were carefully placed at the proper locations. The distances between the geophones were checked multiple times before continuing the next step.
4) The sand was lightly pluviated using a funnel around the geophones to insure no gap between the geophones and the sand as in the push tests.
5) The remaining sand was pluviated up to the required height using buckets (drop height of 6 inches was used just as done in constructing the sand bed in the push tests).

Each geophone test was conducted in two stages because the laterally loaded sphere tests were carried out at two different depths (10 inches and 20 inches). The first stage was measuring the wave velocities with the geophones embedded with 10 inches of sand. After the first stage was completed, another 10 inches of sand was added on the top of the sand bed in the first stage. In the second stage, the measurements were carried out with 20-inch embedment depth.

At the start of each geophone test, the function generator was used to trigger the source geophones to generate propagating waves in the sand. The receiver geophones would vibrate and record the travel time when the propagating waves arrived. The travel time could be calculated based on the difference of the times arriving the two receiver geophones, Δt. With the known front-to-front distance between the receiver geophones Δd, the wave velocity could be calculated using the velocity equation, $V = \Delta d / \Delta t$.

5.4.4 Geophone Tests Results

To verify the repeatability of the measure wave velocities, five independent two-stage (10-inch and 20-inch embedment depths) geophone tests were conducted. Each test included 10 runs to obtain each wave velocity. Table 5.5 summarizes the velocities derived from these tests.

Table 5.5: Results of geophone tests (Gilbert et al., 2018).

Derived Parameter	Embedment depth of 10 inches (Average $\pm$ Std. Dev.)	Embedment depth of 20 inches (Average $\pm$ Std. Dev.)
VS (fps)	330 ± 10	380 ± 15
VP (fps)	510 ± 15	570 ± 25
ν	0.15 ± 0.06	0.12 ± 0.06

The reasons for the deviation of the measurement included: (1) the uncertainty of picking arrival times of the waves; (2) the variation in the soil structure around the geophones; (3) the variation of the geophone spacings caused by the manually placing the geophones; (4) and the environmental noise from the working electricity equipment.

5.4.5 Modification of Soil Input Parameters based on Geophone Tests

To relate the V_s versus depth profile measured in the field dynamic tests into the G_{max} versus depth profile, the relationship between V_s and G_{max} can be expressed as:

$$G_{\max} = V_s^2 \times \rho \tag{5.1}$$

where ρ is the total mass density of the soil. To build the relationship between G_{max} and σ_0' from the G_{max} versus depth profile, the mean effective confining pressure, σ_0', is calculated by:

$$\sigma_0^{'} = \frac{\sigma_v^{'} + 2\sigma_v^{'} K_0}{3} \tag{5.2}$$

where K_0 is determined by $K_0 = \nu/(1-\nu)$ and σ_v' is effective vertical stress. In this constitutive model, Poisson's ratio is simplified to be constant during loading, although it changes slightly with applied strain.

Bauer (2018) calculated the total unit weight of the sand equaling to 0.06 pci and the void ratio equaling to 0.56 in the tank. Figure 5.25 shows the predicted shear velocity versus depth profile in the tank based on the relationship of $\log G_{max} - \log \sigma_0'$ from the torsional shear tests and Poisson's ratio of 0.12.

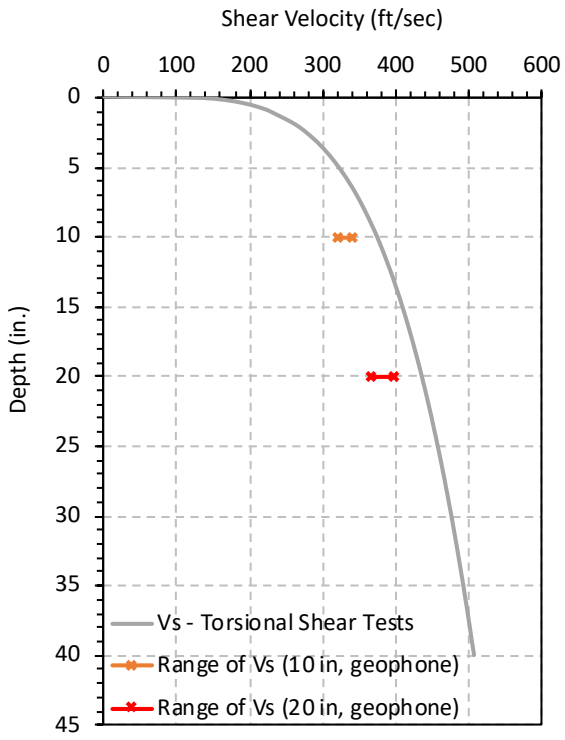

Figure 5.25: Shear velocity profile predicted by the results from torsional shear tests.

The shear velocity predicted from the torsional shear tests was higher than the shear velocity measured by geophone tests in the soil tank. To better represent the shear velocity measured in the tank, the relationship of $\log G_{max} - \log \sigma_0'$ needed to be modified depended on the geophone tests results. After modification, an upper bound and a lower bound shear velocity profiles were formed to match the shear velocities measured in the geophone tests at depths of 10 and 20 inches. Table 5.6 shows the input parameters of the soil constitutive model after the modification and Figure 5.26 shows the modified shear velocity profiles with the measured ranges of shear velocities.

Table 5.6: Input parameter of the soil consistutive model modified by the geophone tests.

All-Purpose sand (in the soil tank)				
$\boldsymbol{v}$	0.12		0.15	
	Lower Bound	**Upper Bound**	**Lower Bound**	**Upper Bound**
$\boldsymbol{C_{G1}}$	13233	15374	12872	14894
$\boldsymbol{n_g}$	0.44			
$\boldsymbol{C_1}$ (%)	0.062			
$\boldsymbol{C_2}$	0.7			
$\boldsymbol{C_3}$	1.0			
$\boldsymbol{C_4}$	0.09			
$\boldsymbol{\alpha_a, \alpha_b, \alpha_c}$	0.001			
$\boldsymbol{\gamma}$ $(\boldsymbol{pcf})$	105			
$\boldsymbol{K_0}$	0.136			

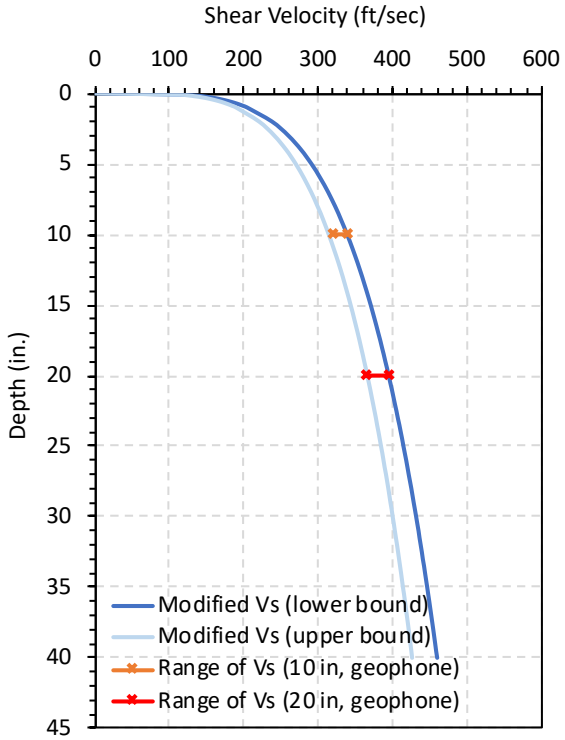

Figure 5.26: Predicted shear velocity profile modified by the geophone tests.

5.5 RESULTS OF THE LATERAL PUSH TESTS

The lateral push tests were performed on 2-, 3-, and 4-inch spheres and were embedded with 10 or 20 inches. Three spheres with different diameters and two embedment depths totaled six monotonic test scenarios. Figure 5.27 to 6.32 show the tests results of the 2-, 3-, and 4-inch spheres, respectively, at 10 or 20 inches of embedment. All the tests results have fairly good repeatability. The reason that the tests for the 3-inch sphere have the largest deviation is because the 3-inch sphere was used to find the repeatable testing routine that would create consistent results. So, more tests were run on the 3-inch sphere and the other spheres were added later to evaluate the effect of varying sphere diameters. The tests for the 4-inch sphere at the embedment depth of 20 inches have the best repeatability. It is as expected that tests performed with a larger sphere at a deeper embedment depth would have better repeatability.

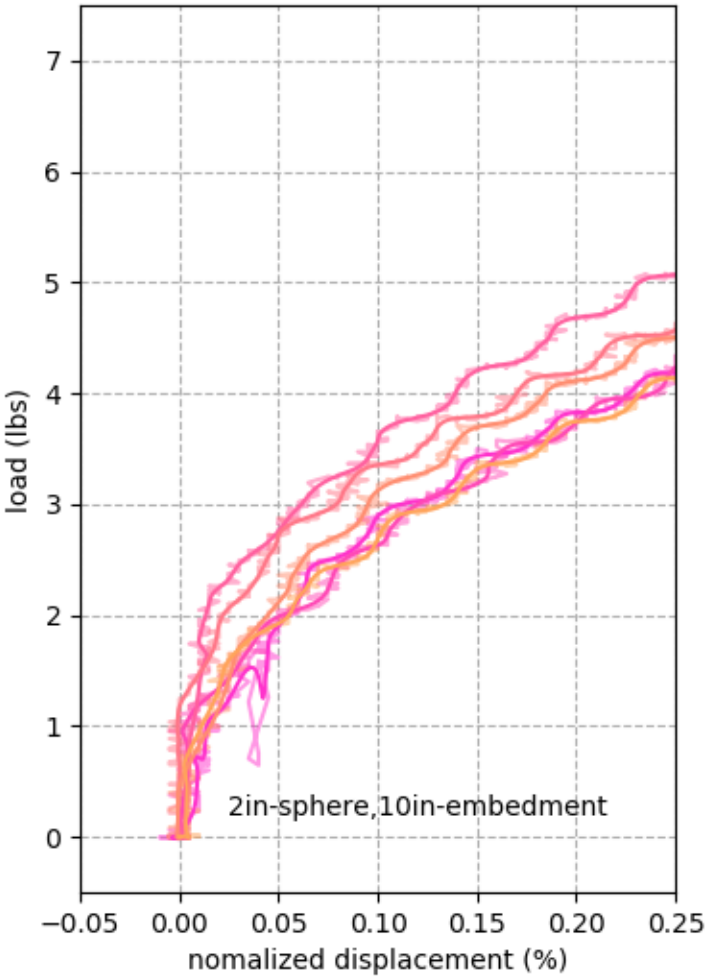

Figure 5.27: Push tests results for 2-inch sphere at embedment depth of 10 inches.

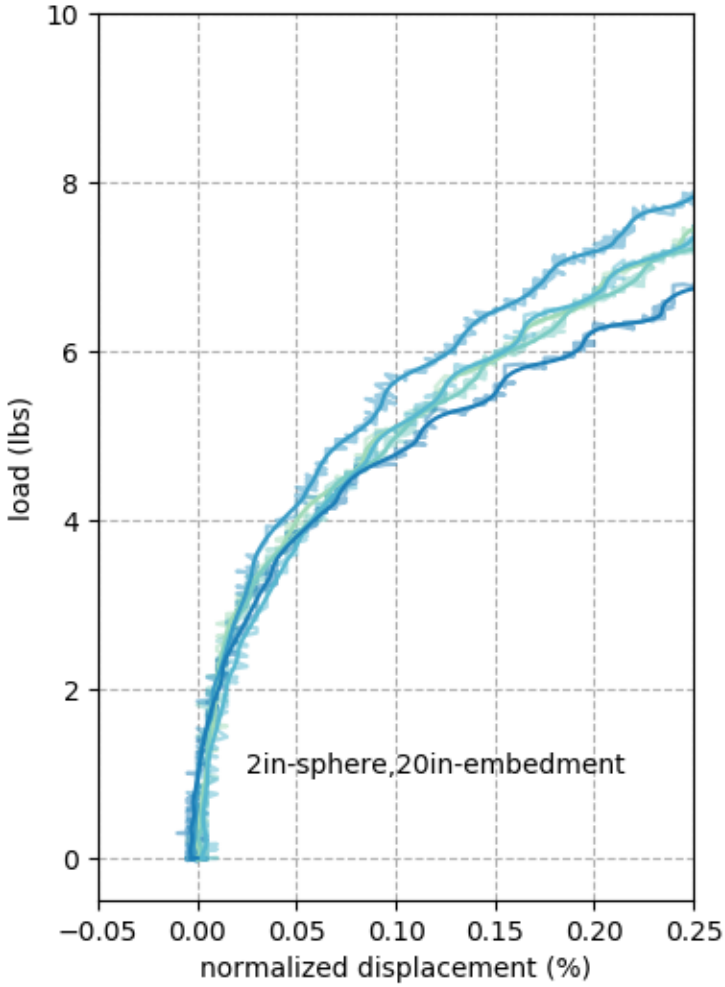

Figure 5.28: Push tests results for 2-inch sphere at embedment depth of 20 inches.

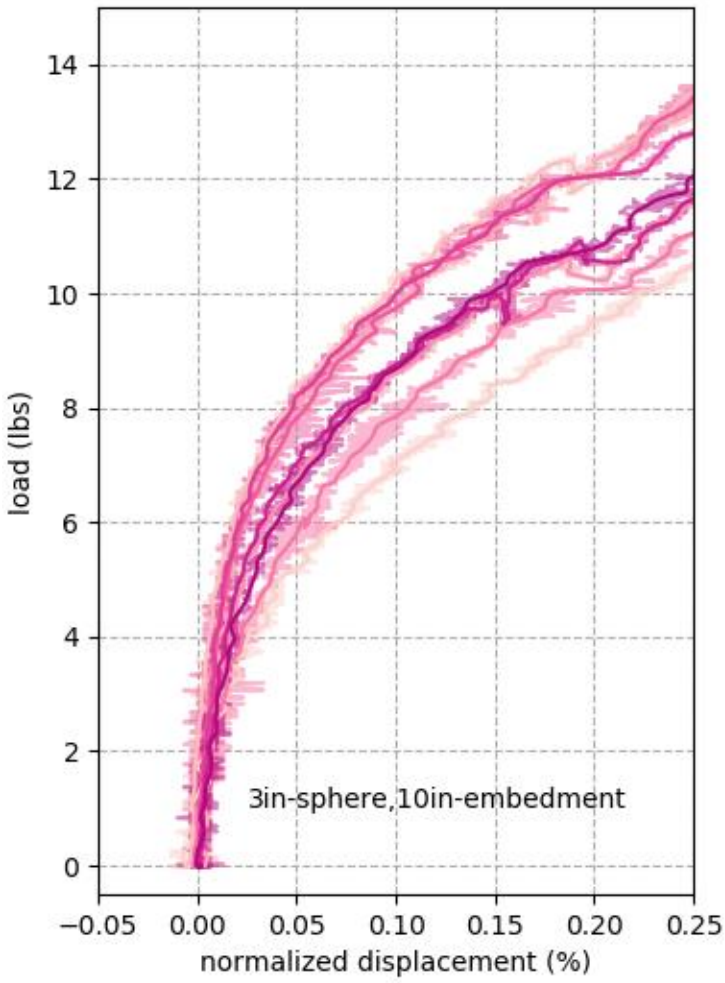

Figure 5.29: Push tests results for 3-inch sphere at embedment depth of 10 inches.

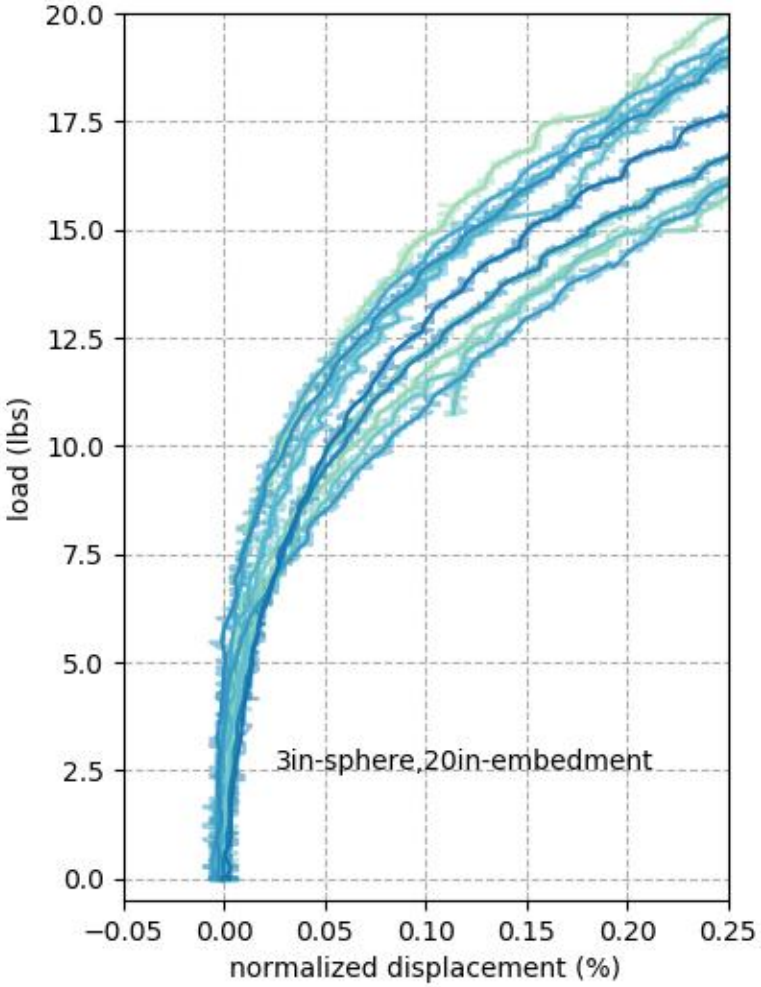

Figure 5.30: Push tests results for 3-inch sphere at embedment depth of 20 inches.

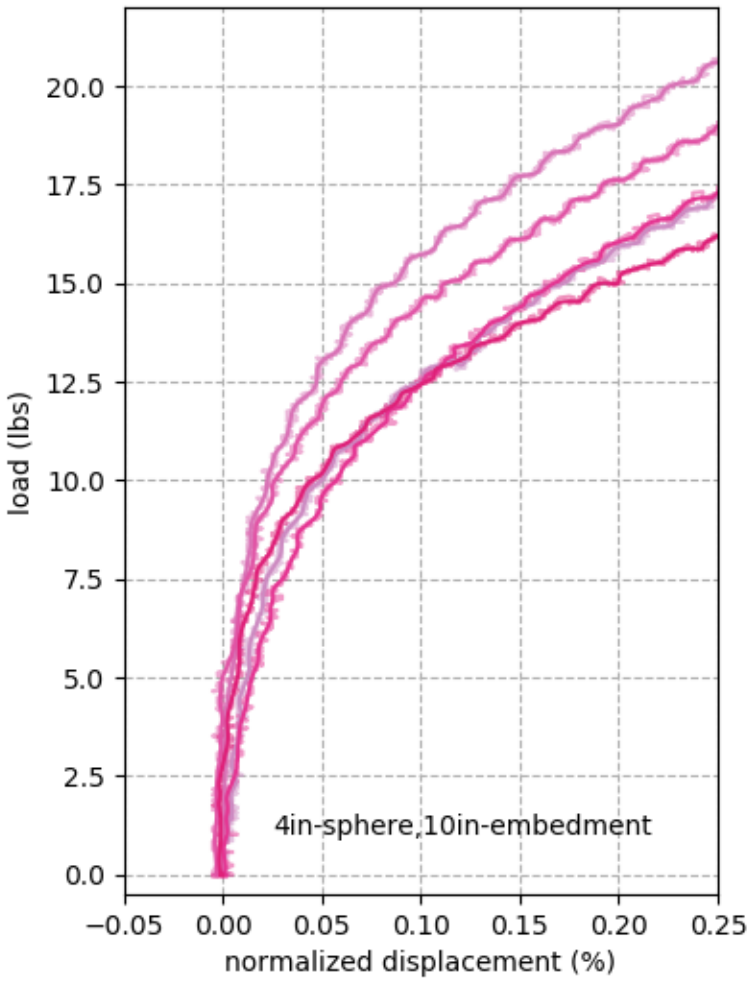

Figure 5.31: Push tests results for 4-inch sphere at embedment depth of 10 inches.

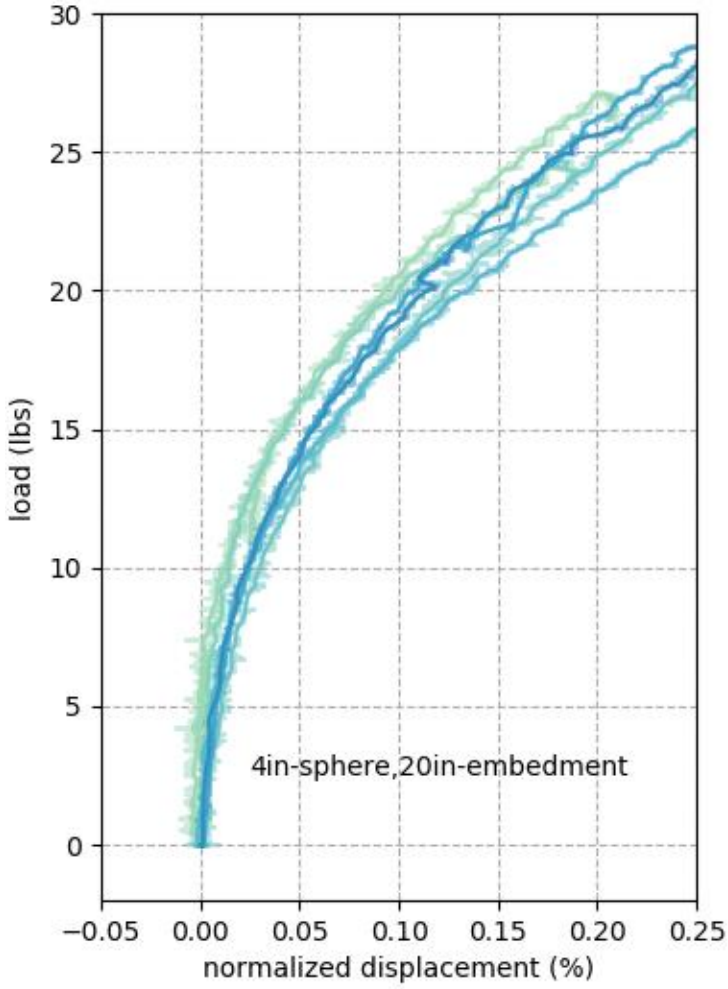

Figure 5.32: Push tests results for 4-inch sphere at embedment depth of 20 inches.

5.6 NUMERICAL MODELING OF LATERAL PUSH TESTS

3-D FEM models of Abaqus were established to simulate the lateral push tests on the 2-, 3-, and 4-inch spheres at embedment depths of 10 and 20 inches. The results obtained from 3-D FEM model were compared to the laboratory tests.

5.6.1 3-D FEM Models of Lateral Push Tests

The horizontal loading on the test sphere in the middle of the soil tank implied a plane of symmetry in the problem geometry and therefore, only half of the geometry was discretized into the 3-D FEM model (Figure 5.33). The 3-D FEM model included (1) the sand body, (2) the test sphere, and (3) the interface between the sand body and the sphere:

1) Sand body: the height of the sand body was depended on the embedment depth of the laboratory tests. The sphere was at the center of the sand body. At the base of sand body, all three displacement components in the three-coordinate directions (X, Y, and Z) were restrained to zero. For the side boundaries on the Y-Z plane and the back boundary (far away from the sphere) on the X-Z plane, the displacement components X and Y were restrained to zero. To ensure that the front boundary on the X-Z plane was a plane of symmetry, the displacement normal to this plane was set to zero. The material of the sand was modelled using the subroutine of the proposed soil constitutive model. The input properties of the sand were based on the torsional shear tests, triaxial compression tests, and geophone tests.
2) Test sphere: the test sphere was modeled as a rigid sphere which cannot deform. The displacement was applied at the center of the sphere.
3) Interface: the interface between the test sphere and the sand body was defined as frictionless.

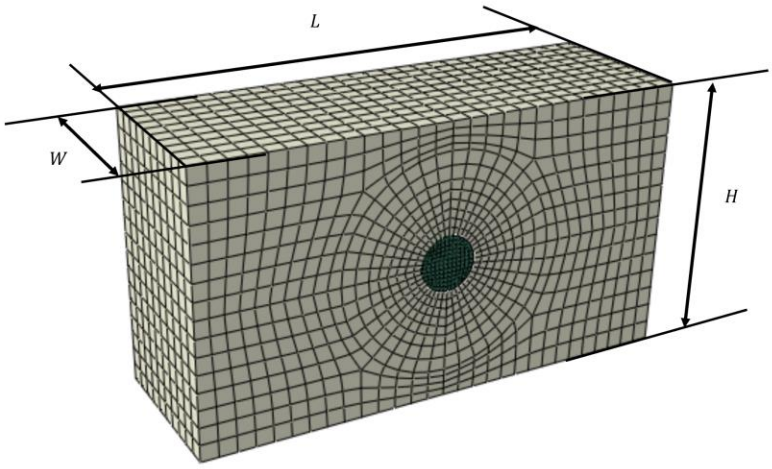

Figure 5.33: Abaqus model of lateral push tests on spheres.

5.6.2 3-D FEM Model of Boundary Effect Analysis

Boundary effects are an important issue that need to be addressed in the FEM analysis. To investigate the influence of boundary effects, five 3-D FEM models were created with different boundary dimensions of soil body as shown in Table 5.7. The diameter of the sphere was chosen as 4 inches, which was the largest sphere used in the laboratory tests.

Table 5.7: Boundary dimensions for different models.

Model #	***L* (inches)**	***W* (inches)**	***H* (inches)**
1	30	10.5	42
2	30	21	42
3	36	12	42
4	40	21	42
5	50	21	42

Figure 5.34 shows the comparison between the 3-D FEM models with different boundary dimensions. The dimensions of Model#3 were accepted as the dimensions used

in the 3-D FEM models, which boundary caused little effect on the results of simulation and the size was same as used in the laboratory lateral push tests.

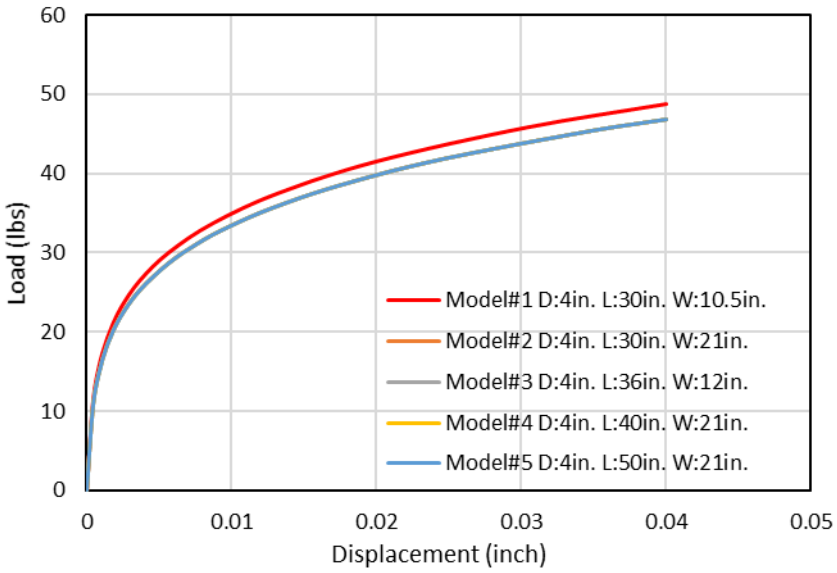

Figure 5.34: Comparison for the analysis of boundary effect.

5.6.3 Numerical Modeling Results

3-D FEM models with four different sets of input parameters were conducted to compare with the results of the lateral push tests: (1) at the embedment depth of 10 inches, the Poisson's ratio was 0.15 and the shear velocity varied from 320 to 340 fps; (2) at embedment depth of 20 inches, the Poisson's ratio was 0.12 and the shear velocity varied from 365 to 395 fps; (3) at embedment depth of 10 inches, the Poisson's ratio varied from 0.09 to 0.21 and the shear velocity was 330 fps; (4) at embedment depth of 20 inches, the Poisson's ratio varied from 0.06 to 0.18 and the shear velocity was 380 fps. The mean and the deviation of the Poisson's ratio and the shear velocity were determined by the results of the geophone tests shown in Table 5.5. The comparisons of the first and second sets

could illustrate the influence of the shear velocity on the predicted results of load-displacement curves. The comparisons of the third and fourth sets could demonstrate the effect of the Poisson's ratio on the simulated results. Table 5.8 shows the input parameters of the soil for the constitutive model for each set of tests.

Table 5.8: Input parameter of the soil constitutive model for 3-D FEM model of lateral push tests.

All-Purpose sand (in the soil tank)								
Set #	**#1**		**#2**		**#3**		**#4**	
	Lower	**Upper**	**Lower**	**Upper**	**Lower**	**Upper**	**Lower**	**Upper**
$\boldsymbol{v}$	0.15	0.15	0.12	0.12	0.09	0.21	0.06	0.18
$\boldsymbol{C_{G1}}$	12872	14894	13233	15374	14894	13421	14894	13421
$\boldsymbol{n_g}$	0.44							
$\boldsymbol{C_1}$ (%)	0.062							
$\boldsymbol{C_2}$	0.7							
$\boldsymbol{C_3}$	1.0							
$\boldsymbol{C_4}$	0.09							
$\boldsymbol{\alpha_a, \alpha_b, \alpha_c}$	0.001							
$\boldsymbol{\gamma\ (pcf)}$	105							
$\boldsymbol{K_0}$	0.136							

Figures 5.35 to 5.40 show comparisons of first and second sets between the measured and predicted load-displacement curves for the varying sphere diameters at embedment depths of 10 inches and 20 inches. As shown in figures, the predicted load-displacement curves are sensitive to the change of the shear velocity. For all the spheres, the curves extracted from 3-D FEM models overlay the load-displacement curves obtained from laboratory tests, which show they have good agreement between the predicted and experimental results. The predicted load at the 0.25% diameter is proportional to the projection area of the sphere in the loading direction.

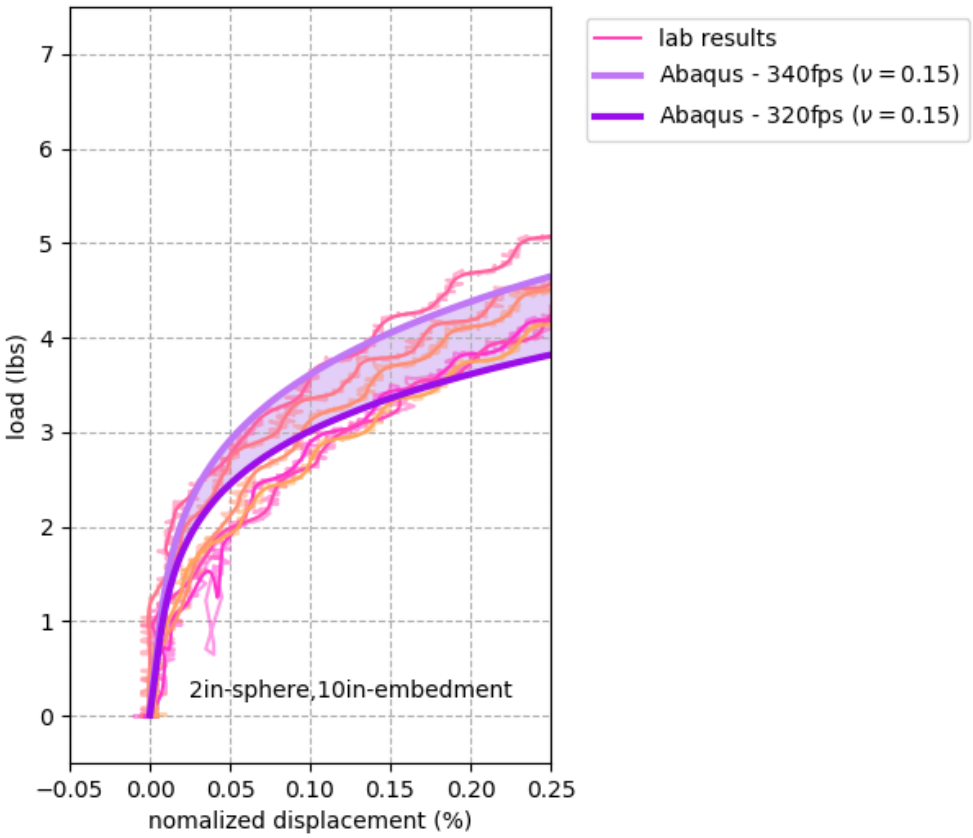

Figure 5.35: Comparison between measured and predicted load-displacement curves for 2-inch sphere at embedment depth of 10 inches. (Soil Profile – #1).

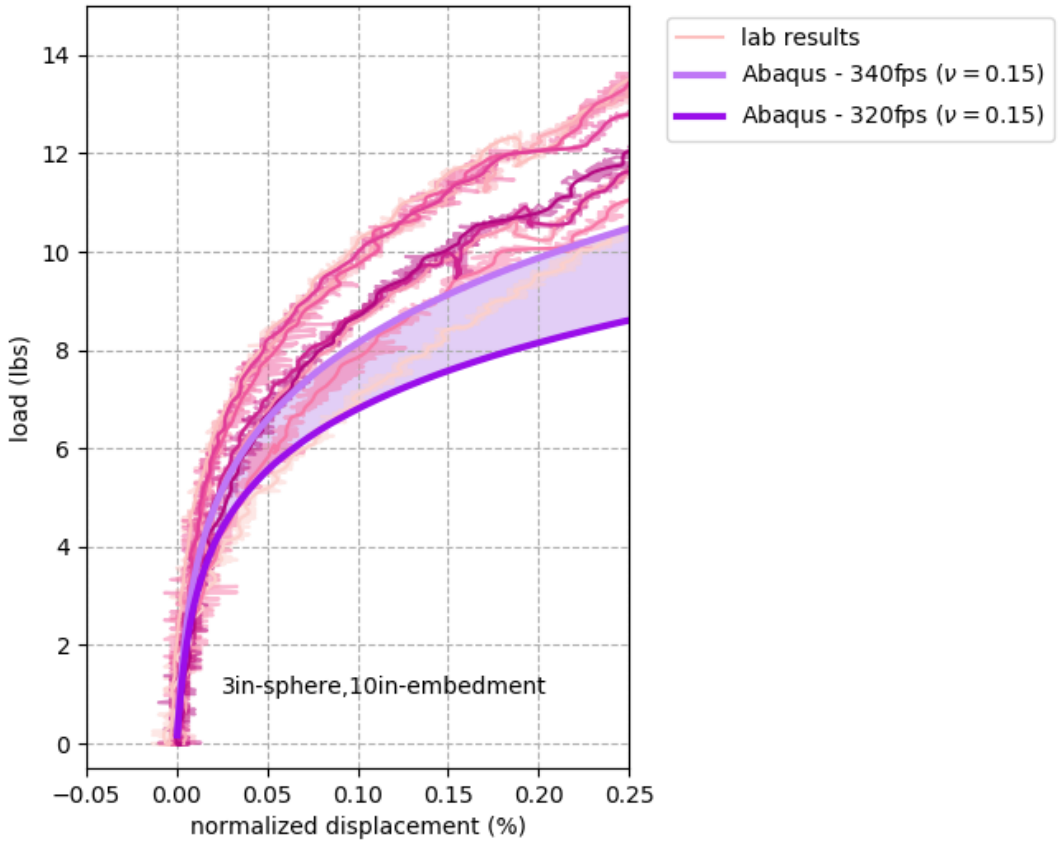

Figure 5.36: Comparison between measured and predicted load-displacement curves for 3-inch sphere at embedment depth of 10 inches. (Soil Profile – #1).

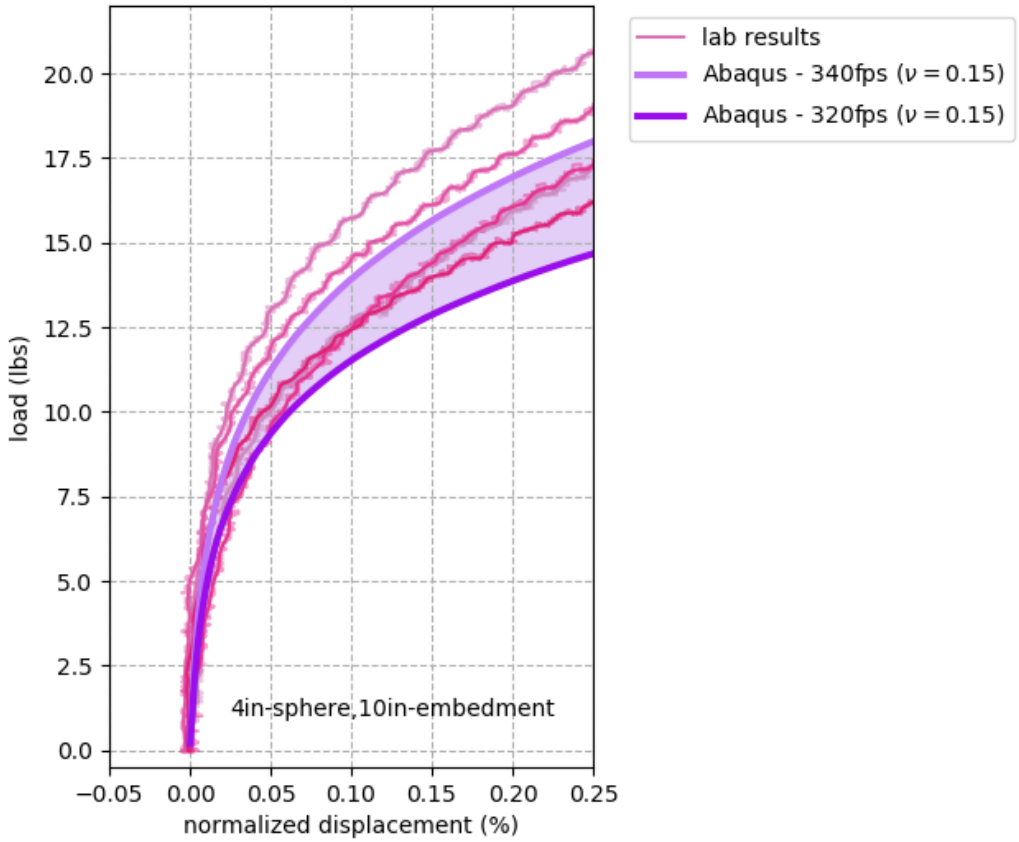

Figure 5.37: Comparison between measured and predicted load-displacement curves for 4-inch sphere at embedment depth of 10 inches. (Soil Profile – #1).

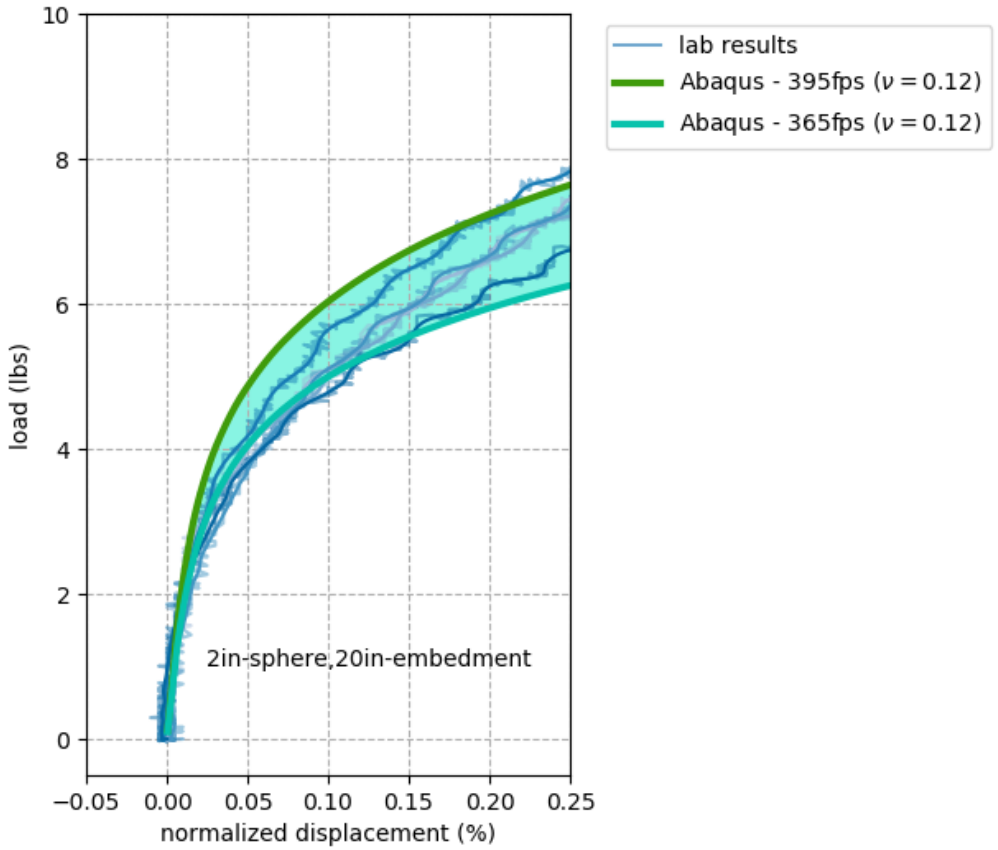

Figure 5.38: Comparison between measured and predicted load-displacement curves for 2-inch sphere at embedment depth of 20 inches. (Soil Profile – #2).

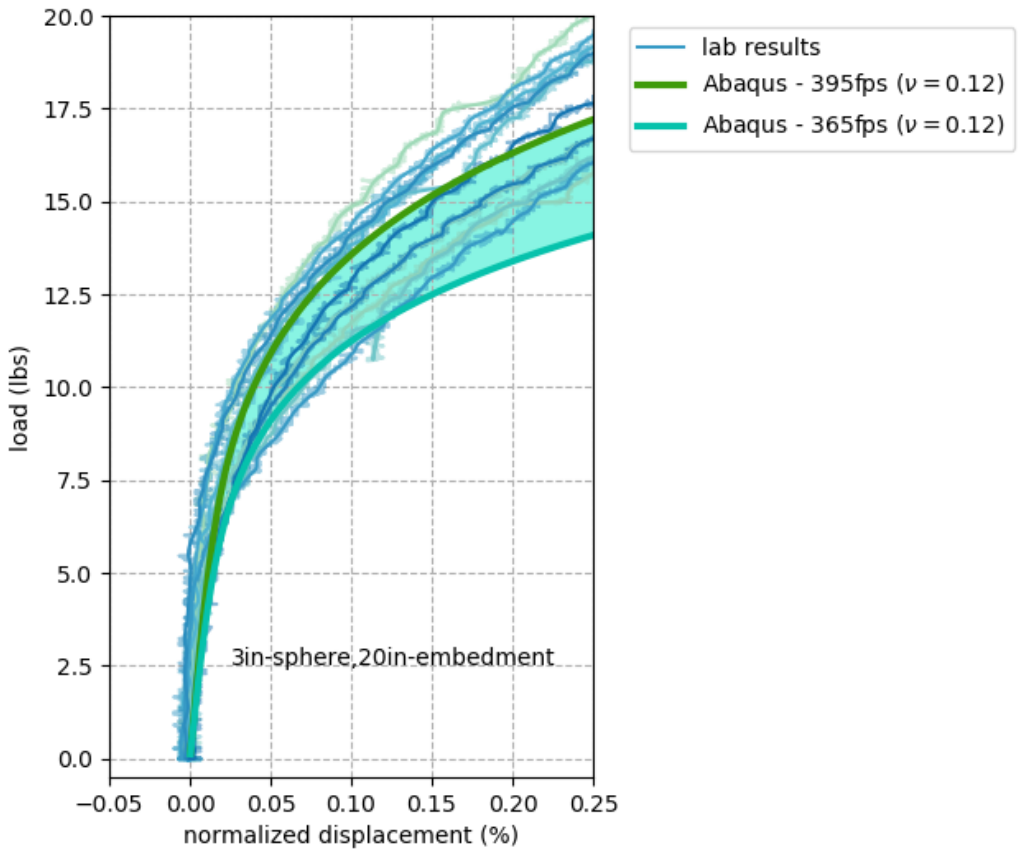

Figure 5.39: Comparison between measured and predicted load-displacement curves for 3-inch sphere at embedment depth of 20 inches. (Soil Profile – #2).

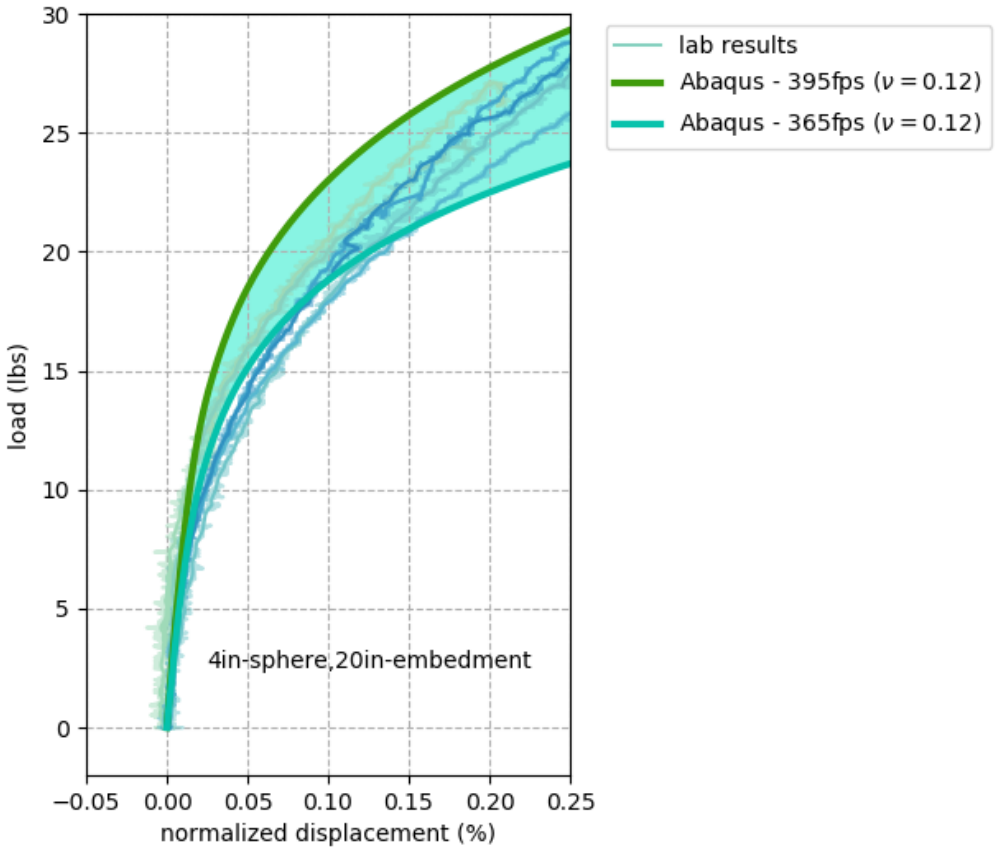

Figure 5.40: Comparison between measured and predicted load-displacement curves for 4-inch sphere at embedment depth of 20 inches. (Soil Profile – #2).

Figures 5.41 to 5.46 show the comparison of the third and fourth sets between the predicted and measured results for the varying sphere diameters at embedment depths of 10 inches and 20 inches. As shown in the figures, the predicted results are also sensitive to Poisson's ratio. The predicted extracted from the 3-D FEM models have a good agreement with the measured results in the lateral push tests.

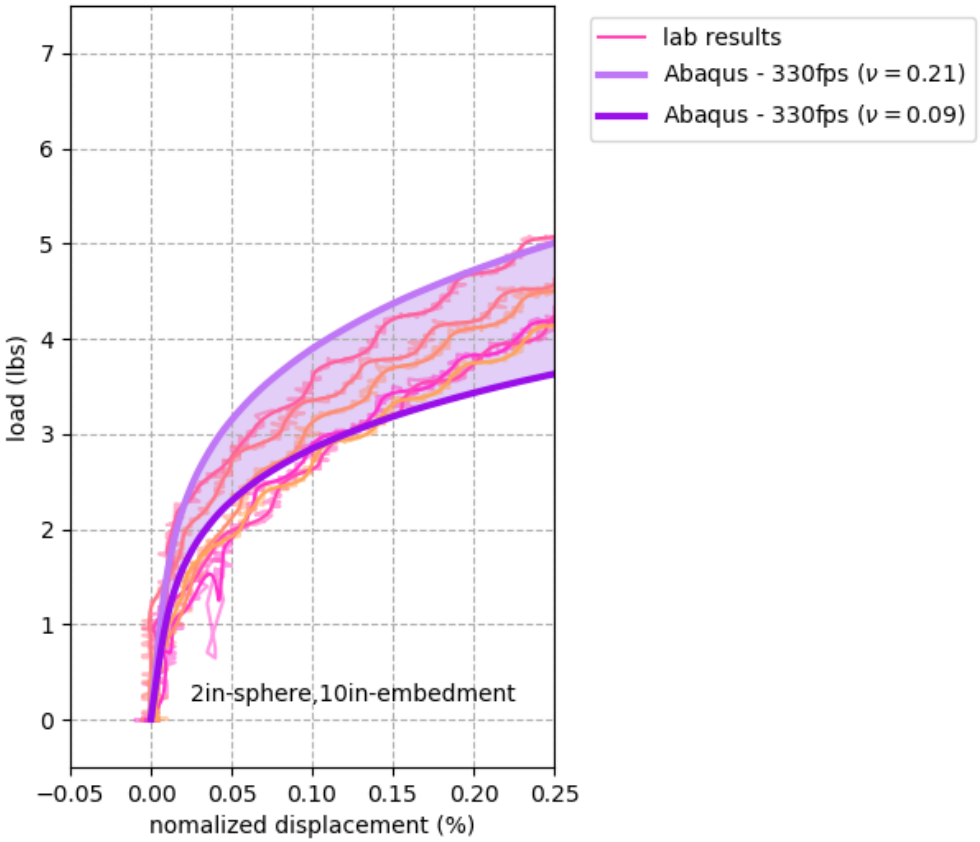

Figure 5.41: Comparison between measured and predicted load-displacement curves for 2-inch sphere at embedment depth of 10 inches. (Soil Profile – #3).

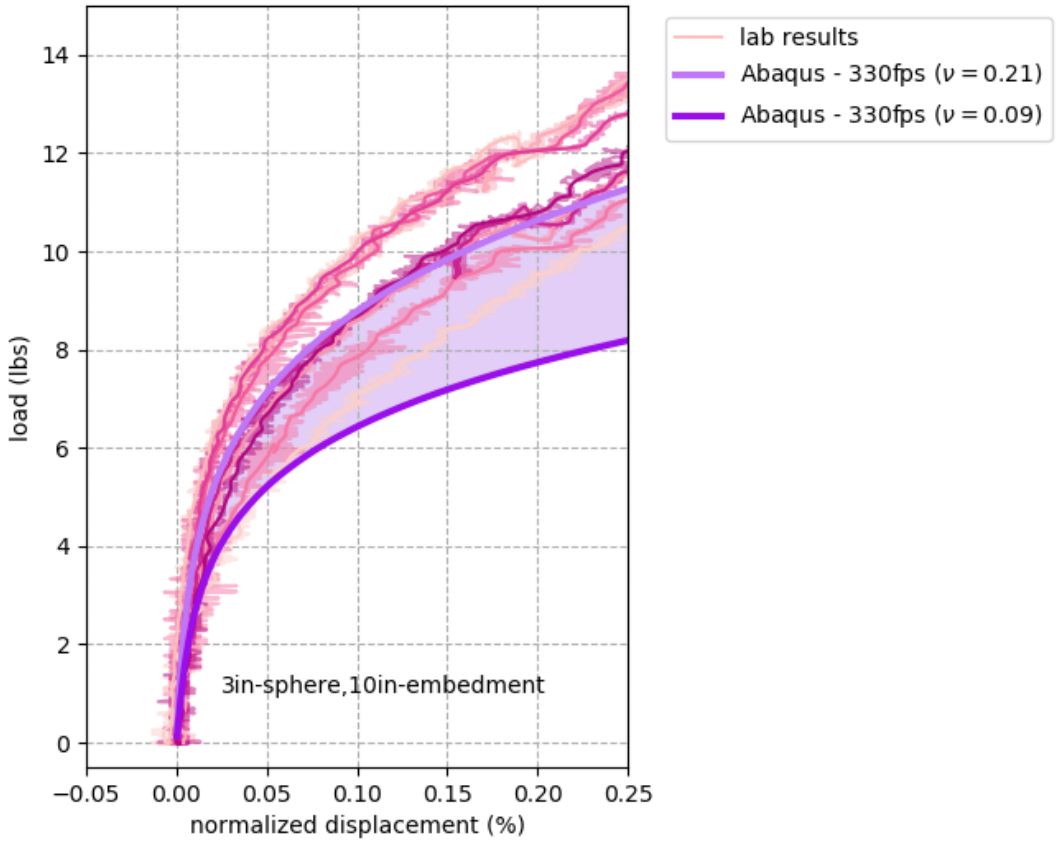

Figure 5.42: Comparison between measured and predicted load-displacement curves for 3-inch sphere at embedment depth of 10 inches. (Soil Profile – #3).

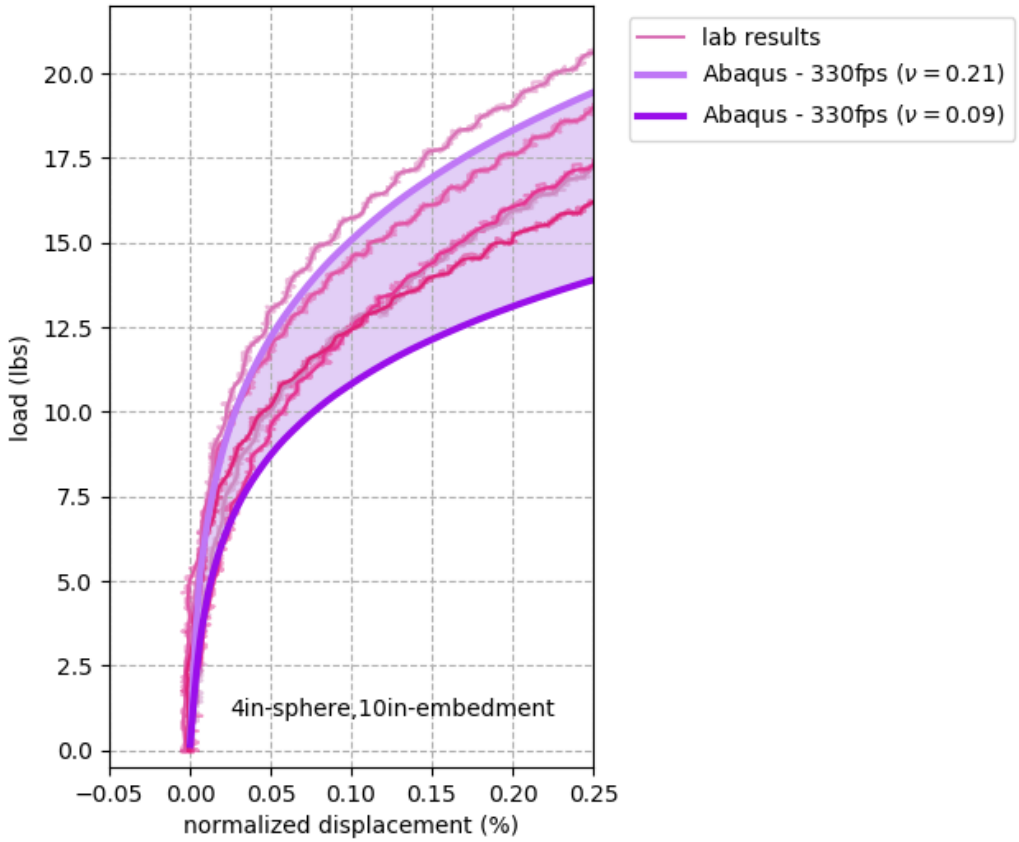

Figure 5.43: Comparison between measured and predicted load-displacement curves for 4-inch sphere at embedment depth of 10 inches. (Soil Profile – #3).

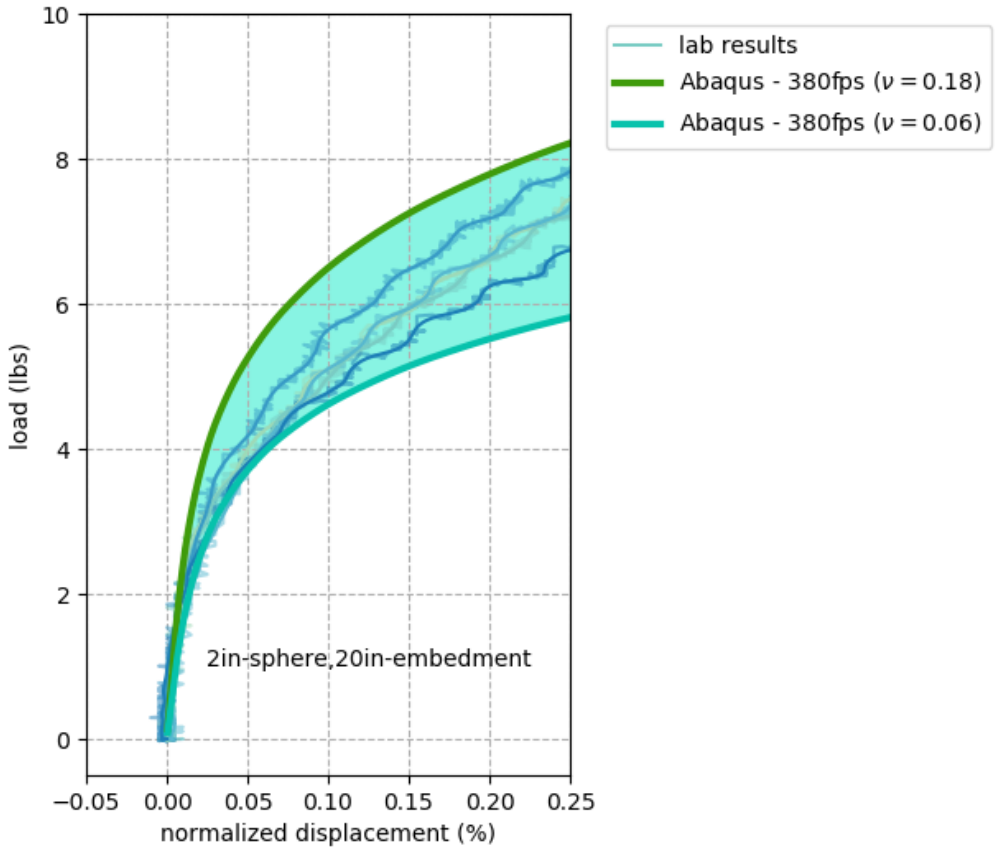

Figure 5.44: Comparison between measured and predicted load-displacement curves for 2-inch sphere at embedment depth of 20 inches. (Soil Profile – #4).

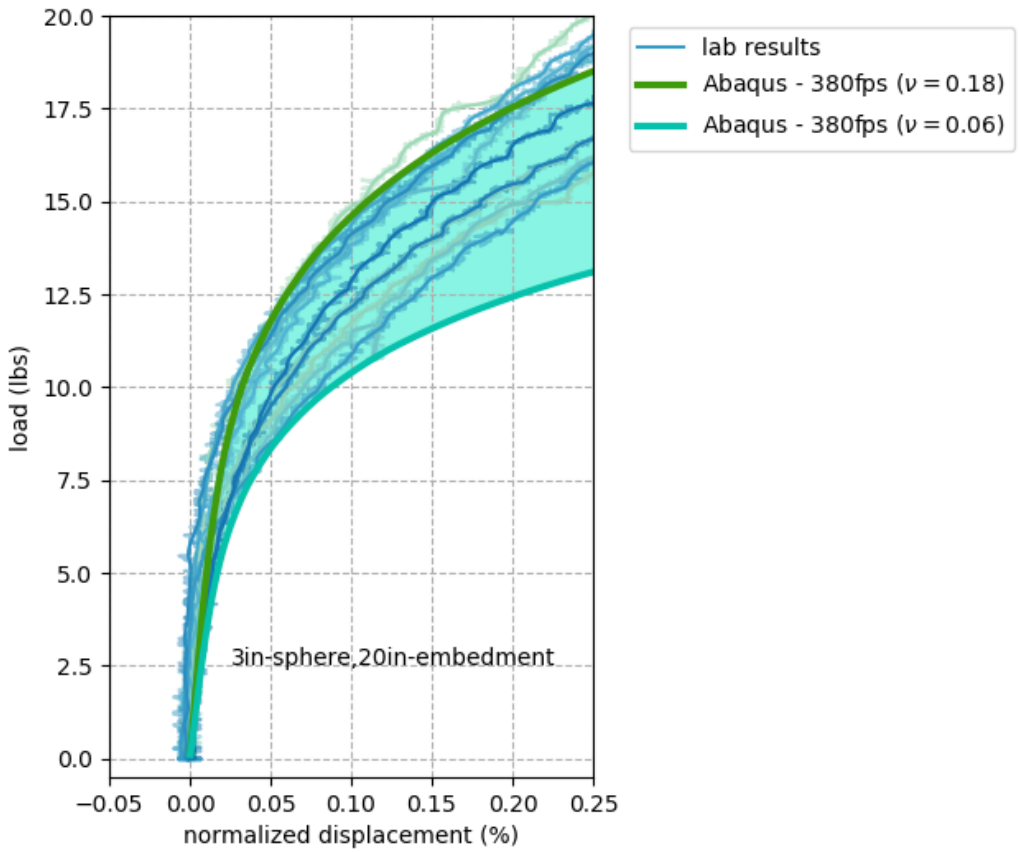

Figure 5.45: Comparison between measured and predicted load-displacement curves for 3-inch sphere at embedment depth of 20 inches. (Soil Profile – #4).

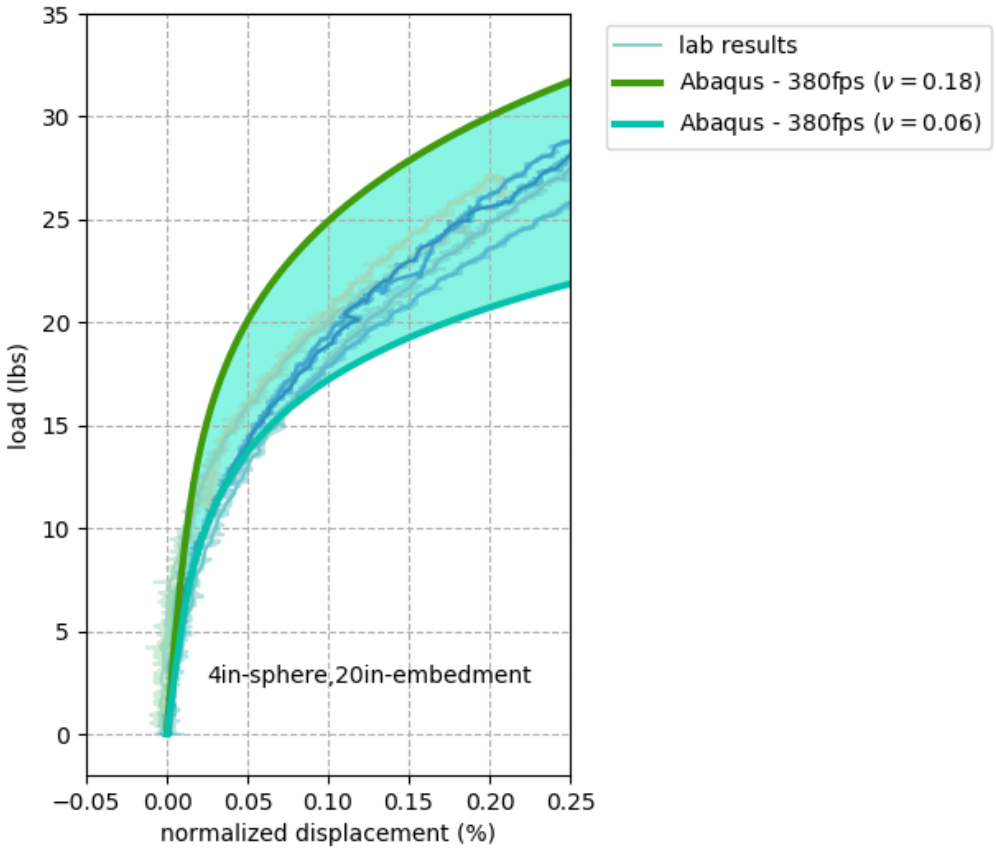

Figure 5.46: Comparison between measured and predicted load-displacement curves for 4-inch sphere at embedment depth of 20 inches. (Soil Profile – #4).

To study the influence of the friction between the sphere and the sand on the predicted curve by using 3-D FEM model, a contact friction coefficient was added on the analysis of the lateral loaded sphere with the diameter of 4 inches and the embedment depth of 10 inches. The contact friction coefficient was equal to 0.46. The slip distance was assumed to be 0.1 inches which was suggested by API RP 2GEO (2014). Figure 5.47 shows the function of the contact friction coefficient with the slip distance.

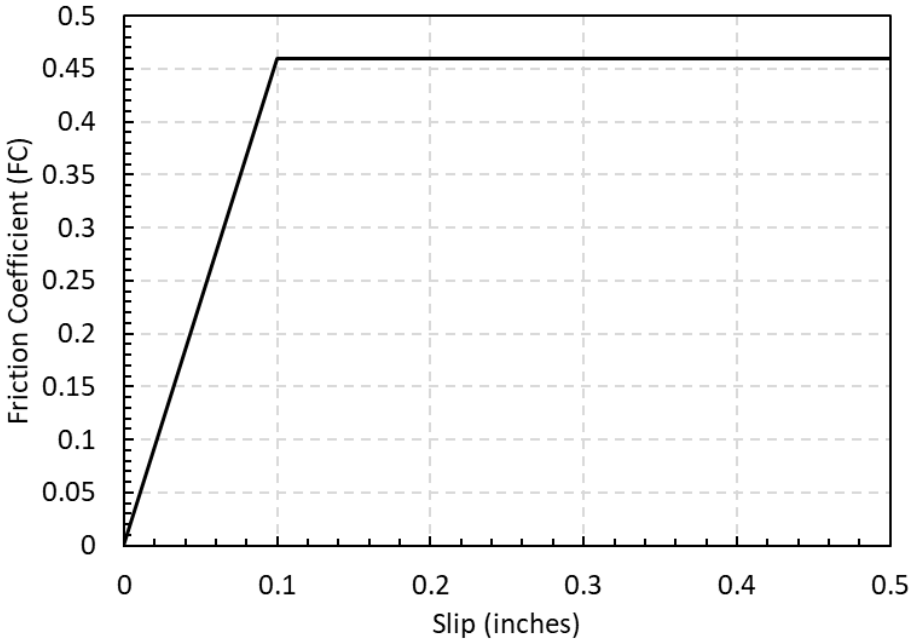

Figure 5.47: Function of contact friction coefficient with the slip distance for lateral loaded sphere test.

Figure 5.48 shows the predicted lateral load versus displacement curves up to 1% of the diameter of the 4-inch sphere with 10-inch embedment depth when the interface between the sphere and the sand is frictionless. At relatively large displacements, the 3-D FEM model underestimates the lateral load needed to push the sphere.

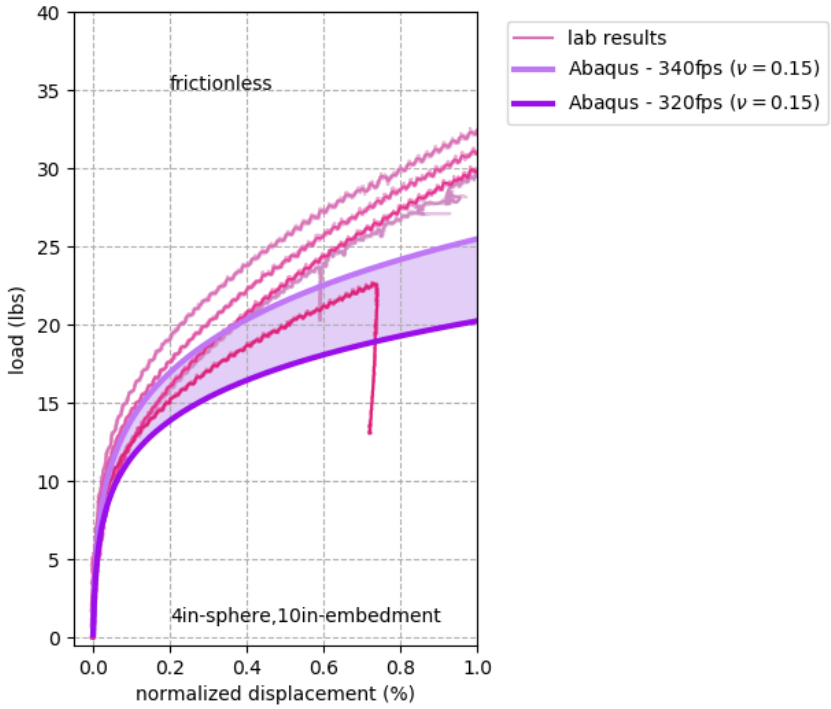

Figure 5.48: Comparison of lateral load versus displacement curves from measurement and prediction using 3D - FEM model of 4-inch diameter sphere with embedment depth of 10 inches (frictionless, 1% diameter displacement).

Figures 5.49a and 5.49b show the predicted lateral load versus displacement curves up to 0.25% and 1% of the diameter of the 4-inch sphere respectively, with the contact friction coefficient in Figure 5.47. The friction makes the predicted lateral loaded versus displacement curve closer to the measured curve, compared to the frictionless condition.

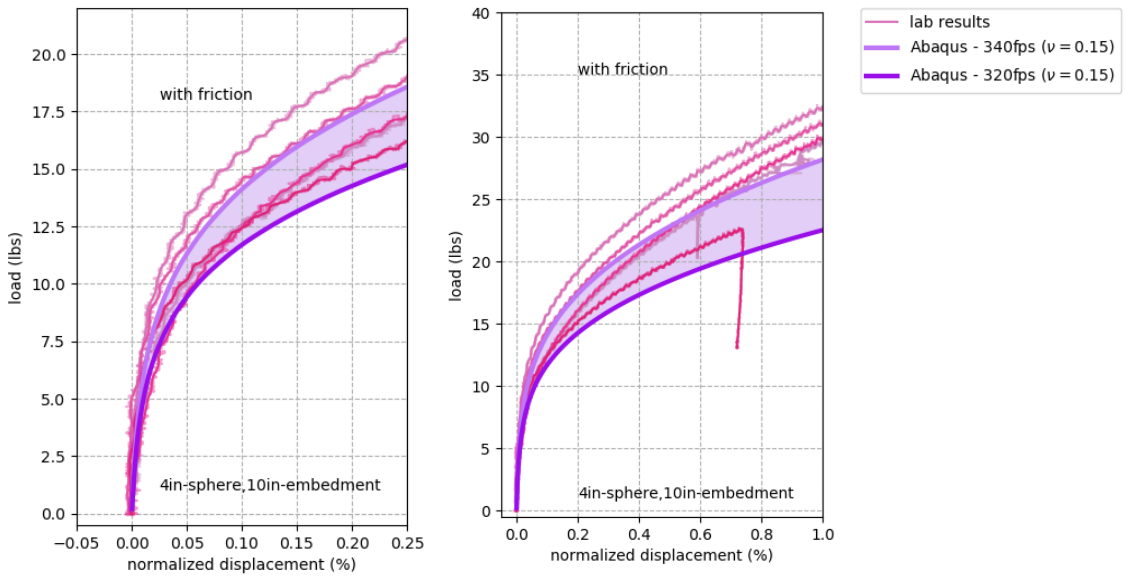

(a) (b)

Figure 5.49: Comparison of lateral load versus displacement curves from measurement and prediction using 3D - FEM model of 4-inch diameter sphere with embedment depth of 10 inches (friction coefficient of 0.46, (a) 0.25% diameter and (b) 1% diameter displacement).

Figure 5.50 shows the influence of the friction coefficient on the predicted lateral load versus displacement curves using 3-D FEM models. The magnitude of friction coefficient has little influence on the response curves at small displacements (less than 0.25% diameter). The predicted lateral load increases with the friction coefficient at large displacement (around 1% diameter), which makes the predicted response curve has a better match with the measured curves.

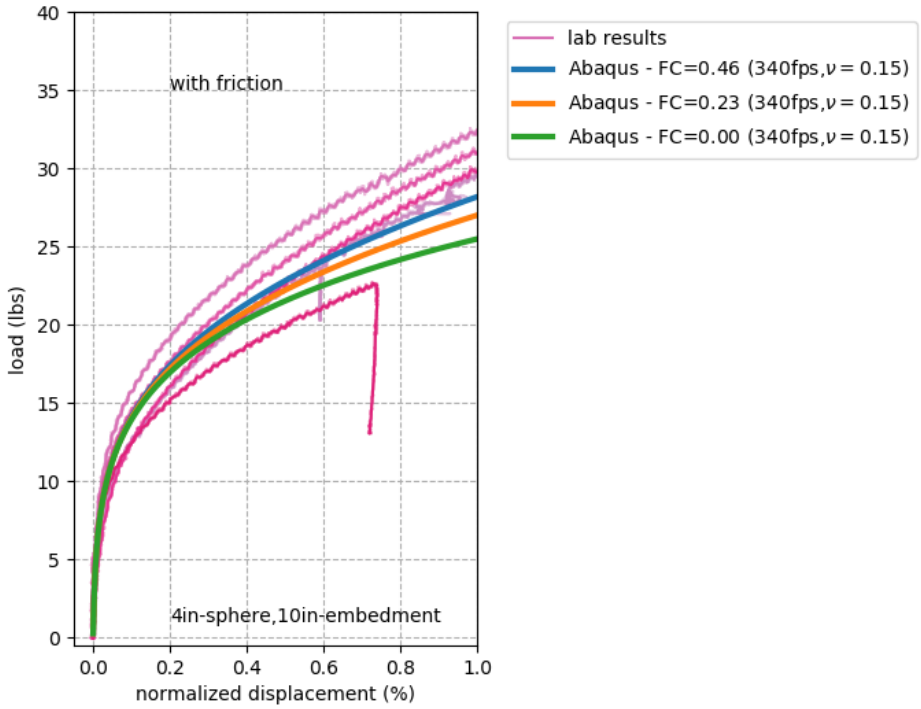

Figure 5.50: Sensitivity analysis of the friction on the lateral load versus displacement curves predicted by using 3D - FEM model of 4-inch diameter sphere with embedment depth of 10 inches ($V_s = 340fps$, 1% diameter displacement).

The results of comparison illustrate that the 3-D FEM model is able to predict the response of a lateral push on the sphere embedded in sand at small displacements by (1) measuring the small-strain properties of the sand and (2) modifying the input parameters for the proposed constitutive model correctly. An accurate measurements of shear velocity and Poisson's ratio are important for a precise prediction using 3-D FEM model at small displacements. For large displacement, a reasonable friction coefficient needs to be assumed.

5.7 PROCEDURE OF USING SOIL CONSTITUTIVE MODEL

In 3-D FEM model, to better simulate the behavior of the sand and the interaction between the structure and the sand, the following procedure is recommended:

1) Measure the shear velocity versus depth profile in the field by using field tests (i.e., SASW, SCPT, and geophone tests) and estimate the density of the in-situ sand.
2) Obtain the relationships of $\log G_{max} - \log \sigma_0$ and $G/G_{max} - \log \gamma$ at small strains (i.e., $\gamma < 0.1\%$) from the resonant column and torsional shear (RCTS) tests on the sand with the same density estimated from the field .
3) Obtain the relationship of stress and strain at large strains (i.e., $\gamma > 2\%$) from the conventional triaxial compression tests on the sand with the same density estimated from the field.
4) Determine the input parameters (C_{G1}, n_g, C_1, C_2, C_3, C_4) of the soil constitutive model by best-fit the relationships of $\log G_{max} - \log \sigma_0$ and $G/G_{max} - \log \gamma$ at small strains from the RCTS tests.
5) Modify the input parameters (C_1, C_2, C_3, C_4) of the soil constitutive model by matching the relationship of stress and strain at large strains from the triaxial compression tests.
6) Modify the input parameters (C_{G1}, α_a, α_b, α_c) of the soil constitutive model to match the shear velocity versus depth profile measured in the field.
7) Establish the 3-D FEM model according the dimensions of structure and the conditions of the boundary in the field.
8) Use the subroutine of the constitutive model define the material of the sand in the 3-D FEM model.

5.8 CONCLUSIONS

The major conclusions from the laboratory foundation model tests are as follows:

1) The method developed for preparing a sand bed is repeatable and reliable when conducting lateral push tests.
2) The initial relationship between the lateral load and lateral displacement in the model tests is non-linear, even at very small displacements.
3) Numerical modeling using the 3-D FEM model with the proposed constitutive model using the measured properties of the sand produces results that agree well with the measurements in the lateral push tests. An accurate measurements of shear velocity, Poisson's ratio, and friction coefficient are important for a precise prediction using 3-D FEM model.

Chapter 6: Comparisons of the Measurements from Field Tests with the Numerical Modeling Predictions

The objectives of the analysis on the field tests were:

1) Repeat and verify the procedure of modifying the input parameters of the proposed soil constitutive model, which is suggested in the section of laboratory foundation model test.
2) Verify the performance of the 3-D FEM model of predicting the small-strain behavior of the sand in the problem of a full-scale pile driven in sand.

Two field tests were analyzed using the 3-D FEM models with the proposed soil constitutive model: (1) settlement tests on shallow foundations at NGES test site and (2) lateral load tests on slender piles on Mustang Island. 3-D FEM models with the proposed soil constitutive model were established based on the description of the field set-up, soil investigation of the test site, shear wave velocity measurement at the test site, and the laboratory tests on the soil collected from the field. The results of the 3-D FEM model agreed well with the field measurements.

6.1 NGES PROJECT – SHALLOW FOUNDATION

At the National Geotechnical Experimentation Site (NGES) at Texas A&M University (Figure 6.1), two small-scale footings were constructed to create a dataset of load-settlement curves of footings on granular soil. The two small-scale footings were circular reinforced concrete footings with diameters of 3.0 ft and 1.5 ft and thickness of 1.0 ft. The loads on the footings were applied by a hydraulic jack reacting against the weight of a truck, 'T-Rex'. A load cell was installed between the hydraulic jack and the footing to measure the load. A Displacement transducer was placed on the reference frames near the

footings to measure the settlement. Figure 6.2 shows the photos of the load-settlement tests conducted at the NGES sand site. Kacar (2014) did the load-settlement analysis on these small-scale footings by implementing the subroutine developed based on Menq (2003) and Benz (2007) in the finite element program, PLAXIS. In this study, the load-settlement response of the small-scale footings was estimated by the 3-D FEM model with the proposed constitutive model in Abaqus to compare to the results measured in the field.

Figure 6.1: Location of NGES test site.

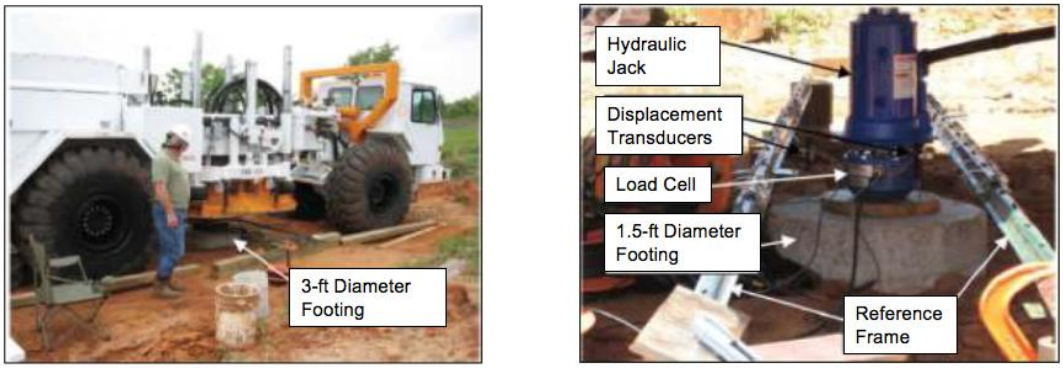

(a) (b)

Figure 6.2: Load-settlement tests at NGES sand site: (a) T-Rex loading the 3-ft diameter footing, (b) set-up of the instrumentation to load and measure the settlement of the 1.5-ft diameter footing (Kacar, 2014).

An investigation of the field site was reported by Braud and Gibbens (1994), which included the soil profile, index properties of the soil, triaxial compression tests on reconstructed samples, etc. The shear wave velocity versus depth profile (V_s profile) was evaluated by field measurement using SASW tests by Park et al. (2009). The relationships of $\log G_{max} - \log \sigma_0'$ and $G/G_{max} - \log \gamma$ were given by the RCTS tests conducted on undisturbed samples at The University of Texas at Austin. This information could be used to modify the input parameters of the soil constitutive model in the 3-D FEM model.

6.1.1 Field Investigation and Soil Properties – NGES Tests

The general field investigation on the NGES test sites was conducted by Briaud and Gibbens (1994), which included SPT, CPT, and laboratory tests on the samples obtained using a drilling rig. The soil at the NGES site was predominantly sand extending to a depth of 36 ft. The sand in the upper 11.5 ft was medium dense and classified as SP-CM in the USCS. Under the layer of medium dense sand, another layer of sand was mixed with clay and gravel. From the depth of 23 ft to 36 ft, the soil turned from silty sand to sandy clay. Beneath the layer of sandy clay, the soil was formed by hard clay which could be ignored in the analysis of the field load-settlement tests. Figure 6.3 shows the soil types and layer depths at the NGES test site. The first layer of 11.5 ft thick layer of SP-SM material had a water content of 12 to 14%, a total unit weight of approximate 126 pcf, and a friction angle of 34 to 36 degrees.

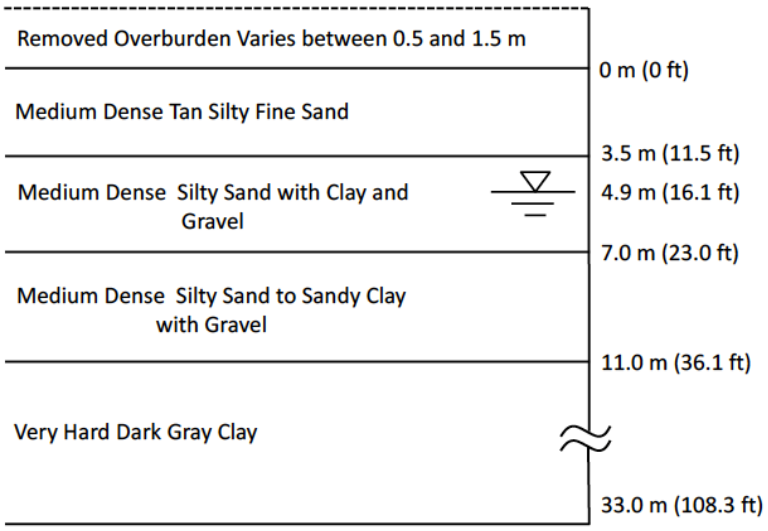

Figure 6.3: Soil types and layer depths at the NGES test site at Texas A&M University (Kacar, 2014).

The V_s profile of the NGES test sites was measured by Spectral-Analysis-of-Surface-Wave (SASW) tests performed by Park et al. (2009) along three lines around the two footings. Figure 6.4 shows the best-estimated V_s depth profile based on the average of three SASW tests. From Figure 6.4, the shear wave velocities at shallow depths were considerably higher than those of a normally consolidated sand, which indicated that negative pore water pressure (capillary stresses) might exist in the sand at shallow depths.

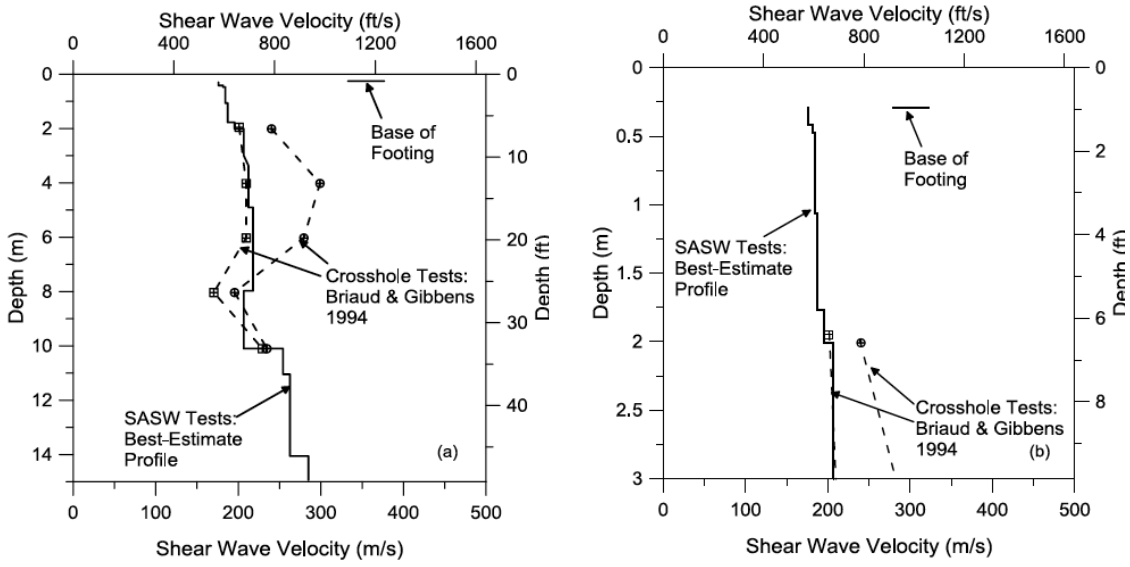

(a) (b)

Figure 6.4: V_s profiles at the NGES sand site (a) to a depth of 49 ft and (b) expanded to show the top 10 ft (Park et al., 2009).

The RCTS tests were conducted on intact specimen obtained at the NGES test site. The specimen was classified as silty sand (SM) with total unit weight of 126.6 pcf and water content of 9.9%. Figure 6.5(a) shows the relationship of $log\, V_s - log\, \gamma$ following the format of Equation 6.1. The slope of the $log\, V_s - log\, \gamma$ relationship, n_s, was 0.15, which was smaller than the range of 0.23 to 0.26 of n_s for uncemented sand in normally consolidated condition. It indicated a cementation of the silty sand in the field. Figure 6.5(b) shows the relationship of $G/G_{max} - log\, \gamma$ for the NGES sand obtained from the RCTS tests.

$$V_s = A_s\left(\frac{\sigma_0'}{P_a}\right)^{n_s} \tag{6.1}$$

where A_s is the shear velocity at an mean effective stress of one atmosphere, P_a is the pressure of one atmosphere.

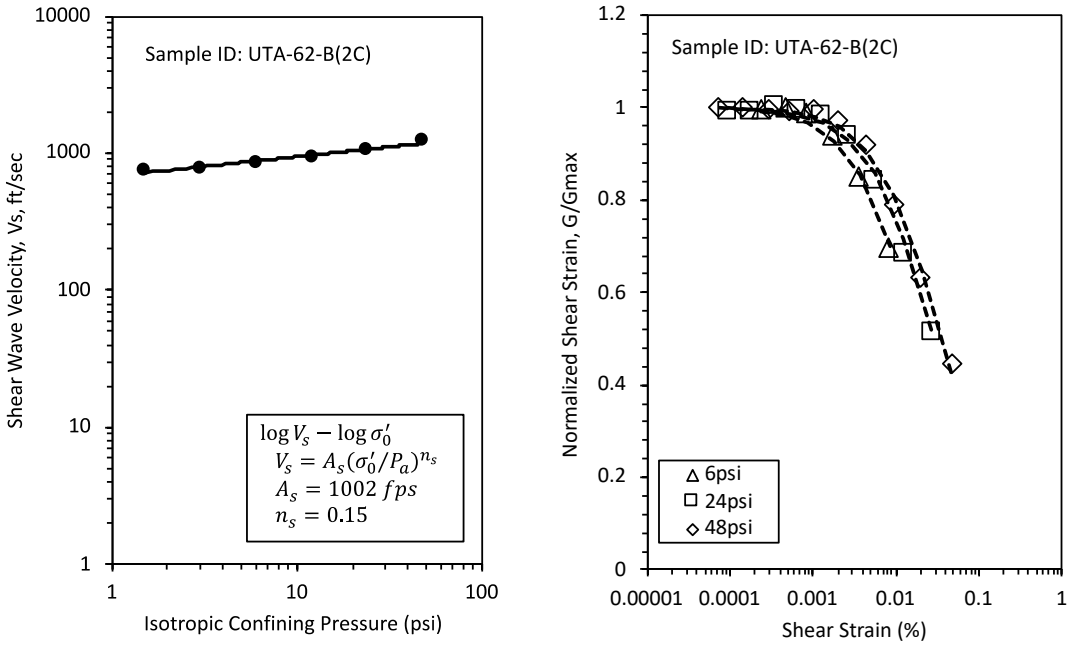

(a) (b)

Figure 6.5: (a) $log\, V_s - log\, \sigma_0'$ relationships for the NGES test site and (b) $G/G_{max} - log\, \gamma$ relationships for the NGES test site obtained from RCTS tests (adapted from Kacar, 2014).

Figure 6.6 shows the results of the triaxial compression (TRX) tests performed on the reconstituted specimens from depth of 10.0 ft at the NGES test site. The specimens were reconstructed to have similar relative density and water content with the in-situ sand. The diameter of the reconstituted specimens was 1.5 inch and height of it was 3.2 inch. The TRX tests were Consolidated/Drained triaxial tests under three different confining pressures: 5 psi, 20 psi, and 50 psi (Braud and Gibbens, 1994).

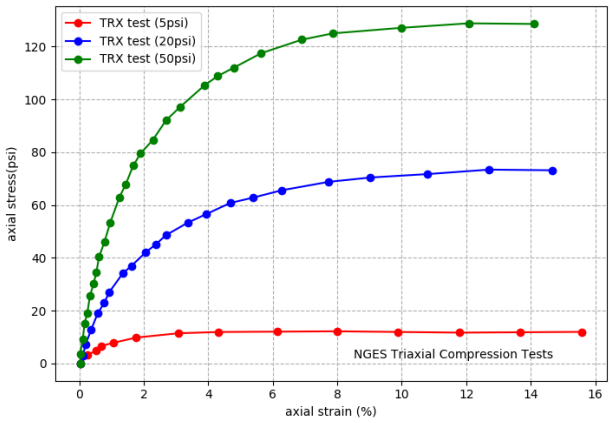

Figure 6.6: TRX tests on the NGES sand (adapted from Braud and Gibbens, 1994).

6.1.2 Modification on the Input Parameters – NGES Tests

Table 6.1 shows the input parameters of the NGES sand determined by RCTS tests on undisturbed specimen. To convert the relationship of $log\, V_s - log\, \sigma_0'$ in the Figure 6.5a to the relationship of $log\, G_{max} - log\, \sigma_0'$, the maximum shear modulus, G_{max}, could be found by:

$$G_{\max} = V_s^2 \times r \tag{6.2}$$

where ρ is the total mass density of the soil. The parameters C_{G1} and n_g (Equation 4.6) were calculated by best-fitting the relationship of $log\, G_{max} - log\, \sigma_0'$ obtained from RCTS tests (Figure 6.7a). The parameters C_1, C_2, C_3,and C_4 (Equations 5.4 and 5.5) were calculated by best-fitting the relationship of $G/G_{max} - log\, \gamma$ from RCTS tests at small strains (Figure 6.7b).

Table 6.1: Input parameters of the NGES sand based on best-fitting the RCTS tests.

C_{G1} (psi)	n_G	C_1 (%)	C_2	C_3	C_4	$\alpha_1, \alpha_2, \alpha_3$
27142	0.32	0.024	0.321	1.092	0.0	0.001

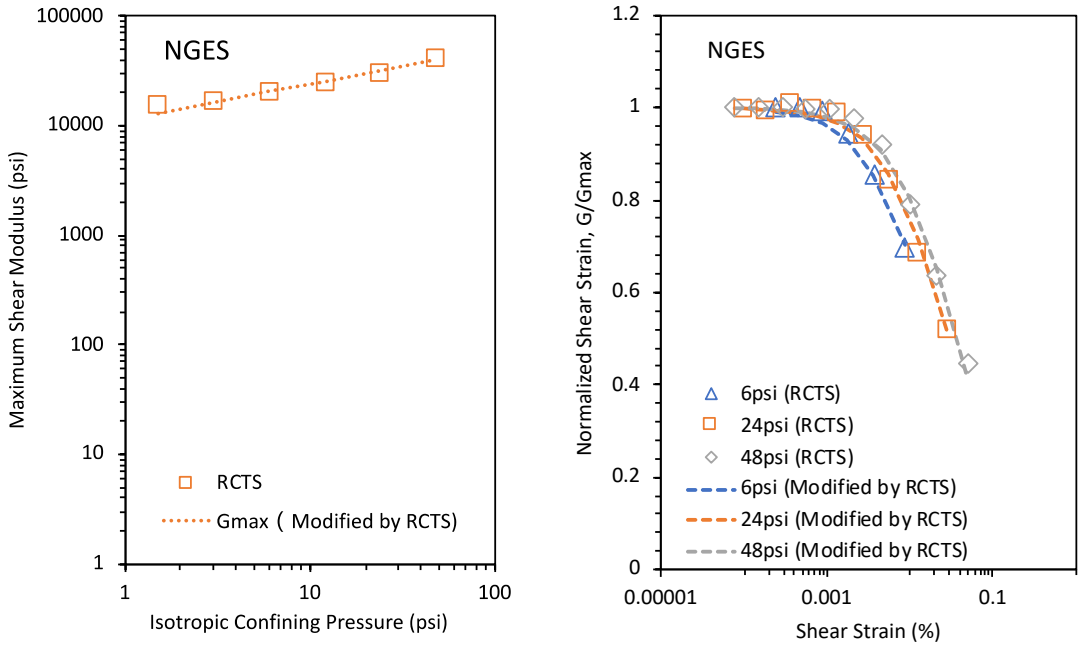

(a) (b)

Figure 6.7: (a) Numerical relationships of $log\ G_{max} - log\ \sigma_0'$ and (b) $G/G_{max} - \log \gamma$ based on input parameters best-fitting the RCTS tests on the NGES sand.

Figure 6.8 shows the comparison of the stress versus strain curves obtained between the TRX tests and the numerical simulation of 3-D FEM model using the input parameters best-fitting the RCTS results (Table 6.1). The numerical simulation highly underestimated the stiffness of the soil when strain was larger than 0.1%.

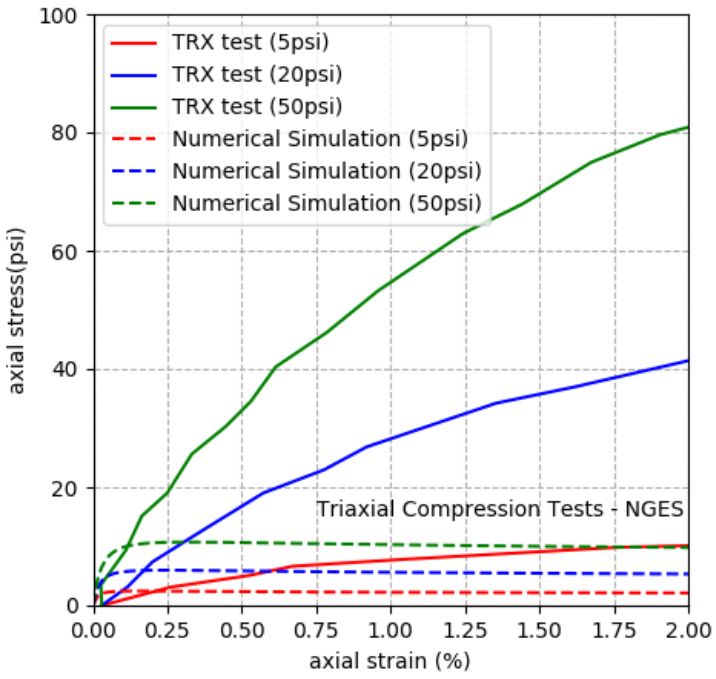

Figure 6.8: Comparison of the stress versus strain curves measured by TRX tests and the predicted based on the input parameters best-fitting the RCTS tests on the NGES sand.

The input parameters modified based on the TRX tests are summarized in Table 6.2. The parameters, C_{G1} and n_g, were kept the same as the values determined by RCTS tests. The modification was governed by two considerations. The first consideration was attempting to have a good agreement between the results of triaxial compression tests and the numerical simulation at strains from 1% to 2%. The second consideration was, when the first consideration was satisfied, making the relationships of $G/G_{max} - log\,\gamma$ still have reasonable agreements between the results of RCTS tests and the numerical simulation at small strain ($\gamma < 0.1\%$). The input parameters in Table 6.2 tried the best to capture to two considerations into the modification. Figure 6.9 shows the comparison of

stress versus strain curves from the TRX tests and numerical simulation and Figure 6.10 shows the relationships of $G/G_{max} - log\,\gamma$ after the modification.

Table 6.2: Input parameters of the NGES sand modified by TRX tests.

$C_{G1}\,(psi)$	n_G	C_1 (%)	C_2	C_3	C_4	$\alpha_1, \alpha_2, \alpha_3$
27142	0.32	0.035	0.32	0.75	-0.2	0.001

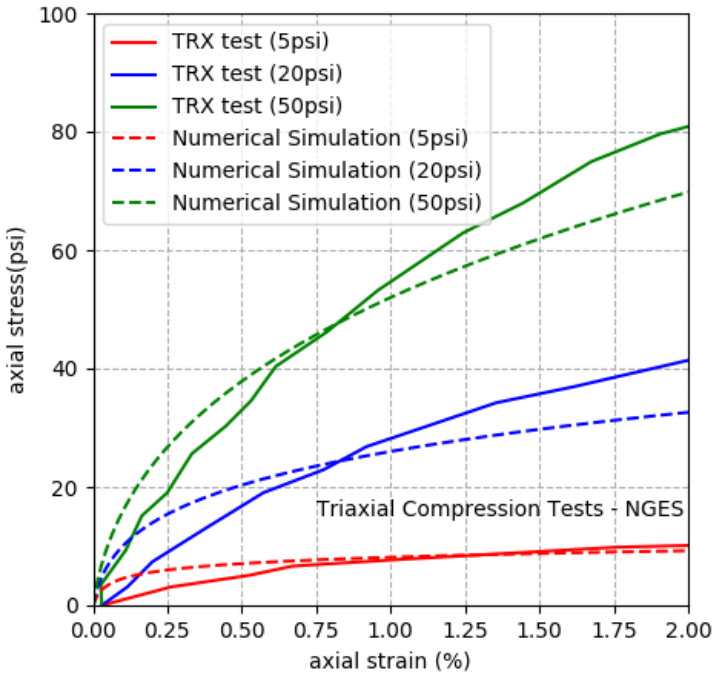

Figure 6.9: Comparison of the stress versus strain curves measured by TRX tests and predicted based on the input parameters modified by the TRX tests on the NGES sand.

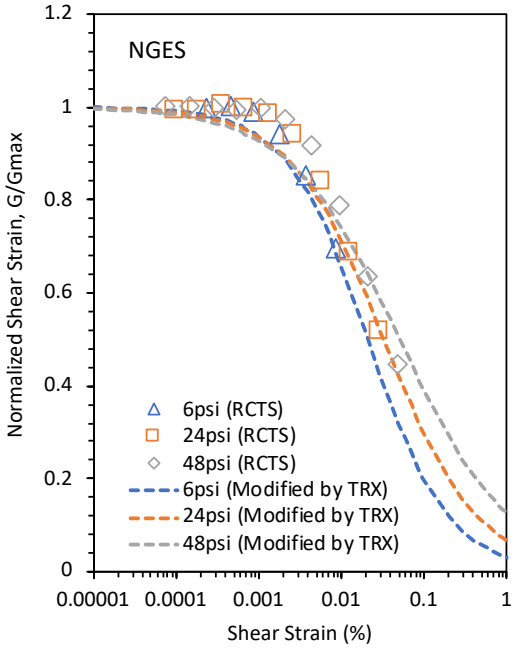

Figure 6.10: Numerical relationship of $G/G_{max} - \log\gamma$ based on input parameters modified by the TRX tests on the NGES sand.

Figure 6.11 shows the comparison of the V_s profiles between the results of SASW tests and the numerical simulation using Equations 7.1 and 7.2 with input parameters modified by the TRX tests (Table 6.2). The vertical effective stress, σ'_v, was calculated using the average total unit weight at the site which was 126 pcf. The Poisson's ratio was assumed to be 0.3. The numerical simulation using input parameters modified by the TRX tests (Table 6.2) overestimated the shear wave velocity measured in the field.

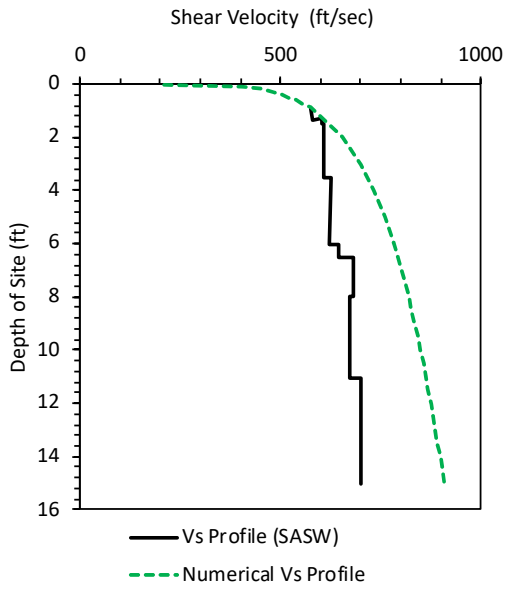

Figure 6.11: Comparison of the V_s profiles measured by the SASW tests and predicted by the input parameters modified by the TRX tests.

Table 6.3 represents the input parameters modified by matching the V_s profile suggested by Kacar (2014). The parameters C_{G1} and n_g were modified and a negative pore water pressure of 2 psi was assumed to make the numerical simulation match the V_s profile better at shallower depths. Figure 6.12 shows the V_s and G_{max} profiles from the SASW tests and the prediction using the input parameters in Table 6.3.

Table 6.3: Input parameters of the NGES sand used in 3-D FEM model.

NGES sand		
	First Layer	**Second Layer**
C_{G1}	13938	15076
n_g	0.228	
C_1 (%)	0.035	
C_2	0.32	
C_3	0.75	
C_4	-0.2	
$\alpha_a, \alpha_b, \alpha_c$ (psi)	2	
$\gamma\ (pcf)$	126	
v	0.3	
K_0	0.428	

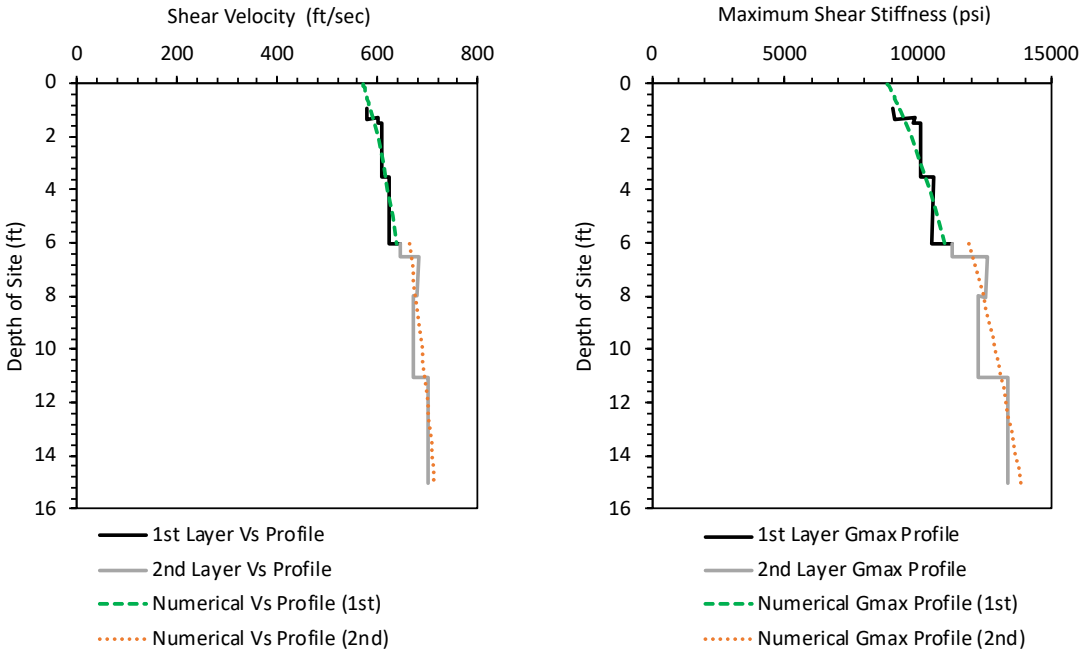

(a) (b)

Figure 6.12: Comparison of (a) the V_s profiles and (b) the G_{max} profiles measured by the SASW tests and predicted by the input parameters modified by the SASW tests.

6.1.3 3-D FEM Model – NGES Tests

Figure 6.13 shows the cross-sectional view of the settlement tests of the small-sale footings. The 3-D FEM models using Abaqus were established to predict the settlements of the footings with diameter of 1.5 ft and 3.0 ft, as shown in Figure 6.14.

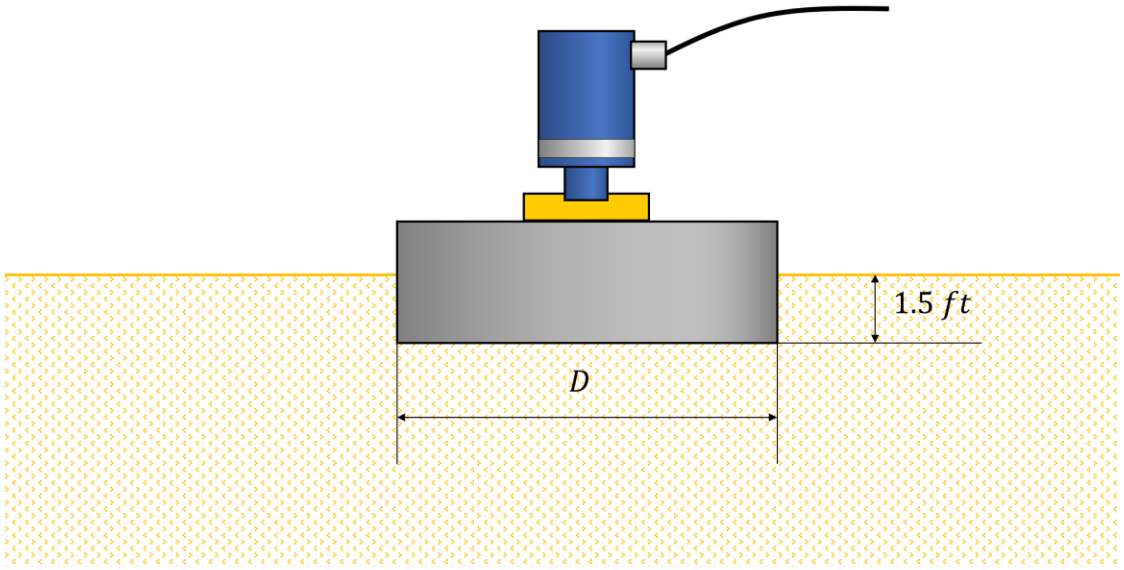

Figure 6.13: Cross-section view of settlement tests on footings at the NGES test site (adapted from Kacar, 2014).

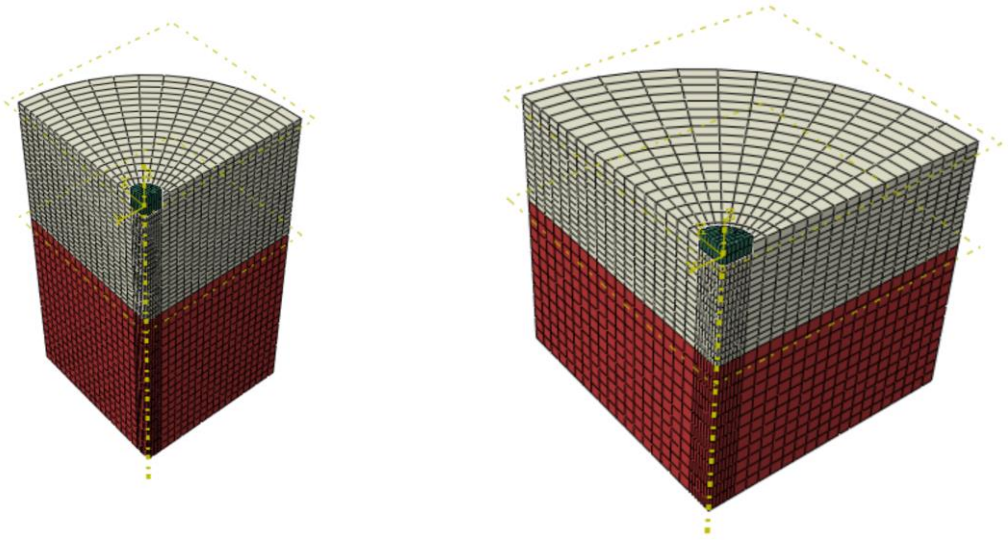

(a) (b)

Figure 6.14: (a) 3-D FEM model of the 1.5-ft footing and (b) 3-D FEM model of the 3.0-ft footing in Abaqus.

Because the symmetry of the footings and the loading system, only 1/4 of the footings and soil were modeled. To eliminate the boundary effects, the soil was modeled as a two layers system with a thickness of 6.0 ft for top layer and 9.0 ft for bottom layer, which was the same as the 2-D FEM model created by Kacar (2014). Horizontally, the soil extended 10 diameters from the edge of the footings with 8-node linear brick elements. The bottom of the model was restrained from the movement along X-, Y-, Z-directions. The face of X-Z plane was restrained from the movement along Y-direction and the face of Y-Z plane was restrained from the movement along X-direction. The boundary of the model which was far away from the footing was restrained from the movements along X- and Y-directions.

The diameter of the footings in the 3-D FEM model was depended on the size of the footings used in the field tests. The bottom of the footing was 0.5 ft beneath the soil surface. The body of the footing was defined as perfect rigid. The interface between the

soil and the footing was assumed as frictionless. A uniform pressure was applied on the top face of the footing.

Figure 6.15 shows the comparison between the measurement and the prediction using 3-D FEM model with soil properties defined by the input parameters modified by the SASW tests (Table 6.3). As seen in the figure, the predicted settlements with the input parameters modified by the TRX tests and SASW tests (Table 6.3) have a reasonable agreement with the measured settlements.

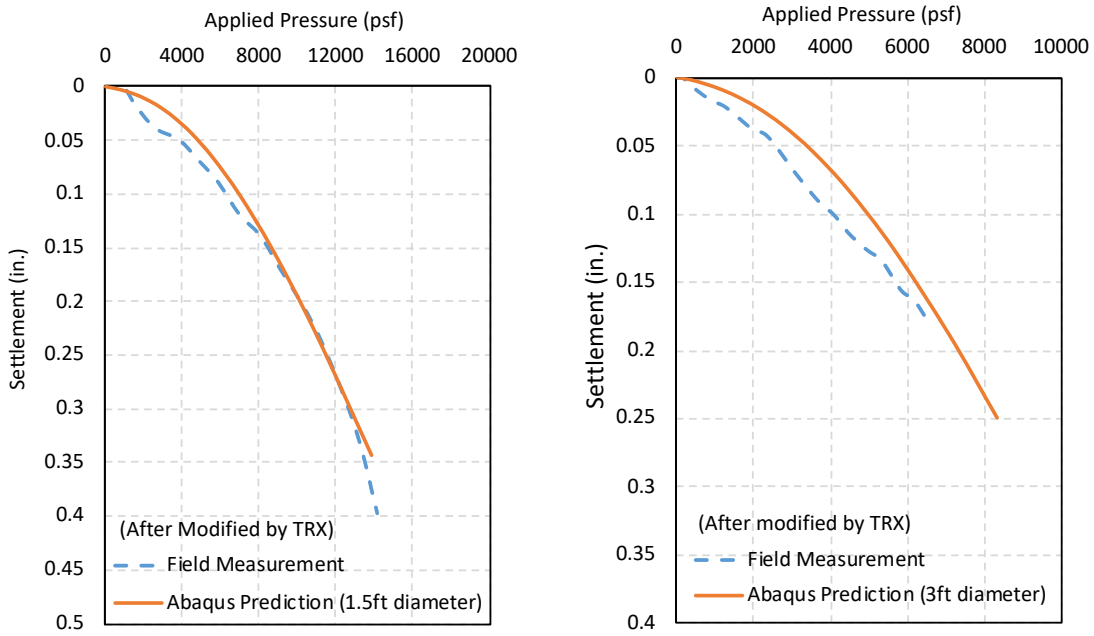

(a) (b)

Figure 6.15: Comparison of the pressure versus settlement curves measured in the field and predicted by the 3-D FEM models using proposed constitutive soil model, (a) 1.5-ft footing and (b) 3.0-ft footing.

6.2 MUSTANG ISLAND TEST – LATERALLY LOADED PILE

This section summarizes the original lateral load tests on the slender piles conducted in 1966 and the additional field investigation performed by UT Austin in 2017. A 3-D FEM model using the proposed constitutive model was established based on description of the lateral load tests, field investigation, and laboratory tests. The results of the 3-D FEM model were compared to the field measured lateral load versus displacement curve and showed good agreement.

6.2.1 Introduction

In the 1966, a series of lateral load tests on two 24-in. long piles in sand were conducted by Cox, Reese, and Grubbs (1974) to develop the conventional p-y curves for the design of laterally loaded piles in sand under static and cyclic loads. Figure 6.16 shows the location of the tests in the northern part of Mustang Island State Park where was a privately held land. Cox, Reese, and Grubbs (1974) conducted two soil borings at the test site where soil consisted of clean fine silty sand and collected the data during the lateral loading of the two piles installed at the site. The conventional p-y methods for sand derived from these field tests became the criteria for the design of laterally loaded piles, which is still being used today.

To supplement the field tests conducted in 1966, additional field investigation was conducted in August 2017 and the laboratory tests were performed on the soil collected from the field. Spectral-Analysis-of-Surface-Waves (SASW) tests were performed at three locations near the original test site. In addition, resonant column (RC) tests were conducted to measure the small-strain and non-linear shear modulus of Mustang Island sand.

Figure 6.16: Location of the test site on Mustang Island.

6.2.2 Field Investigation and Soil Properties

The soil profile at the test site on Mustang Island reported by Cox, Reese, and Grubbs (1974) is shown in Figure 6.17. According to the boring tests at the site, the soil in the top 42 ft was classified as fine sand. The sand from 0 to 20 ft was classified as medium dense, 20 to 70 ft as dense. Figure 6.18 shows the three grain-size distributions of the soil samples recovered from depths of 3, 10, and 15.5 ft, indicates that the cohesionless materials were poorly graded sands. Before the lateral load tests, the site was excavated, so the water table was maintained at the ground surface to simulate conditions which was similar to an offshore condition during the tests. After the completion of the tests, the sand was subsequently back filled.

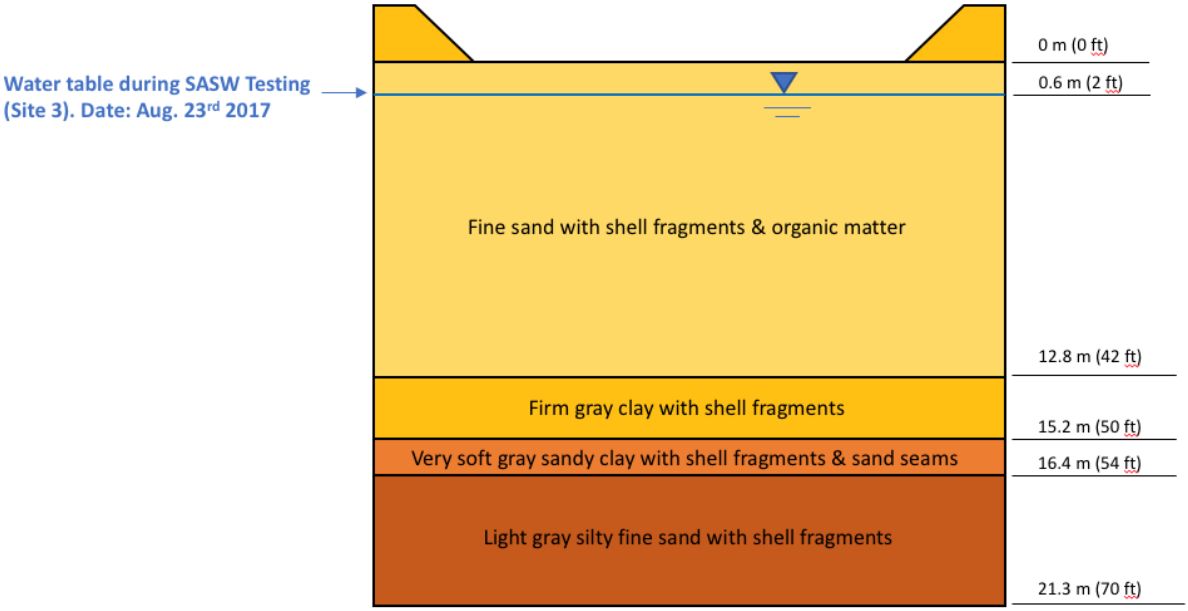

Figure 6.17: Soil types and layer depth at the locations of field testing (adapted from Cox, Reese and Grubbs, 1974).

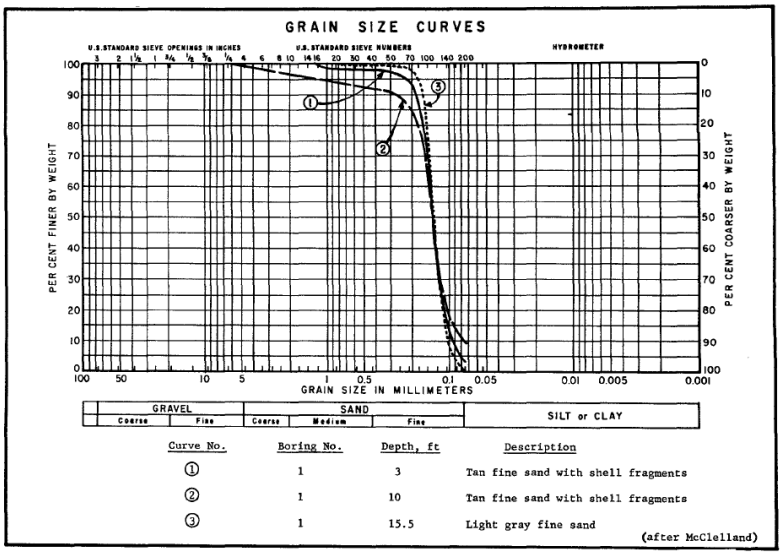

Figure 6.18: Grain-size distribution curves from the samples, depths equal to 3, 10, and 15.5 ft (Cox, Reese and Grubbs, 1974).

Table 6.4: Grain-size distributions of the soil samples of the Mustang Island sand recovered from depths of 3, 10, and 15.5 ft.

	Depth = 3 ft	Depth = 10 ft	Depth = 15.5 ft
D60 (mm)	0.15	0.15	0.15
D50 (mm)	0.14	0.14	0.14
D30 (mm)	0.13	0.13	0.13
D10 (mm)	0.1	0.08	0.11
Cu	1.50	1.88	1.36

In 2017, SASW tests were conducted to obtain the V_s profile at the test site on the Mustang Island. Figure 6.19 shows the locations of the SASW tests, two of them (Line #1 and Line #2) were near the test site and one of them (Line #3) was at the test site. The SASW tests conducted along Line #1 and Line #2 were used to evaluate the shear wave velocity at deeper depths by using long seismic waves generated by shaker truck named "Thumper" (Figure 6.20a). The SASW test conducted along Line #3 was at the test site and this testing was focused on the shear wave velocity of shallower depths near the ground. The wave was generated by sledgehammer impacting a steel plate on the ground surface (Figure 6.20b). Figure 6.21 shows the best-estimated V_s profile from SASW tests.

Figure 6.19: Three lines used for the SASW tests at the test site on Mustang Island.

(a) (b)

Figure 6.20: (a) Shaker truck "Thumper" and (b) a sledgehammer impacting a steel plate.

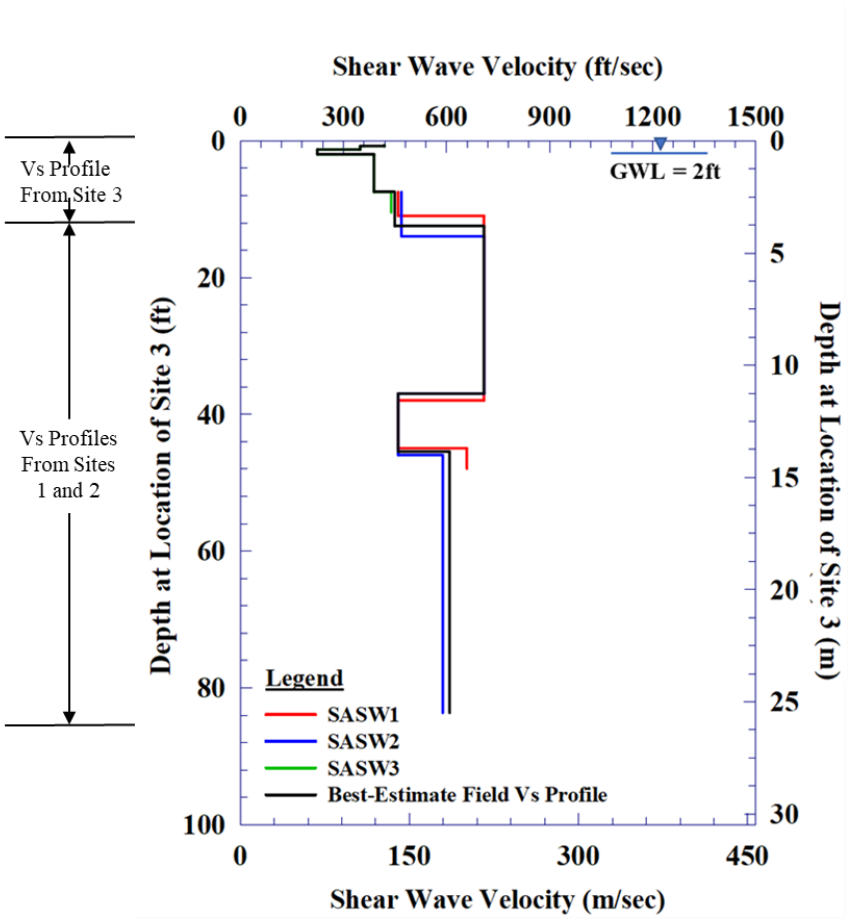

Figure 6.21: Comparison of three V_S profiles determined at Mustang Island and the best-estimated field V_S profile recommended for the test site.

Low-amplitude resonant column (RC-LA) tests and high-amplitude resonant column (RC-HA) tests were performed on grab samples from depths of 1 to 2 ft. Six levels of the confining pressures were selected for the sand specimens; 1.5, 3, 6, 12, 24, and 48 psi. There are two parts of the resonant column procedure: (1) the initial loading RC tests and (2) the unloading RC tests. In the initial loading RC-LA, the confining pressures were increased in steps following the six confining pressure levels. At each confining pressure, RC-LA tests were performed for about 65 minutes to obtain the variation of dynamic properties with time. After RC-LA testing was completed at the highest confining pressure

of 48 psi, the confining pressure applied to the specimen was unloaded in steps from 48 psi to 1.5 psi. RC-LA tests were again performed at each unloading of the specimen for about 35 minutes. RC-HA tests were performed to investigate the nonlinear behavior of the specimen. The RC-HA tests were conducted after the RC-LA tests at 100 minutes. RC-HA tests were performed at 3 confining pressure levels: 3, 12, and 48 psi. At the three confining pressures, the RC-HA tests were conducted at reloading and unloading. Figure 6.22(a) shows the relationship of $log\, G_{max} - log\, \sigma_0'$ and Figure 6.22(b) shows the relationships of $G/G_{max} - log\, \gamma$ from the resonant column tests on Mustang Island sand.

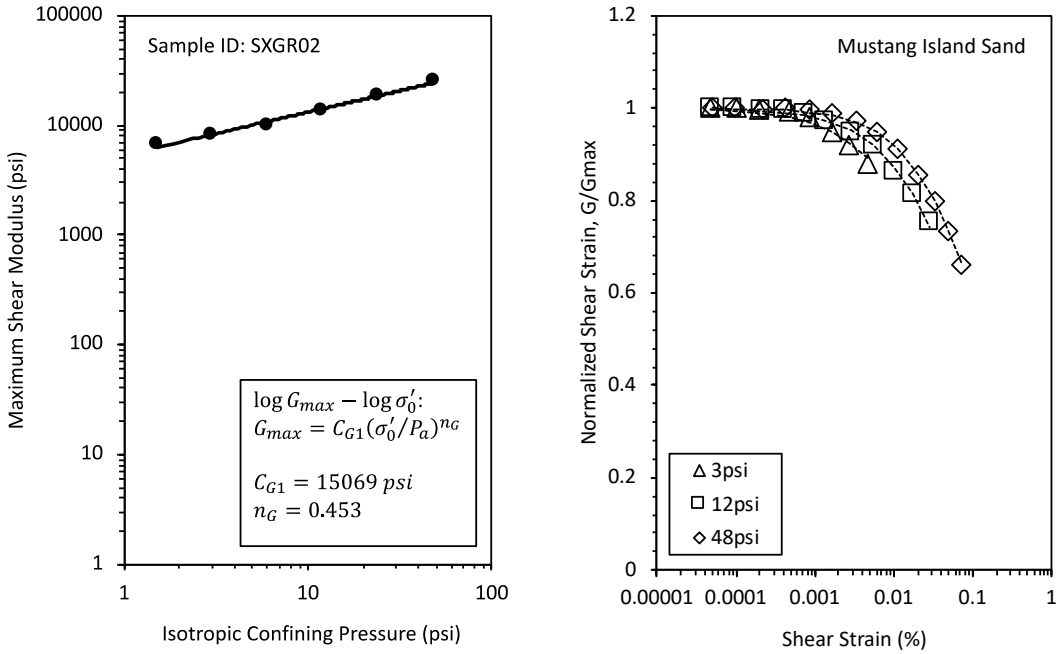

(a) (b)

Figure 6.22: (a) $log\, V_s - log\, \sigma_0'$ relationships for the Mustang Island sand and (b) $G/G_{max} - log\, \gamma$ relationships for the Mustang Island sand obtained from resonant column tests.

Figure 6.23 shows the best-estimated field V_s profile from SASW tests and two adjusted best-fit curves using relationship of $log\, V_s - log\, \sigma_0'$ by resonant column tests.

The best-estimated V_s profile was determined by the SASW tests along Line #1, Line #2, and Line #3. The parabolic dashed lines were the V_s profiles predicted by the small-strain properties of the sand the mean effective stress with the increase of depth. The green dashed lines better represent the V_s profile in Zone 1 and Zone 3. The orange dashed line better represents the V_s profile in Zone 2.

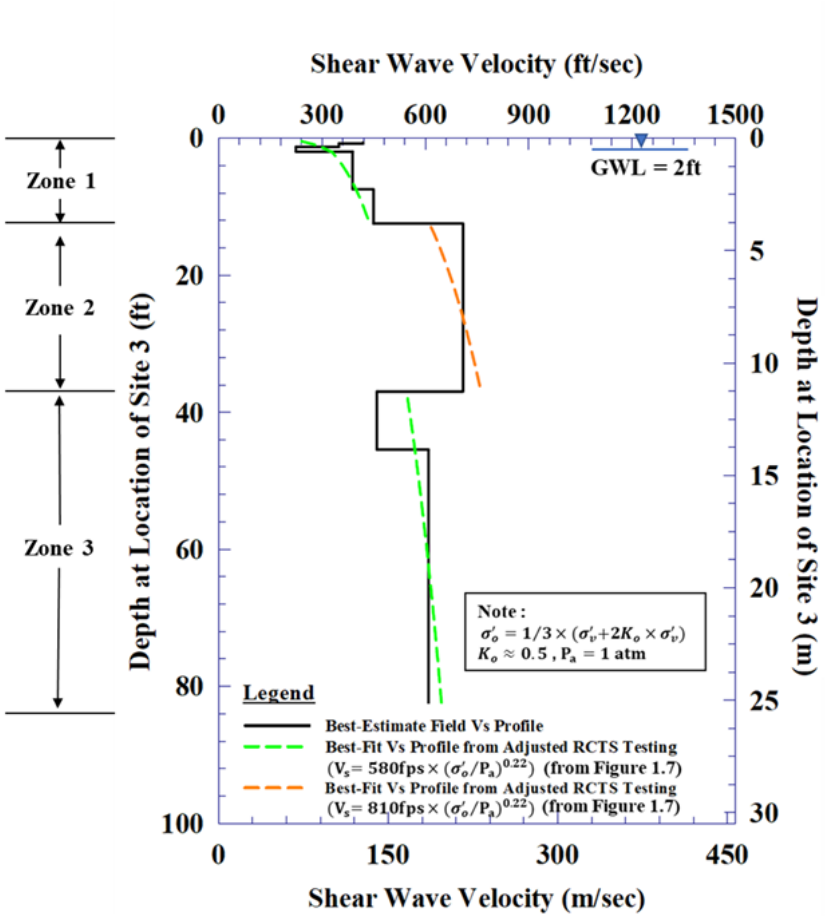

Figure 6.23: Division of the best-estimated field V_s profiles into three zones combined with the recommended laboratory V_s profile for each zone.

Three TRX tests were conducted under confining pressures of 3 psi, 6 psi, and 12 psi (Figure 6.24) to extend the $G/G_{max} - \log\gamma$ curves to larger strains. The water content and the void ratio of the specimens were kept the same as in the resonant column tests. The corresponding Mohr's circles were shown in Figure 6.25 and the calculated friction angle was 35 degrees.

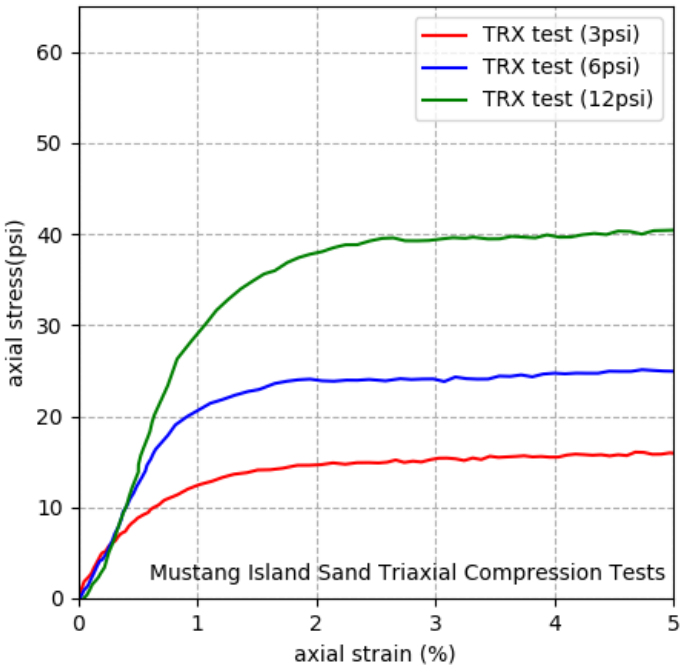

Figure 6.24: TRX tests on the Mustang Island sand.

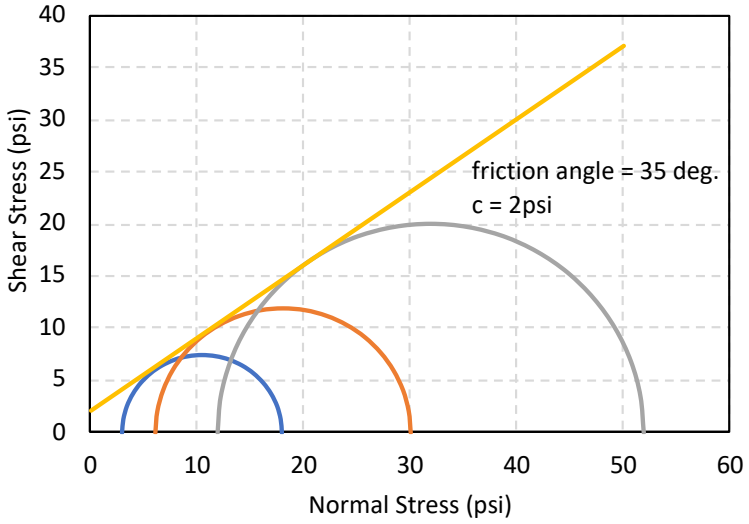

Figure 6.25: Mohr's circles from triaxial compression tests on Mustang Island sand.

6.2.3 Modification on the Input Parameters – Mustang Island Test

To better simulate the specific behavior of Mustang Island sand, the input parameters of the proposed constitutive model needed to be modified based on the results of resonant column tests. The R-squired method was used in the regression analysis to get the best-fit curve between the measured and numerical relationships of $log\, G_{max} - log\, \sigma_0'$ and $G/G_{max} - log\, \gamma$. Table 6.5 summarizes the input parameters of the Mustang Island sand based on best-fitting the RCTS tests. Figure 6.26 shows the comparison between the measured relationships of $log\, G_{max} - log\, \sigma_0'$ and $G/G_{max} - log\, \gamma$ and the numerical relationships based on the input parameters best-fitting the RCTS tests (Table 6.5).

Table 6.5: Input parameters of the Mustang Island sand based on best-fitting the RCTS tests.

$C_{G1}\,(psi)$	n_G	C_1 (%)	C_2	C_3	C_4	$\alpha_1, \alpha_2, \alpha_3$
15068	0.452	0.106	0.311	0.854	0.0896	0.001

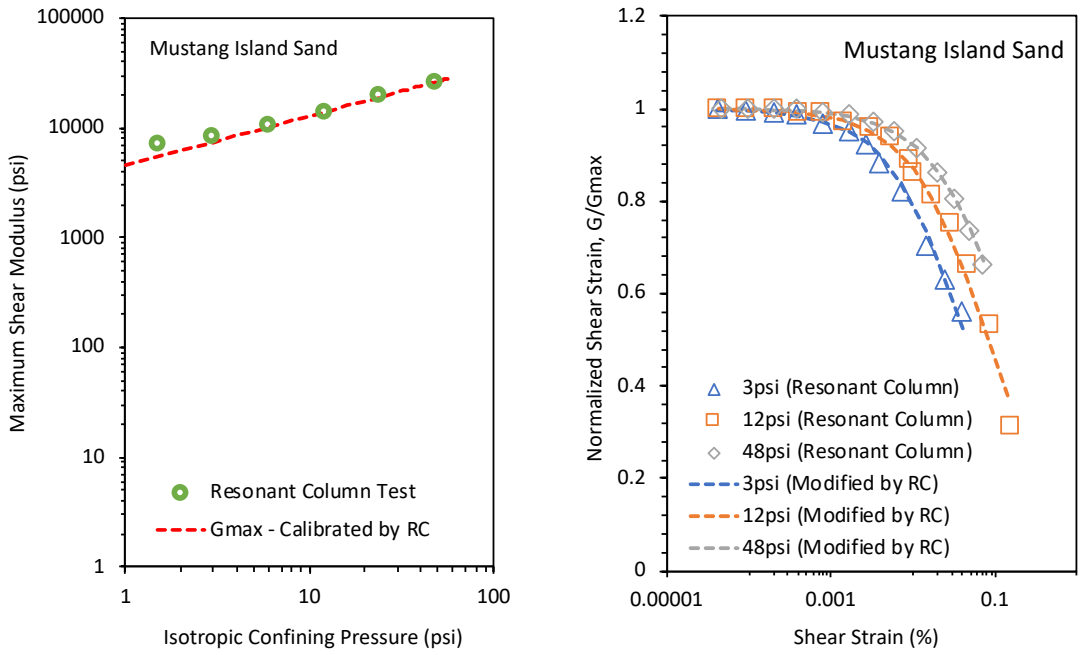

(a) (b)

Figure 6.26: (a) Numerical relationship of $\log G_{max} - \log \sigma_0'$ and (b) numerical relationship of $G/G_{max} - \log \gamma$ based on input parameters best-fitting the RCTS tests on the Mustang Island sand.

Before modifying the numerical $G/G_{max} - \log \gamma$ curves, by using the input parameters just modified by RCTS tests (Table 6.5), the comparison between the 3-D FEM model of simulating triaxial tests and the measurement is shown in Figure 6.27. The numerical simulation overestimated the stiffness of sand.

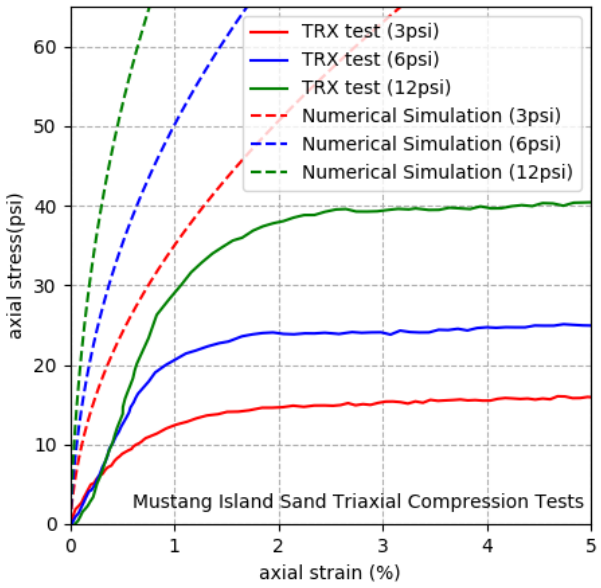

Figure 6.27: Comparison of the stress versus strain curves measured by TRX tests and the predicted based on the input parameters best-fitting the RCTS tests on the Mustang Island sand.

Table 6.6 shows the modified input properties for Mustang Island sand which was modified by the TRX tests. Figure 6.28 shows the comparison between the measurement of the TRX tests and the numerical simulations after the modification. The curves from the numerical simulation had good agreements with the measurement when the strain was larger than 1%. Because the conventional triaxial compression tests had poor capability of capturing the stiffness of the soil at small strains, the curves from the numerical simulation did not attempt to agree with the measured curves at small strains.

Table 6.6: Input parameters of the Mustang Island sand modified by the TRX tests.

$C_{G1}\,(psi)$	n_G	C_1 (%)	C_2	C_3	C_4	$\alpha_1, \alpha_2, \alpha_3$
15068	0.452	0.081	0.4	1.0	0.0	0.001

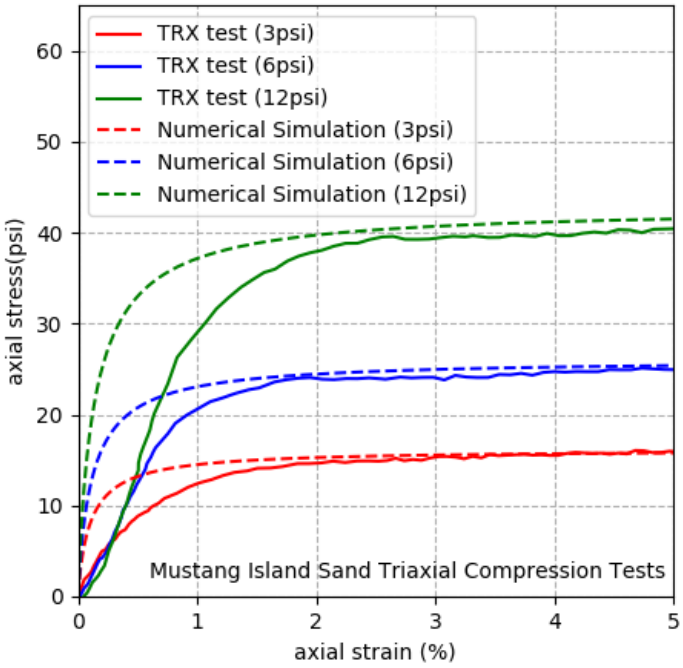

Figure 6.28: Comparison of the stress versus strain curves measured by TRX tests and predicted based on the input parameters modified by the TRX tests on the Mustang Island sand.

Figure 6.29 shows the numerical $G/G_{max} - log\,\gamma$ curves predicted by the modified input parameters based on the TRX tests (Table 6.6). The modified curves still had a good fit with the measurement from the resonant column tests under the shear strain of 0.1%, which meant the modification had little influence on the stiffness of Mustang Island sand at small strains and made the numerical $\mathrm{G/G}_{max} - \log\gamma$ curves perform better in the large strain.

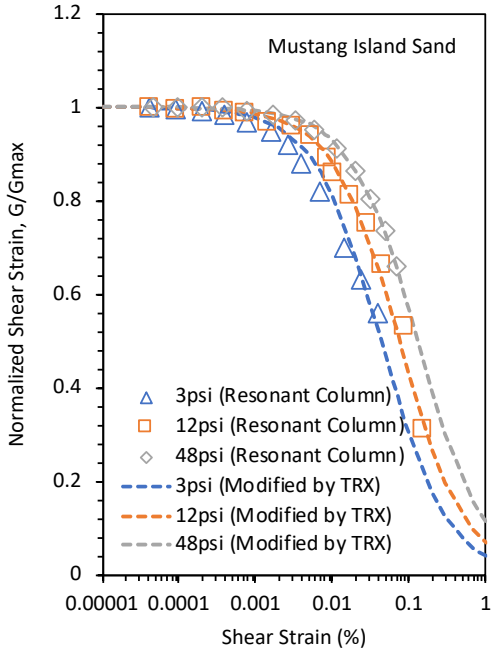

Figure 6.29: Numerical relationship of $G/G_{max} - \log\gamma$ based on input parameters modified by the TRX tests on the Mustang Island sand.

During the SASW tests, the water table was 2 ft below the sand surface. However, according to Cox, Reese and Grubbs (1974), the water table was maintained at the sand surface. Before the lateral load tests, the site was excavated about 5.5 ft of material to reach the water table. In addition, 2.5 ft of clay was removed, and the sand was filled in to bring the soil surface back up to the water table. It was suspected that 2 ft of sand was backfilled after the complete of the lateral load tests. Therefore, the soil surface during the SASW tests was higher than the surface during the lateral load tests. So, the 2 ft of the sand needed to be removed from the V_s profile. Figure 6.30a shows the modified V_s profile based on Figure 6.22. The modified V_s profile was converted to G_{max} profile, as shown in Figure 6.30b, through Equation 5.2 by assuming that the total unit weight of the sand was 120 pcf.

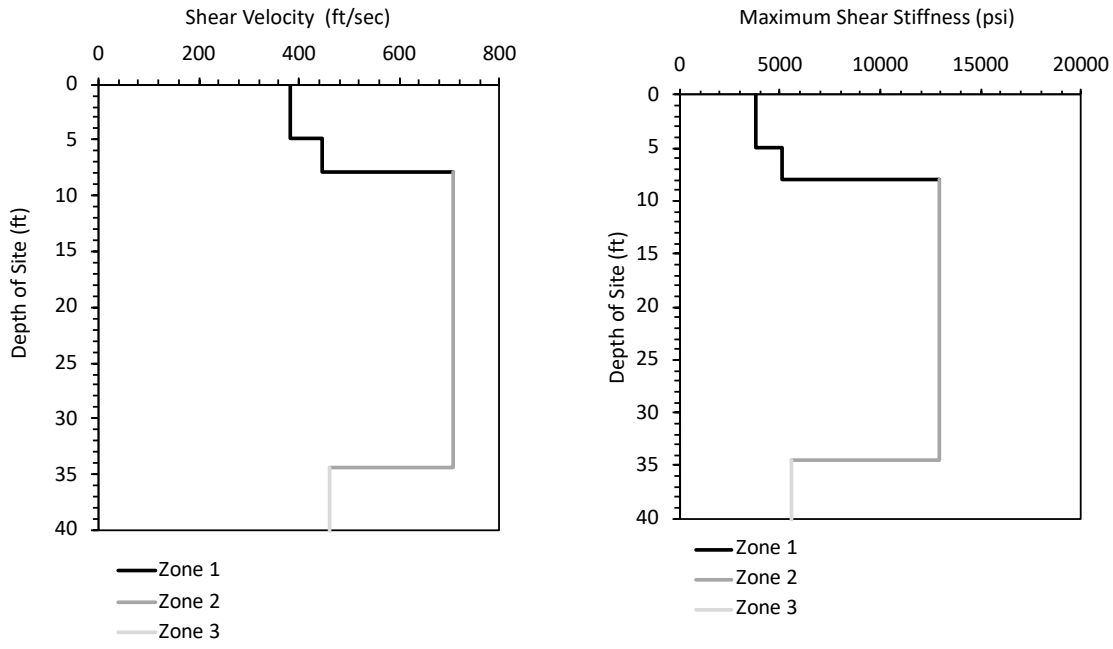

(a) (b)

Figure 6.30: Comparison of (a) the V_s profiles and (b) the G_{max} profiles measured by the SASW tests.

Table 6.7 summarizes the input parameters of the Mustang Island sand modified by the G_{max} profile of the layers of Zone 1 and Zone 2. Because the water table was at the soil surface, so the shear velocity or the maximum shear stiffness at the soil surface should be zero. Figure 6.31 shows the G_{max} profile predicted by the input parameters modified by the RCTS, TRX, and SASW tests (Table 6.7).

Table 6.7: Input parameters of the Mustang Island sand in 3-D FEM model.

	Zone 1	Zone 2
C_{G1} (psi)	15069	18882
n_G	0.452	0.452
C_1(%)	0.081	0.081
C_2	0.4	0.4
C_3	1.0	1.0
C_4	0.0	0.0
α_a, α_b, α_c	0.001	0.001
γ' (pci)	0.0333	0.0333
υ	0.33	0.33
K_0	0.4925	0.4925

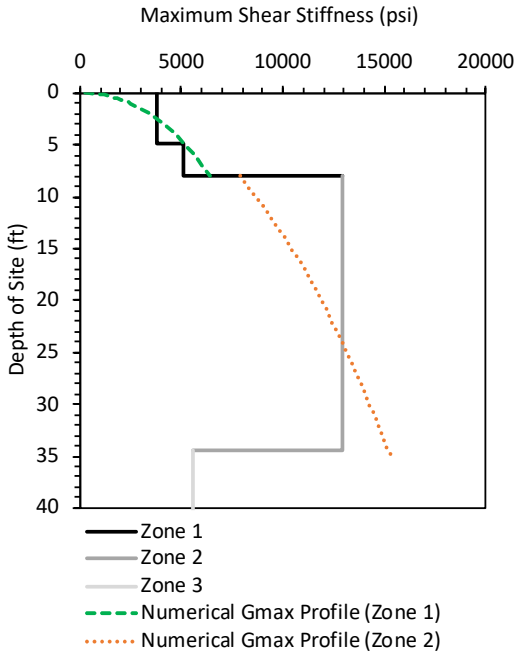

Figure 6.31: the G_{max} profiles measured by the SASW tests and predicted by the input parameters modified by RCTS, TRX, and SASW tests (Table 6.7).

6.2.4 3-D FEM Model - Mustang Island Test

Figure 6.32 shows the set-up of the lateral load tests at Mustang Island. The test piles were 24-inch diameter with a wall thickness of 0.375 inch. The material of the pile

was A-53 Grade-B seamless steel. The embedment length of the pile was 69 ft. The connecting flange, where the load to the free-head pile was applied, was located one foot above the mudline. The test site was excavated in advance of the test so that the water table was maintained at the excavation base during the loading to simulate offshore conditions.

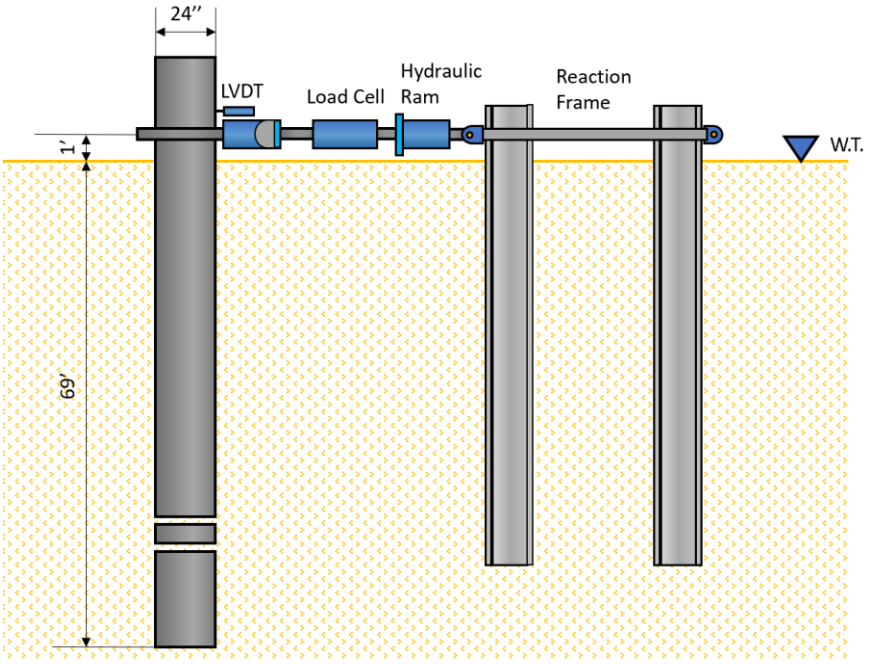

Figure 6.32: Set-up of the lateral load tests on Mustang Island (adapted from Reese, Cox, and grubbs, 1974).

A 3-D FEM model in Abaqus was carried out to simulate the behavior of the pile under the lateral load. In the 3-D FEM model, the diameter of the pile was modeled as 24 inches, which was the same as the diameter of the pile in the field. The length of the pile below the soil surface in the modeling was 406 inches (34 ft), which was less than the real length of the pile used in the field tests. The reasons for just using half length of the pile in the modeling were:

1) For small lateral displacement of the slender pile, the soil near the surface contributed most to the response of the lateral displacement on the pile and;
2) For simulating the soil with half length, the thickness of the sand was half compared to it in the modeling with full length of the pile, which reduced the calculation effort needed for Abaqus.

So the thickness of the soil was the same as the modelled length of the pile. Horizontally, the soil extended 10 diameters from the edge of the pile with 8-node linear brick elements.

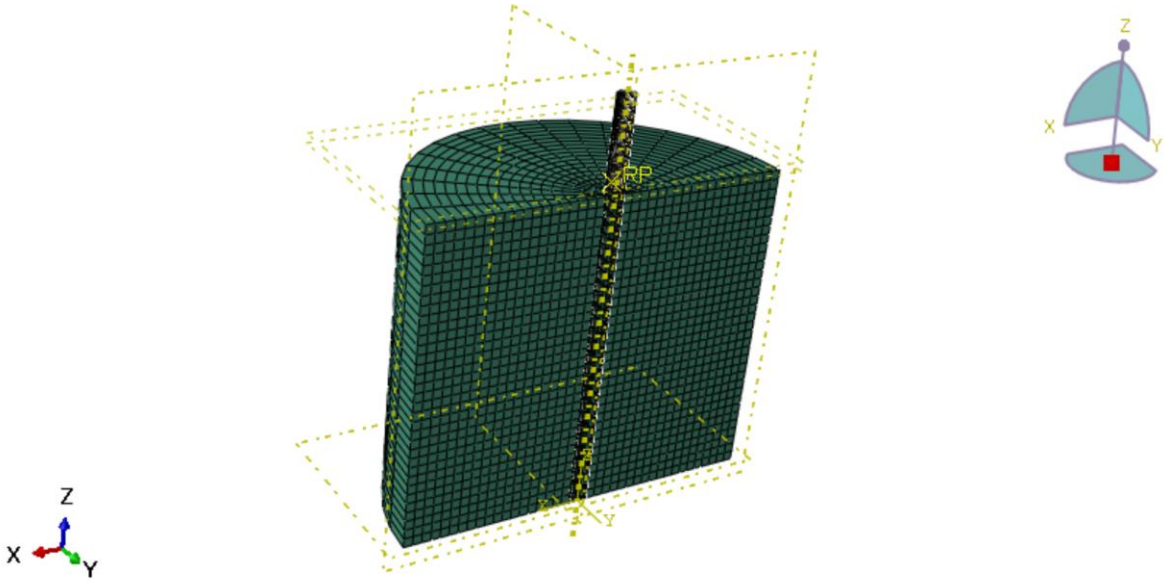

Figure 6.33: 3-D FEM model of the lateral load tests on Mustang Island.

The pile was modeled as hollow pile with a diameter of 24 in, wall thickness of 0.375 in., and an elastic modulus of 29,000,000 psi. The pile was assumed to have a unit weight equal to 0.3 pci and a Poisson's ratio equal to 0.3. The soil-pile interface was assumed to be frictionless. The pile loading was displacement controlled with the displacement applied to the pile in the horizontal direction 1 ft above the ground line. The displacement applied at the loading point was 1% of the diameter of the pile.

Figure 6.34 shows the comparison of the lateral load versus displacement curves between the measurement and the prediction from the 3-D FEM model using the input parameters modified by RCTS, TRX, and SASW tests (Table 6.7). The simulated load-displacement curve captures the non-linearity at small displacements and has a good agreement with the field measurement.

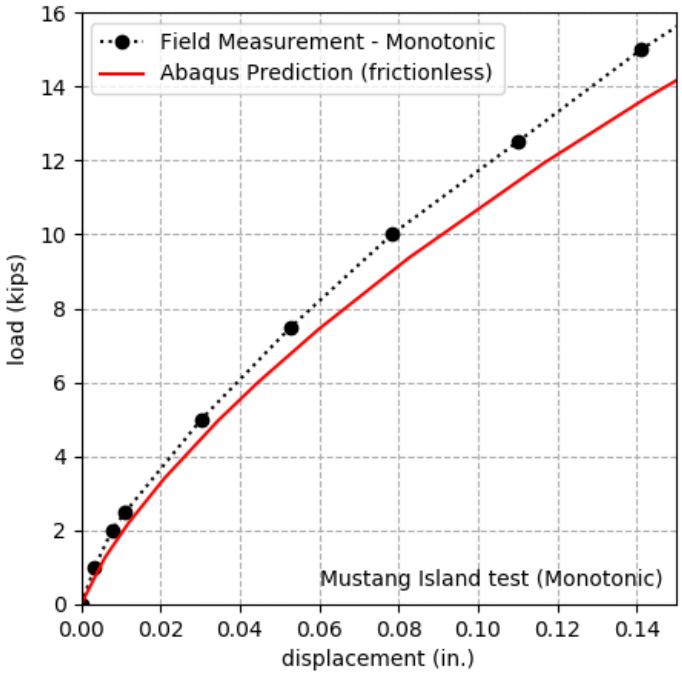

Figure 6.34: Comparison of the load versus displacement curves at small displacements measured in the field and predicted by the 3-D FEM model, Mustang Island test.

LPILE is a program used in the practice to predict the response of the piles under lateral loading conditions. LPILE has a database of p-y curves for a variety of soil types: the "API" p-y curves method was chosen in LPILE analysis to simulate the behavior of the

pile under lateral loading for Mustang Island test. The properties of the sand were listed in Table 6.8.

Table 6.8: Input parameter of the Mustang Island sand for LPILE analysis.

Effective Unit Weight (pcf)	Friction angle (deg.)	k (pci)
58	35	85.66

Figure 6.35 shows the comparison of the lateral load versus displacement curves obtained from LPILE and 3-D FEM model using Abaqus. The prediction from LPILE based on API p-y method underestimates the stiffness in the range of the small displacement and does not capture the non-linearity of the response. The Abaqus prediction has a good agreement with the field measurement and predicts well the non-linearity in the response. At lateral displacements that are similar to offshore wind turbine monopiles in service, i.e., less than 0.05% of the pile diameter or less than 0.01 inches for the lateral load tests, the lateral stiffness of the pile is at least five times greater than the linear result based on the current p-y curves. As a further check of the 3-D FEM model, Figure 6.36 shows the full range of displacement. The Abaqus prediction is lower than the field measurement at large displacements, which is likely due to assuming that the contact interface between the soil and the pile is frictionless in the 3-D FEM model.

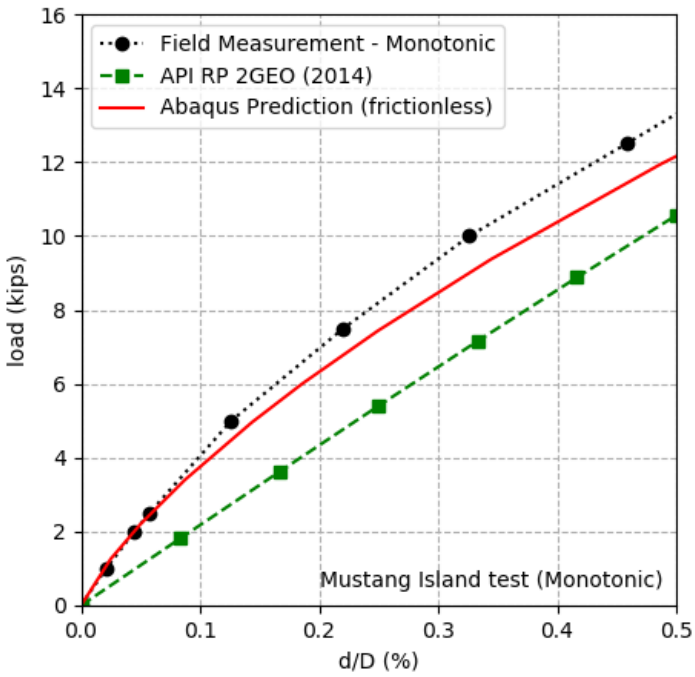

Figure 6.35: Comparison of the load versus displacement curves at small displacements measured in the field, predicted by LPILE using API p-y curves, and predicted by the 3-D FEM model, Mustang Island test.

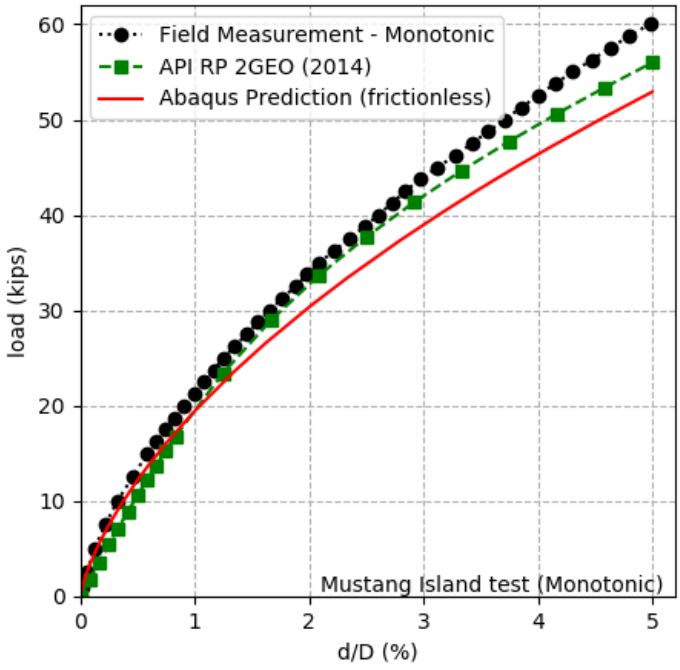

Figure 6.36: Comparison of the load versus displacement curves at large displacements measured in the field, predicted by LPILE using API p-y curves, and predicted by the 3-D FEM model, Mustang Island test.

To be more realistic, a friction coefficient needed to be defined at the surface of the soil and the pile. Table 6.9 shows the recommended friction coefficients for cohesionless siliceous soil for axial loaded pile design in API RP 2GEO (2014). The upper 20 ft of the sand was classified as medium dense, which governed the behavior of the lateral loaded pile. For medium dense sand, API RP 2GEO (2014) suggested using friction coefficient of 0.37. If the sand was classified as dense, the friction coefficient was 0.46. Theoretical t-z curves were used to describe the relationship between mobilized soil-pile shear transfer and local piles displacement at any depth (Figure 6.37). Morsher (1984) suggested that the value of z_{peak} varied from 0.1 to 0.2 inches for sand. Table 6.10 shows a set of combinations of friction coefficients and values of z_{peak}.

Table 6.9: Design parameters for cohesionless siliceous soil (API RP 2GEO, 2014).

Relative Density[a]	Soil Description	Shaft Friction Factor[b] β (-)	Limiting Shaft Friction Values kPa (kips/ft^2)	End Bearing Factor N_q (-)	Limiting Unit End Bearing Values MPa (kips/ft^2)
Very loose Loose Loose Medium dense Dense	Sand Sand Sand-silt[c] Silt Silt	Not applicable[d]	Not applicable[d]	Not applicable[d]	Not applicable[d]
Medium dense	Sand-silt[c]	0.29	67 (1.4)	12	3 (60)
Medium dense Dense	Sand Sand-silt[c]	0.37	81 (1.7)	20	5 (100)
Dense Very dense	Sand Sand-silt[c]	0.46	96 (2.0)	40	10 (200)
Very dense	Sand	0.56	115 (2.4)	50	12 (250)

NOTE The parameters listed in this table are intended as guidelines only. Where detailed information, such as CPT records, strength tests on high quality samples, model tests, or pile driving performance, is available, other values may be justified.

[a] The definitions for the relative density percentage description are as follows:

- Very loose, 0 – 15;
- Loose, 15 – 35;
- Medium dense, 35 – 65;
- Dense, 65 – 85;
- Very dense, 85 – 100.

[b] The shaft friction factor β (equivalent to the "K tan δ" term used in previous editions of API 2A-WSD) is introduced in this document to avoid confusion with the δ parameter used in the Annex.

[c] Sand-silt includes those soils with significant fractions of both sand and silt. Strength values generally increase with increasing sand fractions and decrease with increasing silt fractions.

[d] Design parameters given in previous editions of API 2A-WSD for these soil/relative density combinations may be unconservative. Hence, it is recommended to use CPT-based methods from the annex for these soils.

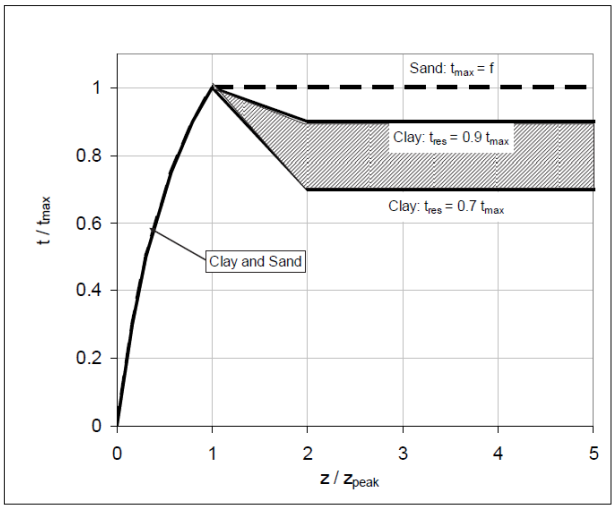

Figure 6.37: Typical axial pile load transfer – Displacement (t-z) curves.

Table 6.10: Combinations of friction coefficients and values of z_{peak}.

Set #	friction coefficient	z_{peak} (inches)
1	0.46	0.1
2	0.46	0.2
3	0.46	0.5
4	0.37	0.1
5	0.37	0.2
6	0.37	0.3
7	0.37	0.4
8	0.37	0.5

Figures 6.38 to 6.39 show the lateral load versus displacement curves after the friction coefficient is added based on Table 6.10. Because the friction between the soil and pile increases the difficulty of obtaining a converged solution, therefore a higher friction coefficient and a lower value of z_{peak} will decrease the degree of completion of the load step. As shown in Figure 6.38, the curve with friction coefficient of 0.37 and z_{peak} of 0.5 inches has the highest degree of completion. In the previous analysis, the lateral load versus displacement is underestimated by the 3-D FEM model with no friction. Figure 6.38 shows the friction coefficient could increase the lateral load at large displacements. Figure 6.39 indicates that a lower value of z_{peak} increases the lateral load with a smaller lateral displacement.

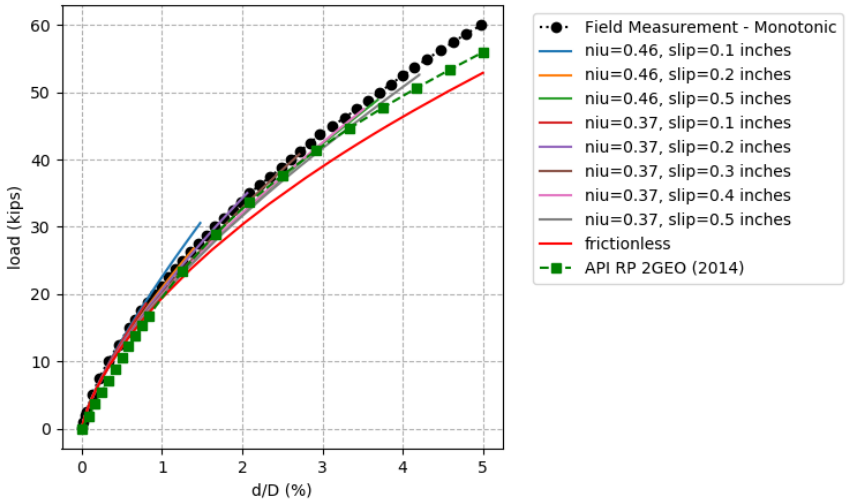

Figure 6.38: Comparison of the load versus displacement curves at large displacements measured in the field and predicted by the 3-D FEM model with different friction coefficients, Mustang Island test.

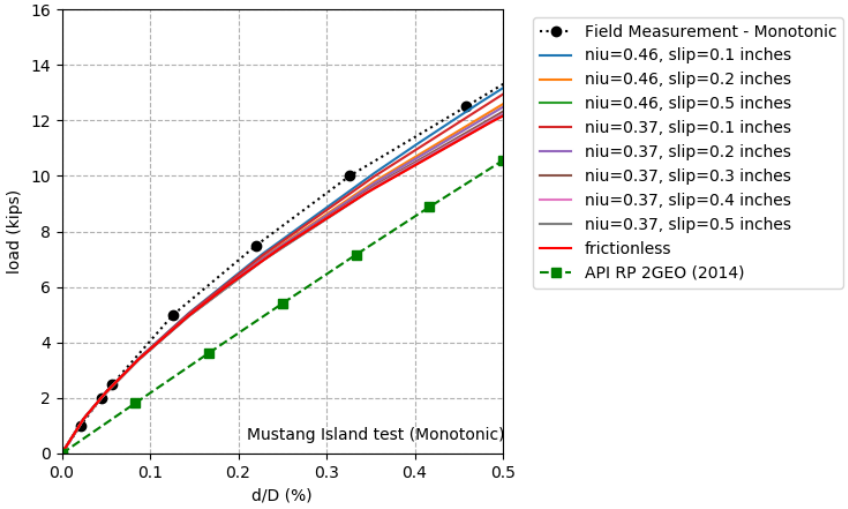

Figure 6.39: Comparison of the load versus displacement curves at small displacements measured in the field and predicted by the 3-D FEM model with different friction coefficients, Mustang Island test.

To solve the issue of convergence met in the problem of large friction, the non-linear geometry effects was turned on (NLgeom=ON) in the loading step of Abaqus. In the status of NLgeom=ON, an automatic stabilization method could be selected to solve the problem of instability in any non-linear quasi-static procedure. A constant "damping factor" was used to calculate an additional stiffness matrix to balance the internal and external forces in a body by performing another iteration if the solution was not converged. While the model was stable and converged well, the "damping factor" had negligible effect on the results. It only worked when a local region went unstable (e.g., infinity displacement induced by zero stiffness). A default value of 2×10^{-4} of "damping factor" in Abaqus was used and adaptive stabilization was triggered for the 3-D FEM model. The viscous forces generated by the "damping factor" were checked by comparing them with the expected nodal forces to make sure that the viscous forces did not dominate the solution. Figure 6.40 shows lateral load versus displacement curves with the use of more realistic friction coefficients and automatic stabilization method. The friction makes the measured and predicted lateral load versus displacement curves have a better agreement. Though the discontinuity is existed in the predicted curves because of the assistance from the automatic stabilization to force the solution to converge.

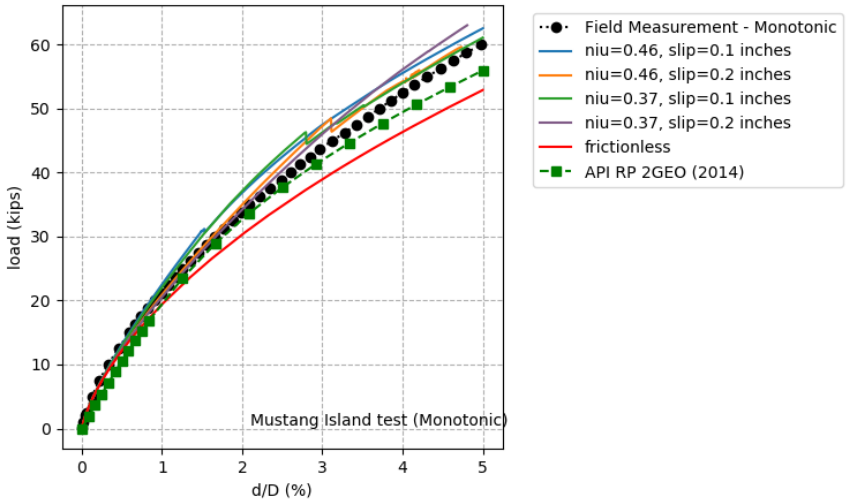

Figure 6.40: Comparison of the load versus displacement curves at large displacements measured in the field and predicted by the 3-D FEM model with different friction coefficients using automatic stabilization, Mustang Island test.

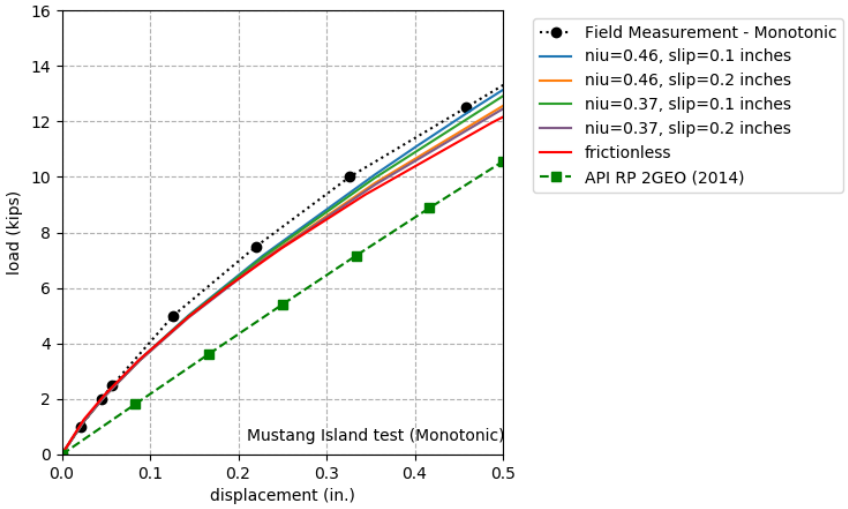

Figure 6.41: Comparison of the load versus displacement curves at large displacements measured in the field and predicted by the 3-D FEM model with different friction coefficients using automatic stabilization, Mustang Island test.

6.3 CONCLUSIONS

The major conclusions from the field tests are as follows:

1) In the analysis of the settlement tests conducted at NGES test site, with the input parameters of the constitutive model modified by laboratory and field tests, the settlements predicted by the 3-D FEM model are in reasonable agreement with the measured settlements for the small-scale footings.
2) In the analysis of the lateral load tests on Mustang Island, the predicted response of the 3-D FEM model matches well with the measured results by using the proposed constitutive model with the input parameters modified by laboratory and field tests. The 3-D FEM model well estimates the pile stiffness and captures the non-linearity of the response in the small range of displacement. As expected, the conventional p-y curves method underestimates the pile stiffness at small displacements and does not predict the non-linearity of the response.
3) To make the 3-D FEM model have a good prediction about the stiffness of the soil at small displacements, the input parameters of the constitutive model need to be modified by the laboratory tests for the small-strain behavior (e.g., resonant column and torsional shear tests), the laboratory tests for the large-strain behavior (e.g., triaxial compression test), and the field tests for the in situ maximum shear modulus (e.g., Spectral-Analysis-of-Surface-Wave test).
4) To make the 3-D FEM model have a good prediction on the lateral load versus displacement curve at large displacements, a reasonable friction coefficient between the pile and soil should be added in the FEM model.

Chapter 7: Recommendations for Improving p-y Methods

Based on the conclusions from the previous sections, two recommendations are proposed for the design of laterally-loaded monopiles in sand at small displacements:

- The conventional p-y methods do not have a good prediction on the initial stiffness and the non-linearity of laterally loaded pile at the small lateral displacements which govern the design of offshore wind turbine monopiles under service loading.
- In order to improve the prediction on the initial stiffness and the non-linearity of laterally loaded piles at small displacements, it is necessary to empirically establish or measure directly for the sand the in-situ maximum shear modulus profile, the relationship between shear modulus and shear strain, the relationship between shear modulus and mean effective stress.

In this section, p-y curves were extracted from the 3-D FEM models of piles with different diameters and were compared to the p-y curves established based on API RP 2GEO (2014), which led the third recommendation for the design:

- The p-y curves used for design of offshore wind turbine monopiles under service loading condition should be revised based on the small-strain properties of the site-specific soils, which include three approaches:
    (1) Extract p-y curves directly from a project-specific 3-D FEM analysis using the proposed soil constitutive model that captures the initial stiffness the non-linearity of sand at small strains.
    (2) Estimate p-y curves by establishing the relationship between the input parameters in the proposed soil constitutive model and the

shape of the curves through conducting parametric study on 3-D FEM models.

(3) Adjust the initial portion of the API p-y curves based on shear velocity (maximum shear stiffness).

7.1 ESTABLISH P-Y CURVES DIRECTLY FROM 3-D FEM MODELS

The best approach is to conduct a 3-D FEM analysis for laterally loaded pile using a constitutive model, incorporating the small-strain properties of the sand, to capture small-strain behavior of the sand. The p-y curves could be extracted directly from the 3-D FEM models of laterally loaded piles at any depths depended on the resolution of meshing the bodies of the soil and the pile. At each depth, the reaction force, p $(lbs/in.)$, in the p-y curve is computed as the sum of the projected contact force in the lateral displacement direction along the contact surface of the pile and the displacement, y $(in.)$, which is the lateral displacement at the center of the pile at the specific depth.

Figures 7.1 and 7.2 show the comparison between the p-y curves extracted from the 3-D FEM model of the Mustang Island pile (friction coefficient=0.46, slip distance=0.1 inches) and the p-y curves established based on API RP 2GEO (2014). As shown in Figure 7.1 for the lateral loaded pile at small displacements, for the p-y curves in the shallower depths, it shows that (1) initial portions of stiffness are underestimated by the API p-y method, and (2) the API p-y method also does not capture the non-linearity of the stiffness at the initial portion. Figure 7.2 shows the lateral loaded pile with the lateral displacement up to $3d/80$ (d is the pile diameter), the two p-y curves have a better agreement with the increasing lateral displacement and deeper depth.

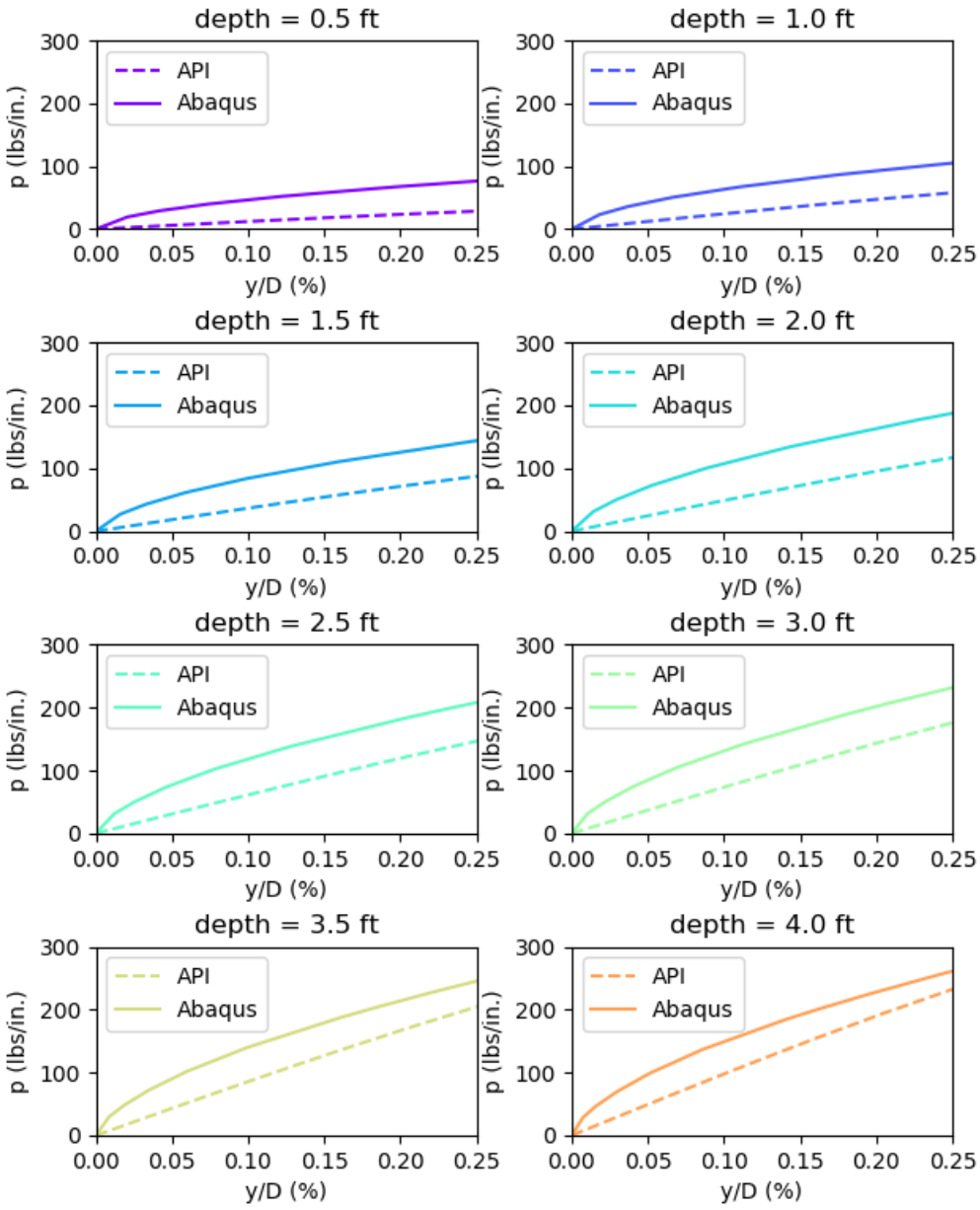

Figure 7.1: Comparison of the p-y curves between the proposed method and API method at small displacements for Mustang Island test.

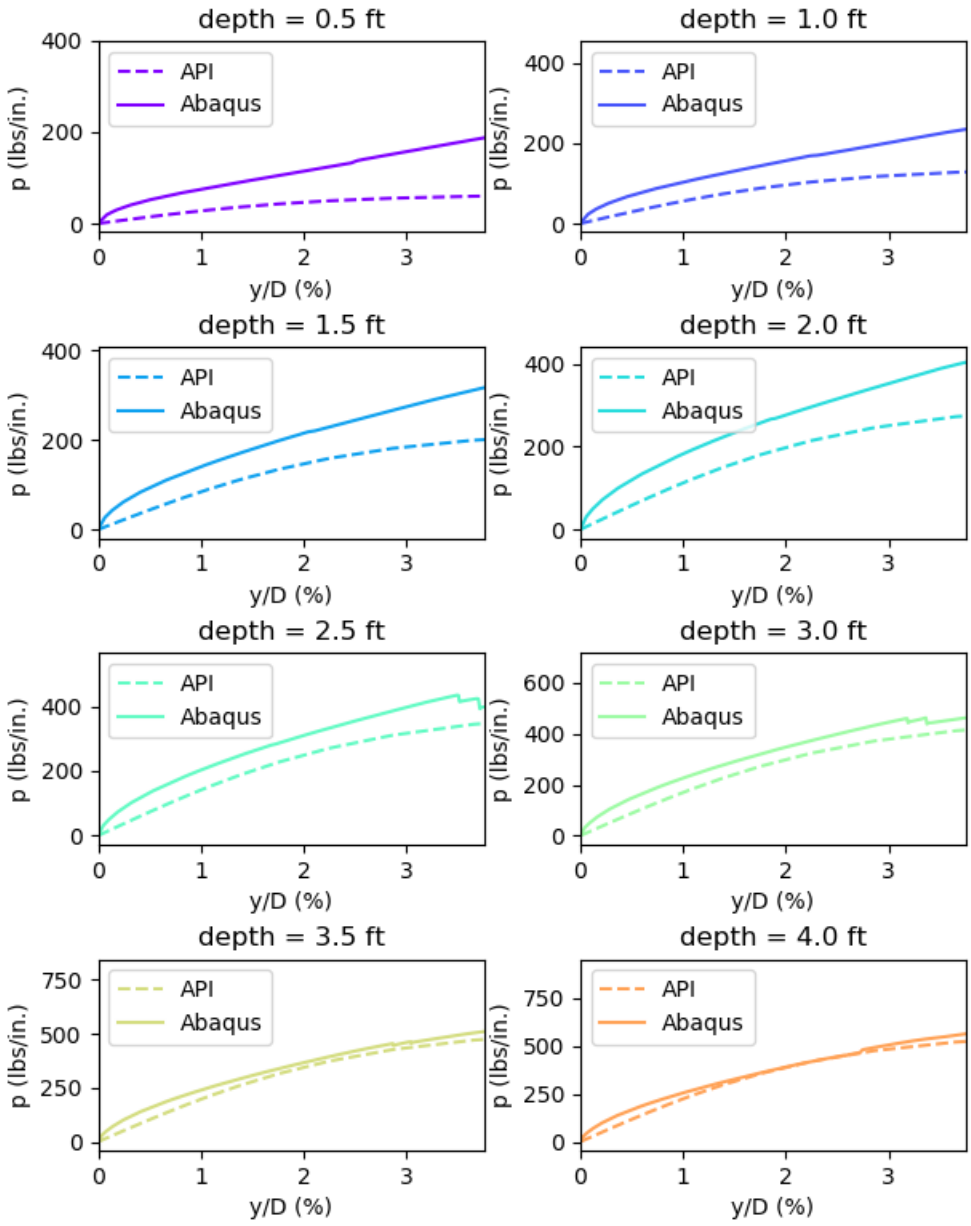

Figure 7.2: Comparison of the p-y curves between the proposed method and API method at large displacements for Mustang Island test.

Figure 7.3 shows the comparison of the lateral load versus displacement curves calculated by p-y methods using the p-y curves extracted from the 3-D FEM model and extracted directly from the 3-D FEM model of the Mustang Island pile. The comparison shows the results from two methods are identical, which indicates the feasibility of applying the p-y curves from 3-D FEM models into the conventional p-y method.

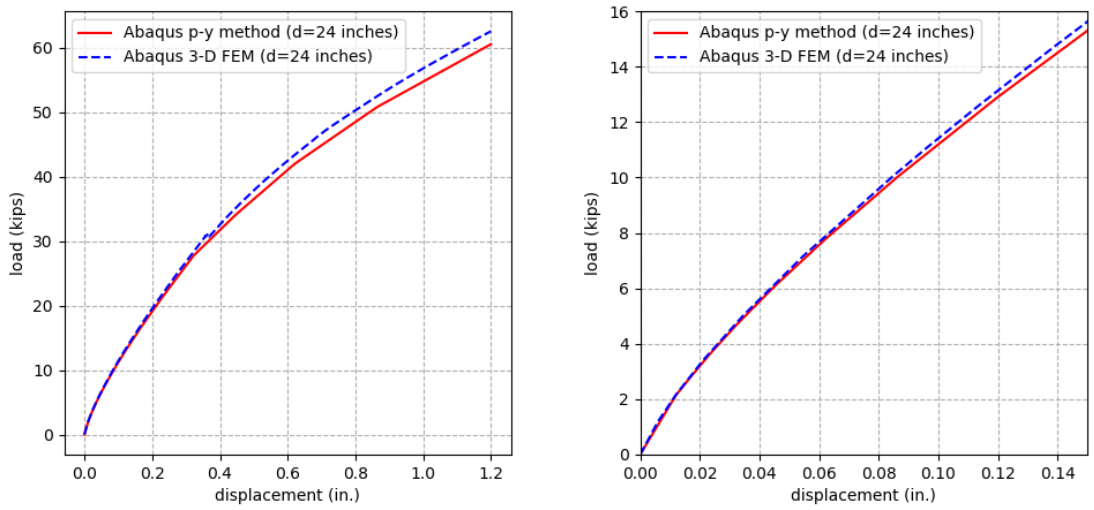

(a) (b)

Figure 7.3 Comparison between the load versus displacement curves predicted by the proposed p-y method and 3-D FEM model on Mustang Island test.

Figure 7.4 shows the normalized p-y curves extracted from the 3-D FEM models at the depth of three diameters for the piles. The displacement is normalized by the diameter of the pile and the reaction force is normalized by the reaction force at the lateral displacement, y, of $3d/80$, where d is the diameter of the pile. The shapes of the normalized curves from 3-D FEM models are similar to each other, the initial portions of the curves from 3-D FEM models are stiffer than the curves established by API RP 2GEO (2014) and predict well of the non-linearity of the stiffness at small displacements. The difference of the shapes of the normalized curves from 3-D FEM models may because the

un-stabilization during the calculation in Abaqus to obtain converged solution, which is induced by the high friction between the pile and the soil.

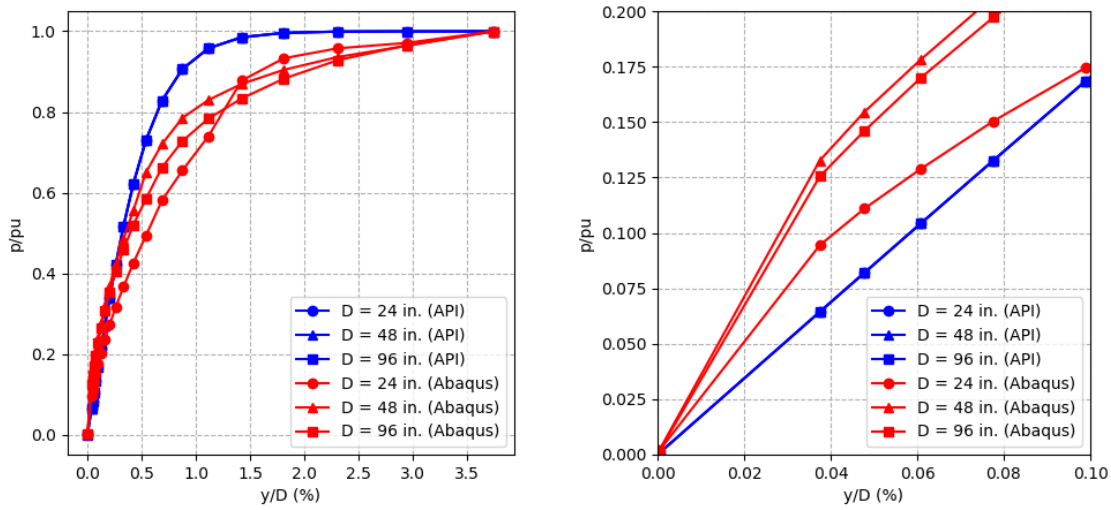

(a) (b)

Figure 7.4: Normalized p-y curves from 3-D FEM models compared with API p-y curves at depth of two pile diameters.

7.2 Simplified p-y Curves Calibrated from 3-D FEM Models

A less accurate approach is to estimate the p-y curves by establishing the relationship between the input parameters in the proposed soil constitutive model and the shape of the curves through conducting the parametric studies using 3-D FEM models.

A preliminary parametric study was conducted to investigate the potential of this simplified approach, which was calibrated from a series of 3-D FEM models to relate the shape of the simplified p-y curves with eight input parameters in the proposed soil constitutive model: (1) pile diameter, d; (2) effective vertical stress versus depth, σ_v'; (3) C_{G1} and n_G describing the maximum shear stiffness, G_{max}; and (4) C_1, C_2, C_3, and C_4 describing the $G/G_{max} - log\,\gamma$ curves (Gilbert et al., 2018).

Table 7.1 summarizes the test program for the pile dimension and the properties of the proposed soil constitutive model in the parametric study. The submerged unit weight was assumed equal to 0.03-pci and Poisson' ratio was assumed to be 0.3 for the sand. Tests from #1 to #5 studied the influence of the pile dimension and they had the same input parameters of the soil constitutive model. Other models in the test program were used to analyze the influence from the other seven parameters.

Table 7.1: Numerical models for parametric study (Gilbert et al., 2018).

Test #	D (in.)	C_G1 (psi)	n_G	C1	C2	C3	C4
1	24	15069	0.45	0.1	0.5	0.85	0.05
2	48	15069	0.45	0.1	0.5	0.85	0.05
3	96	15069	0.45	0.1	0.5	0.85	0.05
4	144	15069	0.45	0.1	0.5	0.85	0.05
5	192	15069	0.45	0.1	0.5	0.85	0.05
6	96	7534.5	0.45	0.1	0.5	0.85	0.05
7	96	11301.75	0.45	0.1	0.5	0.85	0.05
8	96	15069	0.45	0.1	0.5	0.85	0.05
9	96	22603.5	0.45	0.1	0.5	0.85	0.05
10	96	30138	0.45	0.1	0.5	0.85	0.05
11	96	15069	0.5	0.1	0.5	0.85	0.05
12	96	15069	0.45	0.1	0.5	0.85	0.05
13	96	15069	0.4	0.1	0.5	0.85	0.05
14	96	15069	0.35	0.1	0.5	0.85	0.05
15	96	15069	0.3	0.1	0.5	0.85	0.05
16	96	15069	0.45	0.05	0.5	0.85	0.05
17	96	15069	0.45	0.075	0.5	0.85	0.05
18	96	15069	0.45	0.1	0.5	0.85	0.05
19	96	15069	0.45	0.125	0.5	0.85	0.05
20	96	15069	0.45	0.15	0.5	0.85	0.05
21	96	15069	0.45	0.1	0.4	0.85	0.05
22	96	15069	0.45	0.1	0.5	0.85	0.05
23	96	15069	0.45	0.1	0.6	0.85	0.05
24	96	15069	0.45	0.1	0.7	0.85	0.05
25	96	15069	0.45	0.1	0.8	0.85	0.05
26	96	15069	0.45	0.1	0.5	0.6	0.05
27	96	15069	0.45	0.1	0.5	0.7	0.05
28	96	15069	0.45	0.1	0.5	0.85	0.05
29	96	15069	0.45	0.1	0.5	1	0.05
30	96	15069	0.45	0.1	0.5	1.1	0.05
31	96	15069	0.45	0.1	0.5	0.85	0
32	96	15069	0.45	0.1	0.5	0.85	0.02

Test #	D (in.)	C_G1 (psi)	n_G	C1	C2	C3	C4
33	96	15069	0.45	0.1	0.5	0.85	0.04
34	96	15069	0.45	0.1	0.5	0.85	0.06
35	96	15069	0.45	0.1	0.5	0.85	0.08
36	96	15069	0.45	0.05	0.5	0.6	0.05
37	96	15069	0.45	0.075	0.5	0.6	0.05
38	96	15069	0.45	0.1	0.5	0.6	0.05
39	96	15069	0.45	0.125	0.5	0.6	0.05
40	96	15069	0.45	0.15	0.5	0.6	0.05
41	96	15069	0.45	0.05	0.5	1.1	0.05
42	96	15069	0.45	0.075	0.5	1.1	0.05
43	96	15069	0.45	0.1	0.5	1.1	0.05
44	96	15069	0.45	0.125	0.5	1.1	0.05
45	96	15069	0.45	0.15	0.5	1.1	0.05
46	96	15069	0.45	0.1	0.4	0.6	0.05
47	96	15069	0.45	0.1	0.5	0.6	0.05
48	96	15069	0.45	0.1	0.6	0.6	0.05
49	96	15069	0.45	0.1	0.7	0.6	0.05
50	96	15069	0.45	0.1	0.8	0.6	0.05
51	96	15069	0.45	0.1	0.4	1.1	0.05
52	96	15069	0.45	0.1	0.5	1.1	0.05
53	96	15069	0.45	0.1	0.6	1.1	0.05
54	96	15069	0.45	0.1	0.7	1.1	0.05
55	96	15069	0.45	0.1	0.8	1.1	0.05
56	96	7534.5	0.3	0.1	0.5	0.85	0.05
57	96	11301.75	0.3	0.1	0.5	0.85	0.05
58	96	15069	0.3	0.1	0.5	0.85	0.05
59	96	22603.5	0.3	0.1	0.5	0.85	0.05
60	96	30138	0.3	0.1	0.5	0.85	0.05
61	96	7534.5	0.375	0.1	0.5	0.85	0.05
62	96	11301.75	0.375	0.1	0.5	0.85	0.05
63	96	15069	0.375	0.1	0.5	0.85	0.05
64	96	22603.5	0.375	0.1	0.5	0.85	0.05
65	96	30138	0.375	0.1	0.5	0.85	0.05

In the 3-D FEM models, half models of piles with diameters of 24 inches, 48 inches, 96 inches, 144 inches, and 196 inches were established. The piles and the body of the soil had the same height with 768 inches. Horizontally, the soil extended 10 diameters from the edge of the pile. The body of the pile was defined as perfect-rigid body.

To avoid the difficulty of obtaining converged solution and speed up the calculation, the soil-pile interface was assumed to be frictionless. Same displacement was applied at the top and the bottom planes of the pile to move the perfect-rigid pile

horizontally. The largest displacement of the horizontal movement was set to 0.25% of the diameter of the pile. The p-y curves were extracted directly from the 3-D FEM output file.

To parametrize the p-y curves, the lateral displacement was normalized by the diameter of the pile and the load was normalized by the load at 0.25% diameter displacement, $p_{0.25\%}$. The shape of the normalized p-y curves was approximated using the following expression:

$$\frac{p}{p_{0.25\%}} = (1-n)\times\left(\frac{400\times y}{d}\right) + n\times\left(1-\left(\frac{400\times y}{d}-1\right)^2\right)^{0.5} \tag{6.1}$$

where, $\frac{p}{p_{0.25\%}}$ is the normalized load, $\frac{y}{d}$ is the normalized displacement, and n is a parameter controlling the shape of the expression (Figure 7.5).

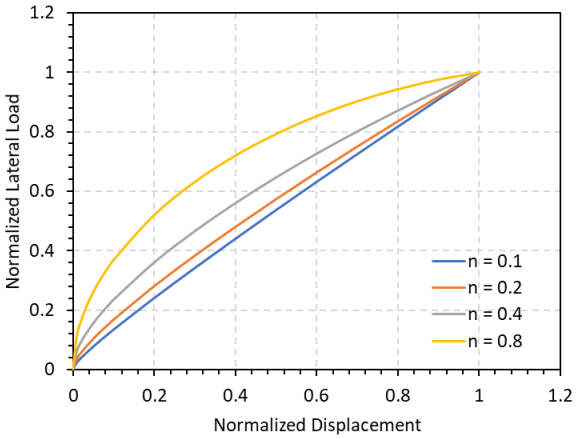

Figure 7.5: Proposed normalized p-y curves.

The study on the parameter n shows that only four parameters, $C_{G1}\,(psi)$, $C_1\,(\%)$, C_2, and C_3 have significant influence on the shape of the normalized p-y curve. The relationship between n and the four parameters is approximated as:

$$n = 0.4 + x_{CG1} \times (C_{CG1} - 15069) + x_{C1} \times (C_1 - 0.1) + x_{C2} \times (C_2 - 0.5) + \frac{x_{C3}}{C_3 - y_{C3}} + z_{C3} \qquad (6.2)$$

where,

$\mathbf{x_{CG1}}$	$\boldsymbol{x_{C1}}$	$\boldsymbol{x_{C2}}$	$\boldsymbol{x_{C3}}$	$\boldsymbol{y_{C3}}$	$\boldsymbol{z_{C3}}$
-2.75E-5	-5.42	1.28	-0.45	1.48	-0.71

The study on the parameter $p_{0.25\%}\ (lbs/in)$ shows that all the eight parameters have significant influence on the magnitude of the load at the 0.25% diameter displacement. The relationship between $p_{0.25\%}$ and the eight parameters is approximated as:

$$p_{0.25\%} = 666 \times A_d \times \left[B_{CG1} \times \left(\frac{C_{G1}}{15069} \right)^{D_{CG1}} \right] \times \left(E_{C1} \times C_1^{F_{C1}} \right) \times \left(G_{C2} \times C_2^{H_{C2}} \right) \times I_{C4} \times J_\sigma / K_{C3} \qquad (6.3)$$

where,

$$A_d = -a_d * d^2 + b_d * d + c_d$$

$$B_{CG1} = a_{CG1} * n_g^2 - b_{CG1} * n_g + c_{CG1}$$

$$D_{CG1} = d_{CG1} * n_g^2 - e_{CG1} * n_g + f_{CG1}$$

$$E_{C1} = a_{C1} * C_3 - b_{C1}$$

$$F_{C1} = c_{C1} * C_3 - d_{C1}$$

$$\mathrm{G}_{C2} = a_{C2} * \exp(-b_{C2} * C_3)$$

$$H_{C2} = -c_{C2} * C_3 + d_{C2}$$

$$I_{C4} = a_{C4} * C_4 + b_{C4}$$

$$J_\sigma = a_s * \sigma_v' + b_s$$

$$K_{C3} = -a_{C3} * C_3 + b_{C3}$$

a_d	b_d	c_d	a_{CG1}	b_{CG1}	c_{CG1}
0.105	1.1	0.023	16.7	16.4	5.12
d_{CG1}	e_{CG1}	f_{CG1}	a_{C1}	b_{C1}	c_{C1}
3.21	1.40	1.56	13.02	3.79	1.45
d_{C1}	a_{C2}	b_{C2}	c_{C2}	d_{C2}	a_{C4}
0.39	5.27	3.17	2.34	0.661	1.34
b_{C4}	a_s	b_s	a_{C3}	b_{C3}	
0.93	0.61	0.33	1.38	2.14	

To extend the feasible displacement of the simplified p-y curves out of the range of 0.25% pile diameter, the simplified p-y curves could be merged with the API p-y curves for larger displacements. If the simplified p-y curves do not intersect with the API p-y curves in the range of 0.25% pile diameter, they need to be extended to larger displacements. In these cases, the simplified p-y curve need be extended with a line that is tangent to the end of the curve until it intersects with API p-y curve (Figure 7.6).

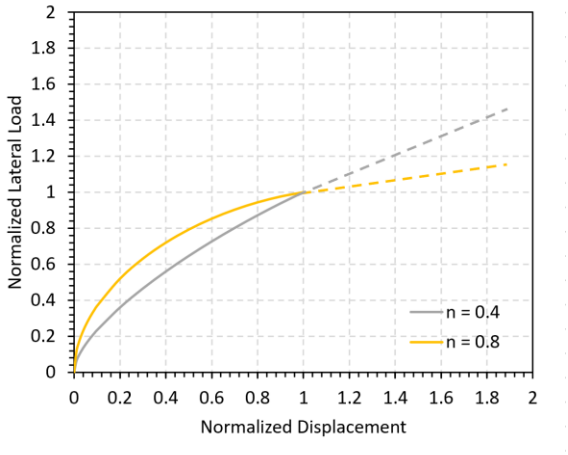

Figure 7.6: Extending the proposed p-y curve out of the range of 0.25% diameter (adjusted from Gilbert et al., 2018).

To verify the performance of the simplified p-y curves, the result of using the simplified p-y curves was compared to the result from 3-D FEM model for Mustang Island test. Figure 7.7 shows that the results are close to each other.

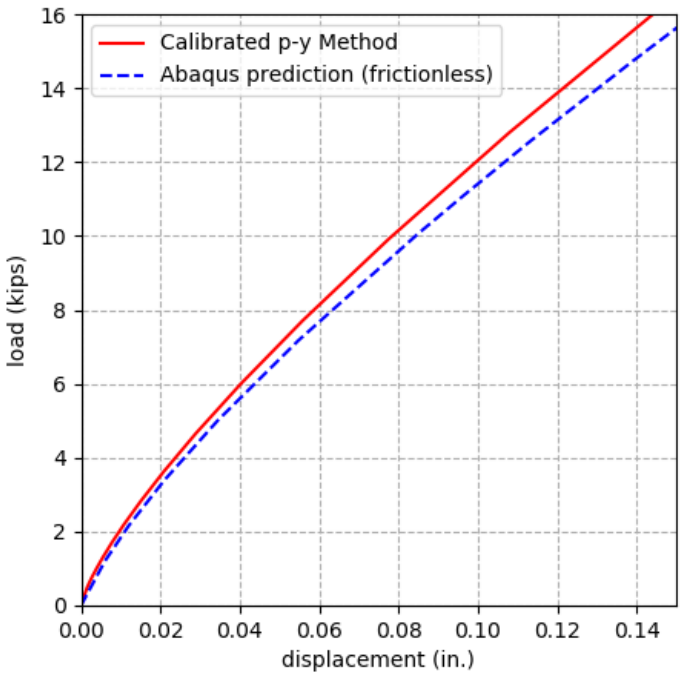

Figure 7.7: Comparison between the load versus displacement curves predicted by the proposed p-y method and 3-D finite element model on Mustang Island Test.

To verify the performance of the simplified p-y curves on the monopiles, a monopile was simulated using the simplified p-y curves and the 3-D FEM model. The pile had a diameter of 195 inches, a wall thickness of 2.36 inches, and a length of 780 inches, which made the ratio of length to the diameter equal to four. Table 7.2 summarizes three different sets of input parameters characterizing the small-stain behavior of sand.

Table 7.2: Parameters of soil used to study proposed parametric model (Gilbert et al., 2018).

	C_{G1} (psi)	n_g	C_1 (%)	C_2	C_3	C_4
Test 1	15069	0.45	0.1	0.5	0.85	0.05
Test 2	11648	0.4	0.05	0.4	0.8	0.01
Test 3	21102	0.43	0.06	0.6	0.75	0.08

Figures 7.8 to 7.10 show the comparisons between the curved derived from the simplified p-y curves and the curves calculated by Abaqus, which have good agreement between the two procedures. The difference in the comparison is because the simplified p-y curves are calibrated from the preliminary parametric study. The simplified p-y curves could be improved by (1) discovering a better expression to describe the shape of the p-y curves, (2) studying the influence of the Poisson's ratio, (3) replacing the parameter of effective vertical stress by using the mean effective stress, (4) non-dimensionalizing all the parameters, and (5) conducting more parametric studies to capture the influence of the input parameters on the shape of the p-y curves.

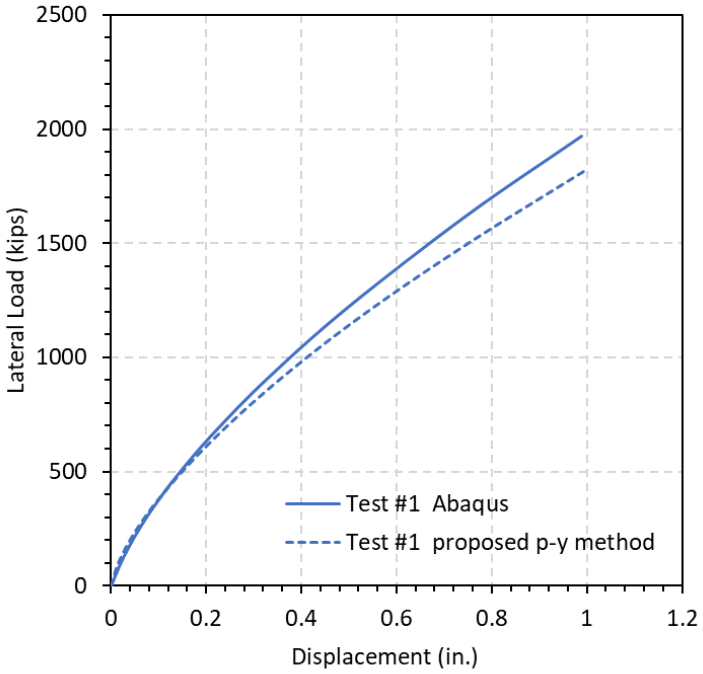

Figure 7.8: Load versus displacement curve from Abaqus model compared with proposed p-y method -Test 1 (Gilbert et al., 2018).

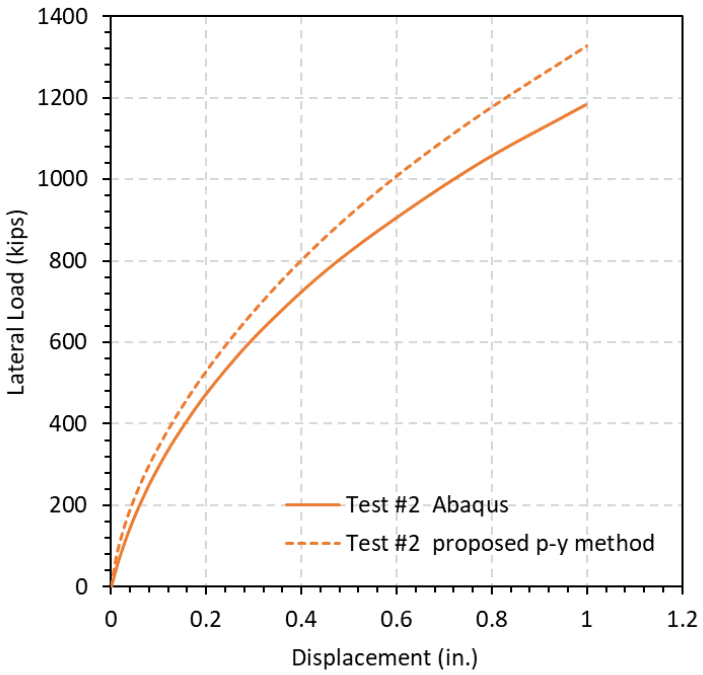

Figure 7.9: Load versus displacement curve from Abaqus model compared with proposed p-y method -Test 2 (Gilbert et al., 2018).

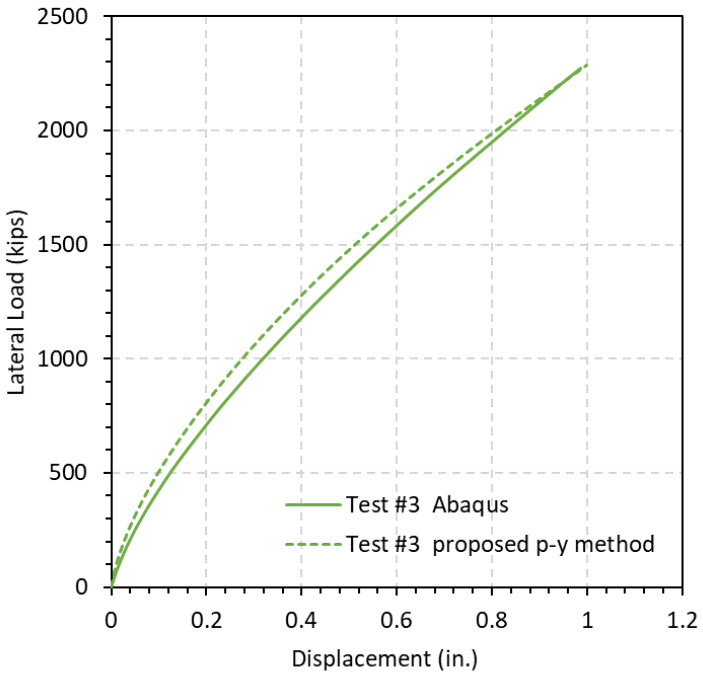

Figure 7.10: Load versus displacement curve from Abaqus model compared with proposed p-y method -Test 3 (Gilbert et al., 2018).

PISA project calibrated a similar simplified p-y curves and an improved 1-D Euler-Bernoulli model in the design recommendation (e.g., Byrne et al., 2017). However, the simplified p-y curves calibrated by PISA project did not capture the non-linearity of the pile response at small lateral displacements as discussed in Section 2.1.5.

7.3 Adjust Initial Portion of API p-y Curves

To incorporate the small-strain properties of the sand into the model of the pile response, the simplest and most practical approach would be relating the initial portion of the API p-y curves with the maximum shear modulus, G_{max}. However, it is difficult to find an explicit and theoretical relationship between the initial portion of a p-y curve and

G_{max} because of (1) the stiffness changing with mean effective stress (which increases as the pile is loaded), and (2) the three-dimensional complexity induced by the free-surface boundary at the top of the soil. Though this approach could be calibrated by the results of field tests or approximated using numerical 3-D FEM analyses as the "true" solution, this approach still could not capture the non-linearity of the initial portion of the p-y curves measured in the field tests and estimated from the FEM models.

Chapter 8: Conclusions

The following major conclusions are drawn from this research:

(1) The analysis on existing results from field laterally-loaded piles tests in sand shows the following:

   (a) The initial lateral load versus displacement relationship in the field laterally-loaded piles test is non-linear, which is not captured by using an elastic subgrade modulus, k, determined by the internal friction angle of soil in the conventional design approach.

   (b) The p-y method from the conventional design approach underestimates the initial stiffness for field laterally-loaded piles tests in sand, and the underestimation is larger in the monopiles tests than in the slender piles tests.

   (c) In the design of laterally-loaded monopiles in sand, the p-y method from the conventional design approach also underestimates the ultimate capacity of the laterally-loaded monopiles at large displacements. However, for the design of laterally-loaded slender piles in sand, the p-y method still has a good agreement with the measured ultimate capacity.

(2) The comparison of measured and designed natural frequencies for offshore wind turbines at Belwind and Northwind illustrates the following:

   (a) The conventional design approach using p-y method underestimates the natural frequencies for offshore wind turbines. In addition, the measured natural frequencies of these wind turbines have been increasing with time and the increase of second natural frequency is more significant than the increase of the fundamental natural frequency.

(b) The designed natural frequencies of offshore wind turbines are sensitive to the accurate evaluation of the pile-soil stiffness determined by the elastic subgrade modulus, k, of sand. The natural frequencies increase the value of k, and k needs to be increased by more than five times to match the field observations. Increasing of k has a larger influence on the second natural frequency than on the fundamental natural frequency.

(c) For the monopiles in the Belwind Offshore Wind Farm under service loading, the predicted lateral displacement at mudline is less than 0.05% of the pile diameter by using the calibrated k to match the field observation.

(3) The development of the proposed soil constitutive model shows the following:

(a) The model of small-strain behavior for sand, Menq (2003), matches the non-linearity of the sand stiffness measured from resonant column and torsional shear (RCTS) tests on two different samples of sand: (1) the sand used in the laboratory foundation model tests and (2) the sand collected from Mustang Island.

(b) The prediction of the proposed soil constitutive model based on Menq (2003) has a good agreement with the measured data from laboratory tests including resonant column tests, torsional shear tests, and dynamic triaxial tests. To be more credible, the relationship of maximum shear modulus, G_{max}, with the mean effective stress and the relationship of normalized shear modulus with the shear strain and mean effective stress must be modified based on RCTS tests.

(c) At relatively low strain levels, the prediction of the hysteretic behavior of the proposed soil constitutive model has a good agreement with the actual data measured from the torsional shear tests.

(4) The analysis on the results of the laboratory foundation model tests, which the sphere is embedded and laterally pushed to simulate the state of stress and strain around a laterally-loaded monopiles, shows the following:

(a) In the laboratory foundation model tests, the initial relationship between lateral load and lateral displacement is non-linear, even at extremely small displacements.

(b) The predictions of the 3-D FEM models with the proposed soil constitutive model capture the non-linearity and the stiffness in the laboratory foundation model tests at small displacements. To achieve the best performance of the 3-D FEM model, the proposed soil constitutive model needs to be modified based on in-situ shear velocity profiles, small-strain behavior of sand measured from RCTS tests, large-strain behavior of sand measured from triaxial compression (TRX) tests.

(5) The analysis on the results of the field tests, including the shallow foundation tests conducted at NGES and the laterally-loaded pile tests carried out on Mustang Island, shows the following:

(a) The predictions of the 3-D FEM models with the proposed soil constitutive model, which is based on field measurement of shear velocity and RCTS tests and TRX tests on laboratory tests, match well with the measured results of the field foundation tests at small displacements. The constitutive model modified by TRX tests still needs

to have a reasonable agreement with the results of RCTS tests at small strains.

(b) In the Mustang Island test, the 3-D FEM model is able to predict the response of the laterally-loaded pile at large displacements with a reasonable contact friction coefficient between the pile and the soil.

(c) To make the 3-D FEM model have a good prediction on the lateral load versus displacement curve at large displacements, a reasonable friction coefficient between the pile and soil should be added in the FEM model.

These conclusions lead to following recommendations for design of laterally loaded monopiles in sand:

(1) The conventional p-y methods do not have a good prediction on the initial stiffness and the non-linearity of laterally loaded pile at the small lateral displacements which govern the design of offshore wind turbine monopiles under service loading.

(2) In order to improve the prediction on the initial stiffness and the non-linearity of laterally loaded piles at small displacements, it is necessary to empirically establish or measure directly for the sand the in-situ maximum shear modulus profile, the relationship between shear modulus and shear strain, the relationship between shear modulus and mean effective stress.

(3) The p-y curves used for design of offshore wind turbine monopiles under service loading condition should be revised based on the small-strain properties of the site-specific soils

Future work is recommended in the following areas to better integrate the results from this research into practice:

(1) To better understand the complicated behavior of laterally loaded monopiles subjected to cyclic loading in service condition, additional analyses need to be conducted on the monitoring data from offshore wind turbine farm and field tests data (e.g., the PISA laterally loaded monopiles in sand).

(2) To simulate the stiffening and the accumulated displacement (or strain) during cyclic loading, the soil constitutive model needs to be improved to accommodate the laboratory tests and field monitoring.

(3) To calibrate a simpler and better p-y curves, more parametric study needs to be conducted to characterize the behavior of the soil reaction around laterally loaded piles at small displacements.

Appendices

APPENDIX A: TORSIONAL SHEAR TEST ON ALL-PURPOSE SAND

University of Texas at Austin

RCTS Testing

SXRG03
Total Unit Weight
γ_t = 105.83 pcf (1.70 g/cm^3)
Dry Unit Weight
γ_d = 105.83 pcf (1.70 g/cm^3)
Initial Void Ratio, e = 0.56
Water Content, w_c = 0.08%
Assumed Specific Gravity, G_s = 2.65
Degree of Saturation, S_r = 0.4%
Relative Density*, D_r= 28%

C_u = 4.9
Minimum Void Ratio, e_{min}*= 0.34
Maximum Void Ratio, e_{max}* = 0.64
(*From Youd, 1973)

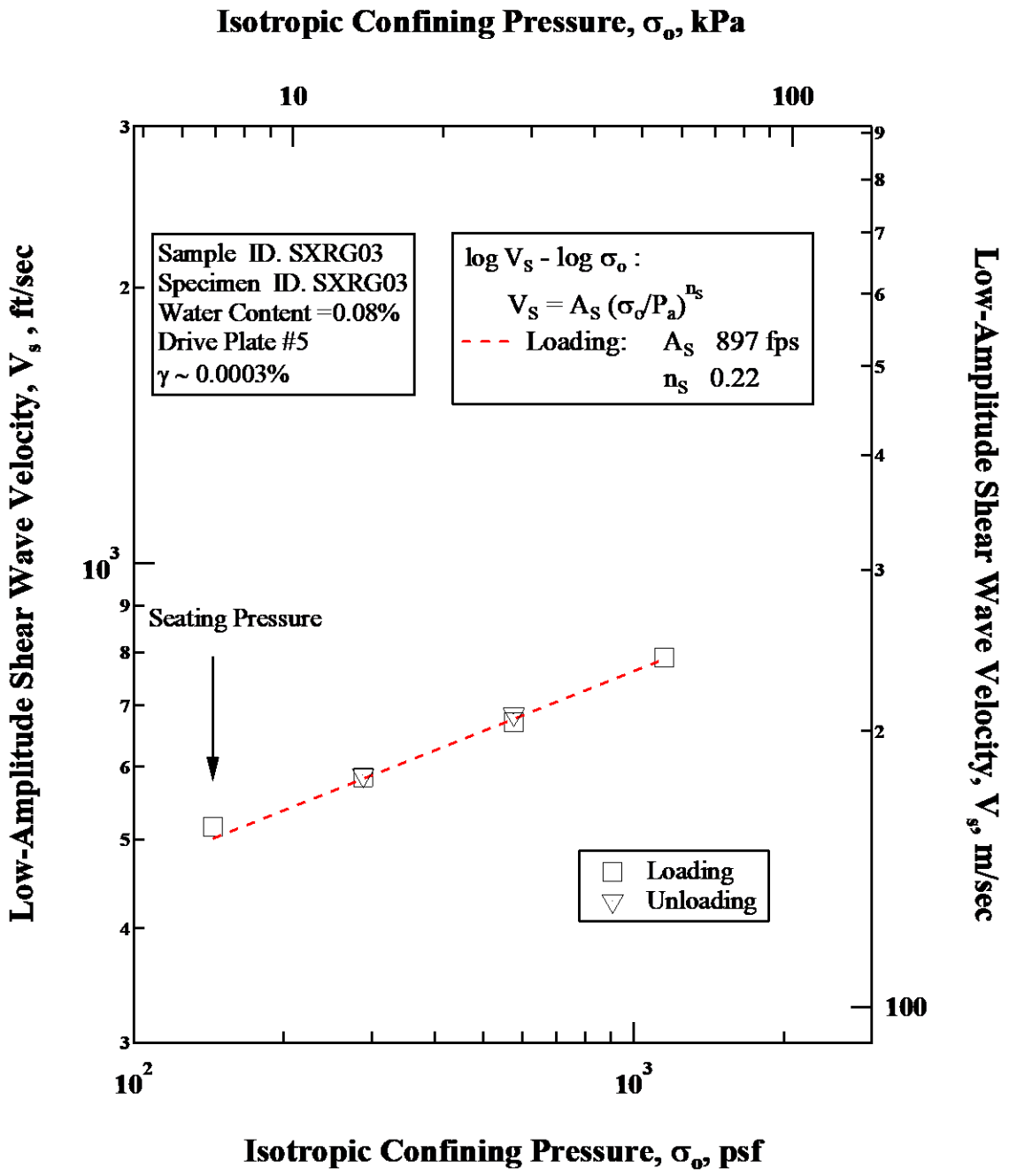

Figure A.1: Variation in Low-Amplitude Shear Wave Velocity with Isotropic Confining Pressure from Resonant Column Tests of Sample SXRG03.

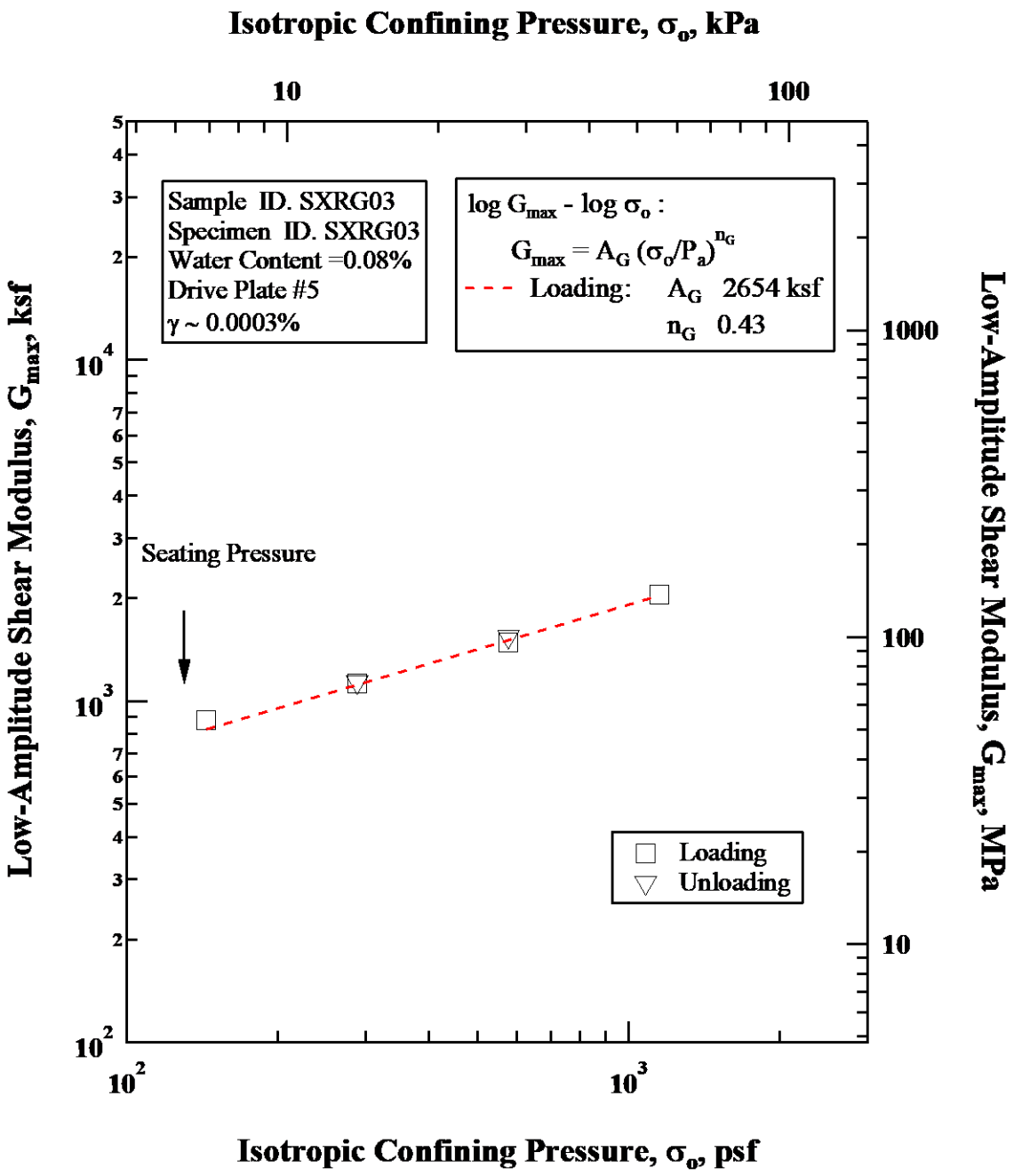

Figure A.2: Variation in Low-Amplitude Shear Modulus with Isotropic Confining Pressure from Resonant Column Tests of Sample SXRG03.

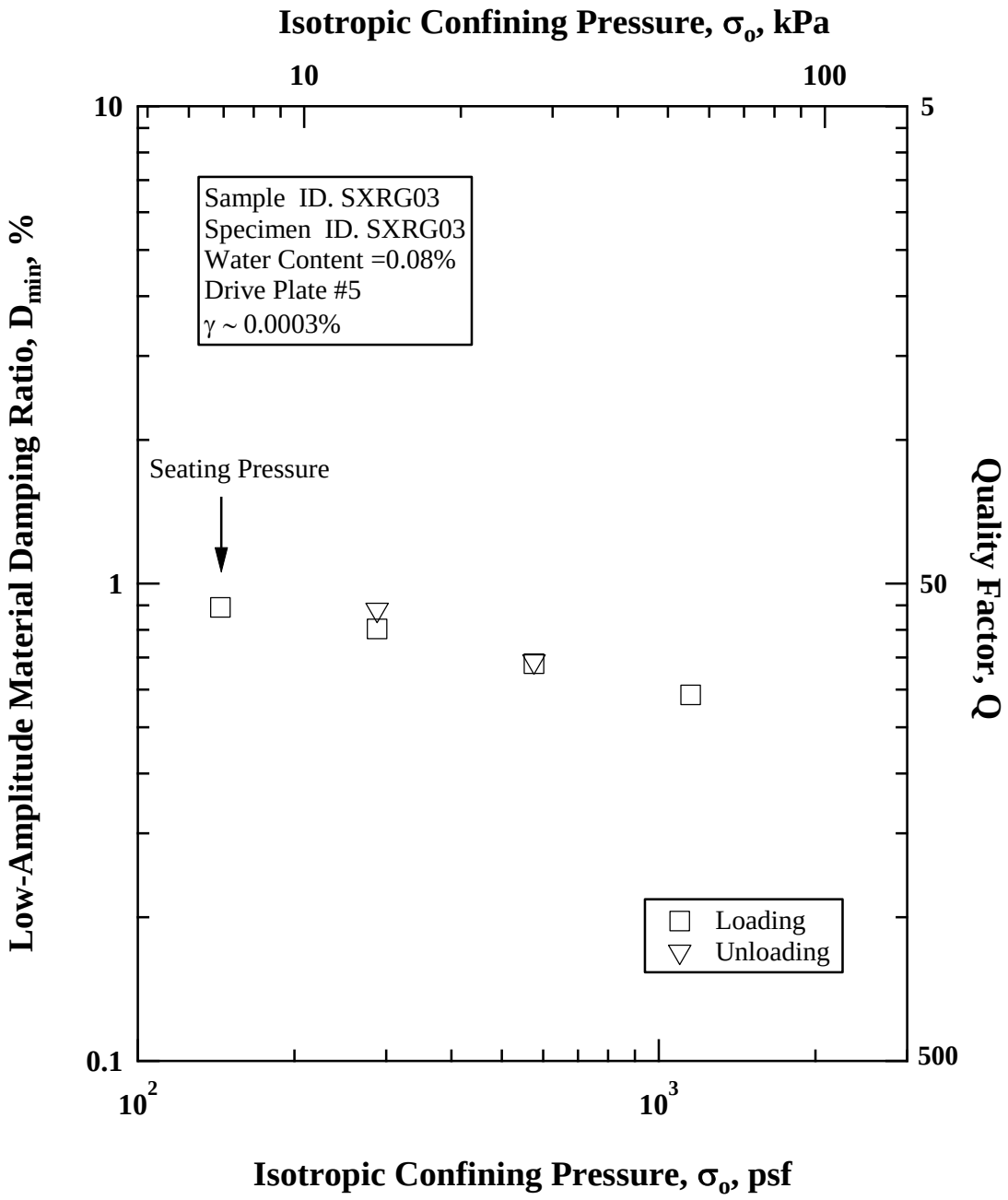

Figure A.3: Variation in Low-Amplitude Material Damping Ratio with Isotropic Confining Pressure from Resonant Column Tests of Sample SXRG03.

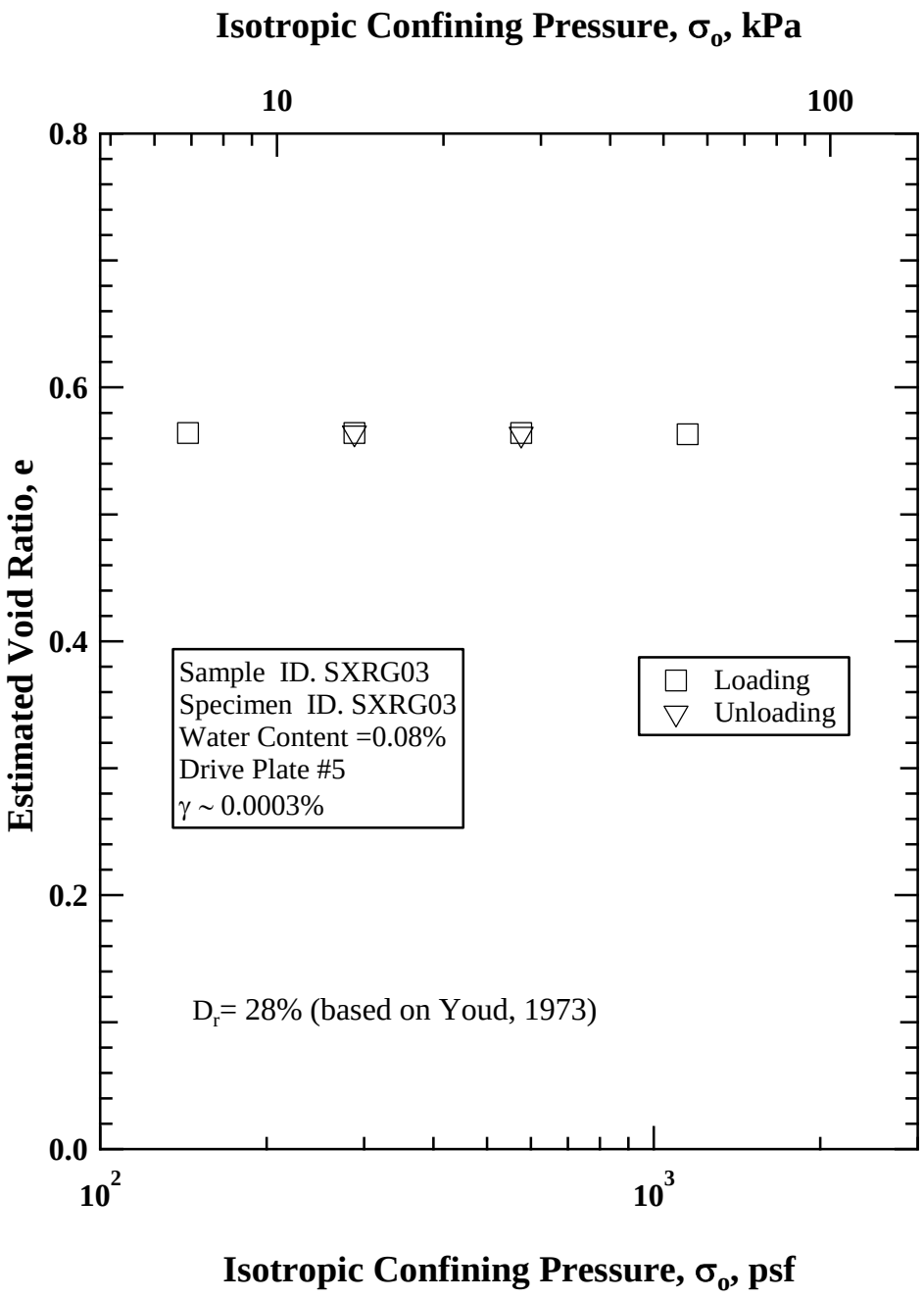

Figure A.4: Variation in Void Ratio with Isotropic Confining Pressure from Resonant Column Tests of Sample SXRG03.

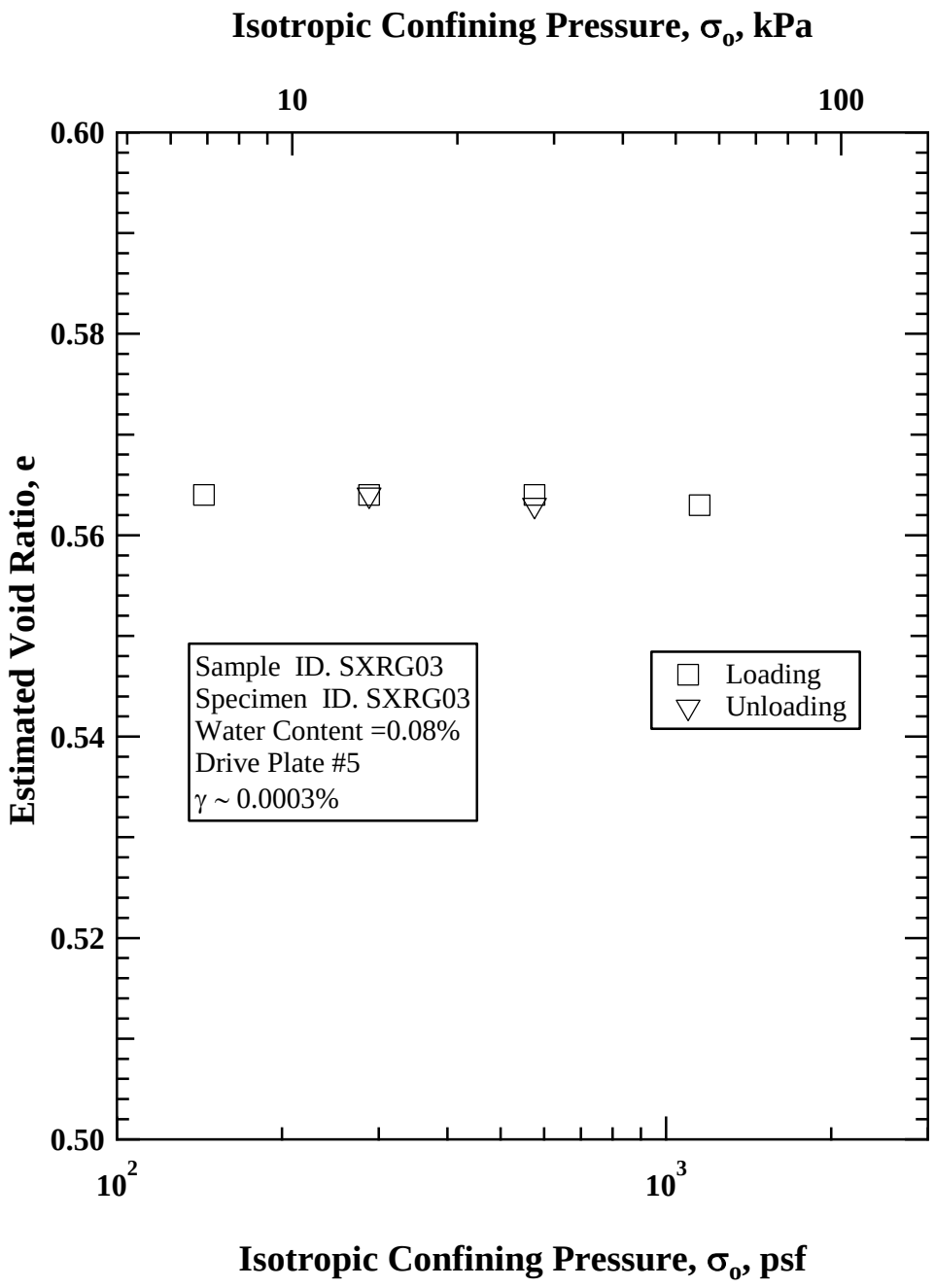

Figure A.5: Variation in Void Ratio with Isotropic Confining Pressure from Resonant Column Tests of Sample SXRG03.

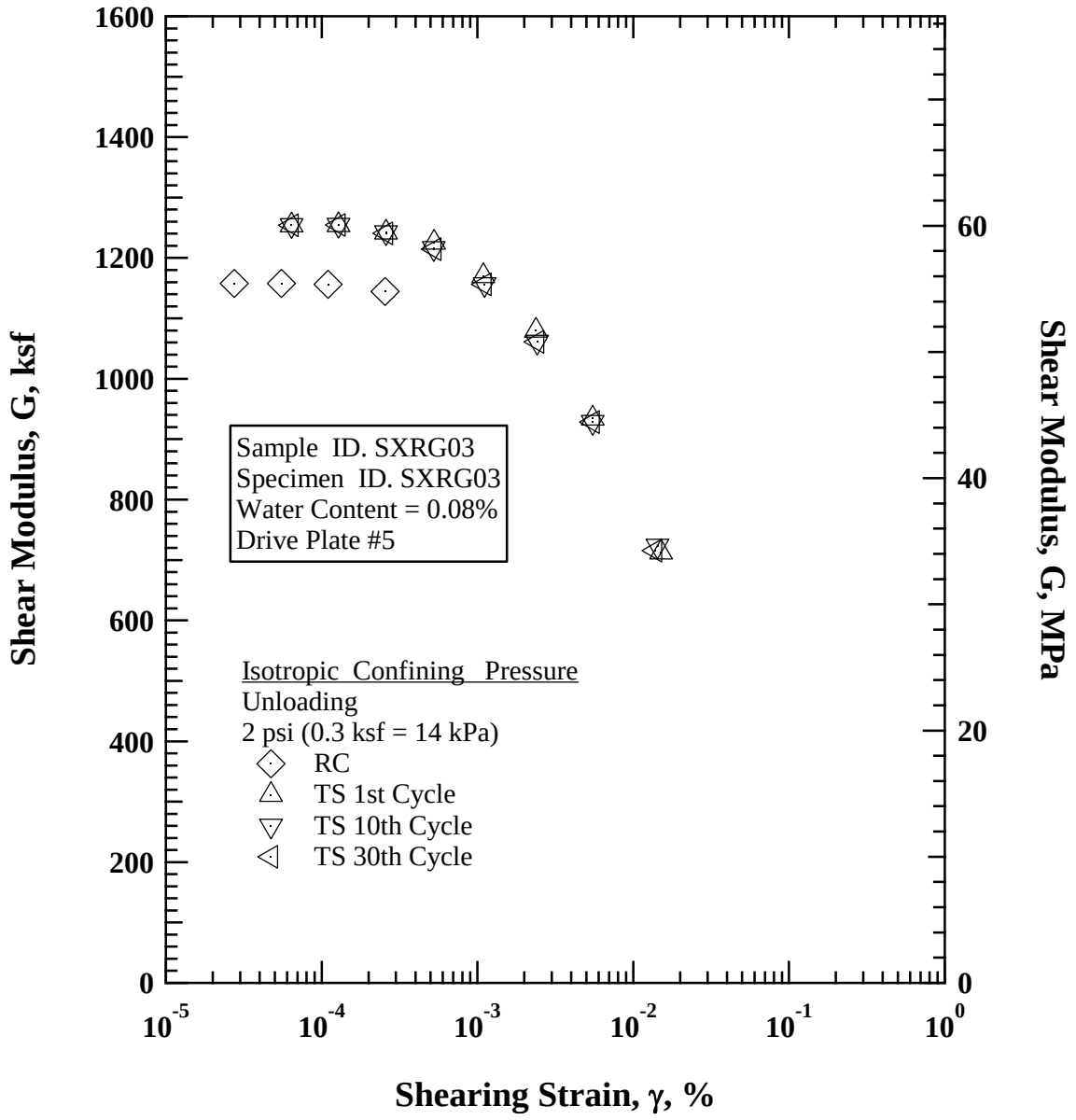

Figure A.6: Comparison of the Variation in Shear Modulus with Shearing Strain at an Isotropic Loading Confining Pressure of 2 psi (0.3 ksf = 14 kPa) from Combined RCTS Tests of SXRG03

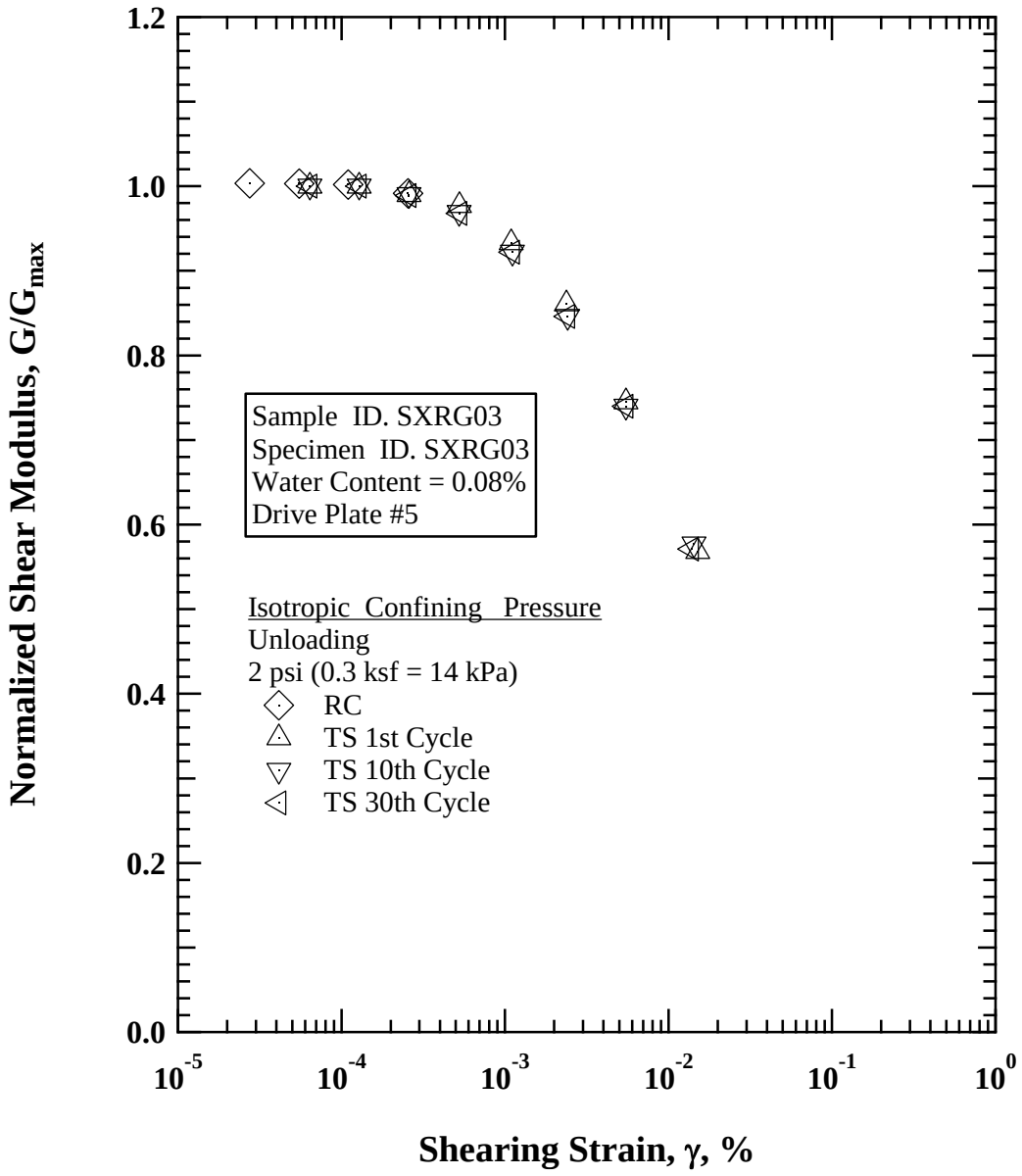

Figure A.7: Comparison of the Variation in Normalized Shear Modulus with Shearing Strain at an Isotropic Loading Confining Pressure of 2 psi (0.3 ksf = 14 kPa) from Combined RCTS Tests of SXRG03.

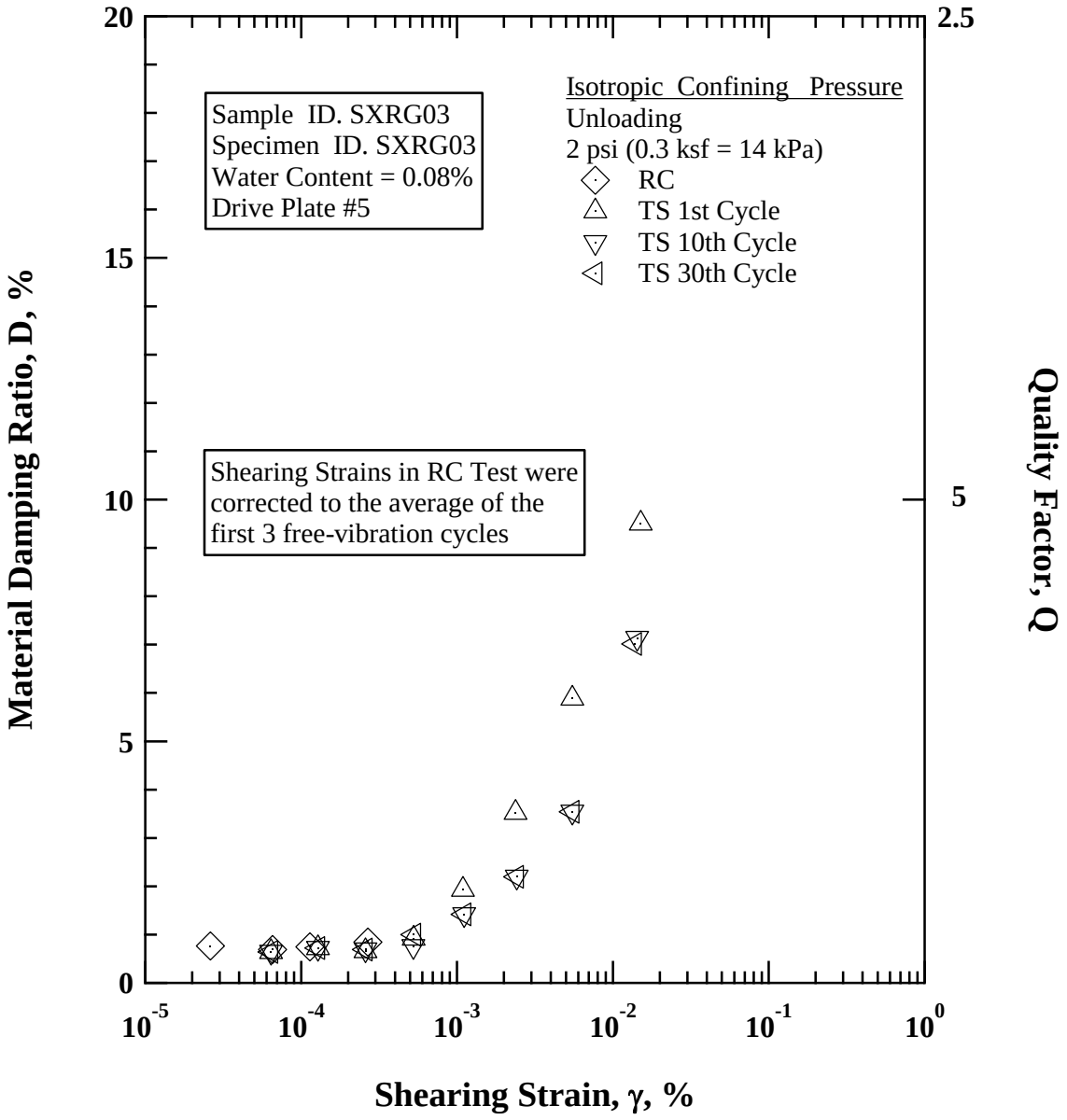

Figure A.8: Comparison of the Variation in Material Damping Ratio with Shearing Strain at an Isotropic Loading Confining Pressure of 2 psi (0.3 ksf = 14 kPa) from Combined RCTS Tests of SXRG03.

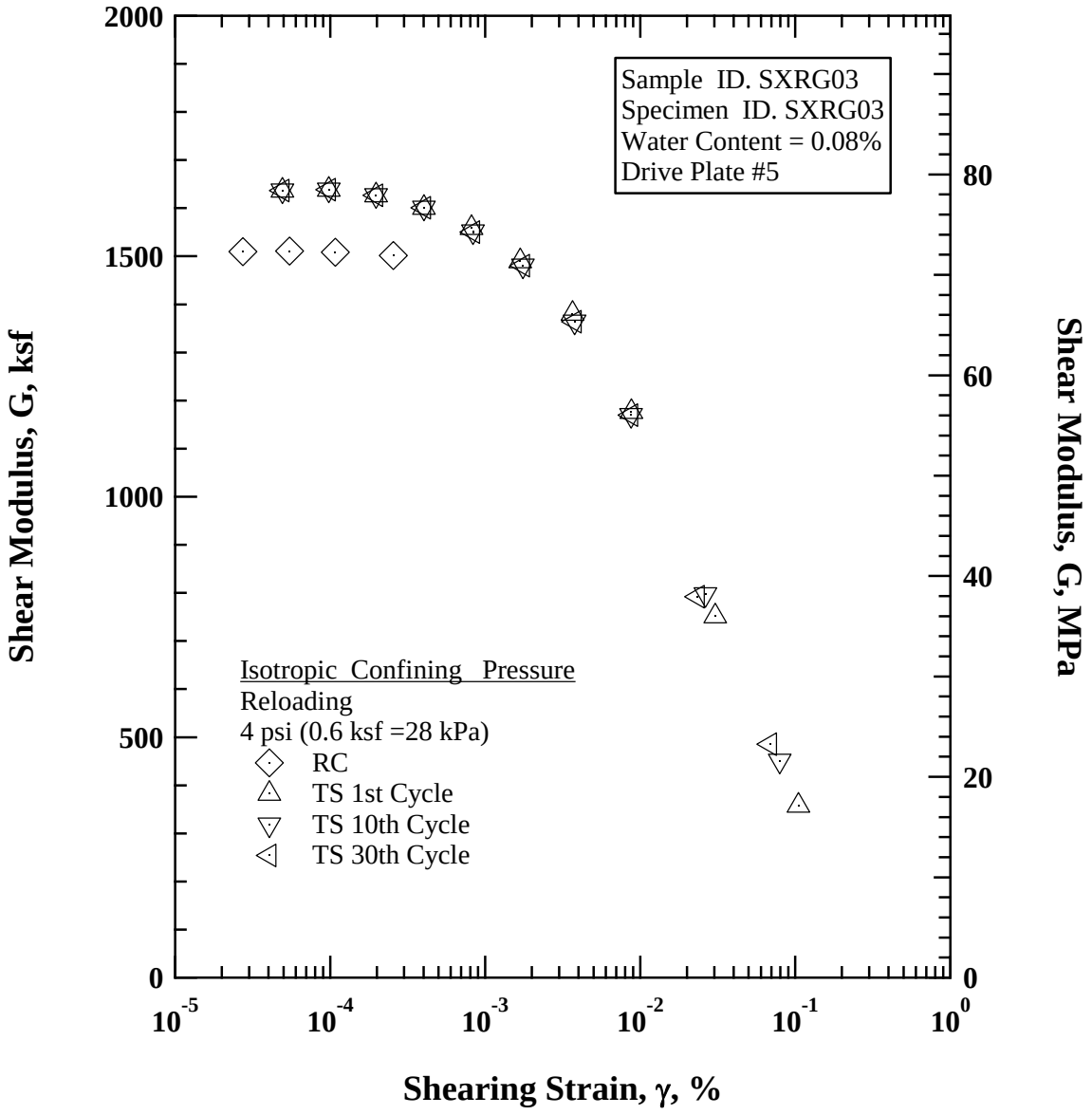

Figure A.9: Comparison of the Variation in Shear Modulus with Shearing Strain at an Isotropic Loading Confining Pressure of 4 psi (0.6 ksf = 28 kPa) from Combined RCTS Tests of SXRG03.

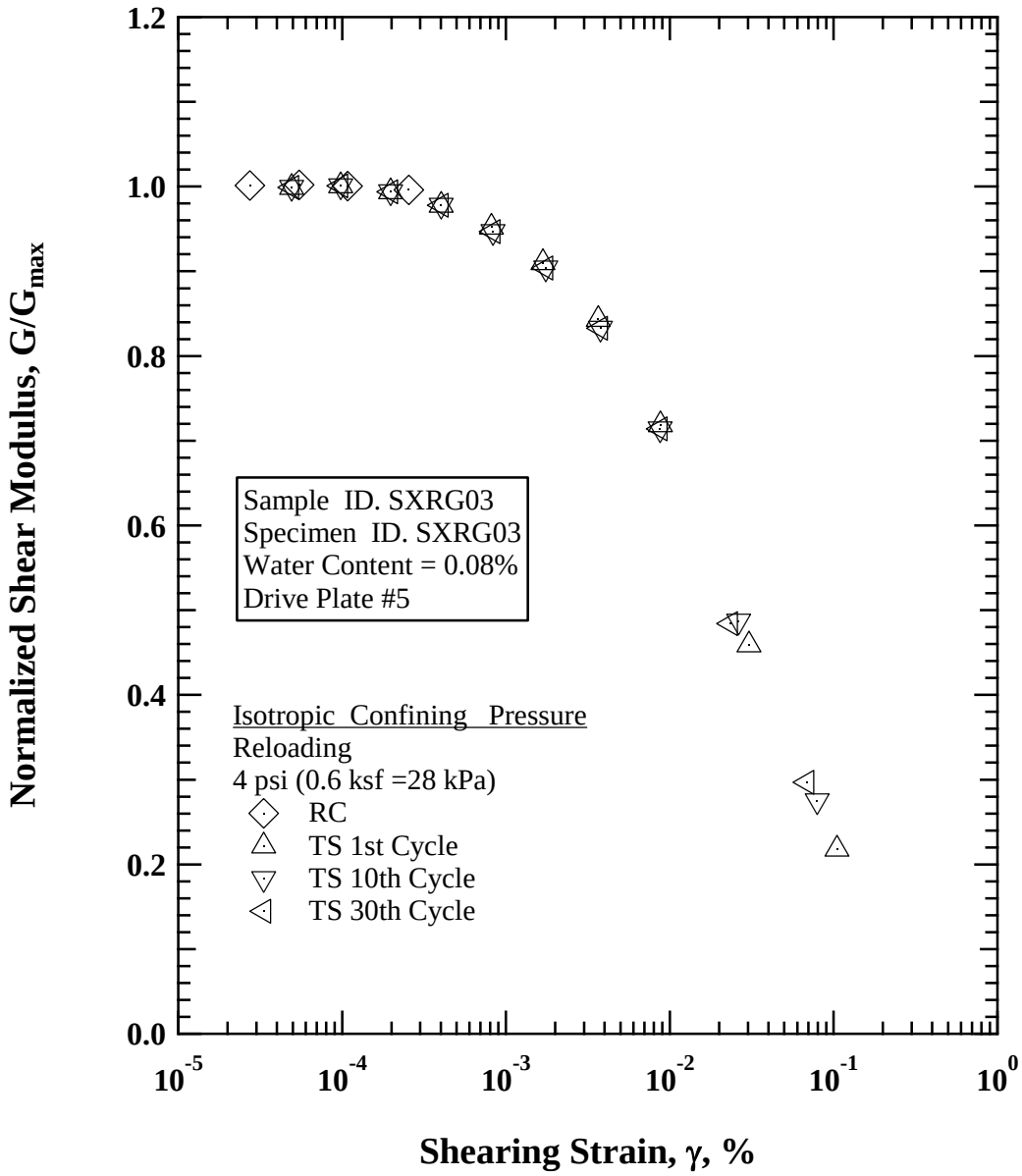

Figure A.10: Comparison of the Variation in Normalized Shear Modulus with Shearing Strain at an Isotropic Loading Confining Pressure of 4 psi (0.6 ksf = 28 kPa) from Combined RCTS Tests of SXRG03.

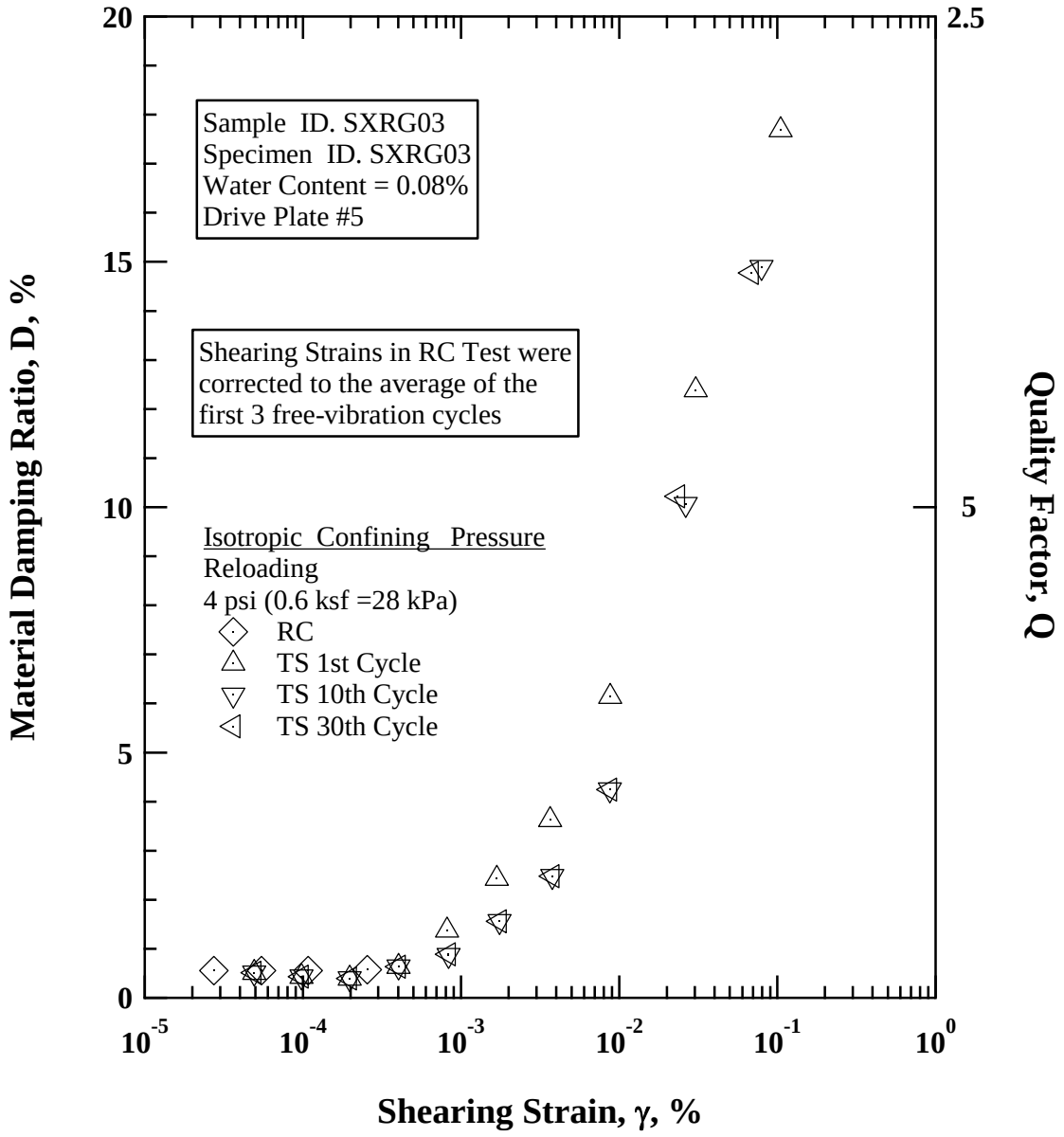

Figure A.11: Comparison of the Variation in Material Damping Ratio with Shearing Strain at an Isotropic Loading Confining Pressure of 4 psi (0.6 ksf = 28 kPa) from Combined RCTS Tests of SXRG03.

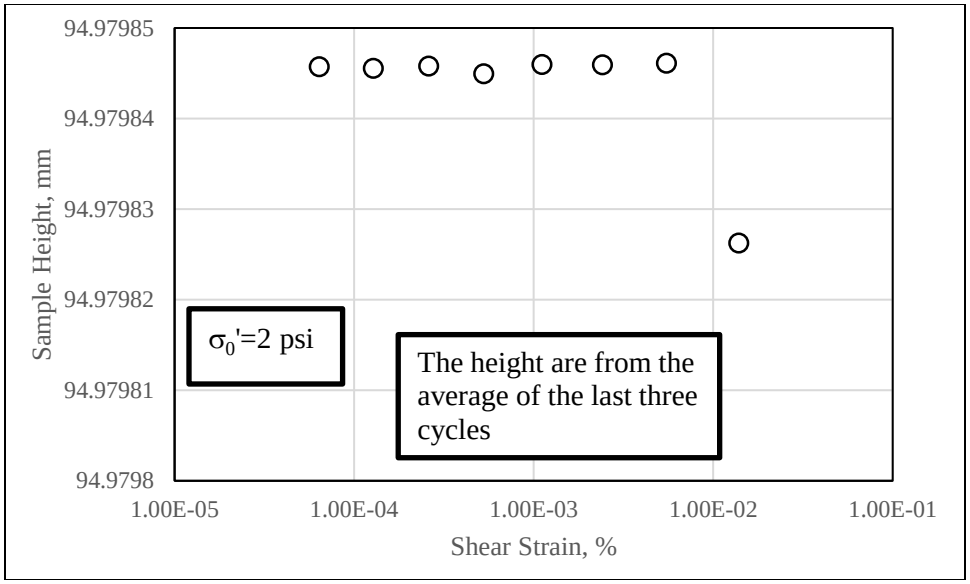
94.97985
94.97984
94.97983
94.97982
94.97981
94.9798
Sample Height, mm
σ_0'=2 psi
The height are from the average of the last three cycles
1.00E-05
1.00E-04
1.00E-03
1.00E-02
1.00E-01
Shear Strain, %

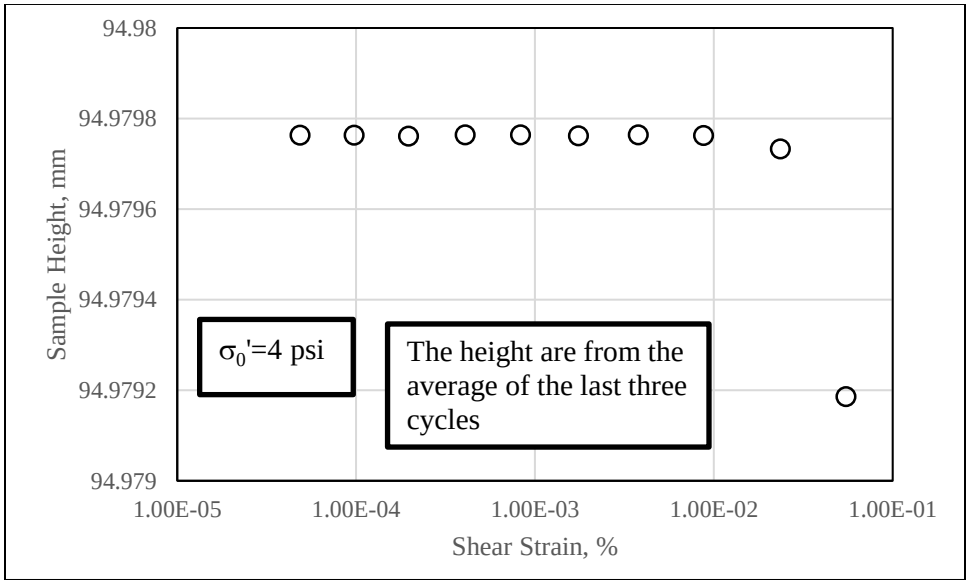
94.98
94.9798
94.9796
94.9794
94.9792
94.979
Sample Height, mm
σ_0'=4 psi
The height are from the average of the last three cycles
1.00E-05
1.00E-04
1.00E-03
1.00E-02
1.00E-01
Shear Strain, %

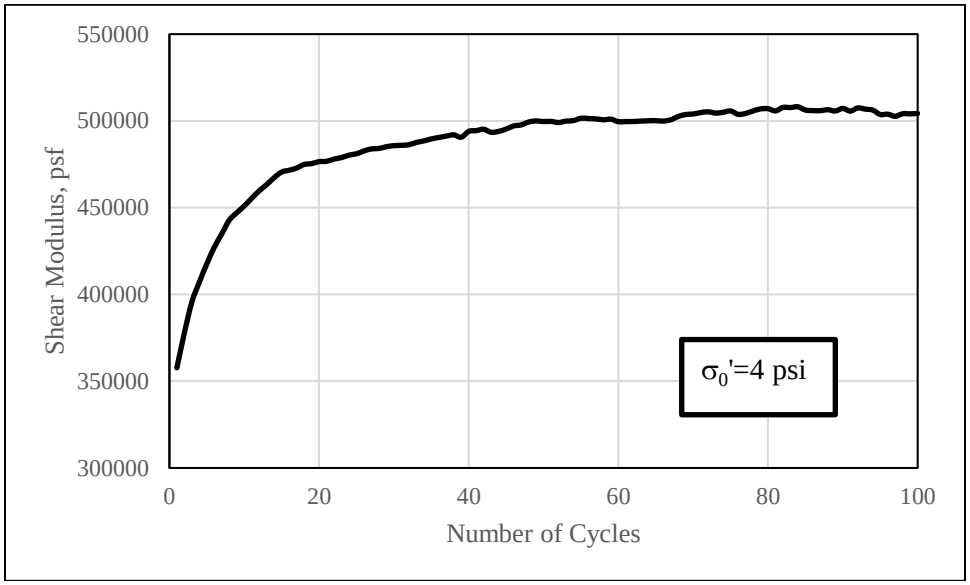
550000
500000
450000
400000
350000
300000
Shear Modulus, psf
0
20
40
60
80
100
Number of Cycles
σ0'=4 psi

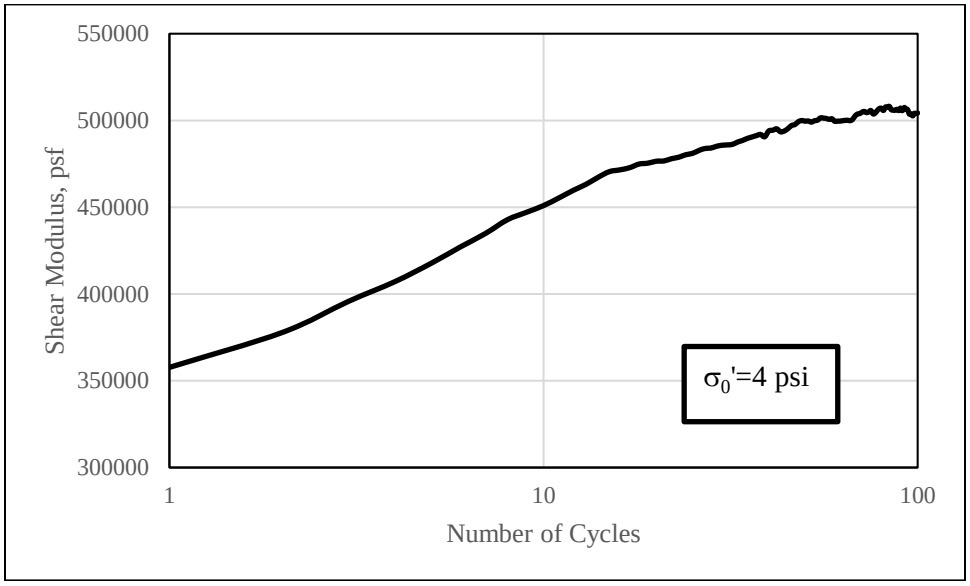
550000
500000
450000
400000
350000
300000
Shear Modulus, psf
1
10
100
Number of Cycles
σ0'=4 psi

APPENDIX B: RESONANT COLUMN TEST ON MUSTANG ISLAND SAND

University of Texas at Austin

RCTS Testing

Total Unit Weight
γ_t = 119.24 pcf (1.91 g/cm^3)
Dry Unit Weight
γ_d = 99.39 pcf (1.59 g/cm^3)
Void Ratio, e = 0.67
Water Content = 20.32%
Specific Gravity = 2.65
Degree of Saturation = 80.97%

C_u = 1.31
Minimum Void Ratio, e_{min} = 0.50
Maximum Void Ratio, e_{max} = 1.02
(From Youd, 1973)

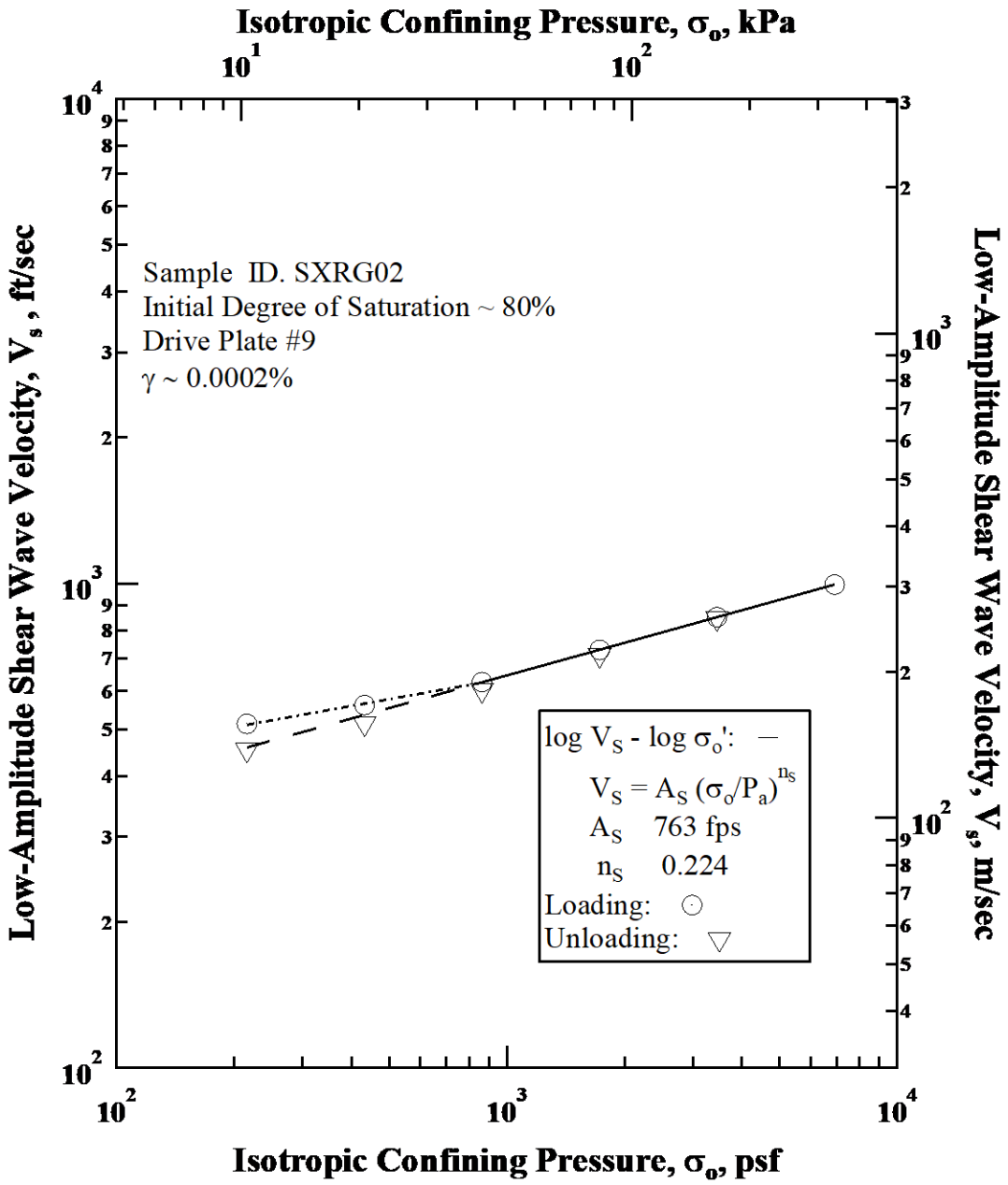

Figure B.1: Variation in Low-Amplitude Shear Wave Velocity with Isotropic Confining Pressure from Resonant Column Tests of Sample SXRG02.

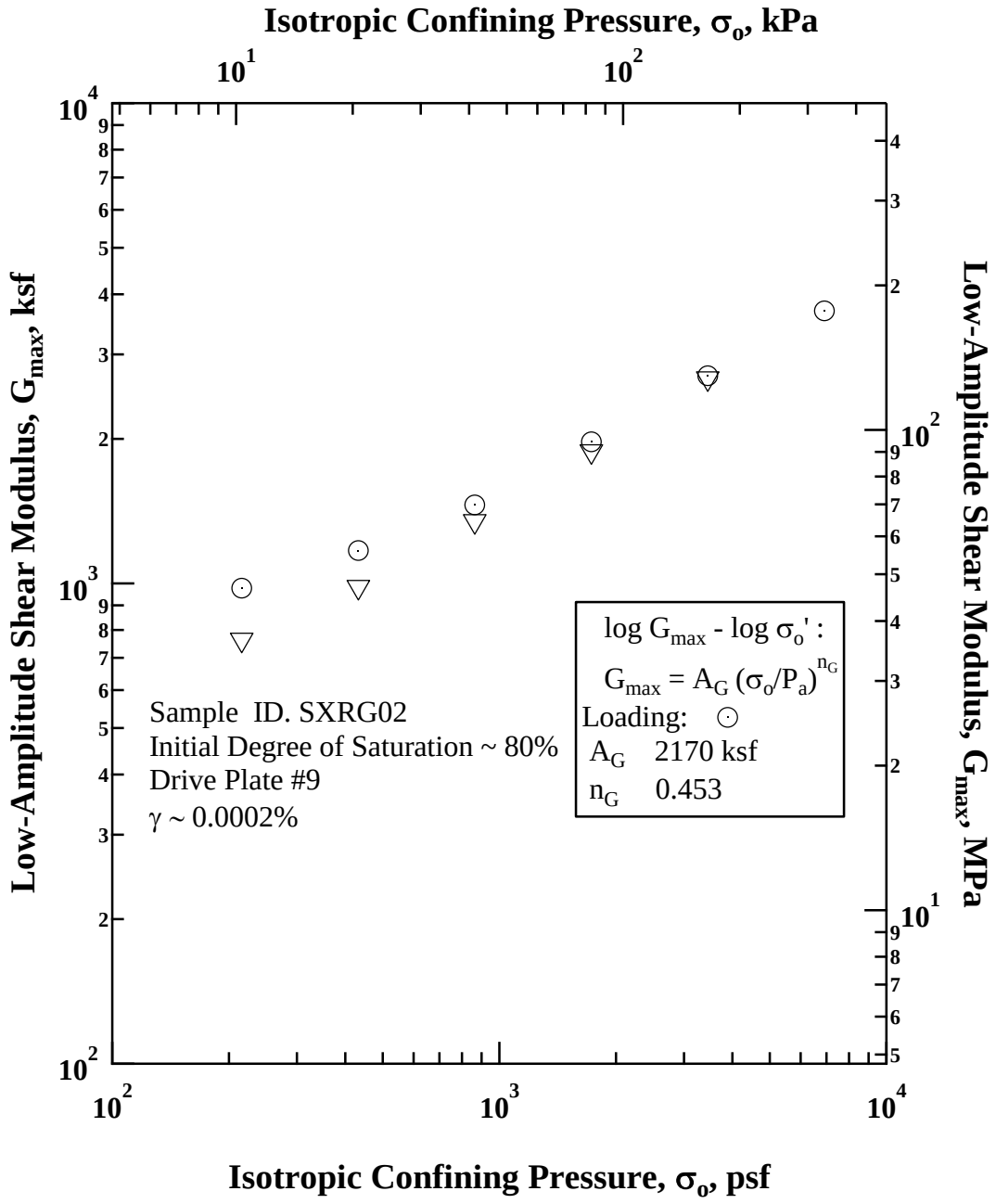

Figure B.2: Variation in Low-Amplitude Shear Modulus with Isotropic Confining Pressure from Resonant Column Tests of Sample SXRG02.

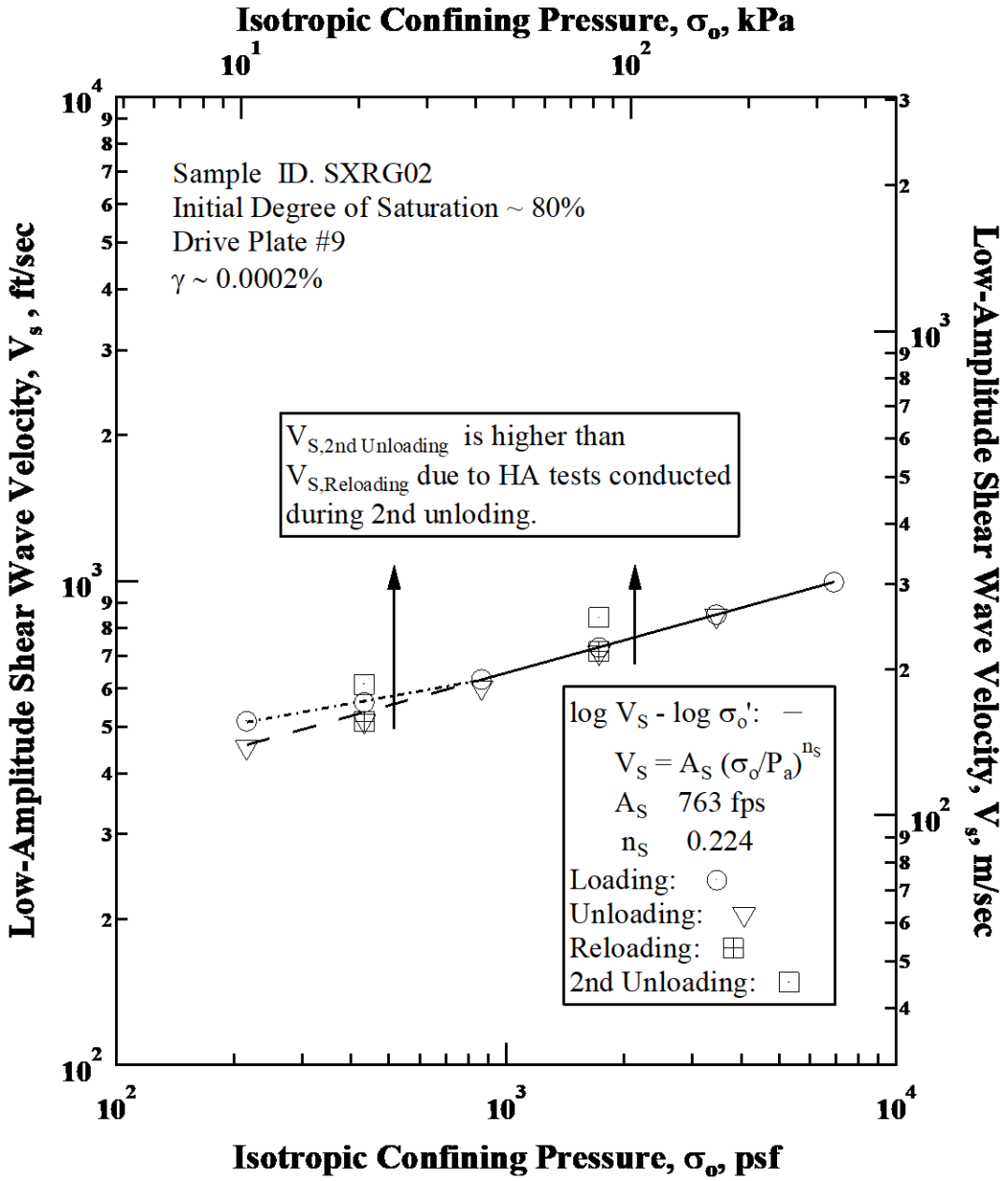

Figure B.3: Variation in Low-Amplitude Shear Wave Velocity with Isotropic Confining Pressure from Resonant Column Tests of Sample SXRG02.

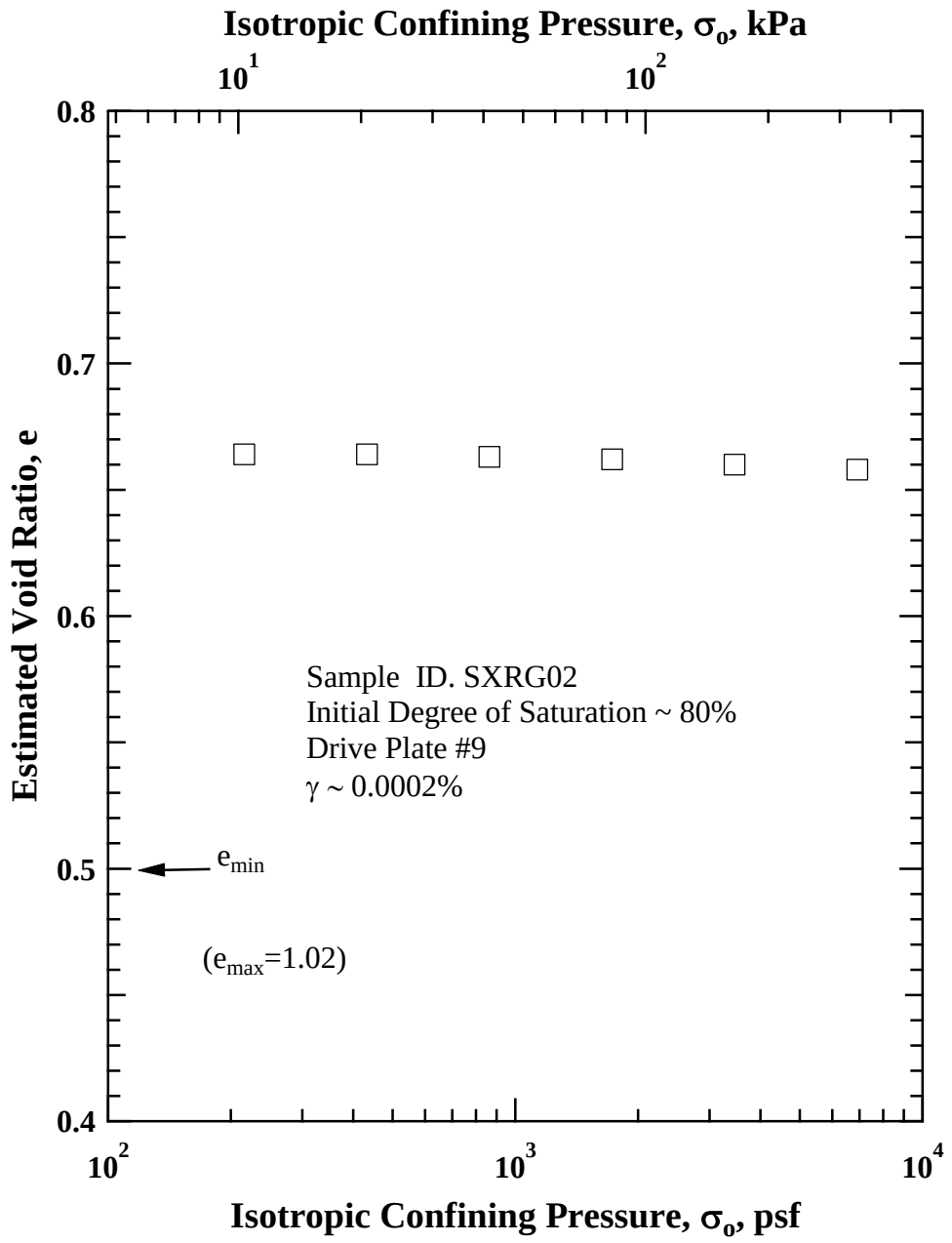

Figure B.4: Variation in Void Ratio with Isotropic Confining Pressure from Resonant Column Tests of Sample SXRG02.

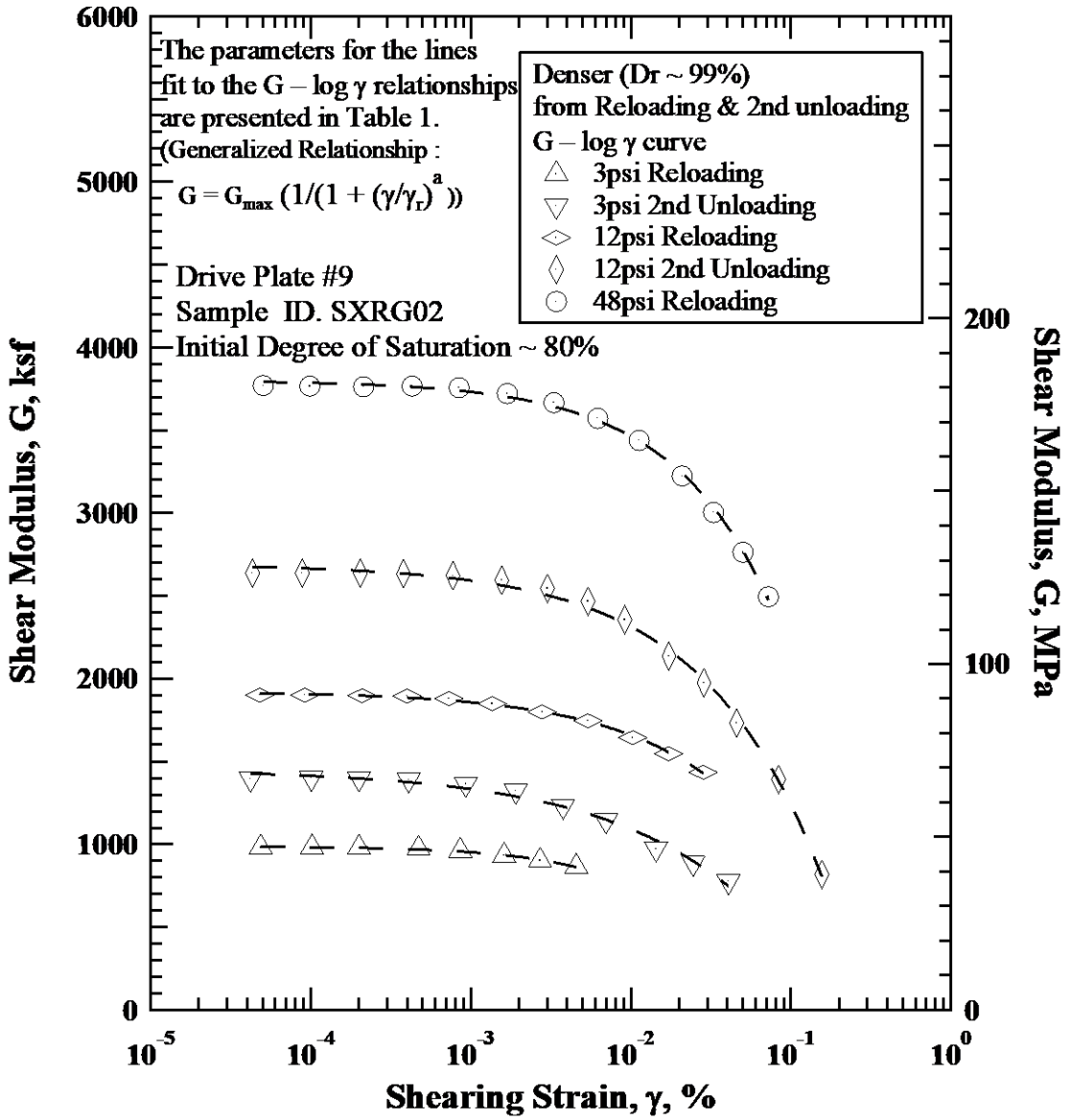

Figure B.5: Variations in Shear Modulus with Shearing Strain at Two Effective Isotropic Confining Pressures of 4, 16 psi from Resonant Column Tests of Specimen SXRG02.

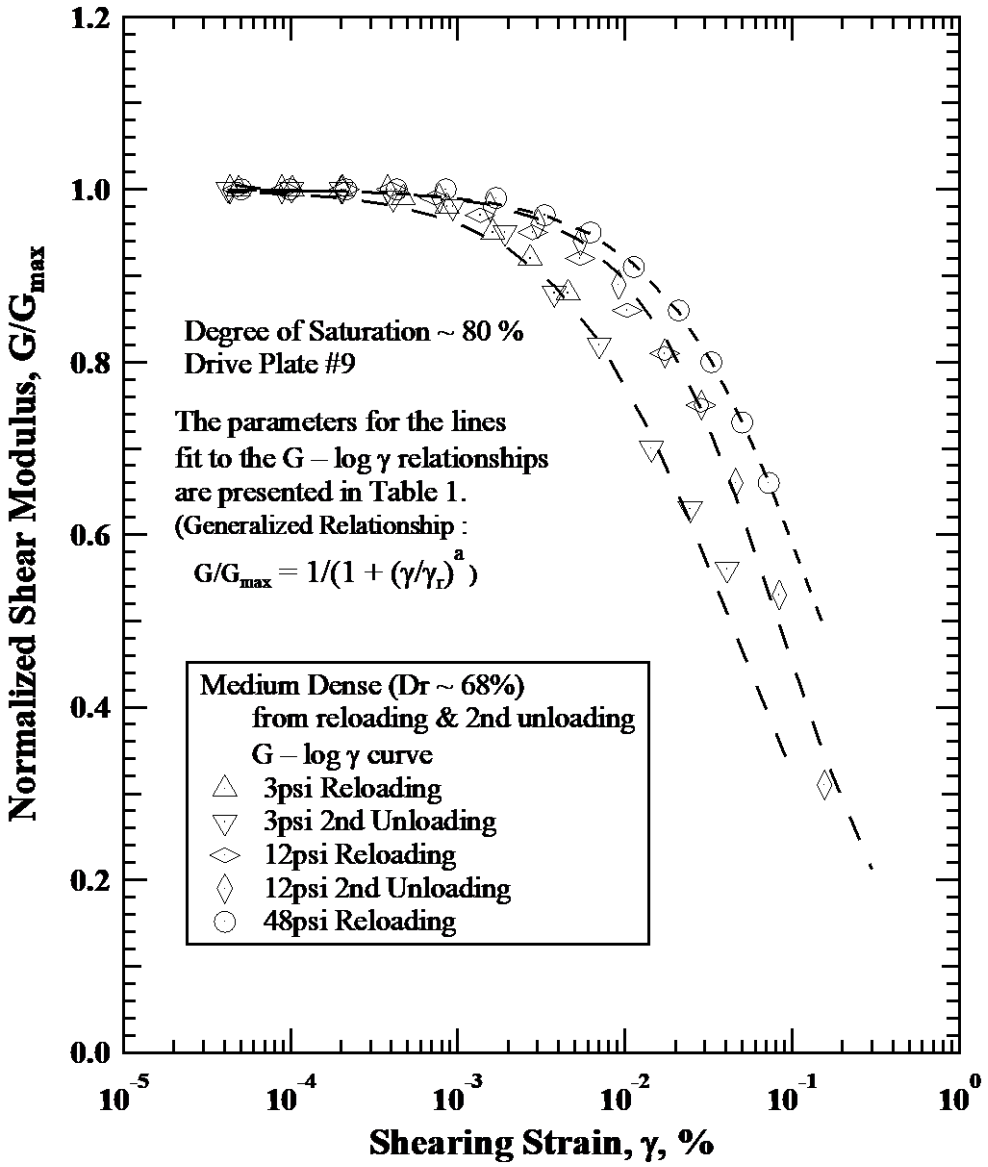

Figure B.6: Variations in Normalized Shear Modulus with Shearing Strain at Three Effective Isotropic Confining Pressures of 3, 12, 48 psi from Resonant Column Tests of Specimen SXRG02.

Table B.1: Parameters Fit to the $G - \mathrm{Log}\,\gamma$ Relationships from Resonant Column Tests of Denser Specimen SXRG02.

Specimen ID.	Confining Pressure (psi)	Estimated Relative Density, D_r1, (%)	Void Ratio, e	Elastic Threshold γ_t^{e2} (%)	Modified Hyperbolic Relationship[3]	
					γ_r (%)	a
SXRG02	3	69	0.659	0.00045	0.042	0.857
	12	71	0.651	0.00177	0.082	1.014
	48	70	0.653	0.00211	0.150	0.913
Notes:	1. $D_r = (e_{max} - e)/(e_{max} - e_{min}) \times 100\%$, e_{max} and e_{min} are estimates based on Youd, 1973, 2. $\gamma_t^e =$ shear strain at which $G/G_{max} =$ 0.98, 3. Modified hyperbolic relationship: $G/G_{max} = 1/(1 + (\gamma/\gamma_r)^a)$, where G_{max} = small-strain shear modulus γ_r = reference shear strain, and, a = curvature coefficient.					

APPENDIX C: SASW TEST AT MUSTANG ISLAND

Figure C.1: Locations of the Three SASW Testing Arrays that were Performed Around the Site on Mustang Island.

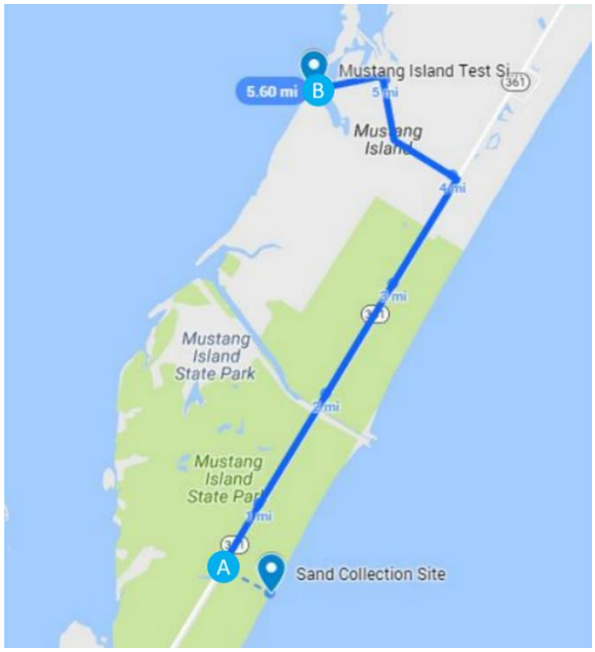

Figure C.2: Mustang Island with Locations of the Original Sample-Collection Site (Site A) and the SASW Test Site (Site B) Where Seismic Vs Profiling was Performed and a Second Soil Sample was Collected.

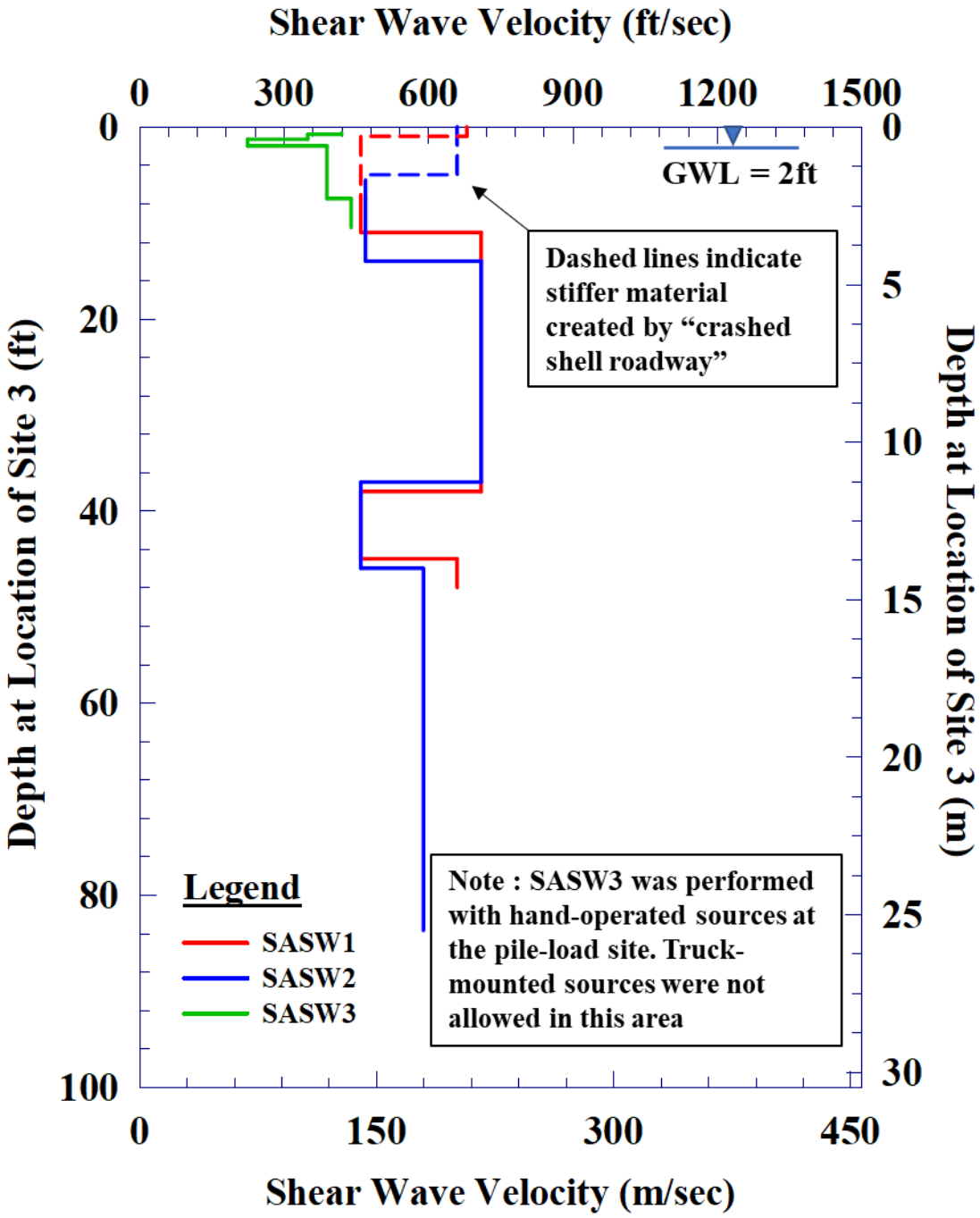

Figure C.3: Comparison of the Three, Shear-Wave Velocity Profiles Determined at Site B on Mustang Island (See Figure C.2).

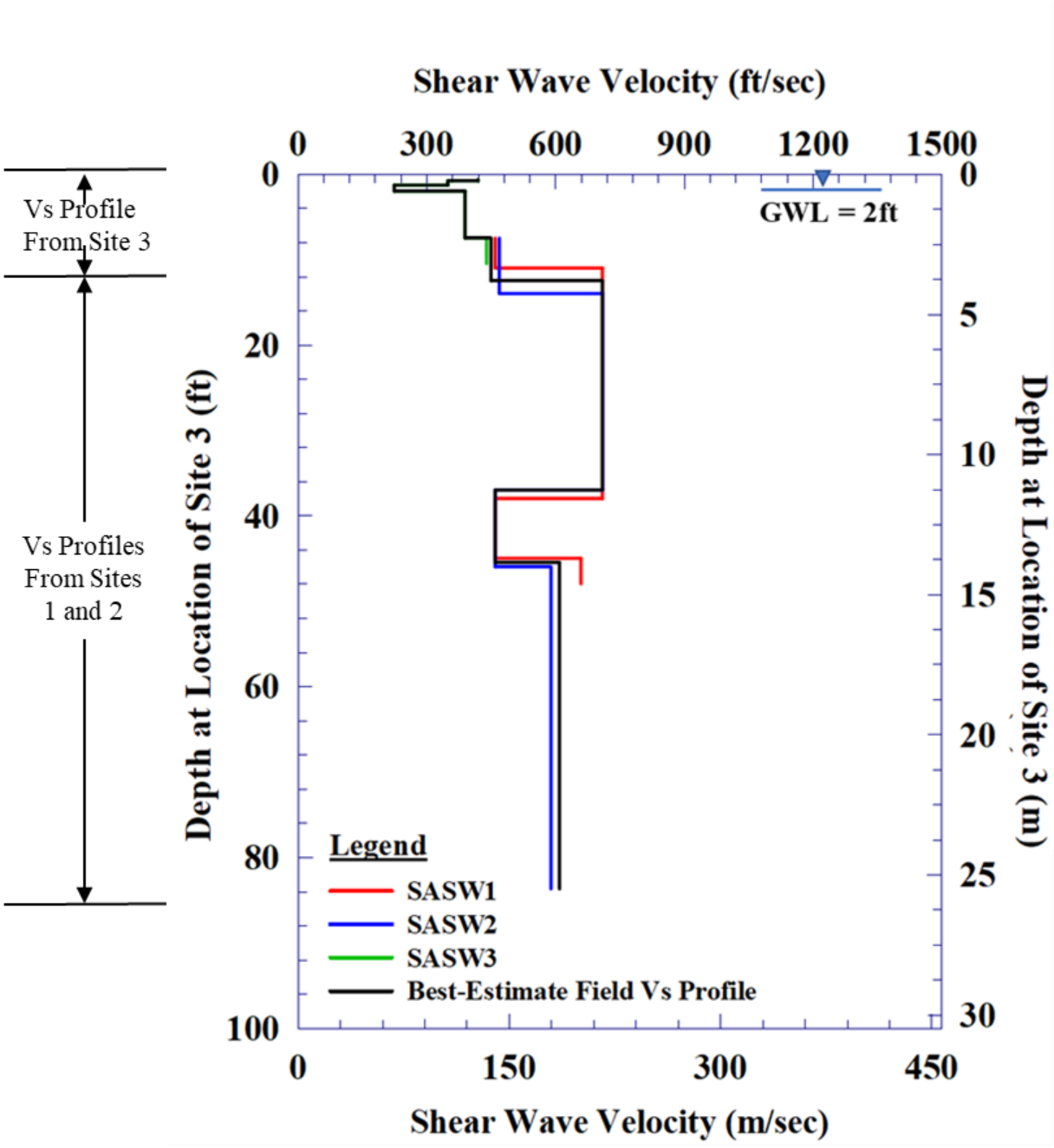

Figure C.4: Comparison of the Three, Shear-Wave Velocity Profiles Determined at Mustang Island and the Best-Estimate Field Vs Profile Recommended for the Test Site.

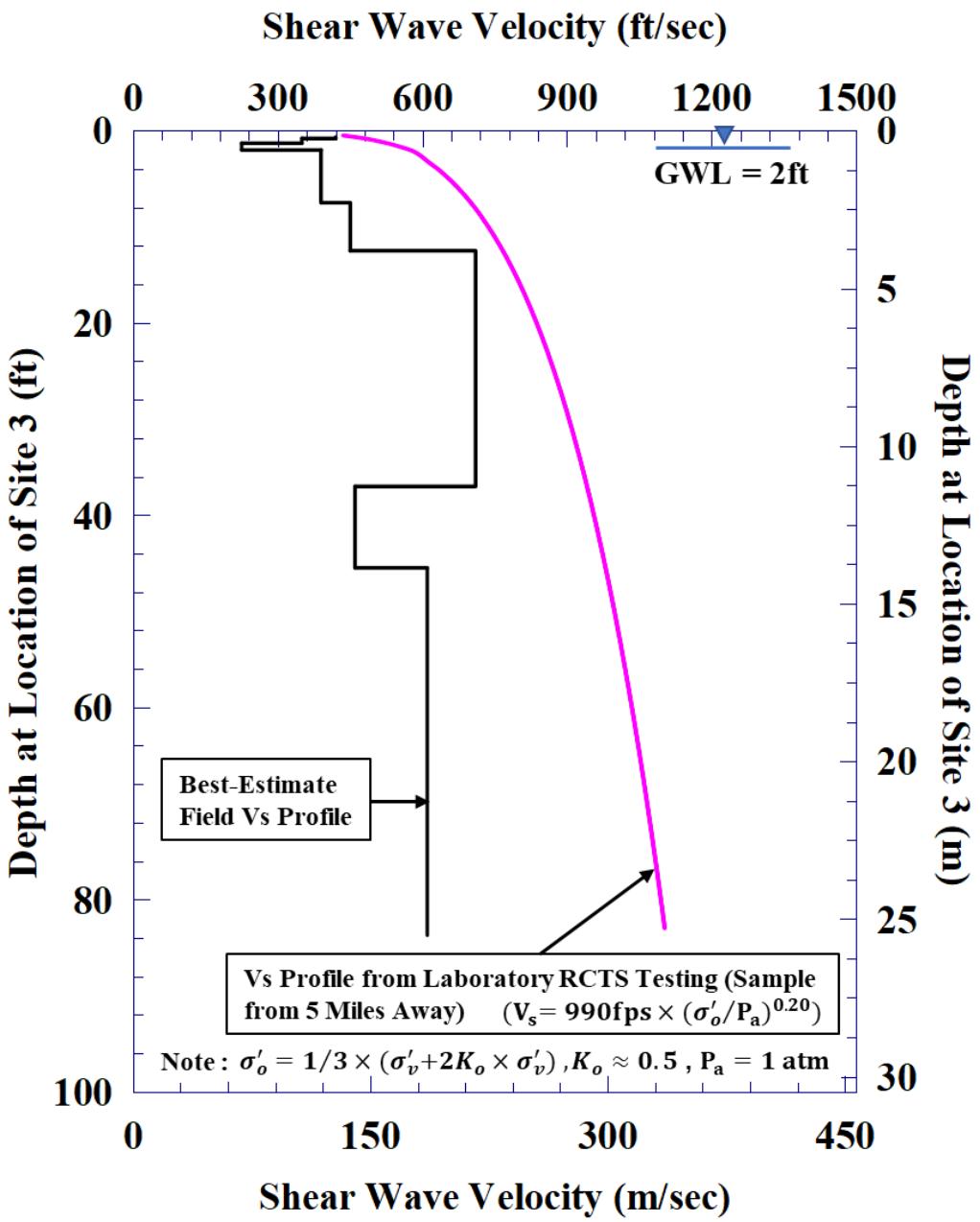

Figure C.5: Comparison of the Best-Estimate Field Vs Profile at the Test Site with the Vs Profile Determined by Laboratory RCTS Testing Using the Sample Recovered about 5 Months Earlier from a Location about 5 Miles Away (Shown in Figure C.2).

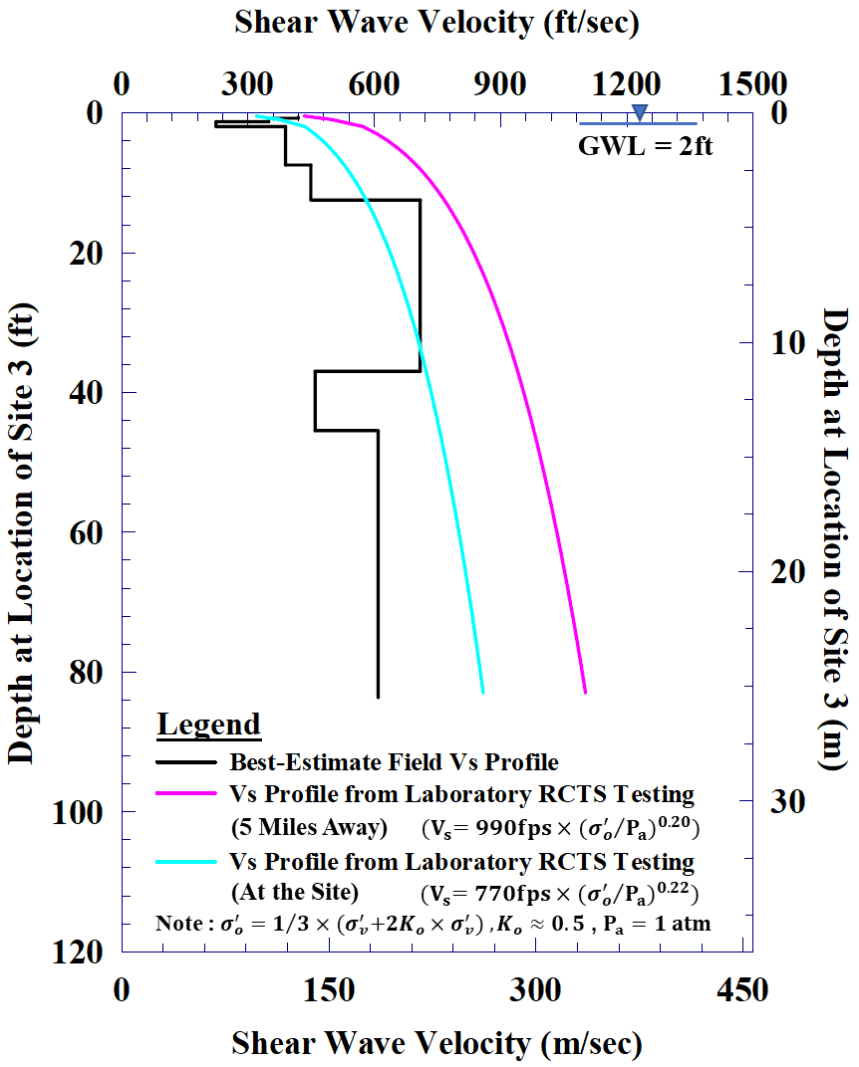

Figure C.6: Comparison of the Best-Estimate Field Vs Profile from SASW Testing and the Vs Profiles Determined by Laboratory RCTS Testing Using a Sample Recovered about 5 Months Earlier from Site A (5 Miles Away) and a Sample from Site B (the Test Site).

Table C.1: Parameters Associated with the Two Soil Samples Tested in the Laboratory Using RCTS Equipment.

Parameter	Sample from Test Site (Site B)	Sample from 5 Miles from Test Site (Site A)
Saturated Unit Weight, γ_{sat} (pcf)	124	127
Total Unit Weight, γ_t (pcf)	120	105
Void Ratio, e	0.67	0.59
Water Content, W_c (%)	20.3	0.1
Specific Gravity, G_s	2.65	2.65
Degree of Saturation, S_r (%)	80.9	0.3

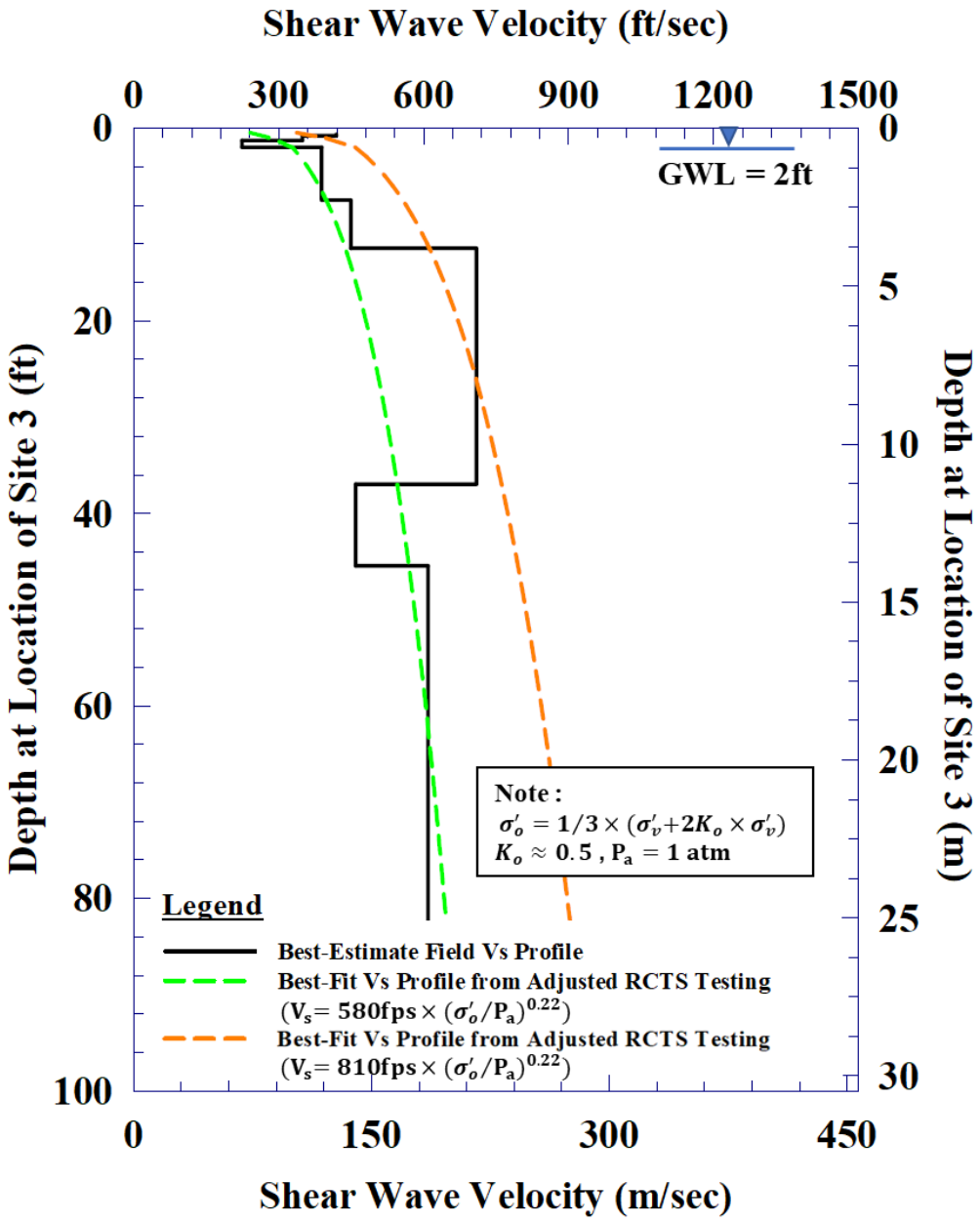

Figure C.7: Comparison of the Best-Estimate Field Vs Profile from SASW Testing and Two Adjusted Best-Fit Curves Using Vs Profiles Determined by Laboratory RCTS Testing.

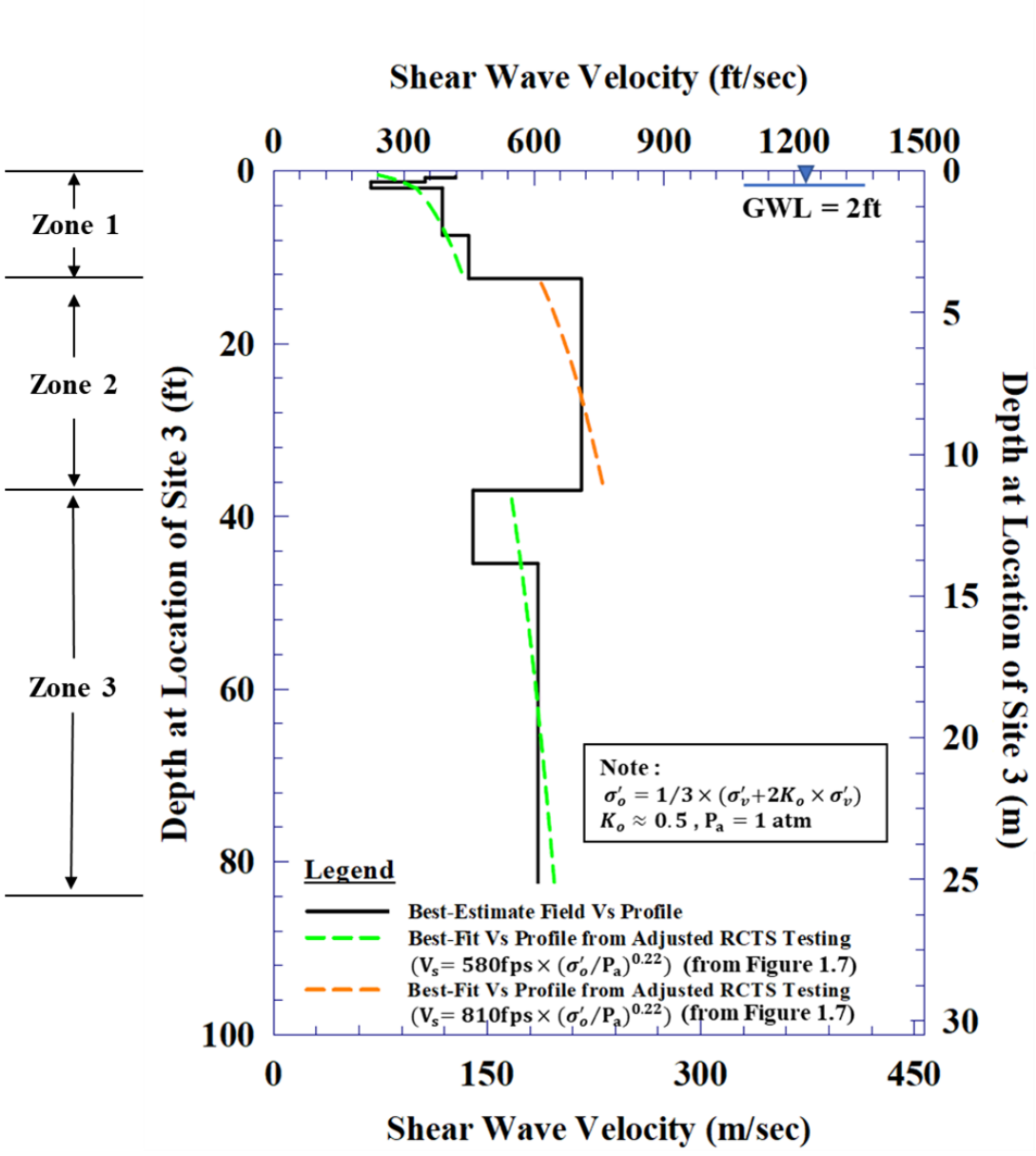

Figure C.8: Division of the Best-Estimate Field Vs Profile into Three Zones Combined with the Recommended Laboratory Vs Profile for Each Zone.

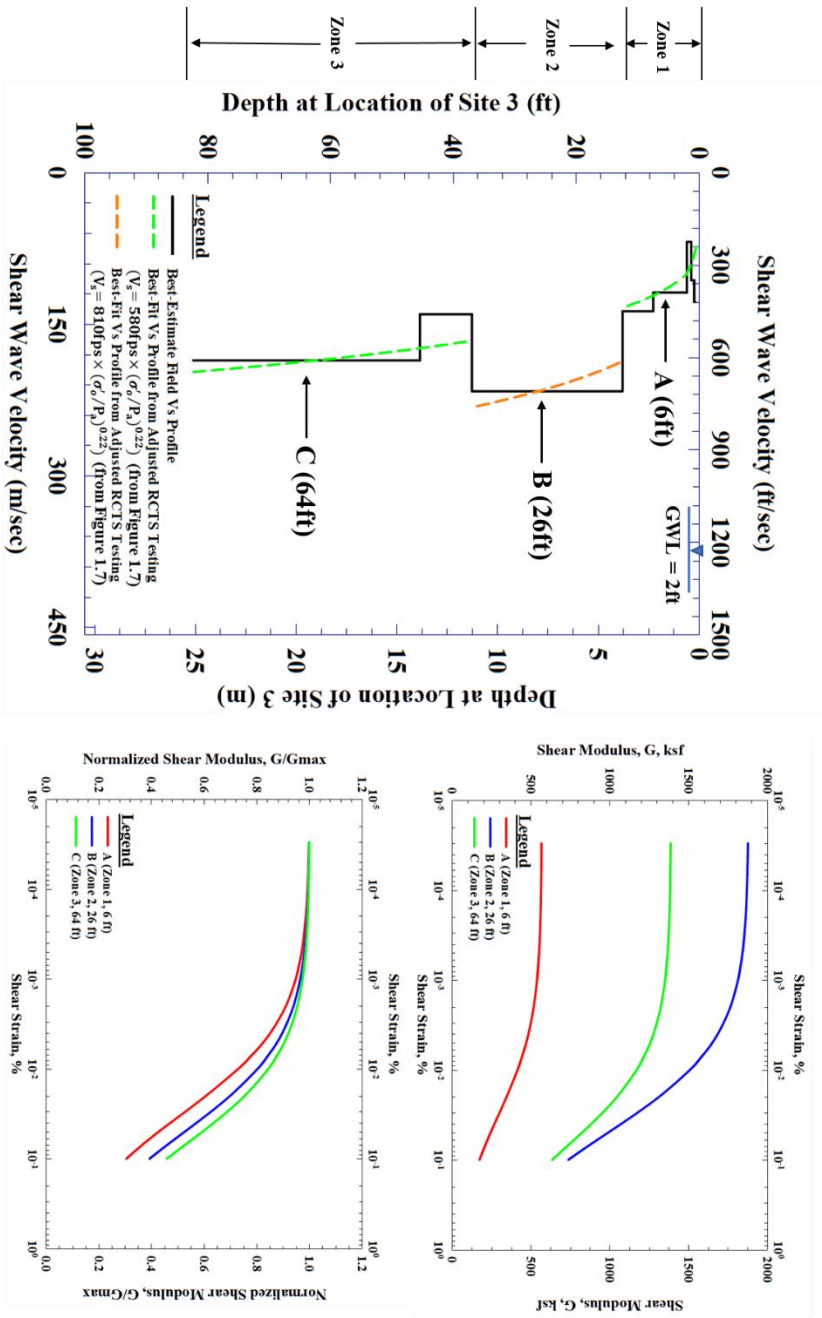

Figure C.9: Comparison of G/Gmax – Log γ Curves and G – Log γ Curves at the Mean Effective Confining Pressure at the Mid-Depth of Each Zone.

Bibliography

API. (2014). API RP 2GEO. https://doi.org/10.1007/978-1-4615-9753-7_11

Austin, S., & Jerath, S. (2017). Effect of soil-foundation-structure interaction on the seismic response of wind turbines. *Ain Shams Engineering Journal*, *8*(3), 323–331. https://doi.org/10.1016/j.asej.2017.05.007

Bauer, J. F. (2018). Laboratory model tests to assess the effects of scale and stress on the stiffness of a laterally loaded foundation in sand. *UT Austin Master Thesis*.

Beiter, P., Nunemaker, J., Tian, T., Musial, W., Lantz, E., & Spitsen, P. (2018). 2017 offshore wind technologies market update, (September). Retrieved from https://www.energy.gov/sites/prod/files/2018/08/f54/71709_0.pdf

Benz, T. (2006). *Small-strain stiffness of soils and its numerical consequences*. *University of Stuttgart*.

Beuckelaers, W. J. A. P. (2017). Numerical modelling of laterally loaded piles for offshore wind turbines. *University of Oxford Ph.D. Dissertation*.

Briaud, J., & Gibbens, R. M. (1994). Predicted and measured behavior of five spread footings on sand.

Byrne, B. W., Burd, H., Mcadam, R., & Houlsby, G. T. (2017). PISA : New design methods for offshore wind offshore site investigation. *Society for Underwater Technology*, (September).

Cox, W. R., Reese, L. C., & Grubbs, B. R. (1974). Field testing of laterally loaded piles in sand. *Proceedings of the 6th Annual Offshore Technology Conference*, 459–464. https://doi.org/10.4043/2079-MS

Darendeli, M. B. (2001). Development of a new family of normalized modulus. *UT Austin Ph.D. Dissertation*, *1542*(9), 33–36. https://doi.org/10.1017/CBO9781107415324.004

Dasgupta, U. S. (2017). Design of laterally loaded monopile foundations in sand for offshore wind turbines. *UT AUSTIN Master Thesis*.

DNV. (2018). Support structures for wind turbines. https://doi.org/10.1016/j.jbiomech.2014.11.025

Doherty, P., Kirwan, L., Gavin, K., Igoe, D., Tyrrell, S., Ward, D., & O'Kelly, B. (2012). Soil properties at the UCD geotechnical research site at Blessington. *Proceedings of the Bridge and Concrete Research in Ireland Conference*, 499–504.

Gilbert, R., Stokoe, K., Huang, Y., Munson, J., Bauer, J., Hosseini, R., … Wang, S. (2018). Laboratory testing of lateral load response for monopiles in sand.

Hanssen, S. B. (2015). Small strain overlay to the API p-y curves for sand.

Hardin, B. O., & Drnevich, V. P. (1972). Shear modulus and damping in soils: design equations and curves. *Soil Mechanics and Foundations Division*, (SM7), 667–692. https://doi.org/10.1017/S000748530002229X

Isenhower, W. M., & Wang, S. (2013). Technical manual for LPile 2018, *2013*(October).

Ishibashi, I., & Zhang, X. (1993). Unified dynamic shear moduli and damping ratio of sand and clay. *Japanese Society of Soil Mechanics and Foundation Engineering*, *33*, 182–191. https://doi.org/10.1248/cpb.37.3229

Kacar, O., & Onur. (2014). Building a framework for predicting the settlements of shallow foundations on granular soils using dynamically measured soil properties. *UT Austin Ph.D. Dissertation*.

Kallehave, D., Byrne, B. W., Thilsted, C. L., & Mikkelsen, K. K. (2015). Optimization of monopiles for offshore wind turbines. *Philosophical Transactions of the Royal Society A: Mathematical, Physical and Engineering Sciences*, *373*(2035). https://doi.org/10.1098/rsta.2014.0100

Knappett, J. A., Caucis, K., Brown, M. J., Jeffrey, J. R., & Ball, J. D. (2016). CHD pile performance: part II – numerical modelling. *Proceedings of the Institution of Civil Engineers - Geotechnical Engineering*, *169*(5), 436–454. https://doi.org/10.1680/jgeen.15.00132

Little, R. L., & Briaud, J.-L. (1988). Full scale cyclic lateral load tests on six single piles in sand (No. TAMU-RR-5640), 1–191.

Luke, B. A., & Stokoe, K. H. (1998). Application of SASW Method Underwater, *124*(June), 523–531.

Masing, G. (1926). Eigenspannungen and verfestigung Beim Messing.

Menq, F.-Y. (2003). Dynamic properties of sandy and gravelly soils. *UT Austin Dissertation*. Retrieved from http://dspace.lib.utexas.edu/bitstream/2152/980/1/menqf032.pdf

Meyer, B. J., & Reese, L. C. (1979). Analysis of single piles under lateral loading. *Technical Report*, (3).

Middelweerd, L. (2017). Sensitivity analysis of the first natural frequency of the offshore wind turbines in the Eneco Luchterduinen wind farm Sensitivity analysis of the first natural frequency of the offshore wind turbines in the Eneco Luchterduinen wind farm. *TU Delft M.S. Thesis*.

Mosher, R. L. (1984). Load-transfer criteria for numerical analysis of axially loaded piles in sand. *Technical Report*, 302.

Munson, J. M. (2018). Development of a laboratory testing methodology to represent small strain soil conditions for laterally loaded monopiles in sands. *UT Austin Master Thesis*.

Murphy, G., Igoe, D., Doherty, P., & Gavin, K. (2018). Computers and geotechnics 3D FEM approach for laterally loaded monopile design. *Computers and Geotechnics*, *100*(August 2017), 76–83. https://doi.org/10.1016/j.compgeo.2018.03.013

Noppe, N., Iliopoulos, A., Weijtjens, W., & Devriendt, C. (2016). Full load estimation of an offshore wind turbine based on SCADA and accelerometer data Full load estimation of an offshore wind turbine based on SCADA and accelerometer data. https://doi.org/10.1088/1742-6596/753/7/072025

Park, K. (2010). Field measurements of the linear and nonlinear shear moduli of cemented alluvium using dynamically loaded surface footings. *UT Austin Ph.D. Dissertation*.

Plaxis. (2018). Plaxis 2D material models manual 2018.

Prendergast, L. J., Gavin, K., & Doherty, P. (2015). An investigation into the effect of scour on the natural frequency of an offshore wind turbine. *Ocean Engineering*, *101*, 1–11. https://doi.org/10.1016/j.oceaneng.2015.04.017

Reese, L. C., Cox, W. ., & Koop, F. . (1997). Analysis of laterally loaded piles in sand.

6th Annual Offshore Technology Conference. https://doi.org/10.4043/2080-MS

Santos, J., & Correia, A. (2001). Reference threshold shear strain of soil . Its application to obtain an unique strain-dependent shear modulus curve for soil Deformation de cisaillement limite de référence des sols . Utilisation pour obtenir une relation unique entre le module de cisaill. *15th International Conference on Soil Mechanics and Geotechnical Engineering*, 267–270.

Stokoe, K. H., & Santamarina, J. C. (2000). Seismic-Wave-Based testing in Geotechnical Engineering. *ISRM International Symposium. International Society for Rock Mechanics.*, *1*(November 2000), 1490–1536.

Tatsuoka, F., Presti, D. Lo, & Kohata, Y. (1995). Deformation characteristics of soils and soft rocks under monotonic and. *Third International Conference on Recent Advances in Geotechnical Earthquake Engineering and Soil Dynamics, II*, 851–879.

Weijtjens, W., Verbelen, T., De Sitter, G., & Devriendt, C. (2016). Foundation structural health monitoring of an offshore wind turbine—a full-scale case study. *Structural Health Monitoring*, *15*(4), 389–402. https://doi.org/10.1177/1475921715586624

Zdravković, L., Taborda, D. M. G., Potts, D. M., & Jardine, R. J. (2015). Numerical modelling of large diameter piles under lateral loading for offshore wind applications Numerical modelling of large diameter piles under lateral loading for offshore wind applications, (August). https://doi.org/10.1201/b18442-105

Vita

Yunhan Huang was born in Jiangsu, China. He received the Bachelor of Science from Hohai University in June 2013 and the Master of Science from The University of Texas at Austin in May 2015. He worked as an Infrastructure Engineer in Meinhardt Shenzhen Office for one year until he started the Ph.D. program at The University of Texas at Austin in August 2016.

Permanent email address: Yunhan_huang@utexas.edu